Dissertation

submitted to the

Combined Faculties for the Natural Sciences and Mathematics

of the Ruperto-Carola University of Heidelberg, Germany

for the degree of

Doctor of Natural Sciences

Presented by

Doris Ho Mer Lin

Singapore

Oral examination: 13th March 2015

Study on the applicability of structural and morphological parameters of selected uranium compounds for nuclear forensic purposes

Reviewers: Professor Dr. Thomas Fanghänel
Professor Dr. Petra Panak

I dedicate this thesis to F.Y.F., without whom, I would not have done my PhD.
May God bless his spirits and soul and keeps him safe always.

Acknowledgements

I begin by first thanking DSO National Laboratories, Singapore for giving me the opportunity and for sponsoring my PhD studies in the Institute for Transuranium Elements (ITU)/University of Heidelberg, Germany.

Next, I will like to thank my supervisor, Professor Dr. Thomas Fanghänel for his supervision and support. It has been my privilege to work in this prestigious institute where he had been the director for more than 8 years. I am also honoured to have been part of the unit of Nuclear Safeguards and Forensics in ITU. I wish to thank Klaus Mayer for his guidance and support and for the collaborations his group has with IAEA, Vienna and CEA, France. The collaborations have been instrumental for my thesis. Therefore, I also wish to thank our collaborators, Andrey Berlizov from IAEA and Fabien Pointurier from CEA for the success we have shared. I will also like to thank colleagues (Patric Lindqvist-Reis and Dieter Schild) from the Institute of Nuclear Waste Disposal (INE), Karlsruhe, Germany for being so supportive while I was using the instrument from their institute.

There are several ITU colleagues I wish to acknowledge, who have made my time in ITU enjoyable and rewarding. Colleagues from nuclear forensics, Adrian Nicholl and Zsolt Varga have been extremely supportive at work. Dario Manara, Markus Ernstberger, Bert Cremer and Thierry Wiss from the unit of Material Research had shown me relentless support and guidance while I was doing my research in their laboratories. A big thank you to Rachel Eloirdi and Lorenzo Fongaro from the unit of Basic Actinide Research and Hot Cells, respectively, for taking an interest in my work and for their patience and guidance.

Summary

Nuclear forensic science or nuclear forensics, is a relatively young discipline which evolved due to the need of analysing interdicted nuclear or radioactive material, necessary for determining its origin. Fundamentally, nuclear forensic science makes use of measurable material properties, referred to as "signatures", which provide hints on the history of the material. As part of the advancement in this multi-faceted field, new signatures are constantly sought after and as well as analytical techniques to efficiently and accurately determine the signatures. The work carried out in this study is part of this fulfilment to investigate new structural and morphological parameters as possible new nuclear forensic signatures for selected uranium compounds.

The scientific goals have been oriented into three parts for investigations in this study. Firstly, five different compositions of uranium ore concentrates (UOCs) were prepared in the laboratory under well-defined conditions. These materials were subsequently characterized by several techniques such as X-ray diffraction, thermogravimetry/differential thermal analysis, Infrared and Raman spectroscopy, mass spectrometry, scanning electron microscopy etc. Such materials were pivotal for comparison with the industrial samples.

Secondly, several uranium compounds, mainly UOCs were measured using Raman spectroscopy. At least three different Raman spectrometers were used and a comparison made in their performance and suitability for nuclear forensics. Raman spectra of industrial uranium materials were interpreted with regard to compound identification and to determination of (anionic) impurities. Anionic impurities that were present were identified and they could provide clues to the processing history of the samples. Statistical techniques such as principal component analysis (PCA) and partial least square-discriminant analysis (PLS-DA) were applied to several Raman spectra. The analysis showed that different compositions of uranium compounds could be discerned based on their spectra. Apart from bulk analysis of the samples, Raman was also used to measure single particles. Results showed that although particle analysis could be slightly less precise in terms of the peak positions, it could still distinguish the different form of ore concentrates. Raman spectroscopy is therefore, a useful technique for probing the molecular structure of different uranium compounds. It can be used not just for forensic purposes, but for nuclear safeguards as well.

Last but not the least, microstructural fingerprints were investigated as part of the search for ways to differentiate different forms of UOCs. Currently, forensic investigations involve studying the morphology of interdicted samples using scanning electron microscope (SEM). This approach has remained qualitative and more quantitative ways are needed to study the variety of samples available. In this study, the concept of morphological fingerprint was explored by studying the sizes and shapes of dispersed particles. Although this method can be tedious, it can be applied to small number of

samples. Two samples were shown to have different sizes but similar shapes and therefore they could be distinguished. A different property of the sample, known as image texture was studied for the first time, using Angle Measure Technique algorithm. SEM images were taken and transformed into numeric data using the algorithm. The data processed by PCA and PLS-DA indicated that image texture could differentiate the samples.

Both structural (Raman spectroscopy) and morphological (using SEM) aspects of UOCs have been studied at great lengths, demonstrating that these signatures may provide useful hints on the history of the material. The data provided in this thesis can serve as a good reference for future nuclear forensic investigations.

Zusammenfassung

Die nukleare Forensik ist ein relativ junger Zweig der Wissenschaft, der aus der Notwendigkeit heraus entstanden ist geschmuggeltes Material (Kernbrennstoffe oder sonstige radioaktive Stoffe) zu untersuchen mit dem Zweck dessen Herkunft zu bestimmen. Die Methodik basiert grundsätzlich darauf, messbare Materialeigenschaften – so genannte "Signaturen" – zu nutzen um Hinweise auf die Historie des Materials zu erhalten. Wesentliche Fortschritte in diesem facettenreichen Bereich werden durch das Identifizieren von neuen Signaturen und die Entwicklung bzw. Anwendung effizienter und genauer Analysentechniken erreicht. Im Rahmen der vorliegenden Arbeit wurden chemische Zusammensetzung und Partikelmorphologie verschiedener Uranverbindungen als neue Signaturen für die nukleare Forensik untersucht.

Die wissenschaftlichen Ziele der Arbeit wurden entlang von drei Schwerpunkten verfolgt:

- Zunächst wurden fünf verschiedene Uranverbindungen, wie sie typischerweise bei der Urangewinnung angetroffen werden (oft als Uranerzkonzentrat oder Yellow Cake bezeichnet), im Labor unter kontrollierten Bedingungen in reiner Form synthetisiert. Diese Verbindungen wurden charakterisiert mit Hilfe von Röntgenbeugungsanalyse, Thermogravimetrie, Differentialthermoanalyse, Infrarotspektrometrie, Raman Spektrometrie, Massenspektrometrie und Elektronenmikroskopie. Der Vergleich dieser Materialien mit industriell gewonnenen Uranerzkonzentraten lieferte wichtige Hinweise zur Interpretation der Signaturen.
- Weiterhin wurden unterschiedliche Uranverbindungen, zu meist Uranerzkonzentrate, mit Raman Spektroskopie untersucht. Dabei wurden drei verschiedene Raman Spektrometer eingesetzt und deren Leistungsfähigkeit mit Blick auf eine Anwendung in der nuklearen Forensik vergleichend untersucht. Die für die industriellen Uranmaterialien erhaltenen Spektren wurden insbesondere mit Blick auf die Identifizierung der jeweiligen Verbindung und die Anwesenheit von Verunreinigungen analysiert. Die anioinischen Verunreinigungen liefern Hinweise auf die Natur der chemischen Prozesse bei der Verarbeitung des Uranerzes. Neben einer Betrachtung der typischen Schwingungbanden wurden auch die kompletten Spektren mit statistischen Techniken wie principal component analysis (PCA) und partial least squares discriminant analysis (PLS-DA) ausgewertet wurden auf eine, wobei die verschiedenen Uranverbindungen sich jeweils zu Clustern gruppierten. Darüber hinaus wurde Raman Spektrometrie auch auf einzelne Partikel angewandt, wobei auch in diesem Fall die unterschiedlichen Uranverbindungen klar identifiziert werden konnten, wenngleich die Peakpositionen weniger genau bestimmbar waren.

Insgesamt zeigten die Untersuchungen, dass Raman Spektrometrie eine äußerst nützliche Methode ist um die molekulare Struktur von Uranverbindungen zu identifizieren und damit sowohl in der nuklearen Forensik als auch im Bereich der Kernmaterialüberwachung einsetzbar.

- Schließlich wurde die Partikelmorphologie untersucht um eine mikrostrukturelle Signatur zu etablieren, die es erlaubt Uranerzkonzentrate aus verschiedenen Prozessen zu unterscheiden. Während bisherige Untersuchungsmethoden unter Verwendung der Rasterelektronenmikroskopie (REM) eher empirisch und qualitativ ausgelegt waren, wurden in der vorliegenden Arbeit die Geometrie und Dimensionen von Partikeln verschiedener Verbindungen und aus unterschiedlichen Anlagen quantitativ erfasst. Obwohl die Methode sehr aufwändig ist, kann sie erfolgreich eingesetzt werden um Material aus unterschiedlichen Prozessen zu unterscheiden. Eine weitere Eigenschaft der Partikel, nämlich deren Oberflächenstruktur oder Textur, wurde erfasst und in numerische Daten umgesetzt. Diese Daten wurden mit PCA und PLS-DA ausgewertet, wobei sich zeigte, dass auch dies eine Signatur ist, die es erlaubt Uranverbindungen mit unterschiedlicher Prozesshistorie von einander zu unterscheiden.

Insgesamt konnte mit dieser Arbeit in umfassender Weise gezeigt werden, dass sowohl die Interpretation molekularer (mittels Raman Spektroskopie) als auch morphologischer (mittels REM) Daten wertvolle Hinweise auf die Historie von Uranverbindungen unbekannter Herkunft geben können. Die Datensammlung, die im Rahmen dieser Dissertation erstellt wurde, stellt eine wertvolle Referenz dar für künftige nuklear-forensische Untersuchungen an Uranverbindungen.

Table of Contents

List of Abbreviations

ADU	Ammonium diuranate
AMT	Angle Measure Technique
ANSTO	Australian Nuclear Science and Technology Organisation
AUC	Ammonium uranyl carbonate
BA	Bulk Analysis
BET	Brunauer, Emmett and Teller method
Cal	Calibration
CV	Cross Validation
FT-IR	Fourier Transform Infrared Spectroscopy
GC-MS	Gas Chromatography Mass Spectrometry
HEU	High enriched uranium
HT-XRD	High Temperature X-Ray Diffraction
ICP-MS	Inductively Coupled Plasma Mass Spectrometry
IR	Infrared Spectroscopy
LIBS	Laser-Induced Breakdown Spectroscopy
ITU	Institute for Transuranium Elements
MA	Mean Angle
MC-ICP-MS	Multi-collector Inductively Coupled Plasma Mass Spectrometry
MDU	Magnesium diuranate
NIR	Near Infrared Reflectance Spectroscopy
PC	Principal Component
PCA	Principal Component Analysis
PLS-DA	Partial Least Squares-Discriminant Analysis
REE	Rare-Earth Element
RMSEC	Root Mean Square of Calibration
RMSECV	Root Mean Square of Cross Validation
ROI	Region of Interest
SDU	Sodium diuranate
SEM	Scanning Electron Microscopy
SPA	Single Particle Analysis
SIMCA	Soft Independent Modelling of Class Analogy
SIMS	Secondary Ion Mass Spectrometry

STEM	Scanning Transmission Electron Microscopy
TEM	Transmission Electron Microscopy
TG/DTA	Thermogravimetry/Differential Thermal Analysis
TIMS	Thermal Ionisation Mass Spectrometry
UNH	Uranyl nitrate hexahydrate
UH	Uranyl hydroxide
XRD	X-Ray Diffraction

1. Introduction

1.1 The concept of Nuclear Forensics

Following the fall of the former Soviet Union in 1991, a new discipline coined as *Nuclear Forensic Sciences* or *Nuclear Forensics* has emerged. The aftermath of the breakdown resulted in insufficient control of the large supplies of nuclear material and consequently, material often went missing. The first cases of nuclear or other radioactive material detected out of regulatory control were reported in Switzerland and Italy in the same year and subsequently, more cases were found in other parts of Europe [1-3]. Nuclear and other radioactive materials pose risk to human health and safety as they emit radiation and should be properly handled. More importantly, in the context of this work, nuclear materials are also fissionable and these pose a proliferation concern. Illegal possession of such material could indicate a malicious intent.

Nuclear forensics plays a pivotal role in determining the origin of any 'found' material and contributes to strengthen the safeguards of such material to assume legitimate use. It is the analysis of intercepted illicit nuclear or radioactive material and any associated material to provide evidence for nuclear attribution [4]. Answers to questions such as 'What is the material and what was its purpose?', 'Who was the last legal owner?', 'How was it produced?' must frequently be provided.

In order to provide answers, nuclear forensics relies strongly on the analysis of measurable or characteristic parameters, also often referred to as *signatures* or *fingerprints*. In this research field, these parameters refer to any physical, chemical, isotopic characteristics associated with the material. Over the past two decades, several parameters or combination of parameters, have been used in nuclear forensic investigations depending on the nature of the seizures. These parameters will be described in the later part of this chapter.

In the period 1993-2013, International Atomic Energy Agency (IAEA) has registered 2489 confirmed incidents in its Incident and Trafficking Database (ITDB), by 126 participating states. Nearly half of the reported incidents (1242) occurred in the period of 2007-2012 and out of these cases, 10 % were related to nuclear materials [5]. IAEA has five categories of nuclear materials: unirradiated direct use material, irradiated direct use material, alternative material, indirect use material and commercial radioactive sources [4]. Of utmost concern are the highly enriched materials such as uranium (> 20 % ^{235}U) and plutonium (< 7 % ^{240}Pu) as they could be used to construct nuclear weapon. Although there are few cases with such materials [6], their occurrences cannot be undermined.

Interdicted nuclear materials can be found in different physical forms, purity, enrichment and even quantity. Such materials are produced via the different stages of the nuclear fuel cycle. Therefore, the fuel cycle is delineated here with a focus of the subject of

interest, i.e. production of uranium ore concentrates (UOCs), or colloquially known as yellow cakes. Processes leading to the production of UOCs (front end of the fuel cycle) are more emphasized than the back end cycle, due to easier access to front-end fuel cycle materials.

1.2 Uranium Fuel Cycle

1.2.1 Mining

Nuclear fuel cycle is an industrial process encompassing all the activities involved in the production of electricity in nuclear power reactors [7]. It begins with the mining of uranium from the various ores that can be found on Earth. The most common or primary mineral is uraninite (also known as pitchblende), which is UO_x where x varies from 2 to 2.5. Uranium is largely mined by three methods: open pit, underground mines or by in-situ leaching (ISL) and the choice largely depends on the depth of uranium deposits. In underground and in open pit mining, the ore containing uranium has to be mined out and transferred to a separate milling facility where the actual uranium dissolution is done. In contrast to that, ISL leaches uranium without having the need to dig out the ore.

1.2.2 Milling

Following the mining process, milling of the ore proceeds with a number of stages. These facilities are usually found close to mines and a single mill could also process ores from several mines or pits [8]. Milling stages include weighing, sorting, crushing, sampling and grinding. Comminution is necessary to reduce the particle size of the mined ore so that uranium can be readily extracted by leaching. If alkali treatment is used, finer grinding is necessary for the effective extraction of uranium [9]. For certain vanadium containing uranium ores, roasting of the ores is required to improve the solubility of important constituents and to improve the physical characteristics of the ores [10, 11].

1.2.2a Leaching of uranium ore

The ores are subsequently leached for uranium and this process is based on acidic or basic dissolution of uranium. Leaching with sulphuric acid is more predominant due to its cost effectiveness. Sulphuric acid is preferred over hydrochloric or nitric acid due to environmental reasons [11]. Oxidation of the insoluble U(IV) must take place in order to oxidize to the +6 state, which can be readily recovered. In the case of acidic leaching, oxidation is carried out in the presence of a catalyst ferric ion, independent of the reagent used as oxidant ($NaClO_3$ or MnO_2 or O_2), which then regenerates ferric ion from ferrous ion.

$$UO_3 + 2H^+ \rightarrow UO_2^{2+} + H_2O \quad (1.1)$$

$$UO_2 + 2Fe^{3+} \rightarrow UO_2^{2+} + 2Fe^{2+} \quad (1.2)$$

$$6Fe^{2+} + NaClO_3 + 6H^+ \rightarrow 6Fe^{3+} + NaCl + 3H_2O \quad (1.3)$$

In the case of alkaline leaching, carbonate from sodium bicarbonate, sodium carbonate or carbon dioxide is used in the leach circuit. This method is mainly used when the gangue materials contain carbonate or other acid consuming components. Although alkaline leaching may not be as effective (considerably slower) as acid leaching for the recovery of uranium, it is more advantageous for high carbonate ores. The alkaline process is also much more selective compared to the acidic process and can be described by the chemical reactions below.

$$2UO_2 + O_2 \rightarrow 2UO_3 \quad (1.4)$$

$$UO_3 + CO_3^{2-} + 2HCO_3^- \rightarrow [UO_2(CO_3)_3]^{4-} + H_2O \quad (1.5)$$

Oxygen is normally used as the oxidizing agent to transform U(IV) into the more soluble U(VI). The buffering action of bicarbonate is necessary to prevent the further formation of sodium diuranate [11]:

$$UO_3 + 3Na_2CO_3 + H_2O \rightarrow Na_4(UO_2)(CO_3)_3 + 2NaOH \quad (1.6)$$

$$2Na_4(UO_2)(CO_3)_3 + 6NaOH \rightarrow Na_2U_2O_7 + 6Na_2CO_3 + 3H_2O \quad (1.7)$$

The El Dorado plant operating in Beaverlodge, Saskatchewan, Canada and one of the two circuits of Atlas, Utah, USA used the alkaline leaching process with O_2 as oxidant and direct precipitation with NaOH. Some plants used acid leach followed by precipitation with NaOH. These include the plants in Somair, Niger and Ranstad, Sweden.

1.2.2b Solid-liquid separation

A liquid-solid separation follows the leaching process before the concentration and purification steps. The leached solids have to be separated from the uranium bearing solutions and this can be done with practically any solid-liquid separating device, e.g. thickeners, filters or cyclones. Counter-current washing in thickeners, also known as counter-current decantation (CCD) is frequently used. Filters may be preferred over thickeners for higher grade ores. Flocculents such as polyacrylamides can facilitate solid-liquid separation.

1.2.2c Concentration and purification

After the leaching process, the concentration and purification steps follow. The solution containing uranium, also termed as pregnant strip solution is processed further by ion exchange (IX) and/or solvent extraction (SX).

Uranyl carbonates or sulphates formed from the leaching process are essentially anionic complexes and are extracted by strong base resins containing tertiary or quaternary amines as functional groups in the case of IX. The efficiency of this process depends highly on the pH of the liquid phase and the presence of other anionic species that can compete for the absorption process. In the acid system, a pH between 1.5-2.0 ensures that $UO_2(SO_4)_3^{4-}$ is the predominant uranyl species among other anions such as SO_4^{2-}, HSO_4^-, UO_2SO_4,

$UO_2(SO_4)_2^{2-}$. In the alkaline system, pH is adjusted to 9-10 for the loading step. The basic principles can be illustrated in the following equations:

$$4RX + [UO_2(SO_4)_3]^{4-} \leftrightarrow R_4[UO_2(SO_4)_3] + 4X^- \quad (1.8)$$

$$4RX + [UO_2(CO_3)_3]^{4-} \leftrightarrow R_4[UO_2(CO_3)_3] + 4X^- \quad (1.9)$$

where R is normally a long-chain aliphatic amine and X is the anionic exchanger on the resin. Due to a high preference for $UO_2(CO_3)_3^{4-}$ and the presence of fewer foreign anions, the alkaline process results in a higher degree of selectivity. After the preferential absorption of the analyte of interest, the absorbed analyte must be stripped from the resin. This is done using a medium that elutes uranium complexes from the resin. Elution can be done with (1 M) chloride or nitrate solutions. However, these anions interfere with subsequent loading since they have stronger binding affinity for the column resins. Therefore, elution is preferably carried out with sulphates for regeneration. In the case of the alkaline system, sodium carbonate and sodium bicarbonate solutions are used for extraction. The ion-exchange technique can be operated batch-wise or continuously.

Unlike IX that can tolerate slight cloudiness, the liquor must be clarified for SX. For SX, the uranium ions/complexes are extracted into the organic phase, which is immiscible with the aqueous feed solution. The concentrated or purified uranium complexes are subsequently rinsed and then back-extracted into the aqueous phase. Generally, two different types of organic extractants are used for extraction, namely the alkylated phosphoric acids and the higher aliphatic amines dissolved in a solvent, commonly kerosene. The acids act as cation exchangers and the acidic hydrogens are replaced by the uranyl ions. The neutral species is then extracted into the organic phase.

$$UO_2^{2+}(aq) + 2(RO)_2PO_2H\,(org) \rightarrow UO_2[PO_2(OR)_2]\,(org) + 2H^+(aq) \quad (1.10)$$

Concentrated mineral acids or dilute acids are used to strip uranium from the organic solvent. Solvent extraction with amines is selective for uranium. Solutions of tri-octylamine dissolved in kerosene with a modifier like isodecanol is widely used. They have strong affinity for uranyl sulphates and formed ion-pairs of the type $(R_3NH^+)_2[UO_2(SO_4)_2]^{2-}$ that are soluble in the organic solvents. Uranium can be stripped off from the solvent by nitrates, chlorides, sulphates, carbonates, hydroxides and acid.

In general, SX is the preferred option when there is a relatively high concentration of uranium in the feed. For lower concentrations (less than 1g/L), the IX process is more suitable. IX is also more suitable for alkaline carbonate solutions.

Alternatively, a combination of the two techniques has been developed. Known as ELUEX, uranium can be treated by IX followed by SX. The first IX stage recovers almost quantitatively uranium, thus increasing the concentration of uranium with a consequent reduction in mass flow. The second SX stage purifies further and it's more effective since the uranium concentration is higher and the process can be scaled down by a factor of 20-30. For

instances, the plant of Rössing in Namibia and several facilities in USA (Union Carbide and Federal American Partners, Pathfinder, Lucky Mc) used the ELUEX process.

For a high grade ore and sufficiently pure pregnant liquor, it is possible to skip the above concentration/purification steps and undergo precipitation directly, such as McArthur River (Canada) facility.

1.2.2d Precipitation of uranium ore concentrates

The term direct (double) precipitation is used for the precipitation of pregnant solutions without any prior purification (by IX or SX) for the acidic process. Otherwise, a classic precipitation is normally carried out following the purification step. Direct double precipitation is a two-stage process; the 1st stage is carried out with lime to precipitate iron and other impurities like sulphates and hydroxides. Sulphates are precipitated as calcium sulphate or gypsum. The 2nd stage of the precipitation is then carried out with ammonia, magnesia or hydrogen peroxide [12].

As mentioned earlier, leaching with alkaline medium is a selective process and thus this leads to the possibility of direct precipitation with sodium hydroxide. This process is normally carried out at a temperature range of 50 to 80 ^{o}C for 6 to 12 hours. In cases when vanadium is present and can co-precipitate with uranium, direct precipitation is not favourable. It may be necessary to add an additional stage of treatment. In Canada, sodium vanadate is readily removed by calcination of the precipitate (by roasting).

Precipitation of the pregnant liquor from the acidic circuit can occur with hydrogen peroxide, magnesia, ammonia or ammonium hydroxide. The most common precipitating reagent has been gaseous ammonia or ammonium hydroxide with the following reaction.

$$2UO_2(SO_4)_3^{4-} + 6NH_4OH \rightarrow (NH_4)_2U_2O_7 + 6SO_4^{2-} + 4NH_4^{+} + 3H_2O \qquad (1.11)$$

This is normally done at temperatures ranging from 30 to 50 ^{o}C and the terminal pH is between 7 to 8 [12]. It should be noted that basic uranyl sulphate can be formed as it requires only one-third of the ammonia needed to form the diuranates.

$$2UO_2(SO_4)_3^{4-} + 2NH_4OH + 6H_2O \rightarrow (UO_2)_2SO_4(OH)_2.4H_2O + 5SO_4^{2-} + 2NH_4^{+} \qquad (1.12)$$

Uranium can also be precipitated by MgO where the final pH is between 7.0 and 7.5.

$$UO_2SO_4 + MgO + xH_2O \rightarrow UO_3.xH_2O + MgSO_4 \qquad (1.13)$$

where x is between 1 and 2.

Precipitation with hydrogen peroxide has gained considerable attention owing to few reasons. Firstly, the use of ammonia as precipitant caused environmental problem as a pollutant, whereas hydrogen peroxide decomposes to harmless oxygen and water. Secondly, the specifications on the chemical purity of the product have become more stringent, thus the selective peroxide precipitate is favourable. Thus, precipitation with peroxide received much

interest as it is a selective process: important impurities such as vanadium and molybdenum are oxidized to soluble peroxo complexes like VO_5^{3-} and MoO_5^{2-} [13]. The precipitation reaction can be represented as follows:

$$UO_2(SO_4)_3^{4-} + H_2O_2 + 2H_2O \rightarrow UO_4.2H_2O + 3SO_4^{2-} + 2H^+ \quad (1.14)$$

Generally, the peroxide is added as 70 % H_2O_2 and in excess at about 25 ^oC. Due to the acid formation, neutralization and maintaining the pH at 3.5 with ammonia or sodium hydroxide is required. Precipitation with H_2O_2 is carried out in Rabbit Lake (Canada) and Mobil, El Mesquite and Irigaray (USA).

Precipitation of the alkaline stripping solutions after purification is performed in the same way as the direct precipitation technique. However, the time required is considerably shorter (2 to 4 hours) and at ambient instead of elevated temperature. The terminal pH is 12. Magnesium hydroxide may be used in place of sodium hydroxide and peroxide precipitation could also be required to prevent co-precipitation of other metals. In such case, acidification of the alkaline stripping solutions should precede the precipitation. The precipitation processes seen in the above therefore produces a class of compounds known as uranium ore concentrates (UOCs), or colloquially known as yellow cakes.

1.2.3 Conversion

These intermediate products are further refined and converted into UF_6. This can be done either by the wet or dry process depicted in the Figure 1.1.

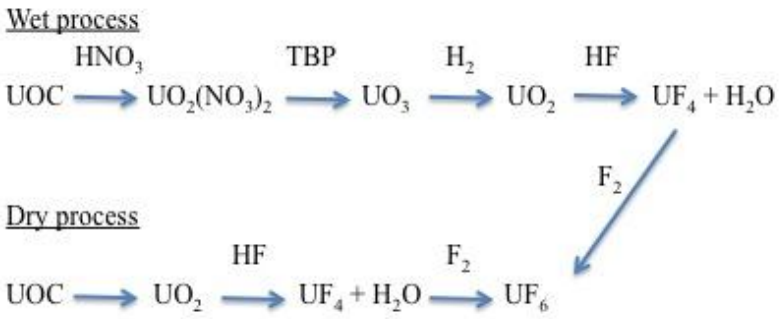

Figure 1.1: Conversion of uranium ore concentrate to UF_6 via wet or dry process

After obtaining UF_6, the gaseous product can either be further processed to enrich its fissile ^{235}U content or it is used to produce UO_2 for fuel fabrication (natural isotopic composition for e.g. CANDU reactors). After isotopically enriched, the UF_6 is also converted to UO_2 and one typical route is via the production of ADU. ADU is eventually calcined to uranium dioxide schematically represented as:

$$UF_6 \text{ (enriched in } ^{235}U) + NH_4OH \rightarrow ADU \rightarrow UO_2$$

1.3 Nuclear forensic investigations

Over the past two decades, nuclear forensics has advanced by re-purposing and adapting techniques that had already been used for nuclear safeguards, material science and geochemistry. As the variety of chemical and physical forms of nuclear material in the nuclear fuel cycle is large, various types of such materials have become part of nuclear forensic investigations. In the following section, the case studies are summarized and more importantly, signatures are described and utilized for interpretation. Such information can be categorized as *endogenic* or *exogenic* whereby the former refers to self-explanatory data (predictive approach) and the latter requires reference data for comparison (comparative approach) [14, 15].

It is reiterated that the compounds of interest in the present work are uranium ore concentrates. As seen in the uranium fuel cycle, UOCs are intermediate products containing natural uranium. While the focus resides mainly with UOCs, signatures that are applicable to other forms of nuclear material will also be mentioned.

Besides the development of signatures for interdicted industrial UOCs, it is worth noting that there are numerous reports investigating various aspects on the properties of specific UOCs, in the context of nuclear fuel fabrication. Although these topics may not be directly related to nuclear forensics, there is relevant information that can be useful for further research or reference. These details are provided in Appendix A.

1.3.1 Uranium

Uranium pellets are not uncommon interdicted material. The first seizure leading to nuclear forensic investigations in the Institute for Transuranium Elements (ITU) involved 72 uranium pellets (1.1 kg) intercepted in Ausburg, Germany in March 1992. Physical dimensions and isotopic composition of the pellets were sufficient to indicate the intended use of this low enriched uranium (2.5 % ^{235}U) pellets for a Russian graphite-moderated reactor [1]. In a different case that also occurred in Germany (Ulm), 202 uranium pellets were retrieved from a bank safe. The shape of the pellets had identified them as fuel for light water reactors. The ^{235}U enrichment of 4.38 % indicated that the pellets were meant for reload. Two nuclear fabrication plants were identified as possible origins and eventually the roughness of the fuel surface helped to identify the plant [16].

Cases involving pellets may be easier to be solved than powder. This is due to the fact that physical characteristics (such as dimensions) of fuel pellets for commercial uses are well documented and databases are available and can be relied upon [1, 2]. In contrast, powders are intermediate products and such comprehensive databases compiling characteristic parameters are not available. A case involving highly enriched uranium (HEU) powder was investigated (seizures from Czech Republic). Apart from measuring the usual

parameters of uranium content and its isotopic composition, age and impurities, the microstructure of the sample provided a large clue to its processing history although the origin remained to be speculated [2].

1.3.2 Plutonium

Plutonium is a product from the reactor, produced by neutron irradiation of uranium. In the event of analysing intercepted materials containing plutonium, its isotopic composition can indicate the reactor type which has been used to produce the material.

A well-known incident happened at Munich Airport, Germany in August 1994 where 560 g of mixed oxide (U-Pu) powder and 210 g of Li-metal were seized. The mixture contained three components: particles of uranium (hexagonal U_3O_8), rod-shaped PuO_2 and PuO_2 platelets. The plutonium isotopics was high in ^{239}Pu (87 % - weapons-grade) and low in ^{235}U (1.6 %). Particle analysis with secondary ion mass spectrometry (SIMS) suggested that the different plutonium particles were produced from the same source as their $^{240}Pu/^{239}Pu$ ratios were similar. This, together with the presence of enriched ^{6}Li led to the suspicion that there might be intention to build a nuclear device [3].

1.3.3 Uranium ore concentrates

Nuclear forensics applied to the analysis of real cases involving UOCs has also been reported. Three such cases have been published. One of the earliest cases happened in Australia where five barrels of yellow cake were stolen [17]. Another sample involving UOC was analyzed in ITU (Find-26). The incident took place in December 2003, when 3 kg of radioactive material was found in a shipment of scrap metal in Rotterdam Harbour, the Netherlands. The shipment had arrived from Jordan and through nuclear forensic investigations, the found UOC was eventually traced back to a facility in Iraq [18]. More recently, the Australian Nuclear Science and Technology Organisation (ANSTO) published another case of unknown UOC (NSR-F-130509), where extensive nuclear forensic analysis had been carried out [19]. The more recent two case studies shall be referred to in the following section where the details of several measurable parameters that have been developed for nuclear forensics are reported.

1.4 Signatures used in nuclear forensics

Signatures of natural uranium are associated with either or both of the two categories, geological origin or process related, similarly to the other nuclear forensics relevant materials e.g. plutonium or HEU. Signatures are measurable parameters involving, e.g. the measurement of the major component, uranium or minor components such as trace elements or impurities.

1.4.1 Isotope ratios

1.4.1a Lead and strontium

Lead (Pb) has four known stable isotopes (Pb-204, Pb-206, Pb-207 and Pb-208) of which only Pb-204 is non-radiogenic and the other three are derived from the decay of uranium and thorium radionuclides. The isotopic composition of natural lead is 1.4 ± 0.1 % ^{204}Pb, 24.1 ± 0.1 % ^{206}Pb, 22.1 ± 0.1 % ^{207}Pb and 52.4 ± 0.1 % ^{208}Pb [20]. In uranium ores, uranium is present at much higher level than in the crust of Earth. When computed as a ratio of Pb-204, these correspond to ratios of ^{206}Pb/^{204}Pb, ^{207}Pb/^{204}Pb and ^{208}Pb/^{204}Pb as 17.2 ± 1.2 %, 15.8 ± 1.1 % and 37.4 ± 2.6 % respectively [20]. As the U content, the Th content and the age of a deposit may vary, the huge variation between mines is observed which can be a useful signature in determining the origin of UOCs. The presence of high levels of ^{208}Pb formed by the decay of ^{232}Th was also found to be indicative of certain deposit types such as quartz-pebble conglomerate, known to contain high amounts of thorium. Additionally, given the low contribution of natural lead (< 60 %), the age of the deposit can be obtained from the ratio of ^{207}Pb/^{206}Pb thus adding another signature for attribution [21]. However, high within-mine variability of lead isotopic composition has to be taken into account.

^{87}Sr is not constant in nature and the origin of its variations is due to the long half-life of the parent nuclide ^{87}Rb. The isotopic ratio of ^{87}Sr/^{86}Sr of UOCs was therefore assessed for provenance. This ratio appeared to be a more robust indicator (less affected by production process) as the within-mine variability of the investigated UOCs were much lower than observed for the lead isotope ratios. The ratios also varied over a wide range of UOCs and therefore, it could be used to differentiate samples of different origin as well as to verify the origin by comparing with known samples [21].

Both isotopic ratios have been applied in the forensic analysis of UOCs from real incidents [18, 22].

1.4.1b Oxygen

The use of ^{18}O/^{16}O for nuclear forensic purposes has also been exploited on uranium oxide samples [23-25]. It is in fact, only usable for such samples [1]. The isotopic oxygen ratio in rainwater and surface water is known to vary depending on geolocation. Since water is commonly used as a solvent in uranium processing, differences in ^{18}O/^{16}O due to geographical location is expected in the UO_2 product [1, 14].

1.4.1c Sulphur

The use of sulphur isotope ratio (^{34}S/^{32}S) for origin assessment in UOCs has been recently published. As outlined earlier, sulphuric acid is widely used in leaching process. Clear differences in sulphur isotopic composition of δ^{34}S (δ^{34}S takes into account values of

$^{34}S/^{32}S$ of a standard) could be observed in UOCs. Low $\delta^{34}S$ values were found in certain facilities (El Mesquite, Crow Butte, USA Mobil) where in-situ carbonate leaching was carried out and could possibly be used as a predictive signature. However, there were overlaps in the $\delta^{34}S$ values between samples of different origins and therefore in such cases, the isotopic composition of sulphur should be used as a comparative signature instead [26].

1.4.1d Neodymium

Measurement and use of $^{143}Nd/^{144}Nd$ as a possible signature for uranium bearing material such as uranium ores and UOCs has recently been developed. This isotopic ratio was found to be indicative of certain ore deposit types and the within-mine variability was also smaller when compared to those of Pb and Sr [27].

1.4.2 Age or production date

The age of a nuclear material refers to the time that has elapsed since its last chemical separation or purification. With the ideas drawn from age dating in geological or archaeological processes [28], this parameter makes use of the fact that parent nuclides decay to daughter nuclides. The ratio of parent and daughter nuclides provides an indicator of the material age and thus serves as a built-in chronometer. This parameter is extremely important in the determination of the material origin as it may serve to exclude certain production or reprocessing plants that were not in operation or were not processing the type of material at the given time based on the determined production date.

This predictive signature can be based on different parent-daughter nuclides, e.g. $^{234}U/^{230}Th$, $^{235}U/^{231}Pa$ and $^{236}U/^{232}Th$ [29]. The last parent-daughter pair applies only to irradiated and reprocessed uranium since ^{236}U does not occur in nature [29]. The study of $^{234}U/^{230}Th$ and $^{235}U/^{231}Pa$ requires low detection limit of ^{230}Th and ^{231}Pa due to the long half-lives of ^{234}U (2.46×10^5 years) and ^{235}U (7.04×10^8 years) and consequently, slow in-growth of the daughter nuclides [30]. Therefore, very sensitive methods like inductively coupled plasma mass spectrometry (ICP-MS) [29, 31, 32], thermal ionization mass spectrometry (TIMS) [29] or alpha spectrometry [29, 30] have to be used for such kind of analysis. The long half-lives of uranium isotopes also limits direct (i.e. simultaneous) measurement of both parent and daughter nuclides while indirect methods (isotope dilution) for determining parent/daughter ratio offer low uncertainties but require spikes to be added. The lack of long-lived Pa isotopes that could serve as spike results in the preferred application of the chronometer $^{234}U/^{230}Th$ [29, 31, 32], due to availability of well certified Th reference materials as tracer for quantification [32].

Apart from the abovementioned, the alternative parent-daughter pairs are $^{234}U/^{214}Bi$ [31] and $^{238}U/^{234}Th$. The former is applicable or limited to HEU or very old nuclear materials due to the long time required for Bi to grow in amount [31]. In the case of latter pair, the

opposite applies. The long half-life of ^{238}U (4.5 x 10^9 years) and short half-life ^{234}Th (24 days) meant that secular equilibrium of the system is reached after ca. half a year and therefore, age determination can only be applied to young material.

Age determination is also known to plutonium material and several parent/daughter nuclide pairs are feasible: $^{238}Pu/^{234}U$, $^{239}Pu/^{235}U$, $^{240}Pu/^{236}U$, $^{241}Pu/^{241}Am$ and $^{242}Pu/^{238}U$ [28, 33, 34].

Besides the age, reactor type can also be identified from the isotopes of plutonium since it is produced by neutron irradiation of uranium. This can be explained by the fact that different types of reactors show different neutron energy spectrum and neutron flux. As the reaction probabilities (known as cross sections) of the different Pu isotopes vary with neutron energy, different reactor types will produce Pu of different isotopic composition [3, 14, 33, 34].

1.4.3 Molecular composition (based on Mid Infrared Spectroscopy and Near Infrared Reflectance Spectroscopy)

The molecular structure or composition of UOCs has already been probed with infrared spectroscopy [35] and near infrared reflectance (NIR) spectroscopy [36, 37]. Both techniques offer rapid analysis and distinction between different classes of UOCs results from the use of multivariate analysis. The two techniques are based on different principles of the interaction of photons with matter. Infrared spectroscopy is based on the absorption of incident light while reflectance spectroscopy is based on the scattering or reflection of light. Infrared spectroscopy applied to the sample from Rotterdam Harbour identified the material as ammonium uranyl carbonate [18]. In addition, process-related impurities, like nitrates and sulphates were also detected. The presence of these anions had provided some clues to the processing history of the material. Visible/NIR was applied for the analysis of the real case sample in Australia [22].

1.4.4 Elemental information based on Laser-Induced Breakdown spectroscopy (LIBS)

Laser-Induced Breakdown spectroscopy (LIBS) ablates the surface of a sample using a laser and atomises/ionizes the sample. An emission spectrum is produced, comprising of thousands of lines. In a study, 11 yellow cakes belonging to different geographical locations were measured and the complex spectra treated with statistical techniques such as Principal Component Analysis (PCA) and Soft Independent Modeling of Class Analogy (SIMCA). With the use of SIMCA model, the identification rate was 100 % for all samples [38]. This technique requires no sample preparation and certainly looks promising not just for rapid analysis in the laboratory, but also for on-site measurements.

1.4.5 Impurities or trace elements

1.4.5a Anionic impurities

The study of anionic impurities in yellow cakes have been reported using ion chromatography [39, 40]. Several anions such as Cl^-, F^-, Br^-, NO_3^-, SO_4^{2-} and PO_4^{3-} can be detected by this method. The use of the ratio (based on the concentration of two anions such as SO_4^{2-}/Cl^-) was found to be a more robust indicator than the individual anion concentration [40]. Such ratios were applied to the Australian sample. The presence of phosphates, if any, could suggest that phosphate-based rocks or material were used to produce the yellow cake [40]. In addition, the presence of fluorides, which is not a reagent used in the mining or milling process would suggest that the material might have originated from fluoride containing mineral like apatite [22].

1.4.5b Metallic impurities (rare-earth elements)

The rare-earth elements (REEs) are essentially a group of 17 metallic elements (the 15 lanthanides, yttrium and scandium). The chemistry of these elements are known to be highly similar [41]. The patterns of their occurrence have been demonstrated to vary with the type of uranium ore deposit. The REE patterns remain largely unchanged even after the milling process and therefore, they provide strong evidence about the origin of the interdicted UOC samples [18, 22]. In consequence, these patterns are an extremely important signature for providing information about the type of ore used to produce the UOC [19, 42, 43].

1.4.5c Organic impurities

Several organic compounds are used in the milling process particularly in the SX step described earlier. There has been only one study that reported the observations of dioctylamine, triisoctylamine and Alamine® 336 in UOCs using the technique of sorptive extraction with Twister® stir bar and detection by gas chromatography-mass spectrometry [44].

1.4.6 Microscopic techniques used in nuclear forensics

In the preceding section where signatures for nuclear materials in particular, UOCs have been discussed, the accompanying techniques used to make the measurements have also been highlighted. Table 1.1 reflects the summary of the signatures and techniques coupled with the type of approach (predictive or comparative). In the following section, microscopic techniques that are also used in a typical nuclear forensic investigation are outlined.

1.4.6a Scanning electron microscopy (SEM)

The use of electron microscope was found to be very valuable in forensic analysis. This is a common way to study the morphology and microstructure of the questioned material (Fund-26) and comparisons can also be made with samples from suspected origin (NSR-F-

130509). In principal, a focused beam of electrons with high energy is rastered over the sample and as a result of the interaction, different types of electrons are produced and detected separately, in function of the position of the incident electron beam. Images are therefore produced, capturing the topography (secondary electron mode or SE) or the contrast of the sample dependent on the Z number of the elements present (back scattered electron mode or BSE).

Apart from the use to study UOCs in a forensic analysis [1, 18, 22], SEM has also been used in other incidents, e.g. to analyze uranium pellets from Lithuania [2], uranium pellets intended for Russian type graphite moderated reactor (RBMK) originating from Kazakhstan or Russia [1], high enriched uranium powder from Czech Republic [2], mixed oxide (MOX) powder at Munich airport [3], plutonium powder seized at Tengen, Germany [3], radioactive waste containing plutonium from WAK, Karlsruhe, Germany [3].

1.4.6b Transmission electron microscopy (TEM)

Unlike SEM, TEM is an instrument that requires very skilled and knowledgeable operator plus delicate sample preparation. Besides, the delicate and expensive equipment is certainly not readily affordable by any nuclear forensics laboratory. Therefore, the use of TEM in nuclear forensic studies has only been scarcely described. It was used as part of a study to investigate the behaviour of uranium peroxide precipitation [45].

In nuclear forensics, TEM is typically used to analyze grain size [1]. A good example of the use of TEM (and complementary with SEM) was the case of seized samples of uranium-plutonium mixed oxide powder in Munich, which has been mentioned earlier. SEM image of the PuO_2 platelets from seized sample was compared to that of a PuO_2 reference material (from known fabrication plant) that showed no difference between the two samples. However, TEM images of both samples revealed significant difference between them [14]. The exclusion principle could be applied to exclude that particular fabrication plant.

1.4.7 Other techniques

There are other techniques, for example, alpha spectrometry, gamma spectrometry, secondary ion mass spectrometry that are used for nuclear forensic investigations [14]. In addition, classical forensics is also an important component in nuclear forensic science, especially in situations where individuals are to be identified [1].

Table 1-1: Signatures developed for the analysis of UOCs for nuclear forensics purposes (based on literature).

Analyte(s) of interest	Technique(s) used to determine analyte(s)	Information derived from analysis	Type of signature
40 elements including REEs, Pb isotopes, U isotopes	ICP-MS, XRF[1], TIMS, SIMS [19]	Identification of type of ore deposit	Comparative signature
Pb (^{204}Pb, ^{206}Pb, ^{207}Pb, ^{208}Pb) and ^{87}Sr/^{86}Sr isotopes	MC-ICP-MS [21]	Possible identification of origin of mine; age of uranium deposit based on Pb isotopes	Predictive (Pb age)/Comparative signature
Pb isotopes and trace elements (Cr, By, Er, Eu, Fe, Gd, Hf, La, Mo, Ny, Yb)	MC-ICP-MS [46, 47]	Possible identification of mine	Comparative signature
66 Elements and anions (F^-, Cl^-, Br^-, NO_3^-, PO_4^{3-}, SO_4^{2-})	ICP-SFMS Ion chromatography [39, 40]	Provides information about processing history, indicating of deposit type and possible identification of mine	Predictive (F^-)/Comparative signature
Rare-earth elements (REEs) pattern	ICP-MS [42, 43]	Possible identification of origin of mine & type of uranium deposit	Predictive signature
^{238}U/^{235}U and ^{235}U/^{234}U in UOCs	MC-ICP-MS [48]	Possible identification of origin of mine & type of depositional settings	Predictive/Comparative signature
^{228}Th/^{232}Th	ICP-MS [49], alpha spectrometry	Production date	Predictive signature
UOCs	Near infrared reflectance [36, 37]	Composition of major phase	Comparative signature
UOCs (major) and anionic impurities (SO_4^{2-}, NO_3^-, CO_3^{2-})	Infrared spectroscopy [35]	Composition of major and minor phases	Predictive/Comparative signature
All elements	LIBS [38]	Possible identification of mine	Comparative signature
Non-volatile organics (Alamine® 336, decanol)	GC-MS [44]	Possible indication of processing history based on minor organics	Predictive/Comparative signature
^{34}S/^{32}S	MC-ICP-MS [26]	Possible identification of origin of mine and indication of use of sulphates during processing	Predictive/Comparative signature
^{143}Nd/^{144}Nd	MC-ICP-MS [27]	Possible identification of origin of mine and the ore type	Predictive/Comparative signature

[1] X-Ray Fluroscence

1.5 Developing new signatures

As demonstrated, nuclear forensics is a multi-faceted discipline. Ideally, a unique signature provides all the answers to the investigations. However, in practice, investigations always involve the measurement of several signatures in order to gain a high level confidence in the conclusions. This is why, research is always carried out to develop new signatures for the measurement of nuclear materials. This is the objective of the present work; exploring structural and morphological parameters as possible signatures for uranium compounds.

1.5a Raman spectroscopy

Uranium bearing materials have already been studied with Raman spectroscopy. For instance, there are more than 200 uranium minerals and several of such minerals were studied by Raman spectroscopy [50-65]. Closer to this study, different types of uranium compounds including uranium ore concentrates have also been measured by Raman spectroscopy. Characterization of U_3O_8 [66], UO_2 [67, 68], UO_3 , UO_2F_2 [69, 70], U_4O_9 [71], UF_5 and UF_6 [70] had been carried out by several authors. There were also some studies such as recognizing uranium oxides in soil [72], observation of an oxidized corrosion product of depleted uranium containing uranyl ions [73] as well as uranyl peroxide in the case of H_2O_2 leached UO_2 fuel pellet [74]. The combined use of Raman spectrometry and SEM to study several micrometer-sized UOCs particles has also been reported [75, 76]. Such studies can be useful in the context of nuclear safeguards where material are sampled by swiping the surface of nuclear installations and the delicate analysis of dust particles could provide valuable information [76].

Surface-enhanced Raman spectroscopy (SERS) has also been developed to detect uranium in environmental samples without the need to pre-treat [77]. Although there have been several studies made on different types of uranium compounds, none has exploited the measurements for nuclear forensics. It is therefore in the interest of this study, to look into the feasibility of Raman spectroscopy on a suite of varying compositions of UOCs for nuclear forensics.

There are several advantages of this technique. It is largely a non-destructive technique due to minimal or no sample preparation, relatively fast analysis and ability to measure all states of matter (solids, liquids, gases) and solutions, as well as the ability to measure the samples in closed sample holder. This is due to the fact that water is a weak Raman scatterer (as compared to infra-red where water has a strong absorption) and certain containments like glass hardly interfere. In addition, modern Raman spectrometers are capable of making measurements on micrometer-sized particles, thus small amount of material is sufficient for analysis. The miniurization of Raman spectrometers certainly explains its widespread use in cultural heritage [78, 79], archaeometry, geology [80-82], classical forensics [82, 83], homeland security [83-85] and even terrestrial/planetary sciences [86]. Commercial systems are also equipped with a database of spectra where embedded matching algorithms can aid in identification of unknowns including mixtures [87].

In this study, several uranium solids (largely UOCs) have been measured with different Raman spectrometers. These include a hand-held Raman spectrometer from Ahura Scientific®, a bench-top model Senterra from Brukers® and a delicate laboratory sized T64000 from Jobin Yvon®.

1.5b Morphology

The concept of a microstructural fingerprint was initiated to complement isotopic and elemental fingerprints, especially in cases where isotopic composition may not be conclusive [88]. Besides, microscopy is a technique that provides totally different information (i.e. morphology) about the sample as compared to chemical analytical techniques.

As seen in section 1.4.6a, SEM has been used to probe the morphology of interdicted material. It is also, on the other hand a challenging technique for developing measurable parameters for powder samples like UOCs. SEM is typically applied to investigate the shape, appearance and particle size distribution [1]. The same concept of particle size distribution can also be applied onto UOCs. These measurable parameters are aimed at providing clues to the processing history and/or the origin of the questioned material. So far, no study has been done to characterise these industrial UOCs using SEM.

Another aspect of studying the same samples with SEM is also introduced here; image texture analysis. This technique is not new. It is a frequent tool used in the food industry to investigate the texture of pasta, for example [89]. However, its application in nuclear forensics is new. It has been applied to UOCs synthesized in the laboratory as well as some industrial materials [90]. In that study, the author obtained SEM images at very high magnification of 50000x and the textures were analysed using techniques such as pattern spectra or granulometric curve or gray-level co-occurrence matrix. In the present study, a different approach was taken for exploring image texture analysis. SEM images would be taken at rather low magnifications of 1000x and 250x instead and a different algorithm, known as Angle Measure Technique (AMT) [91] would be used to access the texture of several industrial samples.

It is noteworthy that apart from microscopy, there are other methods that can be used to study particle sizes. These are based on variety of principles and can be categorized into three basic classes; ensemble, counting and separation [92]. Ensemble methods refer to the measurement of all particles in a sample at the same time. Laser diffraction and dynamic light scattering are common examples of ensemble methods where the techniques are known to be fast but tend to suffer from low resolution. Microscopy falls into the counting category. Individual particles are counted and are subsequently binned to obtain size distribution. A huge advantage of microscopy over other techniques is its ability to evaluate shapes as well. Differential sedimentation is one of the few separation methods and in this case, the use of centrifugal force helps to separate the particles according to their sizes.

Some of these techniques have been used to study the precipitation behaviour of UOC (Appendix A). The main interest surrounding such studies is due to the influence of starting material

or the precursor on the properties of UO_2 powder or pellet [93-96]. It has been well established that the properties of the final product is inherited from that of the precursor.

For instance, Rajagopal *et al.* studied the particle size distribution of ammonium uranates and the corresponding U_3O_8 after an hour of calcination at 850 °C [97]. Ammonium uranates were prepared by conventional aqueous method and their particle sizes were compared to those prepared by homogenous method (NH_3 generated in-situ by urea hydrolysis). The Malvern particle size analyser reported in that paper was likely to be based on laser diffraction. Manna *et al.* also used a laser particle size analyser coupled with microscopy (SEM and TEM) to study the crystal growth of ADU and its morphology with time [98].

In addition, there are also other methods such as sieve analysis and cascade impactors that can also provide size distribution. The particles are separated by a number of sieves or disks that have a certain cut-off size. Pan *et al* used sieve analysis to obtain particle size distribution of AUC samples produced under various conditions [99]. Besides providing the phase of the material, the line broadening of XRD pattern can also provide the average size of crystallites. Choi *et al.* used this method to compare the crystallite size of three UO_2 powder originating from three different plants producing AUC [100]. Clayton and Aronson had also determined from the crystallite size of UO_2 that the temperature of preparation had more influence on the size more than the method of preparation [101].

Despite numerous studies that have been conducted in relation to nuclear reactor physics, few such studies have been attempted for yellow cakes in relation to nuclear forensics. In such a context, the interest lies mainly in establishing a link between the observed morphology of the yellow cakes and their processing history.

One of the aims of this work is therefore to explore this link. Due to the complex milling process and inadequate information or understanding of the processing history of industrial materials, it makes little sense to embark investigations on these materials. Alternatively, yellow cakes are prepared in the laboratory and their morphology studied accordingly with SEM. In this paper, morphology is considered in three ways. Fundamentally, SEM images taken at different magnifications provide a qualitative description of the material. Semi-quantitative or quantitative approaches, being less conventional and obviously more challenging are explored. The study of sizes and shapes of particles after dispersion in ethanol and texture analysis of images are two aspects that will be dealt with.

1.6 Treatment of data with multivariate analysis

While it remains important for methods developed for signatures to be validated through the use of reference material (if applicable), the use of multivariate analysis or chemometrics for data analysis is also frequently applied in the field of nuclear forensics. Chemometrics was first defined in 1974 to mean the extraction of chemically relevant information from data produced in chemical

experiments. The use of mathematical models has been clearly suggested [102]. It is particularly useful when there are huge numbers of variables in the dataset such as spectroscopic data. IR [35], NIR [36] and LIBS [38] applied to UOCs were all analysed using tools of chemometrics. Of noteworthy was the use of such statistical analysis to query the interdicted sample against a uranium database containing the measurement results of more than 6000 individual sample analyses [22].

The use of similar chemometrics tools is henceforth foreseen in this study, whereby huge data matrices obtained by Raman spectroscopy and image texture analysis will be treated and evaluated as possible signatures for nuclear forensic purposes.

1.7 Scientific goals of this study

In summary, the main goals of this study are highlighted as follow:

- To correlate morphology of material with production process through the use of laboratory prepared yellow cakes.
- To exploit the spectral information of UOCs provided by Raman spectroscopy for nuclear forensics and to compare the performance of different instruments.
- To systematically investigate morphology of UOCs as signatures for nuclear forensics in three different ways.
- To evaluate the data, where appropriate, using tools of chemometrics.

2. Investigated Materials

2.1 General description

There are two different categories of uranium compounds (mainly UOCs) in this study. These UOCs are obtained from the following sources: the laboratory (laboratory synthesized) and the industries (industrial material). There are a total of 10 laboratory prepared material (Batch I and II) and 136 industrial materials. The laboratory synthesized UOCs are discussed in depth and can be found in Chapter 3. Out of the 136 industrial samples, 79 came from Springfields, UK, 28 from refineries, Port Hope and Blind River, Canada, 26 from IAEA and the last 3 samples belonged to the ITU.

2.2 Breakdown of the composition of UOCs/Breakdown of samples by countries

As seen from Figure 2-1, 79 samples that came from Springfield, UK were in fact largely UOCs (77 samples) that were obtained from different parts of the world. They were produced in 22 countries of which, 70 % of the samples came from USA (36.7 %), Canada (21.5 %) and Australia (10.1 %). It is important to note that this figure does not reflect the world's production of UOC.

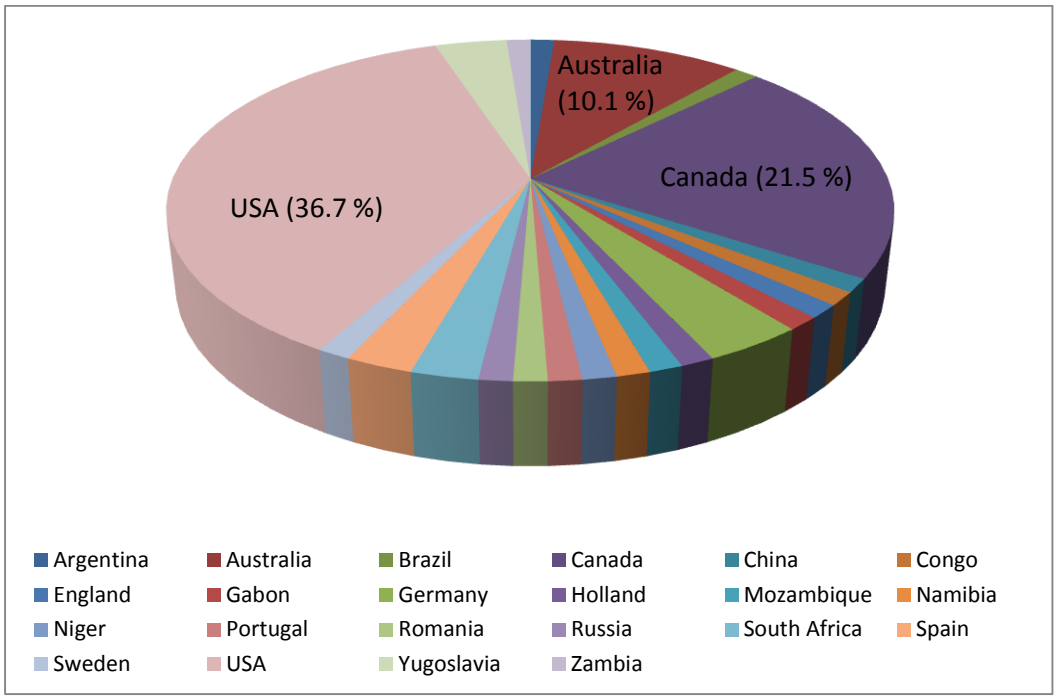

Figure 2-1: Demographics of the 79 samples obtained from Springfield, UK

In addition, information was also provided about the history of these samples (although not necessary known for all samples). Such information include, mining and milling location, its operational period, the type of deposit and the specifics of the milling process. It is important to note that complete information is not always the case and it can be difficult to obtain additional information from open literature, at least not for every sample.

From the same set of samples, Figure 2-2 illustrates the various compositions of this group of samples. More than half of the samples are made up by ADUs (35.4 %) and uranyl hydroxides (21.5 %). This reflects the industrial importance of certain UOC such as ADU. It was one of the most commonly produced UOCs. Appendix B (Figures B-1 to B-14) provides a visual appearance of all the samples that have been measured in this study.

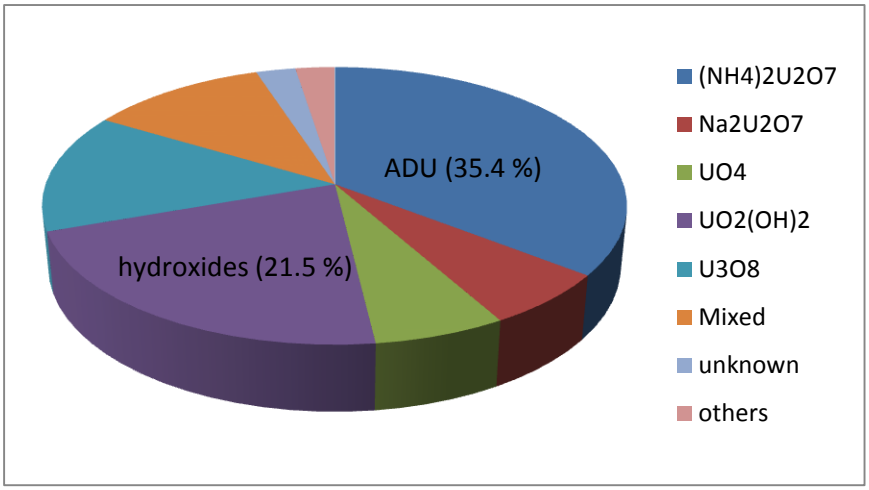

Figure 2-2: Composition of the 79 samples from Springfield, UK

2.3 Supplementary information

Appendix B (Table B-1) provides an overview of the various techniques that have been applied to the numerous samples. These techniques are Raman spectroscopy, infrared spectroscopy and scanning electron microscopy.

This table does not include other techniques such as Inductive coupled plasma mass spectrometry, elemental analysis (of carbon, nitrogen and oxygen), X-ray diffraction, thermal gravimetry/differential thermal analysis, Transmission electron microscopy were applied mainly to the laboratory synthesized samples described in Chapter 3.

3. Preparation and characterization of 5 different compositions of uranium ore concentrates

As seen in Chapter 2, there are many facilities worldwide that are producing UOCs and some of these samples are available in ITU for research. As mentioned in Chapter 1, the aim of this study is to develop new signatures or measurable parameters, besides existing signatures for analysing this class of compounds, in the event that a nuclear forensic investigation is to be undertaken. Two potential signatures were studied in details, Raman and microstructural fingerprint. Prior to the analysis of the industrial UOCs, five such materials have been prepared in the laboratory. The approach or purposes are at least two-fold: firstly, like most data obtained during a nuclear forensic investigation, some form of comparison is necessary to verify the findings. As there is no UOC standard, it makes sense to prepare these materials so that any measurements made can be compared between the laboratory synthesized and industrial UOCs. In addition, preparing these materials under known conditions meant that their 'processing history' is known, in contrast to some industrial UOCs. The milling process is made up of several stages of purification and concentration and this complexity may make it less straightforward to correlate potential signatures with the processing history. Laboratory prepared UOCs are therefore extremely useful for the research and development of signatures. In addition, these materials help to conserve the industrial samples that are limited and needed to be utilized wisely.

3.1 Materials

Uranyl nitrate hexahydrate, ($UO_2(NO_3)_2.6H_2O$, UNH) was the starting material for all reactions. The various precipitating conditions are summarized in Table 3-1. About 5 g of UNH was dissolved in 25 ml or 50 ml of ultrapure water in a glass beaker while the precipitating reagent(s) was added drop-wise from a burette into the beaker during continuous mixing. Each of the products was washed with the appropriate solvent and the preparation of all the five compounds were carried out at least twice under similar conditions. For the first set of compounds, these were dried overnight at room temperature (denoted as Batch I) and for the second set of compounds (denoted as Batch II), they were dried overnight in an oven at 105 °C. Measured parameters such as pH and temperature are shown in Table 3-1 recorded for the material of Batch II. Conditions are similar for Batch I. Figure 3-1 shows the typical experimental set-up for such UOC preparation, yielding typically a few grams of material.

Table 3-1: Parameters that were used to produce (Batch II) yellow cakes in the laboratory.

Final product[2]	**Precipitating reagent**[3]	**pH (initial-final)**	**Temperature (°C) (initial-final)**	**Washing solvent**	**References**
Ammonium uranyl carbonate $(NH_4)_4UO_2(CO_3)_3$	25 % (w/v) ammonium carbonate	1.47-7.81	49.8-47.9	Ethanol	[103-105]
	$UO_2(NO_3)_2 + 3(NH_4)_2CO_3 \rightarrow \underline{(NH_4)_4UO_2(CO_3)_3} + 2NH_4NO_3$				
Ammonium diuranate $(NH_4)_2U_2O_7$	25 % ammonium hydroxide	1.70-8.58	68.8-65.0	Water	[106]
	$UO_2(NO_3)_2 + NH_4OH \rightarrow \underline{(NH_4)_2U_2O_7} + 4NH_4NO_3 + 3H_2O$				
Sodium diuranate $Na_2U_2O_7$	50 % (w/v) sodium hydroxide	1.85-10.92	78.9-75.0	Water	[106]
	$2UO_2(NO_3)_2 + 6NaOH \rightarrow \underline{Na_2U_2O_7} + 4NaNO_3 + 3H_2O$				
Uranyl hydroxide $UO_2(OH)_2$	10 % w/v magnesium oxide	2.03-8.76	Room temperature	Water	[12, 107]
	$UO_2(NO_3)_2.6H_2O + 2MgO \rightarrow \underline{UO_2(OH)_2} + 2MgNO_3 + H_2O$				
Uranyl peroxide $UO_4.2H_2O$	30 % hydrogen peroxide	2.17-0.34	Room temperature	Cold hydrogen peroxide	[106]
	$UO_2(NO_3)_2 + H_2O_2 + 2H_2O \rightarrow \underline{UO_4.2H_2O} + 2HNO_3$				

[2] Molecular mass of each elements are expressed in g/mol: U (238.0289), O (15.9994), H (1.00794), C (12.011), N (14.00674), Na (22.9898)
[3] Precipitate is underlined

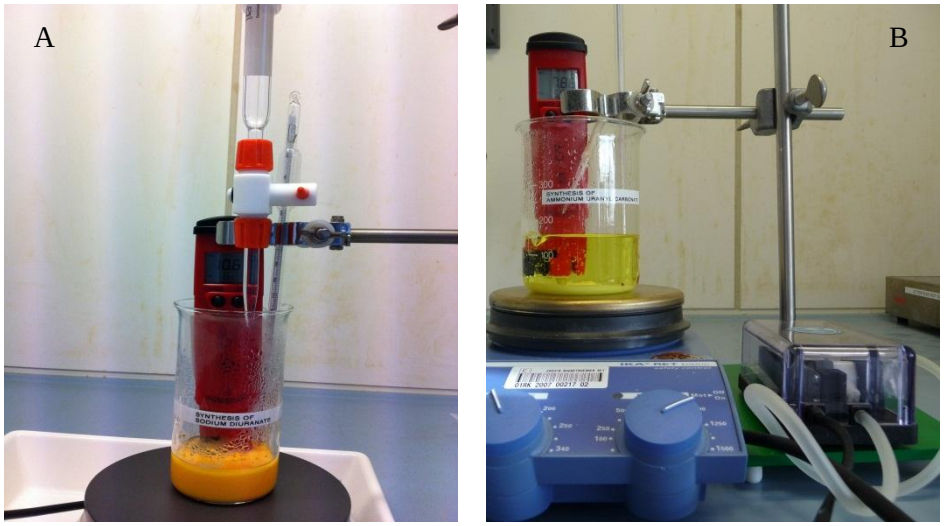

Figure 3-1: Experimental setup for sodium diuranate where mixture is stirred using stirrer bar (A); Experimental setup for AUC where air was used to agitate the mixture (B).

With the exception of AUC, the physical appearances (in particular, the colour) between the same composition of material dried at room temperature or 105 ^{o}C were identical. AUC that was dried overnight in oven at 105 °C was bright orange while the one dried at room temperature was bright yellow.

3.2 Methods for characterization

3.2.1 Infrared spectroscopy

The infrared spectra of the samples were taken using the KBr pellet method. A small quantity of the synthesized UOC (about 1 mg) was mixed and ground with KBr (about 100 mg). The homogenous mixture was then pressed into a pellet using 3630 X-Press (SPEX Industries Inc., USA) with an applied pressure of 600 MPa for 8 min. Prior to use, KBr was dried at 105 °C and subsequently kept in a desiccator. Fourier-transform infrared (FT-IR) measurements were performed using Perkin Elmer System 2000 spectrometer (Perkin Elmer Ltd, Beaconsfield, UK) with the spectra range of 400-4000 cm^{-1} using a resolution of 2 cm^{-1}.

3.2.2 Raman spectroscopy

A bench-top Raman spectrometer model, Senterra (Bruker Corporation, Germany) was used to make the Raman measurements. The laser frequency and power used were 785 nm and 1-10 mW respectively, depending on the sample. Too much laser power can potentially destroy the sample. A 20x objective was chosen and each sample was measured for 10 s. The details of Senterra spectrometer can be found in Chapter 4.1.2. Prior to measurements, the powders were pressed into pellets using 3630 X-Press with a lower applied pressure of approximately 74 MPa for 8 minutes.

3.2.3 X-ray diffraction (XRD)

Ex-situ or room temperature XRD patterns were acquired with a Bruker D8 diffractometer mounted in a Bragg-Brentano configuration with a curved Ge monochromators (111), a Cu X-ray tube (40 kW, 40 mA), a Vantec detector and a Si wafer (111) as sample holder. Data were collected on a full diffraction angle range 2θ = 5-120° with 0.0092° increment in each step.

In situ HT-XRD patterns were acquired with a Bruker D8 powder diffractometer installed in a glove-box and mounted in a Bragg–Brentano configuration with a curved Ge monochromator (111), a Cu X-ray tube (40 kV, 40 mA), a Vantec detector, and an Anton Paar HTK2000 heating chamber equipped with a Pt heating plate. Data were collected on a full diffraction angle range 2θ = 10-100°, in steps of 0.017°, with a counting time of 2 s per step. The explored temperature range spanned the interval 30 – 1000 °C, with the sample kept under static synthetic air (21 vol.% O_2 + 79 vol.% N_2) with a starting pressure of 800 x 10^2 Pa. Prior to measurement, MgO was used to check the calibration of the furnace chamber. Temperature relative errors were determined to fall within 5 % in the whole investigated interval.

3.2.4 Thermogravimetry/Differential Thermal Analysis (TG/DTA)

The apparatus used was NETZSCH Simultaneous Analyzer STA 449 Jupiter. TG/DTA analyses were carried out under flow of oxygen (> 99.99 % purity) at a heating rate of 10 °C/min on a temperature range of 30 °C till 1000 °C. The obtained XRD patterns were subsequently compared using the programme known as Match!/Phase Identification from Powder Diffraction (version 1.11f) from Crystal Impact, Germany. When applicable, the likely phase of the material was determined by the closest match.

3.2.5 Mass spectrometry

3.2.5a Determination of uranium concentration by Inductive Coupled Plasma-Mass Spectrometry (ICP-MS) and Isotope Dilution Mass Spectrometry (IDMS)

Typically, around 100 mg of the sample was weighed and dissolved in high purity concentrated HNO_3 (use of HF is avoided) and subsequently diluted in high purity 5 % HNO_3. An internal standard Th was added to compensate for possible instrumental drift. Measurements were made in triplicates for ICP-MS as described in the internal document of ITU [108].

For ID-TIMS, an aliquot of about 500 mg of diluted sample was mixed with appropriate amounts of the spiking solution consisting of isotopically pure ^{233}U (50-100 µg/g) aimed at a ratio of ^{233}U: ^{238}U = 1. Measurements were made in duplicates [109].

3.2.5b Determination of impurities in the matrices of uranium

Sample was weighed and diluted in high purity 5 % HNO_3. 10 ng/g Rh was added as an internal standard to correct for any instrumental drift. Measurements were made in triplicates [110].

3.2.6 Determination of Carbon, Nitrogen and Oxygen by direct combustion

The quantification of C, N and O was conducted either individually (for carbon) or simultaneously (oxygen and nitrogen) and the methods were based on the combustion of sample at high temperature (reaching a maximum of 3000 K) under a flow of oxygen or helium, for carbon or nitrogen and oxygen, respectively.

3.2.6a Carbon

The determination of carbon (based on combustion-infrared detection) was carried out with the CS-800 instrument (Eltra GmbH, Germany). 30 to 50 mg of the sample, depending on the carbon content, was placed in a ceramic crucible. Melting of the sample occurred inside the induction furnace under pure oxygen carrier gas. The released carbon interacted with the oxygen, forming CO_2 eventually. CO_2 was detected by means of infrared light absorption at a specific wavelength of 2640 cm^{-1}. Measurements were repeated in duplicates [111].

3.2.6b Nitrogen

The determination of nitrogen (based on combustion-thermal conductivity detection) was carried out with the ONH-2000 instrument (Eltra GmbH, Germany). 10 to 30 mg of the sample, depending on the element content, was placed in a tin capsule and subsequently in a nickel basket. During analysis, the sample was automatically dropped into a single-use graphite crucible. The material was fused under a flow of helium and nitrogen was released as a gas. It was detected using a thermal conductivity cell. Measurements were repeated in triplicates [112].

3.2.6c Oxygen

The determination of oxygen (based on combustion-infrared detection) was carried out with the ONH-2000 instrument (Eltra GmbH, Germany). The sample was placed in a tin capsule and subsequently inside a nickel basket. During analysis, the basket was automatically dropped in a single-use graphite crucible placed in the electrode furnace. Oxygen present in the sample combined with the carbon from the crucible, forming CO initially and CO_2 thereafter using CuO in a catalytic furnace. Measurements were repeated in triplicates [112].

3.2.7 Scanning electron microscope

VEGA-TESCAN TS5130LSH (Oxford instruments) was used for taking SEM images. It operates with a tungsten filament in the range of 200V-30 keV with an emission current till 300 µA. It is equipped with a SE detector and a BSE detector. Magnification range is 3-1,000,000x with the spatial resolution down to 3 nm.

3.2.8 Transmission electron microscopy

A TecnaiG2 (FEI^{TM}) TEM instrument model was used in this study, modified to enable the examination of radioactive samples [113]. The system is equipped with a Gatan^{TM} Tridiem GIF camera, an energy-dispersive X-ray analysis system, and a high-angle annular dark-field detector for the scanning transmission electron microscope imaging. For sample preparation, a small amount of sample was ground and crushed in methanol. It was subsequently transferred into a container and left to settle. A droplet of the suspension was then deposited on a copper grid containing carbon film.

3.3 Results from the characterization techniques

3.3.1 IR and Raman spectroscopic techniques

Figures 3-2 to 3-6 depict the combined IR and Raman spectra taken for the five products that were prepared in the laboratory. The U-O bands of UO_2^{2+} in ADU can be found at 906 cm^{-1} (ν_3) and 816 cm^{-1} (ν_1) for IR and Raman, respectively (Figure 3.2). They also correspond to the anti-symmetric and symmetric stretch of the uranium-oxygen bonds, respectively. The IR band at 462 cm^{-1} can be attributed to the bending mode of U-O. The sharp band at 1385 cm^{-1} belongs to the nitrate from the starting material UNH, while the peak at 1400 cm^{-1} indicates the presence of nitrogen-hydrogen (N-H) bonds due to symmetric deformation of ammonia [35]. In addition, the fairly broad peaks at 3145 cm^{-1} and 3468 cm^{-1} indicate respectively, N-H and O-H stretching vibrations.

In contrast to the IR, the N-H bands are not observed in the Raman spectra. Although the spectrum is shown till 3320 cm^{-1} only, low resolution mode (up to 3820 cm^{-1}) was also run but no N-H peaks were observed (spectrum is not shown here). The IR peaks at 1625 cm^{-1} and 3468 cm^{-1} (broad) corresponded to the bending (δ_{H2O}) and stretching modes of oxygen-hydrogen bonds (O-H). These bands are also not seen in the Raman spectra. There are however quite a number of Raman peaks observed at lower wavenumbers such as 558 cm^{-1}, 450 cm^{-1}, 323 cm^{-1}, 248 cm^{-1}, 205 cm^{-1} and 120 cm^{-1}. It is postulated that the first three peaks could be related to U-O(II) stretch, while the latter three peaks could be related to U-O(I) bending [114]. II and I refer to the equatorial and axial plane of the bonds, respectively.

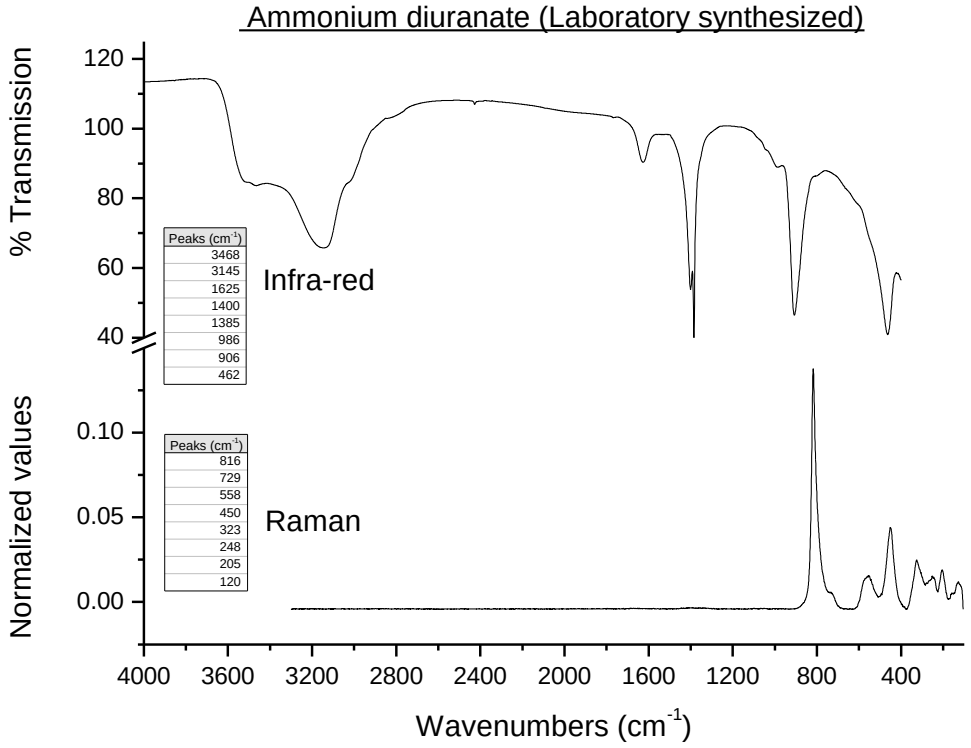

Figure 3-2: Infrared (top) and Raman (bottom) spectra of the laboratory prepared ammonium diuranate.

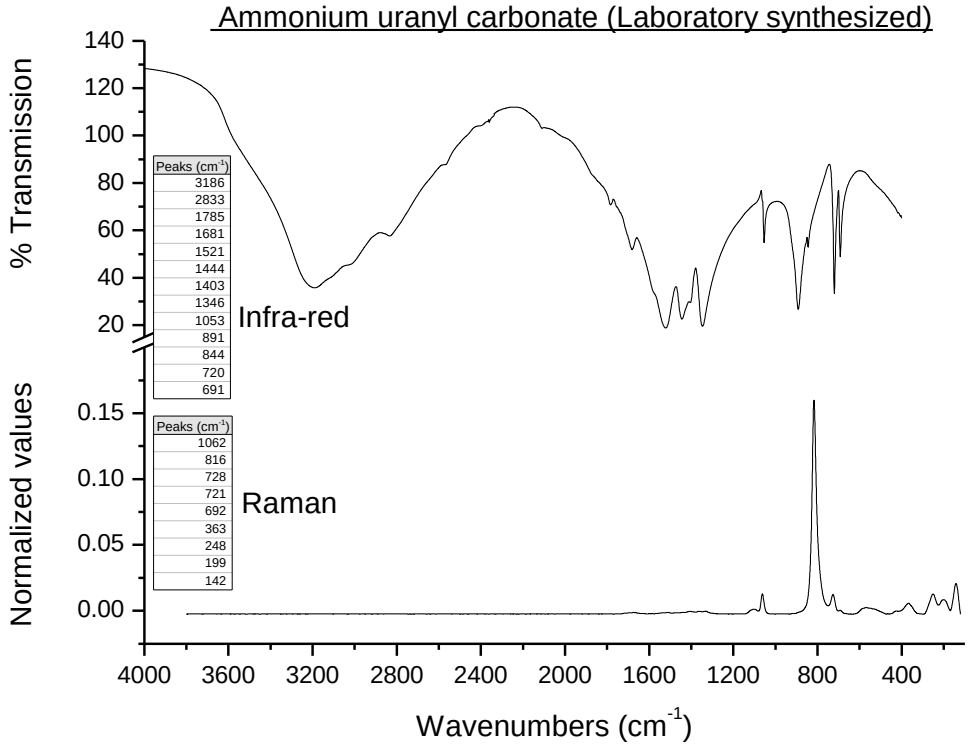

Figure 3-3: Infrared (top) and Raman (bottom) spectra of the laboratory prepared ammonium uranyl carbonate.

Several peaks appeared in the IR spectra of AUC (Figure 3-3) due to the presence of carbonates for example, 691 cm^{-1}, 720 cm^{-1}, 844 cm^{-1}, 1053 cm^{-1}, 1346 cm^{-1} and 1520 cm^{-1} are all vibrations deriving from carbonate (ν_1- ν_6) [115]. The peak at 891 cm^{-1} is assigned to $\nu_3(UO_2^{2+})$, while

3186 cm^{-1} and 1444 cm^{-1} indicate the presence of ammonium ions; $\nu_3(NH_4^+)$ and $\nu_4(NH_4^+)$, respectively as these are IR active vibrations. Tetrahedral ammonium ion has two other non-IR active modes; 1681 cm^{-1} for $\nu_2(NH_4^+)$ and 2833 cm^{-1} for $\nu_1(NH_4^+)$ and therefore, they are observed at very low intensities. It is worth mentioning that the IR spectra obtained in this work resembled highly the spectra reported in literature [115], where AUC was precipitated with gaseous reagents.

The Raman spectrum of AUC is simpler with fewer peaks. The peaks at 692 cm^{-1}, 721 cm^{-1} and 728 cm^{-1} are attributed to deformations of CO_3^{2-}, while the peak at 1062 cm^{-1} is assigned as a stretch [116]. It is difficult to assign the peak at 363 cm^{-1}. The slightly stronger peak at 248 cm^{-1} may be attributed to deformation of UO_2^{2+} (this peak was assigned as U-O(I) bending in ADU) while the peaks at 199 cm^{-1} and 142 cm^{-1} are possibly librations of CO_3^{2-} and UO_2^{2+} respectively [116].

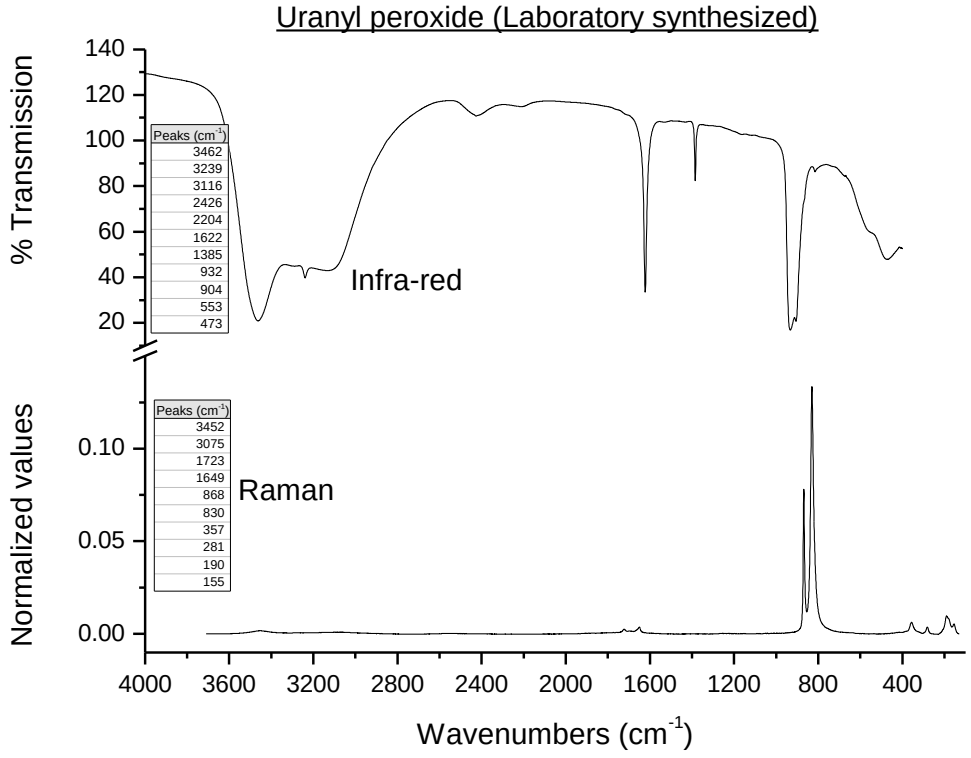

Figure 3-4: Infrared (top) and Raman (bottom) spectra of the laboratory prepared uranyl peroxide.

The IR of UO_4 shows the presence of U-O bonds in slightly different environment and hence the appearance of two equivalent strong peaks at 904 cm^{-1} and 932 cm^{-1} (Figure 3-4). The two peaks at 553 cm^{-1} and 473 cm^{-1} are assigned as ν_{as} ($U\text{-}O_{peroxo}$) [117]. The peak at 1385 cm^{-1} is again due to the nitrate residual. A similar peak if present, should appear at ~1050 cm^{-1} (most intense peak of nitrates) in the Raman spectrum but this peak is not observed. This demonstrates the difference in sensitivity between both techniques. The peaks at 3462 cm^{-1}, 3239 cm^{-1} and 3116 cm^{-1} are again the stretching mode of O-H. The strong peak at 1622 cm^{-1} is the bending mode of water. All the above values corresponded well with that reported in literature for the yellow cake $UO_4.2H_2O$ [117].

In this synthesis, $UO_4.2H_2O$ (also known as metastudtite as the mineral) was obtained after the precipitated material $UO_4.4H_2O$ (also known as studtite as the mineral) was dried overnight at 105

°C. The strongest evidence can be obtained from the Raman spectrum as the ν_1 (U=O) shifted from 817 cm^{-1} (spectrum of $UO_4.4H_2O$ from Batch I is not shown) to 830 cm^{-1} [117]. It is interesting to note that this is the only material that could be measured with the higher frequency laser at 532 nm without any fluorescence. It is also due to the use of higher energy that allowed the observations of O-H stretching modes and in contrast to, was not observable with lower energy laser of 785 nm. This part shall be further discussed in Chapter 4.4.3.

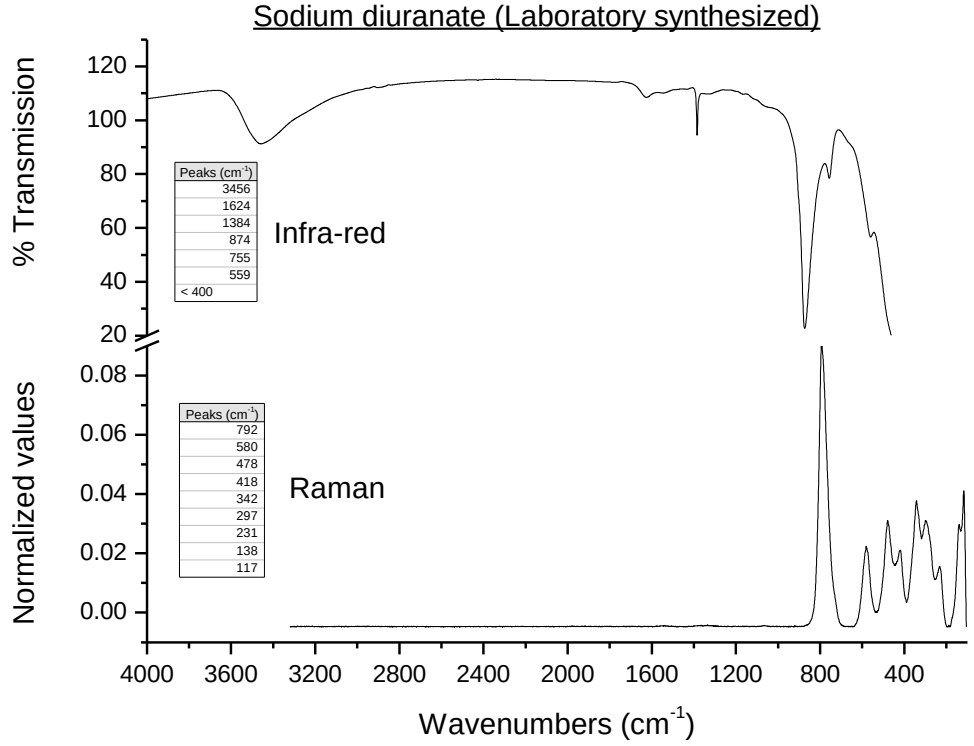

Figure 3-5: Infrared (top) and Raman (bottom) spectra of the laboratory prepared sodium diuranate.

Figure 3-5 shows the IR and Raman spectra of sodium diuranate. Published IR and Raman data reported more peaks than the one in this study [118]. Raman peaks are strong although somewhat broader. The dominant Raman peak at 792 cm^{-1} is very close to published values of 788 and 779 cm^{-1}. This is ν_1 or symmetric stretch of the uranyl ion. The equivalent ν_3 or asymmetric stretch occurs at 874 cm^{-1} observed in the IR spectrum. Traces of nitrate remained in the material evident by its presence in IR. In addition, traces of water can also be found in the same spectrum. There are many distinct Raman bands but these cannot be easily attributed. However, vibrations due to U-O(II) or U-$O_{equatorial}$ stretch, Na-O vibrations, and U-O(I) or U-O_{axial} bend are likely to be present. It is relevant to add that the Raman spectrum of this material is similar to the Raman spectra of industrial material known to have the composition of sodium diuranate.

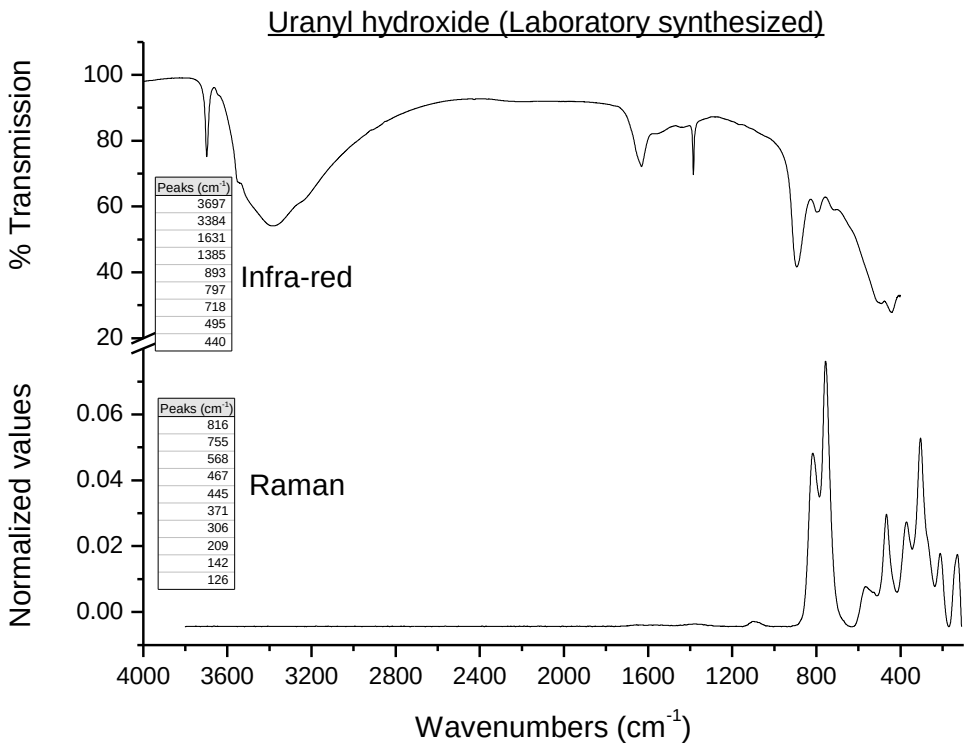

Figure 3-6: Infrared (top) and Raman (bottom) spectra of the laboratory prepared uranyl hydroxide.

The presence of MgO is evident from the peak at 3697 cm^{-1} and some nitrate is observed in the IR spectrum as well (Figure 3-6). The IR bands for α-$UO_2(OH)_2$ are reported to be 3340 cm^{-1} {ν(UO-H)}, 970 cm^{-1}, 882 cm^{-1} {$\nu_3(UO_2^{2+})$} and 540 cm^{-1} {ν (U-O)} [119]. These are somewhat shifted from the values reported in this laboratory prepared uranyl hydroxide. The peak at 1631 cm^{-1}, δ(H_2O) is supposedly absent in α-$UO_2(OH)_2$ but similar values were reported for schoepite, $UO_3.2.25H_2O$ and metaschoepite, $UO_3.2H_2O$. It is interesting to note that $UO_2(OH)_2$ can also be presented by $UO_3.H_2O$ [119]. The former formula suggests a closer relationship to schoepite and metaschoepite, but it does not reflect well the molecular composition of this compound. Since the composition of this amorphous material could not be identified by XRD, it is not possible to interpret the spectra with certainty.

It is relevant to add that magnesium diuranate (MDU) is reportedly the yellow cake that is precipitated when magnesia is used. This is the process used in Jaduguda mines in India [120]. The discrepancy is clearly not well understood. Among the inventory of industrial UOCs available in ITU (Table B-1 of Appendix B), there exists a single sample of yellow cake that has the assumed/known composition of MDU. The Raman spectra of this particular sample bears some strong resemblance to that of laboratory prepared using $Mg(OH)_2$ (spectra not shown here).

3.3.2 XRD patterns (phase determination)

The XRD pattern obtained from the five materials are shown in Figures 3-7 to 3-11, along with the Powder Diffraction File (PDF) data of the reference material(s), whose pattern(s) was found to resemble most, the XRD pattern of the material.

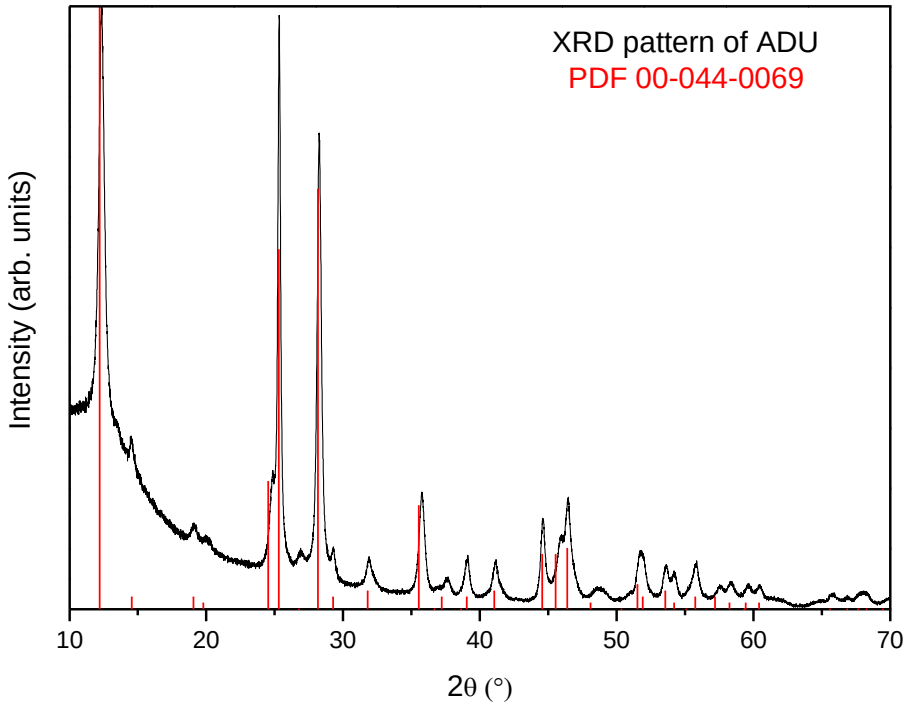

Figure 3-7: XRD pattern of the laboratory prepared ammonium diuranate (black line) matched to reference material PDF 00-044-0069 (red lines).

Figure 3-7 shows the XRD pattern obtained from the ADU produced in the laboratory (black line) matched to the ADU (PDF 00-044-0069) [121] from the database (red lines). There is slight discrepancy between the XRD pattern of ADU with the reference material. The crystal structure is reported to be hexagonal, while the space group is not defined. It is postulated that the synthesized material (addition of 25 % NH_4OH to UNH) is ADU with a likely composition of $2UO_3.NH_3.3H_2O$. A detailed study of ADU from Batch I was also investigated with high temperature XRD and the results were complemented with TG/DTA. The sample was also heat treated to selected temperatures and the room temperature XRD patterns were obtained for comparison. This is described in Appendix C.

The crystal structure of AUC is well known. It is monoclinic with the proposed space group of C2/c [104, 115, 122, 123]. In Figure 3-8, The XRD pattern of the AUC produced in the laboratory (black line) matched very well to the AUC (PDF 04-012-7120) [123] from the database (red lines). Therefore, it is confirmed that the synthesized material is AUC with the composition of $(NH_4)_4UO_2(CO_3)_3$.

It is noteworthy that the mass ratio of carbon to uranium (C/U) of 7.5 has been emphasized in literature in order to ensue the constant composition of $(NH_4)_4UO_2(CO_3)_3$ [99]. However, it appears that in order to maintain the ratio, a large quantity of ammonium carbonate (~ 125 g in 500 ml to be

added to 5g of U in 50 ml water) would be required to produce a few grams of stoichiometric AUC. Therefore, in this experiment, the ratio was not maintained since the goal of this synthesis was not to produce the exact composition of AUC.

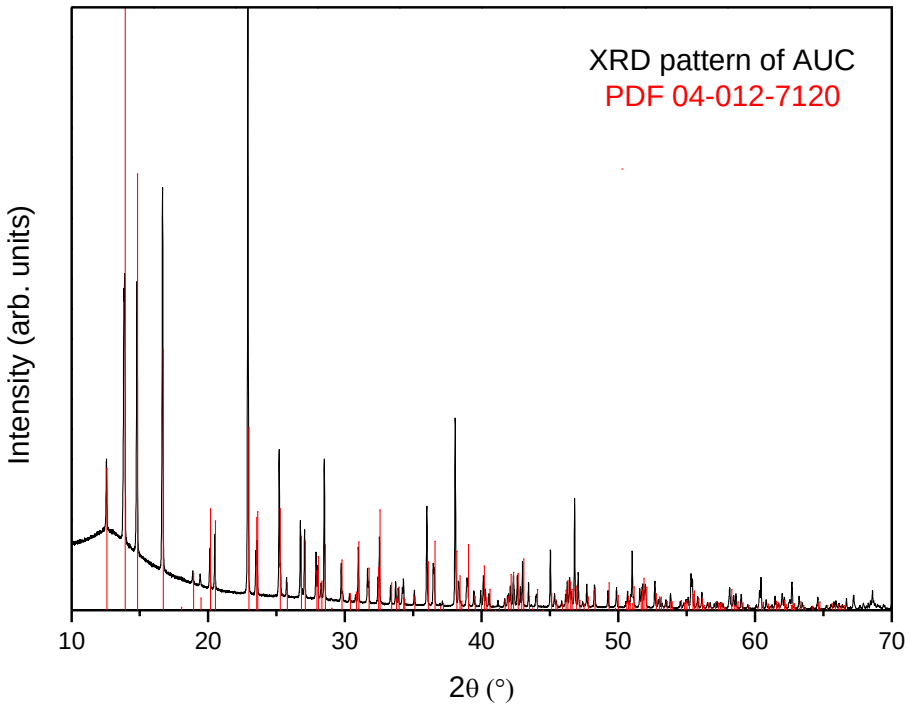

Figure 3-8: XRD pattern of the laboratory prepared ammonium uranyl carbonate (black line) matched to reference material PDF 04-012-7120 (red lines).

Figure 3-9 shows the XRD pattern of $UO_4.2H_2O$ that was produced in the laboratory (black line) and it was well matched to $UO_4.2H_2O$ (PDF 00-016-0207) [124] from the database (red lines). The crystal structure is known to be orthorhombic with the probable space group of *Immm* [124-127]. It is confirmed that the synthesized material is $UO_4.2H_2O$.

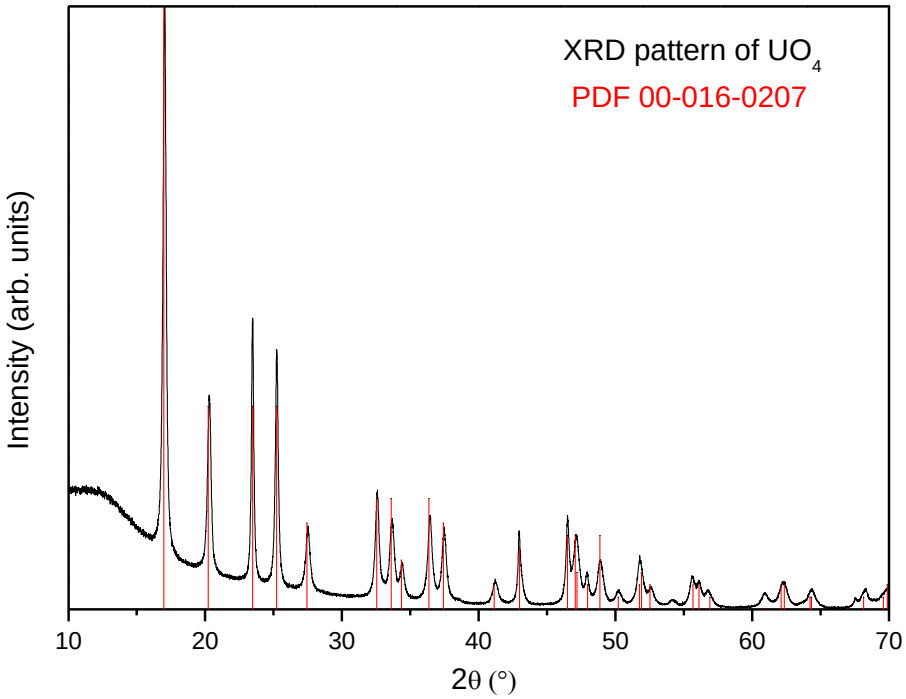

Figure 3-9: XRD pattern of the laboratory prepared uranyl peroxide (black line) matched to reference material PDF 00-016-0207 (red lines).

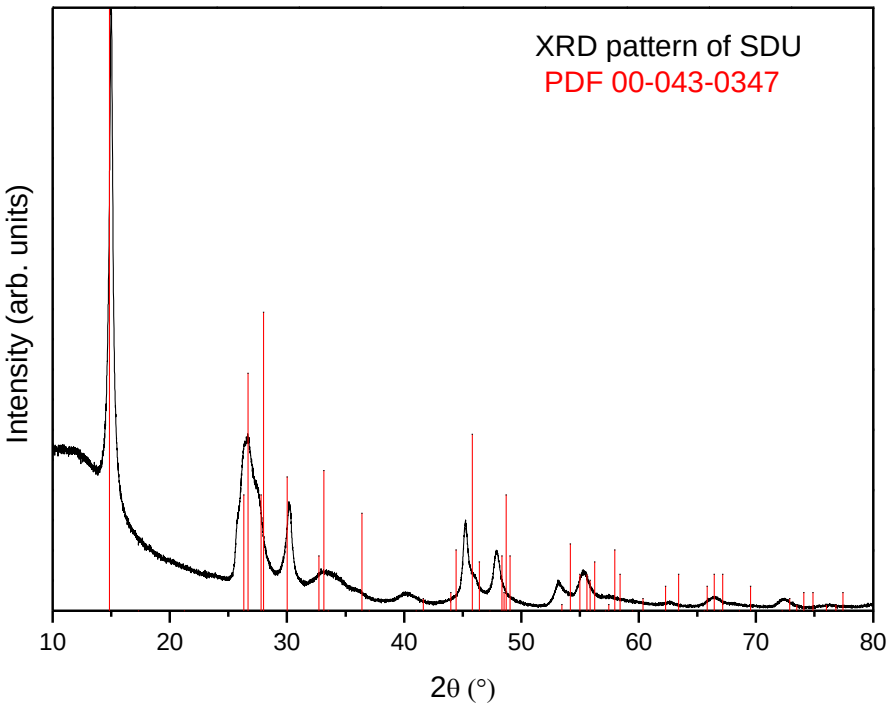

Figure 3-10: XRD patterns of the laboratory prepared sodium diuranate (black line) and reference material PDF 00-043-0347 (red lines).

Figure 3-10 shows the XRD pattern of the laboratory prepared sodium diuranate, $Na_2U_2O_7$ (black line). The reference pattern (PDF 00-043-0347) from the database (red lines) is also shown. However, the patterns do not match perfectly, which is in agreement with Plaue's work [90]. He had prepared this material in a similar fashion and had dried the material at 85 °C and had concluded that

the material was amorphous and not readily identifiable by XRD pattern matching. In addition, the author reported different compositions of sodium uranium oxides when the material was processed at temperatures of 150 °C and above.

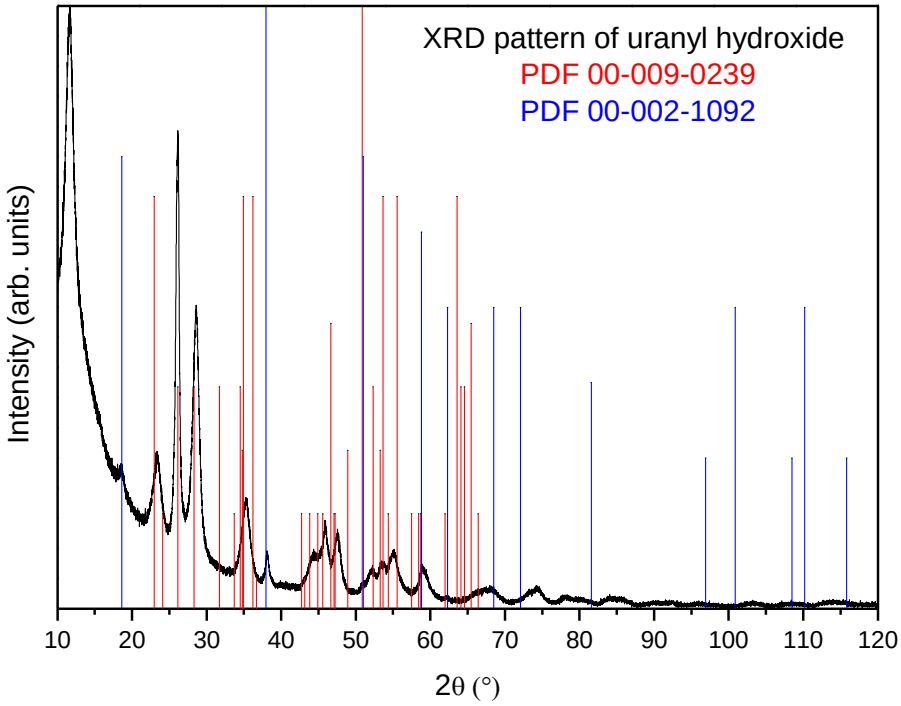

Figure 3-11: XRD patterns of the laboratory prepared uranyl hydroxide (black line) and reference material PDF 00-016-0207 (red lines) and PDF 00-002-1092 (blue lines).

Figure 3-11 shows the XRD pattern of the laboratory prepared uranyl hydroxide $UO_2(OH)_2$ (black line) and that of reference patterns (PDF 00-009-0239) (red lines) and MgO (PDF 00-002-1092) (blue lines). The patterns do not match perfectly and similar to sodium diuranate, it implies that this material is also amorphous. Traces of MgO could also be identified. This observation is also in accordance to Plaue's results, where no match could be obtained for this material unless it is processed at 600 °C [90].

3.3.3 Thermogravimetry/Differential Thermal Analysis

Figure 3-12 shows the TG/DTA curves of ADU with the determined composition of $2UO_3.NH_3.3H_2O$ by XRD study. There have been numerous studies reporting on the thermal decomposition of ammonium uranates [96, 128-132], including a literature survey by Woolfrey [133], as well as our recent publication [134]. In the latter, TG/DTA was measured for ADU (Batch I) while in Figure 3-12, TG/DTA was measured for ADU (Batch II). Nonetheless, the TG/DTA profiles were highly similar between both samples. Caution should be exercised while making references to the published TG/DTA data since methods of preparation are frequently varied thus resulting in non-stoichoimetric ADU. Therefore, it is possible that the corresponding TG/DTA profiles may not be in complete agreement.

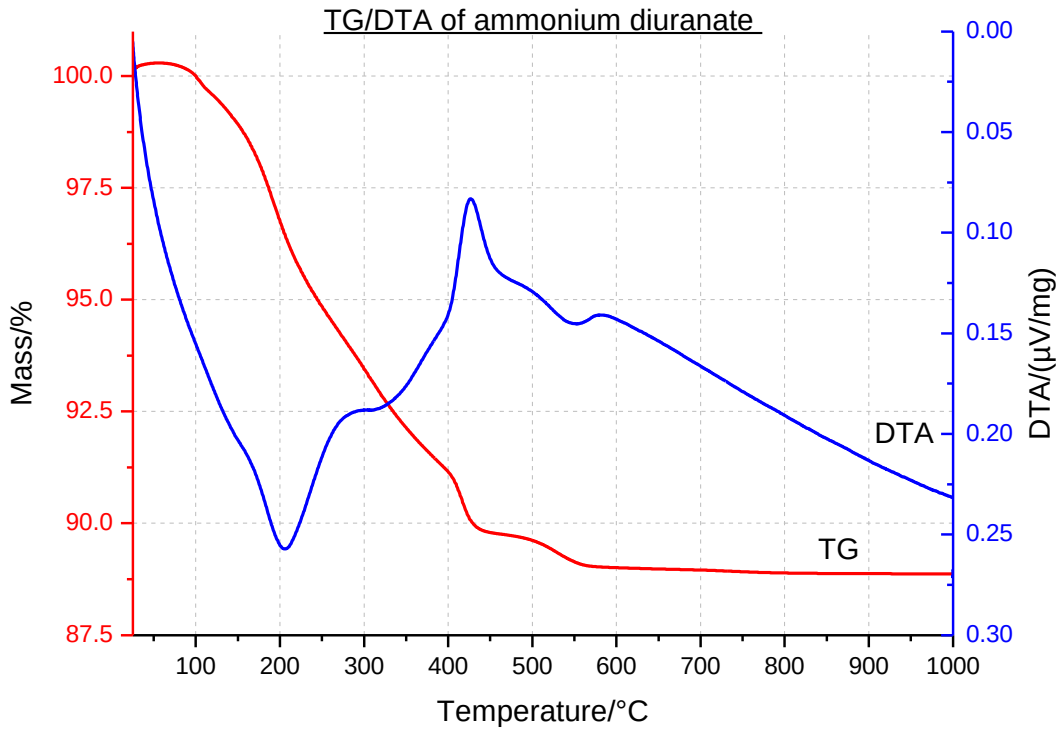

Figure 3-12: TG/DTA curves of the laboratory prepared ammonium diuranate.

TG/DTA of ADU is characterized by an endothermic reaction with a mass loss of slightly over 10 % at temperature approximately 210 °C. This step is associated with the loss of water molecules. Since the material was previously dried at 105 °C, this step should correspond only to the removal of coordinated or chemically bonded water molecules. The loss is slightly higher than the theoretical mass loss of 8.4 %. This meant that the water content appeared to be slightly higher than 3 moles of water. However, it has also been proposed that peaks found around 169 °C and 210 °C could be represented by the melting point and boiling point respectively, of ammonium nitrate that was present in unwashed sample [129]. As seen in Figure 3-2, the IR spectrum of ADU still contained nitrate impurities after washing. Therefore, it is reasonable that the intial presence of minute quantity of ammonium nitrate can eventually contribute to some mass loss. This statement also corroborate with the observations made by the same author that the removal of nitrate and ammonia began before the completion of the removal of water [129, 130].

An exothermic reaction occurred at a temperature maximum of 426 °C where the corresponding mass loss was about 2 %. This is comparable with the theoretical mass loss of 2.6 % and is associated with the removal of NH_3. This reaction has been reported to be in the range of 340-420 °C [131], 350-450 °C [96, 133] and at about 441 °C [129]. This step is associated with the loss of remaining ammonia retained by the solid sample, thus forming UO_3 eventually. The UO_3 at this stage is believed to be largely amorphous (A-UO_3), if not completely amorphous. This was verfied by the in-situ high temperature XRD measurement [134], where the XRD pattern at 400 °C clearly suggested

the presence of an amorphous species. Sato *et al* have already reported that AU thermally decomposes to A-UO_3 at about 400 °C [131].

Finally, an endothermic process took place at a temperature minimum of about 550 °C with a mass loss of less than 1 %. This has been reported in the range of 500-600 °C [131-133] and above 600 °C [128, 129, 132] and is related to the reduction of β-UO_3 to U_3O_8.

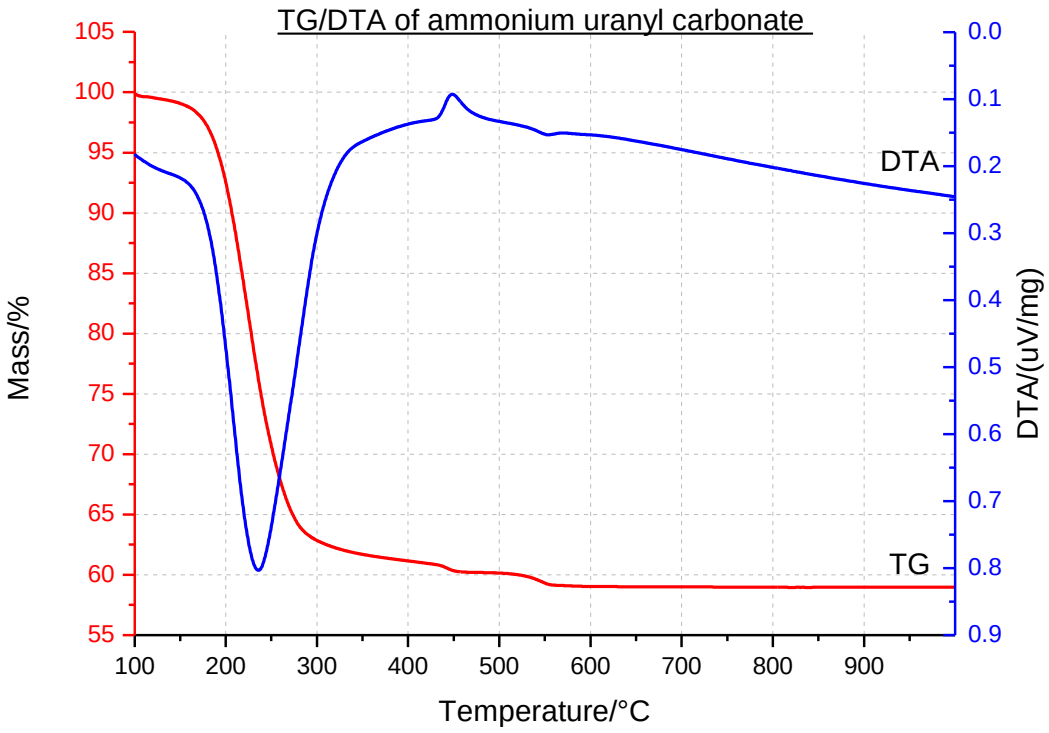

Figure 3-13: TG/DTA curves of the laboratory prepared ammonium uranyl carbonate.

Figure 3-13 highlights the TG/DTA of AUC. A few studies have reported TG/DTA of AUC [103-105, 122, 135-137]. It is characterized by an endothermic reaction with a minimum at 236 °C with a large mass loss of nearly 40 % at 400 °C. This step is always associated with the formation of H_2O, NH_3 and CO_2. However, in this particular study, the mass loss should be attributed to only NH_3 and CO_2, since H_2O molecules present would have been removed by the overnight drying at 105 °C. This is supported by a few observations. Firstly, the mass loss of ~ 40 % is slightly below the values of 42.5-45.5 % reported in literature [103, 104]. Secondly, the minimum was registered at higher temperature in this study (~236 °C) than the same minimum in the same literature (~194 °C). Finally, the AUC of Batch I (dried at room temperature) was also subjected to TG/DTA and its results were in fact, much closer to published values (results are not shown here).

At about 448 °C, an exothermic reaction with ~ 3 % mass loss occurred due to the conversion of an amorphous $UO_3(H_2O)_x$ into its crystalline phase. Again, the maximum of this peak is higher than the published value of 257 °C [104]. Finally, at 554 °C, a 2nd endothermic reaction with ~ 3 % mass loss was observed. This step has been associated with the second CO_2 release peak from residual AUC

reported at similar temperature of ~562 °C [104]. However, this step should correspond to the conversion of UO_3 to U_3O_8.

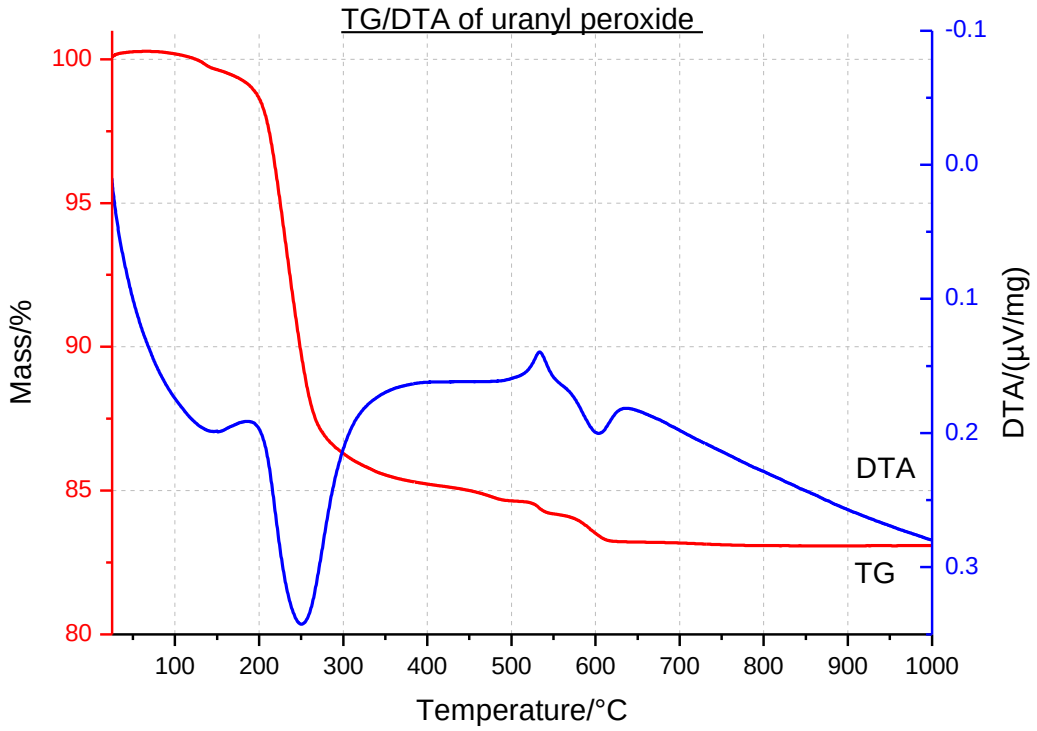

Figure 3-14: TG/DTA curves of the laboratory prepared uranyl peroxide.

Figure 3-14 shows the TG/DTA curves of $UO_4.2H_2O$. The DTA curve is characterized by an endothermic reaction at a temperature minimum of 250 °C with a mass loss of 15 %. This step is associated with the loss of the two crystal water molecules and the loss of peroxide [117]. Sato had attributed an endothermic peak at ~ 240 °C to the decomposition reaction, obtaining amorphous UO_x (x is between 3 to 3.5) [138]. The experimental mass loss of 15 % is in good agreement with the theoretical mass loss of 15.4 %. An exothermic reaction occurring with a maximum at about 533 °C could be attributed to the decomposition of UO_3 to $UO_{2.67}$ [117]. The mass loss associated with the decomposition was determined to be close to the theoretical mass loss of 0.98 %. Lastly, an exothermic reaction occurring at slightly above 600 °C is highly due to the conversion of UO_3 to U_3O_8 [138].

It is noteworthy that the TG/DTA curve of $UO_4.4H_2O$ would be similar to that of $UO_4.2H_2O$ or $[(UO_2)(O_2)(H_2O)_2](H_2O)_2$ since the latter is derived from the former by drying. In addition, the first two water molecules (non-bonded) [125], would be removed at temperatures below 100 °C [117].

Figure 3-15 shows the TG/DTA curves of presumably amorphous $Na_2U_2O_7$ which could not be identified by its XRD pattern. There occurs to be very few reactions as the peaks are not dominant. The DTA curve in this study does resemble the general profile published by Baran and Tympl [139].

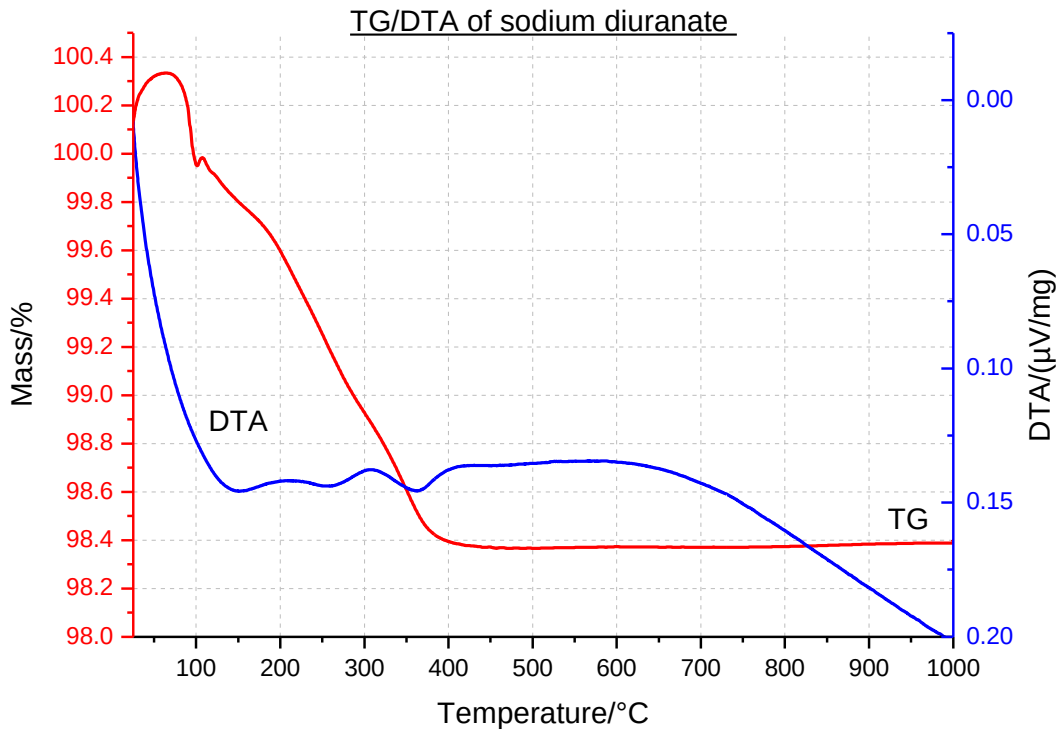

Figure 3-15: TG/DTA curves of the laboratory prepared sodium diuranate.

They prepared two series of material from the addition of sodium hydroxide to uranyl nitrate solution. One set of materials was dried at either 40 ^{o}C for 68 hours and the other at 150 ^{o}C for 44 hours. The first endotherm in this material is observed at ca 150 ^{o}C which can be attributed to the removal of non-stoichiometric water as suggested by the same authors. A 2nd endotherm at slightly above 350 ^{o}C can be attributed to the dehydration of hydroxyl groups [139]. Due to the presence of Na which is involatile, there is no transformation to UO_3 or U_3O_8.

Figure 3-16 depicts the TG/DTA curves of presumably, the amorphous phase of $UO_2(OH)_2$. Apart from Plaue's work, there has not been any study reported on the thermal decomposition of uranyl hydroxide. As this material is not entirely pure, the TG/DTA curves are likely not an accurate reflection of the pure material. However, based on the examples seen so far, deduction can still be made. At temperatures of ~150 °C and ~250 °C, hydroxides are removed. It is not clear what the endothermic reaction with a minimum at ~ 425 °C might be due to. The exothermic reaction with a maximum at slightly above 600 °C is most probably due to the conversion of UO_3 to U_3O_8.

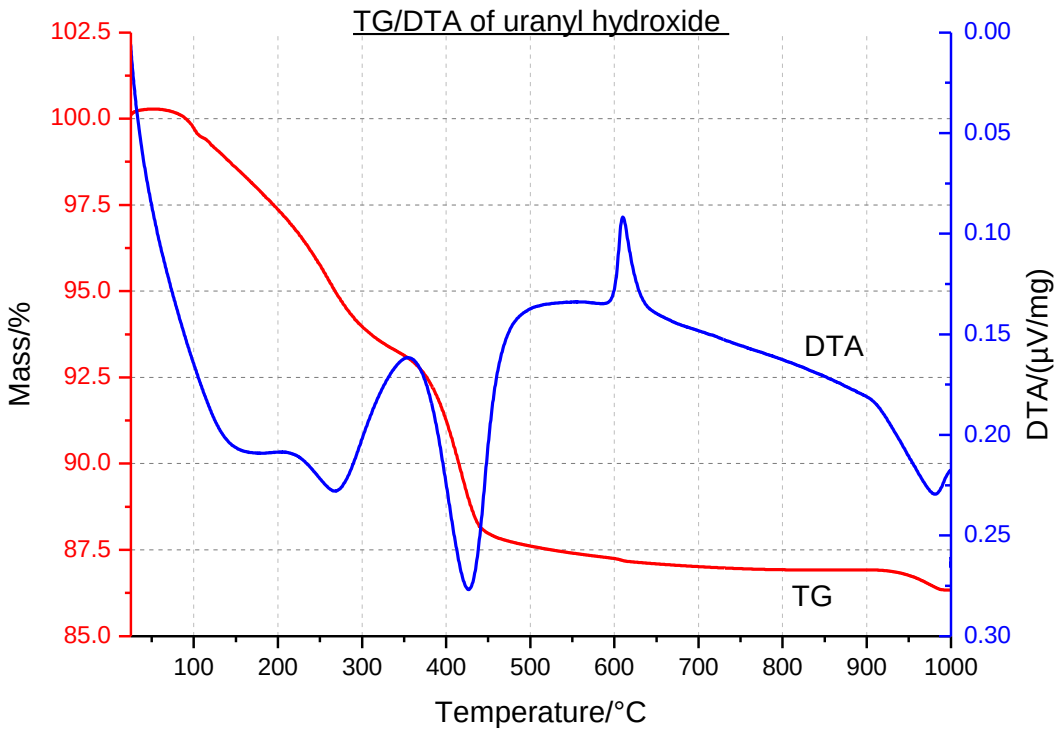

Figure 3-16: TG/DTA curves of the laboratory prepared uranyl hydroxide.

3.3.4 Composition of the samples

3.3.4a Uranium content

Table 3-2 provides the uranium content obtained by both ICP-MS and IDMS for each material. Both values for the same sample were in close agreement with each other for all the five material. The uranium content of ADU, UO_4, and SDU were approximately 1% lower than the expected or theoretical content calculated from the given formulae. In the case of AUC, the uranium concentration obtained were 4-5 % higher than expected and it is in accordance to the work of Tel and Eral for lower C/U ratios [103]. As seen for UH, the content of uranium was 20 % below the expected value. This certainly supports the observation of high MgO content as seen from the IR spectrum.

Table 3-2: Concentration of uranium based on weight %.

Compound	**Determined concentration (wt %)**		**Theoretical (wt %)**
	ICP-MS	**IDMS**	
ADU ($2UO_3.NH_3.3H_2O$)	73.63 ± 0.52	74.27 ± 0.12	76.16
AUC $[(NH_4)_4UO_2(CO_3)_3]$	50.12 ± 0.73	49.31 ± 0.08	45.58
UP ($UO_4.2H_2O$)	69.31 ± 0.42	69.48 ± 0.11	70.41
SDU ($Na_2U_2O_7$)	73.73 ± 0.44	73.50 ± 0.11	75.08
UH $[UO_2(OH)_2]$	56.90 ± 1.65	58.64 ± 0.10	78.29

3.3.4b Mass fraction of oxygen, nitrogen and carbon

The mass fraction of oxygen, nitrogen and carbon, if present in the synthesized yellow cake are shown in Table 3-3. The oxygen content of ADU, AUC and UP was significantly lower than the theoretical or expected values (shown in bold). In the case of nitrogen, ADU appeared to have a lower than expected content. For AUC, the lower content of carbon and oxygen (CO_3^{2-}) and possibly for nitrogen (NH_4^+) are in agreement with the non-stoichiometric AUC that has been produced [103].

Table 3-3: Mass fraction of O, N and C by direct combustion-infrared absorption. Values in bold are referred as the theoretical mass fraction.

Compound	**Mass fraction (%) with 95% confidence**		
	Oxygen	**Nitrogen**	**Carbon**
ADU ($2UO_3.NH_3.3H_2O$)	16-18 **(23)**	1-3 **(4.5)**	
AUC $[(NH_4)_4UO_2(CO_3)_3]$	19.4-21.4 **(33.7)**	5-13 **(10.7)**	5.95-6.03 **(6.9)**
UP ($UO_4.2H_2O$)	20.1-22.1 **(28.4)**		
SDU ($Na_2U_2O_7$)	17-19 **(15.1)**		
UH $[UO_2(OH)_2]$	22.1-24.1 **(21)**		

3.3.4c Concentrations of other elements

Mg is present in significant quantity as an impurity as it was not easy to remove this hardly soluble solid and acid could not be used as it would dissolve the desired product. The measured quantity was determined to be 12.9 ± 1.55 % by weight. In the case of SDU, Na is expected and the measured quantity was 7.40 ± 0.88 % by weight and this is slightly higher than the theoretical value of 6.23 %.

3.3.5 Microscopy features of the material

3.3.5a Scanning Electron Microscopy

SEM images of the prepared samples can be found in Figure 3-17. Each row of images represents a sample taken at different levels of magnification. The 1st row of images was taken for ADU sample. ADU material is highly agglomerated and interestingly, some unusually long needled-like grains could be observed at high magnification. Agglomeration of ADU is typical [93, 94, 97]. A recent publication made by Manna *et al* studied the evolution of the morphology of ADU with time.

After 11 hours of precipitation, the authors reported the observation of agglomerated platelets [98]. The morphology of ADU in this study appeared to be mixed since the needled-like morphology was not entirely a characteristic of the material.

The images of AUC contained discrete particles with varying sizes. SEM images of AUC have been reported elsewhere [99, 100]. Particles can possibly be described as 'angular' and 'euhedral' [140] and cracks are visible on the particles. For such crystalline material, good quality images were obtainable at 50,000x and 100,000x magnification. However, no smaller grain could be observed and therefore each particle of AUC is considered discrete.

The UO_4 particles of this material are agglomerated and the sample appears homogenous. Fine details of the material could not be readily observed even at 50,000x magnification.

No known morphology of SDU has been reported. Although the XRD patterns of this prepared material did not match the reference material of SDU in Match! database, the morphology of the former material is studied. Although agglomerates are also observed for this sample, the images taken at high magnification indicates that the shape of the grains is different from the other samples. Although it may not be distinctly clear from the images, the sample appears to contain platelets.

$UO_2(OH)_2$, the least pure sample of all five was also analysed by SEM (last row of images in Figure 3-17). Presence of impurities was easily detected by using the BSE mode (image is not shown here) and only particles containing UH were selected. Again, agglomeration is visible for this sample. However, the morphology is different and the material appears to contain layers of particles or layers of agglomerated particles.

3.3.5b Transmission Electron Microscopy and Scanning Transmission Electron Microscopy (STEM)

Out of the five laboratory prepared samples analysed by SEM, three (ADU, UO_4, SDU) were selected for further analysis using TEM. The morphology of AUC sample was well characterized by SEM and its morphology is well known, thus it is not analysed further by TEM. The uranyl hydroxide sample was not entirely pure due to the presence of $Mg(OH)_2$ and therefore this material was not analysed too. The TEM images of ADU, UO_4 and SDU are seen in Figure 3-18, 3-19 and 3-20 respectively. Like SEM images, TEM images were also taken at different magnifications. In addition, STEM images were also taken for ADU and UO_4.

In general, TEM provides information on the grain size and grain size distribution. In all the three samples characterized by TEM, the high magnification images suggest that all the three material are polycrystalline, comprising of several crystallites. In the TEM images of sample ADU, the grains have clearly needled-like shape which is characteristic of the sample. These are approximately 100 nm in length. In comparison to SEM images of ADU, only a few such grains could be picked up as they were unusually long. In the same TEM images, one can observe some platelets alongside with the needled grains, of which the former was not observed with SEM.

In the case of UO_4, SEM images did not reveal clearly the microstructure of this material. However, the TEM images revealed that the grains are like long and thick rods. The sample is clearly homogenous and this was the same observation with SEM images. The TEM images of SDU clearly confirm the presence of platelets from SEM images. These platelets are extremely thin or fine as layers of material are evidently present. The dimension of smallest platelets is in the range of 100-200 nm.

One of the goals in preparing these materials in the laboratory is to use these materials for comparison with the industrial samples for further research in nuclear forensics. For the purpose of this study, these laboratory prepared[4] materials are good enough for comparative purposes.

[4] These laboratory prepared materials are not reference materials

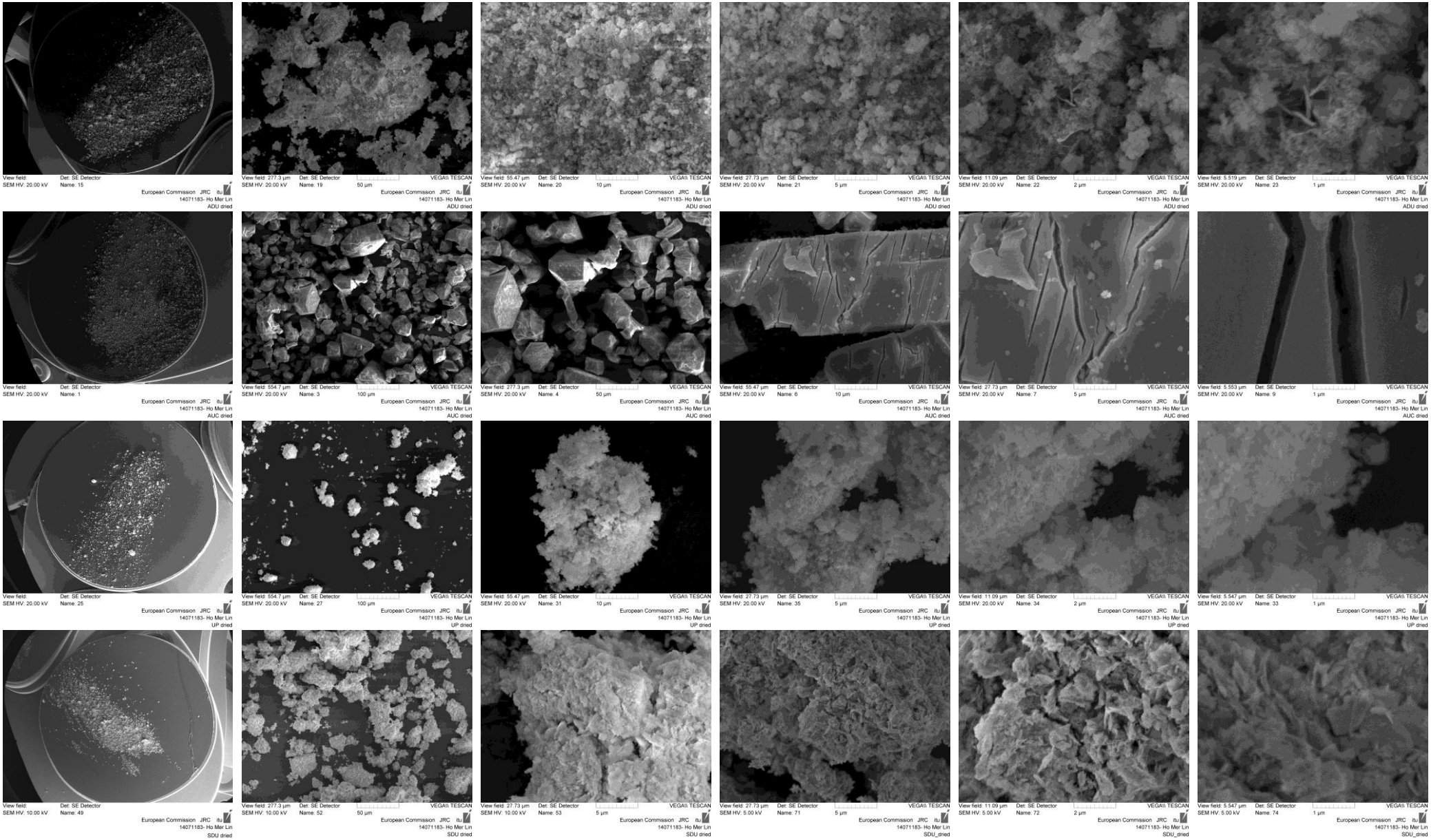
View field: Det: SE Detector
SEM HV: 20.00 kV Name: 15
European Commission JRC itu
14071183- Ho Mer Lin
ADU dried
View field: 277.3 µm Det: SE Detector VEGA\\ TESCAN
SEM HV: 20.00 kV Name: 19 50 µm
European Commission JRC itu
14071183- Ho Mer Lin
ADU dried
View field: 55.47 µm Det: SE Detector VEGA\\ TESCAN
SEM HV: 20.00 kV Name: 20 10 µm
European Commission JRC itu
14071183- Ho Mer Lin
ADU dried
View field: 27.73 µm Det: SE Detector VEGA\\ TESCAN
SEM HV: 20.00 kV Name: 21 5 µm
European Commission JRC itu
14071183- Ho Mer Lin
ADU dried
View field: 11.09 µm Det: SE Detector VEGA\\ TESCAN
SEM HV: 20.00 kV Name: 22 2 µm
European Commission JRC itu
14071183- Ho Mer Lin
ADU dried
View field: 5.519 µm Det: SE Detector VEGA\\ TESCAN
SEM HV: 20.00 kV Name: 23 1 µm
European Commission JRC itu
14071183- Ho Mer Lin
ADU dried
View field: Det: SE Detector
SEM HV: 20.00 kV Name: 1
European Commission JRC itu
14071183- Ho Mer Lin
AUC dried
View field: 554.7 µm Det: SE Detector VEGA\\ TESCAN
SEM HV: 20.00 kV Name: 3 100 µm
European Commission JRC itu
14071183- Ho Mer Lin
AUC dried
View field: 277.3 µm Det: SE Detector VEGA\\ TESCAN
SEM HV: 20.00 kV Name: 4 50 µm
European Commission JRC itu
14071183- Ho Mer Lin
AUC dried
View field: 55.47 µm Det: SE Detector VEGA\\ TESCAN
SEM HV: 20.00 kV Name: 6 10 µm
European Commission JRC itu
14071183- Ho Mer Lin
AUC dried
View field: 27.73 µm Det: SE Detector VEGA\\ TESCAN
SEM HV: 20.00 kV Name: 7 5 µm
European Commission JRC itu
14071183- Ho Mer Lin
AUC dried
View field: 5.553 µm Det: SE Detector VEGA\\ TESCAN
SEM HV: 20.00 kV Name: 9 1 µm
European Commission JRC itu
14071183- Ho Mer Lin
AUC dried
View field: Det: SE Detector
SEM HV: 20.00 kV Name: 25
European Commission JRC itu
14071183- Ho Mer Lin
UP dried
View field: 554.7 µm Det: SE Detector VEGA\\ TESCAN
SEM HV: 20.00 kV Name: 27 100 µm
European Commission JRC itu
14071183- Ho Mer Lin
UP dried
View field: 55.47 µm Det: SE Detector VEGA\\ TESCAN
SEM HV: 20.00 kV Name: 31 10 µm
European Commission JRC itu
14071183- Ho Mer Lin
UP dried
View field: 27.73 µm Det: SE Detector VEGA\\ TESCAN
SEM HV: 20.00 kV Name: 35 5 µm
European Commission JRC itu
14071183- Ho Mer Lin
UP dried
View field: 11.09 µm Det: SE Detector VEGA\\ TESCAN
SEM HV: 20.00 kV Name: 34 2 µm
European Commission JRC itu
14071183- Ho Mer Lin
UP dried
View field: 5.547 µm Det: SE Detector VEGA\\ TESCAN
SEM HV: 20.00 kV Name: 33 1 µm
European Commission JRC itu
14071183- Ho Mer Lin
UP dried
View field: Det: SE Detector
SEM HV: 10.00 kV Name: 49
European Commission JRC itu
14071183- Ho Mer Lin
SDU dried
View field: 277.3 µm Det: SE Detector VEGA\\ TESCAN
SEM HV: 10.00 kV Name: 52 50 µm
European Commission JRC itu
14071183- Ho Mer Lin
SDU dried
View field: 27.73 µm Det: SE Detector VEGA\\ TESCAN
SEM HV: 10.00 kV Name: 53 5 µm
European Commission JRC itu
14071183- Ho Mer Lin
SDU dried
View field: 27.73 µm Det: SE Detector VEGA\\ TESCAN
SEM HV: 5.00 kV Name: 71 5 µm
European Commission JRC itu
14071183- Ho Mer Lin
SDU_dried
View field: 11.09 µm Det: SE Detector VEGA\\ TESCAN
SEM HV: 5.00 kV Name: 72 2 µm
European Commission JRC itu
14071183- Ho Mer Lin
SDU_dried
View field: 5.547 µm Det: SE Detector VEGA\\ TESCAN
SEM HV: 5.00 kV Name: 74 1 µm
European Commission JRC itu
14071183- Ho Mer Lin
SDU_dried

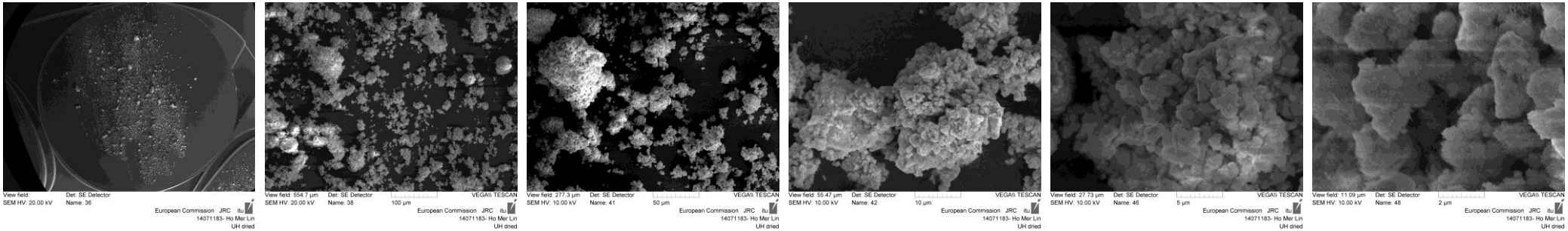

Figure 3-17: SEM images of samples taken at various magnifications; AUC (1st row), ADU (2nd row), UO_4 (3rd row), SDU (4th row), $UO_2(OH)_2$ (5th row).

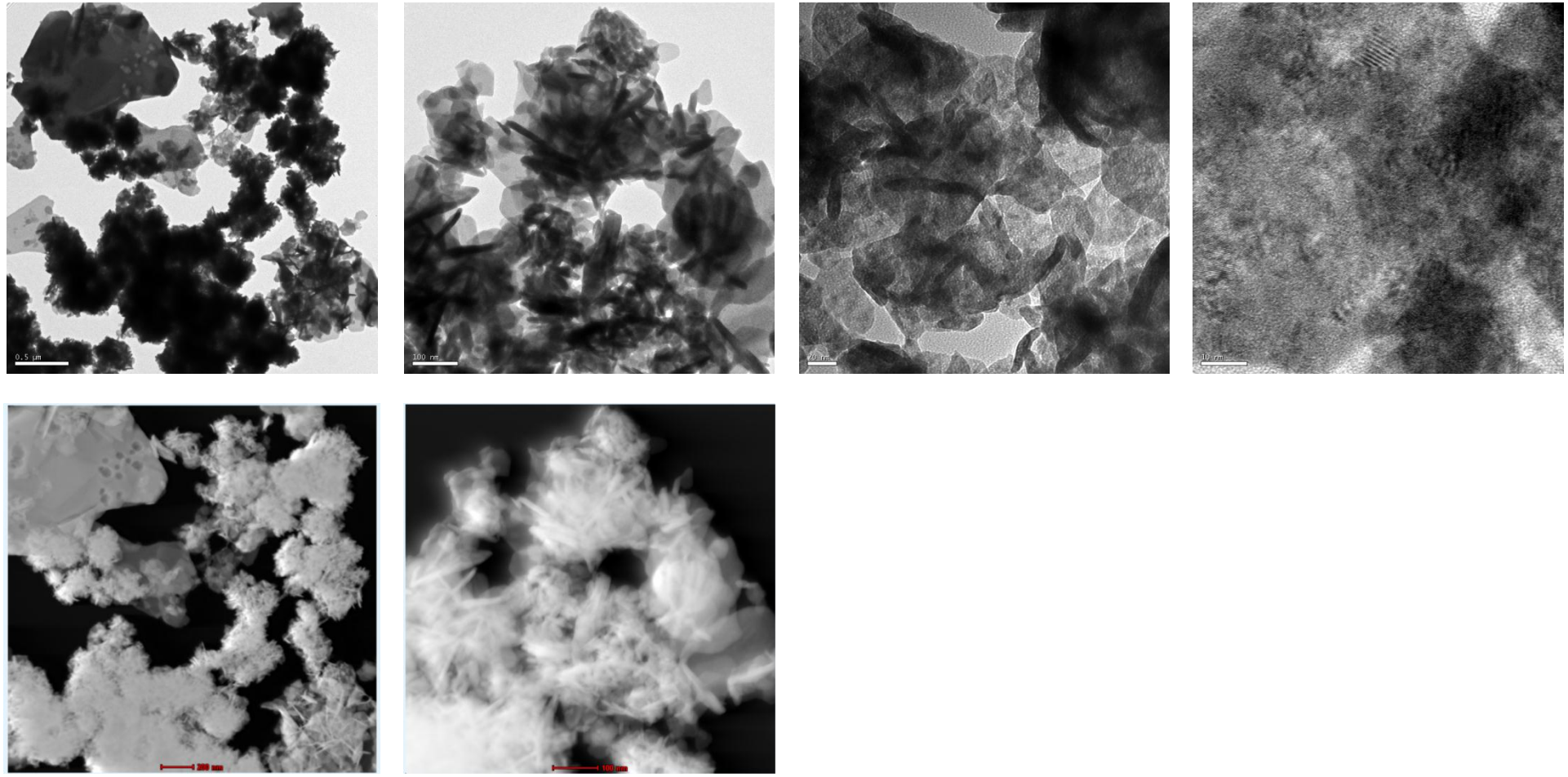

Figure 3-18: TEM (top row) and STEM (bottom row) images of sample ADU taken at different magnifications.

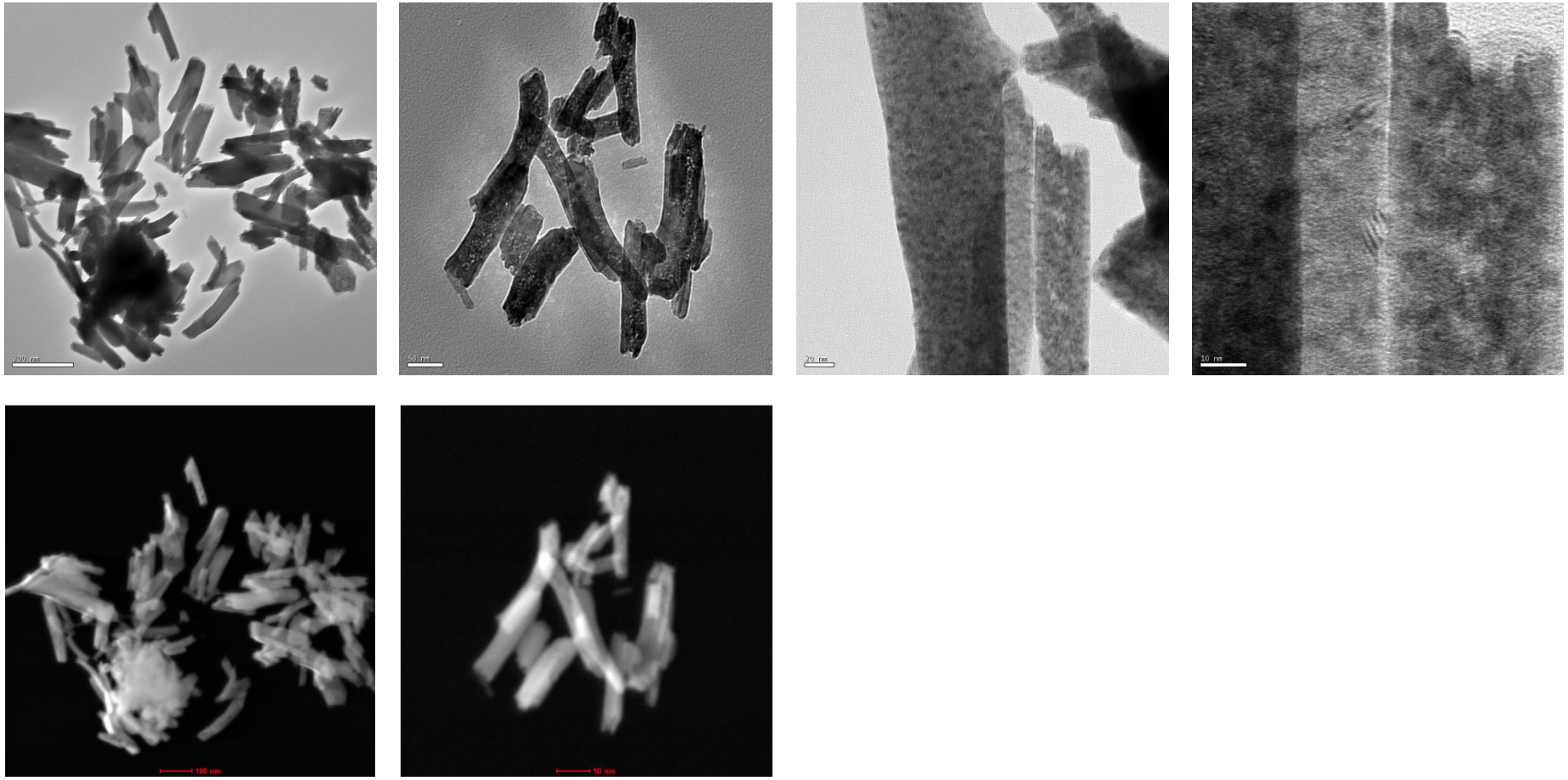

Figure 3-19: TEM (top row) and STEM (bottom row) images of sample UO_4 taken at different magnifications.

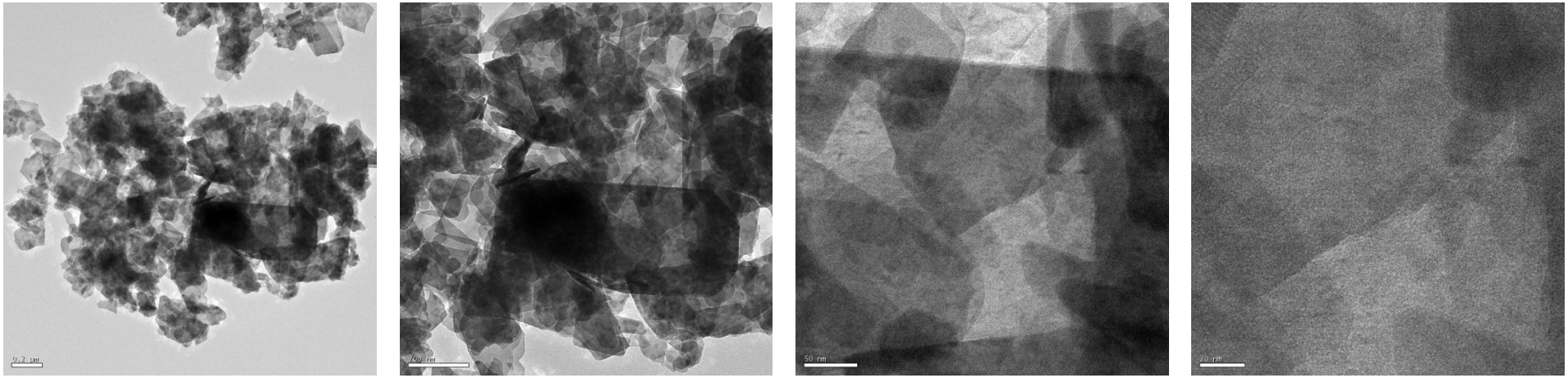

Figure 3-20: TEM images of sample SDU taken at different magnifications.

3.4 Further studies (calcination) carried out on laboratory prepared materials

Beyond the characterization of the prepared materials, three out of the five materials were heated and the temperature treated products were analysed with SEM. In addition, specifically the products of ADU were subsequently characterized by selected tools or techniques (Appendix C). The main goal of this part of the study is to understand the structural and compositional changes in the UOC material when it is subjected to calcination. Drying or calcination is often undertaken industrially to remove water and volatile components and to increase the grade of the product.

Small quantities of sample of either ADU, UP and AUC were placed in crucibles and brought up to selected temperatures based on their TG/DTA profiles.

Figure 3-21 reveals the SEM images of ADU, UP and AUC. Each row of images represents each sample taken at the same level of magnification. It can be readily observed that the morphology of each sample is clearly retained throughout the calcination process. The results are not surprising and are in complete agreement with the established fact that the properties of final product are inherited from the precursors. These confirmed the observations demonstrated by some authors in their studies [98-100].

ADU was one of the most common UOCs produced worldwide. This is also reflected in the inventory of UOCs in ITU where ADUs are more than 30 % (Chapter 2). This does not include oxides that might have been produced via ADU. Since it is very common to find ADU, this material and its calcined products were further characterized by XRD, IR and Raman spectroscopy. The results are found in Appendix C.

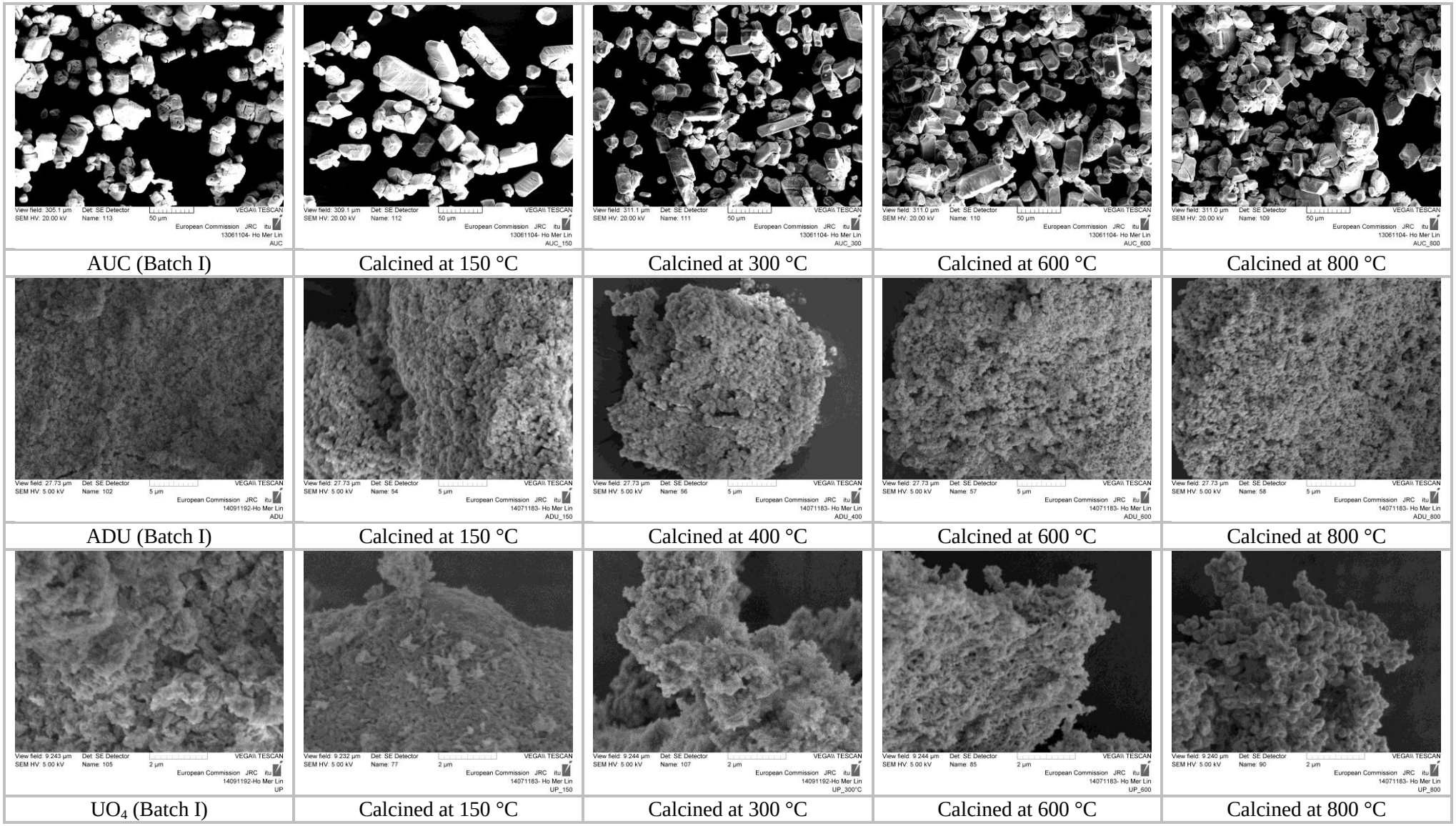

Figure 3-21: SEM images of calcined AUC, ADU and $UO_4.4H_2O$.

3.5 Summary and suggested areas for future study

Five different compositions of yellow cakes were prepared in the laboratory by adding to uranyl nitrate solution, various precipitating reagents. These reagents were ammonium carbonate, ammonium hydroxide, hydrogen peroxide, sodium hydroxide and magnesia, giving rise to $(NH_4)_4UO_2(CO_3)_3$, $2UO_3.NH_3.3H_2O$, $UO_4.2H_2O$, $Na_2U_2O_7$ and $UO_2(OH)_2$ respectively. The prepared materials were characterized with various techniques such as IR, Raman spectroscopy, XRD, TG/TGA, chemical analysis, SEM and TEM.

- Crystalline material of AUC-$(NH_4)_4UO_2(CO_3)_3$, ADU-$2UO_3.NH_3.3H_2O$, $UO_4.2H_2O$ had been prepared. Amorphous material of $Na_2U_2O_7$ and $UO_2(OH)_2$ were prepared.
- From the characterization results, the materials sufficed in quality (as well as quantity) for further research and for subsequent comparison with industrial materials.
- Morphology of material (SEM images) was clearly retained when the material AUC, ADU and UO_4 was heat treated up till 800 ^oC.
- ADU and its calcined products were studied using HT-XRD, room temperature XRD, IR and Raman spectroscopy (Appendix C). The results are interesting and novel. HT-XRD and room temperature XRD were complementary to each other as well as TG/DTA. IR and Raman were also complementary and supported the observations of the XRD and TG/DTA techniques. This helps to deepen the understanding of the material when it undergoes treatment with temperature.
- The techniques, in combination can be extended to other yellow cake material.

4. Applying Raman spectroscopy as a tool in nuclear forensics

Most of the existing nuclear forensic tools (such as mass spectrometry) are extremely sensitive techniques and are used in a laboratory. In this chapter, a different technique, Raman spectroscopy is used to measure several UOCs and other uranium compounds such as UO_2. The concept of Raman scattering is illustrated in Figure 4-1A. An incident light provided by the laser, v_0 is used to excite the sample. When the sample is probed, the photons that make up the light can be absorbed, scattered or there is no interaction at all. Inelastic scattering is the basis of Raman spectroscopy. Some of the energy is transferred onto the sample as vibrations of the chemical bonds and is reflected as peaks in a Raman spectrum. Figure 4-1B illustrates the concept of IR spectroscopy for comparison. In contrast to Raman, IR probes the sample with non-monochromatic light and energy absorbed by the molecules are reflected as peaks in an IR spectrum. Both techniques were used to characterize some of the yellow cakes prepared in the laboratory (Chapter 3).

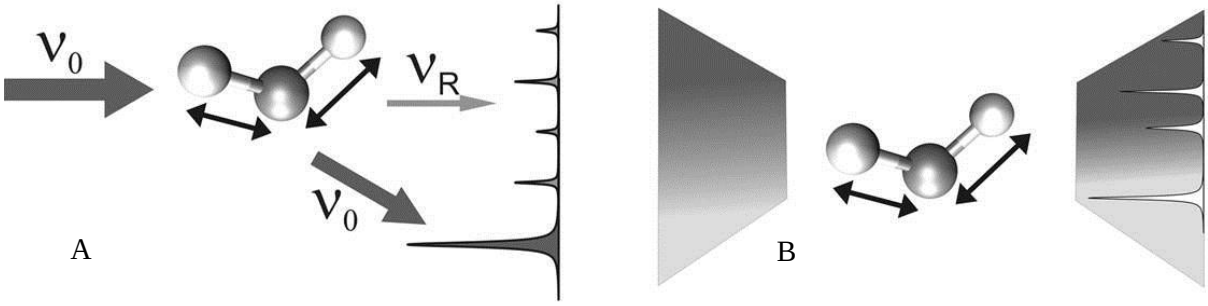

Figure 4-1: Illustration of the excitation of molecular vibrations in Raman (A) and IR (B) spectroscopy. Vibrational Raman transitions correspond to inelastic scattering (ν_R; thin arrow) of the incident monochromatic light and elastic scattering (ν_0; thick arrow). In IR spectroscopy, the vibrational transitions are induced by absorption of light quanta from a continuous light source [141].

4.1 Methods

4.1.1 Sample preparation

Raman spectroscopy is a technique that hardly requires any sample preparation. In this study, minimal preparation was carried out unless necessary, following three different approaches depending on the set-up used for the measurement. For hand-held spectrometer, samples were transferred into 4 ml glass vials for measurements. Samples were also pressed into pellets using 3630 X-Press with an applied pressure of approximately 74 MPa for 8 minutes for measurements with bench-top or laboratory Raman spectrometers. Lastly, small quantity of samples was dispersed onto carbon disks using vacuum impactors for particle analysis with the setup of bench-top spectrometer.

4.1.2 Instrumentation

4.1.2a FirstDefender|RM (Property of IAEA)

A hand-held Raman spectrometer, FirstDefender|RM (thereafter referred to as "hand-held" or "portable") from Ahura Scientific was on loan from IAEA, Vienna. Measurements could be made in two different geometries, in-vial geometry or point-and-shoot geometry. The former requires the sample to be contained in a standard 4 ml glass vial while the latter allows the sample to be probed without any containment. The device is equipped with a single excitation source, a laser radiating at 785 nm. A database containing thousands of spectra is directly installed by the manufacturer in the software of this spectrometer, together with an algorithm for the automatic identification of unknown Raman modes. This library can be further customised by the user.

The spectrometer was checked periodically by measuring a polystyrene sample and comparing its spectrum to a standard spectrum [142]. Acquisitions were usually made under the automatic mode and the speed depended on the signal of each sample. A manual mode was also possible, where selected acquisition times were up to 10 s. More features of the hand-held Raman spectrometer can be found in Table 4-1.

The above acquisition is termed as a normal scan. When a particular sample yielded a good quality spectrum, it was then further subjected to a library scan so that its spectrum could be stored in the database. This mode of acquisition was typically longer than a normal scan as a reasonably good quality spectrum (based on signal-to-noise) had to be obtained before storing in the library.

4.1.2b Senterra (Property of KIT INE)

A bench-top model of Raman spectrometer, Senterra (thereafter referred to as "Senterra") from Brukers is available in the Institute of Nuclear Waste Disposal (INE) of the Karlsruhe Institute of Technology (KIT). The instrument is equipped with two different lasers the wavelengths of which are 785 nm and 532 nm. A silicon test-spectrum was recorded daily prior to any measurements. Calibration was done automatically by the instrument. More features of Senterra can be found in Table 4-1.

4.1.2c T64000 (Property of ITU)

A laboratory Raman spectrometer, T64000 (thereafter referred to as "T64000") from HORIBA Jobin Yvon is available in ITU, Karlsruhe. The instrument is equipped with two lasers radiating at (at least) four different wavelengths, 752.5 nm, 647.1 nm, 514.5 nm and 488.0 nm and can be operated in a single or triple spectrograph configuration. Calibration of the wavenumbers was done with the 520.5 cm^{-1} line of a standard silicon single crystal prior to measurements. More features of T64000 can be found in Table 4-1.

4.1.2d inVia (Property of CEA)

A bench-top model of Raman spectrometer, inVia from Renishaw is available in the Commissariat à l'énergie atomique et aux énergies alternatives (CEA, Bruyère-lès-Chatel), Arpajon. The instrument is equipped with two different lasers radiating at 785 nm and 514 nm. This instrument is used for analysis of micrometer-sized particles. Calibration of the wavenumbers was done with a standard silicon single crystal prior to measurements. More features of inVia can be found in Table 4-1.

4.1.3 Statistical techniques

A PLS Toolbox version 7.5.2 (Eigenvectors Research, Inc., USA) for Matlab version 8.1 (The Matworks Inc, Natick, MA, USA) software were used to analyse part of the data.

Table 4-1: Characteristics of four Raman spectrometers.

Characteristics/Device	Ahura Scientific (Hand-held)	Bruker's (Senterra)	Jobin Yvon (T64000)	Renishaw (inVia)
Laser wavelength (nm)	785	532 785	488.0 514.5 647.1 752.5	514 785
Laser Characteristics (Lasing medium)	Diode (continuous)	AlGaAs (continuous)	Argon or Krypton (continuous)	Argon (514 nm) Diode (785 nm) (continuous)
Laser Characteristics (Laser type)	Semi-conductor	Semi-conductor	Gas ion	Gas ion Semi-conductor
Spot size of laser	0.14-1.8 (mm^2)	20x objective $4 \cdot 10^{-12}$ (4 μm^2)	50x objective $4 \cdot 10^{-12}$ (4 μm^2)	100x objective ~0.4 μm^2
Spectral range[5] (cm^{-1})	2875-250	3710-60 (532 nm) 4480-85 (532 nm)[6] 3320-90 (785 nm) 3820-100 (785 nm)[2]	> 4000 (514.5 nm) Up to ~ 3200 (752.5 nm)	> 4000 (514.5 nm) Up to ~ 3200 (785 nm)
Focal distance of spectrometer (cm)	1.8	20	64	25
Numerical Aperture (NA)	0.23	0.40 (20x objective)	0.50 (50x objective)	0.75 (50x objective)
Power (mW or % transmission[7])	75 (low), 125 (medium) 250 (high)	0.2, 2.0, 5, 10, 20 (532 nm) 1, 10, 25, 50, 100 (785 nm)	Adjustable (1-1000)	300 (785 nm) 50 (514 nm)
Spectral resolution or Full Width Half Maximum (FWHM) (cm^{-1})	7-10	3-5 (typical) 9-15 (Low resolution)	2-4 (single mode) < 1 (triple mode)	Typically around 1
Slit (µm)	No specific slit size	50 x 1000	200	Motorized, from 20-65 µm
Detectors & operating temperature (°C)	Thermo-electrically cooled CCD[8] (-20 to 40 °C)	Air cooled CCD[4] (-50 °C)	N_2 cooled CCD[4] (-150 °C)	Peltier (air) cooled CCD[4] (-70°C)
Typical integration time (s)	Depending on automatic or manual mode (max 10s)	Range: 1 to infinity Typical: 10-50	Range: 1 to infinity Typical: 10-25	Range: 10ms to infinity
Objectives	none	10x, 20x, 40x, 50x	10x, 20x, 50x, 100x	5x, 20x, 50x, 100x
Geometry (°)	180	180	180	180

[5] The response of the detector(s) is not constant throughout the spectral range. In particular, the response of lasers such as 785 nm/ 752.5 nm and 647.1 nm falls drastically at wavenumbers exceeding approximately 1500 and 2500 cm^{-1} respectively
[6] Low resolution mode
[7] Power for inVia is expressed as percentage transmitted
[8] CCD: Charge-coupled device

4.2 Interpretation of Raman spectra

4.2.1 Raman signal from glass container

Several of the measurements were made with the hand-held spectrometer using the point-and-shoot geometry. A broad peak was often observed when the measurement was made through glass vials (standard vials) as seen in Figure 4-2. This peak was considered as an interfering peak since it was rather broad. Although this peak could be readily removed through baseline correction, the point-and-shoot mode was generally more practical, and therefore preferably used.

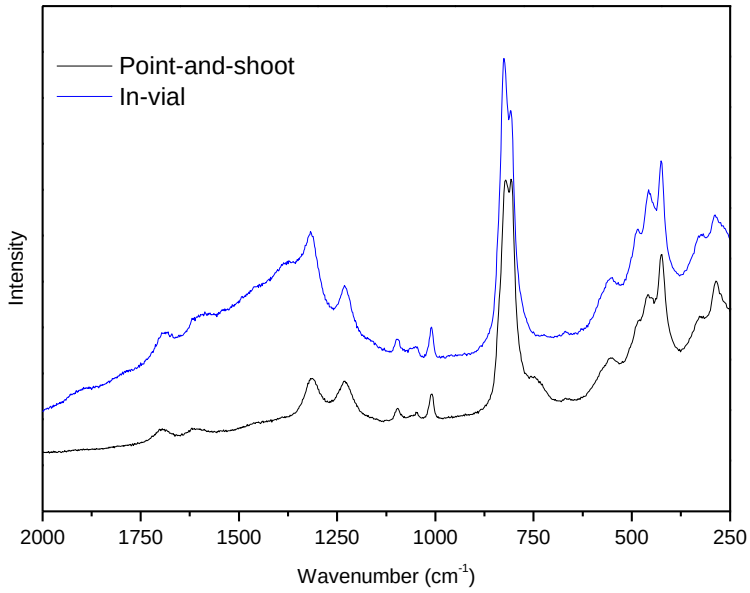

Figure 4-2: Raman spectra of Stanrock using in-vial and point-and-shoot geometry of the hand-held spectrometer.

4.2.2 Raman signal from compounds

Figure 4-2 shows the comparison between the Raman spectra of two ADU samples. One sample was laboratory prepared ADU (Batch I, Figure 4-3A) while the other one was an industrial sample from the Stanrock facility (Figure 4-3B). The laboratory prepared ADU was relatively pure and therefore, the Raman peaks observed at 817, 558, 450 and 327 cm^{-1} are attributed to vibrations belonging to the compound itself. A more detailed interpretation of these peak positions was already provided in Chapter 3.3.1. By comparing with the peaks in Figure 4-3B, three regions of the spectral range could be defined. First, a region termed as I can be assigned to the spectral range 900-250 cm^{-1} or below (if another spectrometer is used). These peaks are related to the main compound. Next, a couple of weak intensity peaks could be observed in region II (1200-900 cm^{-1}). It is important to note that no such peaks are visible in the spectrum of Figure 4-3A, the purer ADU prepared in the laboratory. In addition, the low intensities associated with these peaks indicate that they are likely to be impurities that are present at trace levels. These peaks were also observed in a handful of the industrial samples especially in ADUs and uranyl hydroxides, as highlighted in Figure 4-4 (dotted box).

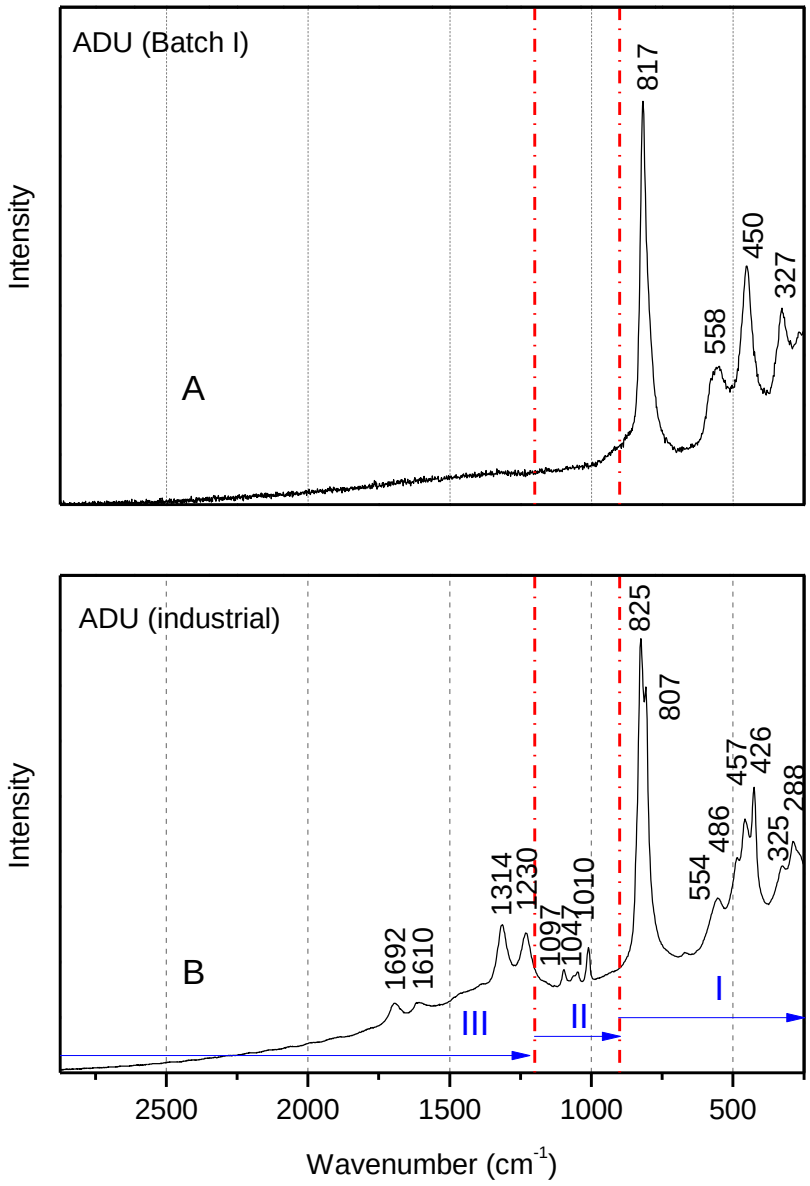

Figure 4-3: Raman spectra taken with hand-held spectrometer; Laboratory prepared ADU (Batch I) (A), Industrial ADU (Stanrock facility) (B). The spectra could be divided into three regions (I, II and III) for interpretation.

Therefore, peaks in region II are of great interest. These impurities are most probably related to the industrial processes used to produce UOCs. Ion chromatography has been successfully applied for the investigation of anions such as nitrates and sulphates [40]. In addition, infrared spectroscopy meant to provide information on the molecular composition of UOCs was also able to detect the anions [35].

The following paragraphs address the identification of these individual peaks. Several chemicals that are potentially impurities in the current UOCs, were measured on the hand-held Raman in order to obtain their spectrum. These chemicals were selected on the basis that they are being used in the industrial process or they are possibly formed as a result of the various processes to produce these UOCs.

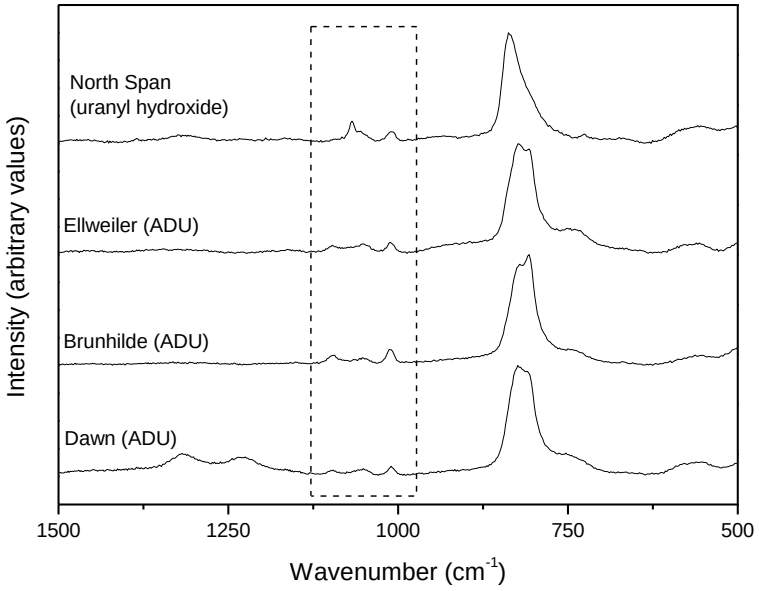

Figure 4-4: Raman spectra of four industrial UOCs (taken with hand-held spectrometer). The box highlights that impurities could be observed with these samples.

For instance, sodium chlorate $NaClO_3$, is used as an oxidant during leaching process and chlorate ion has the most intense peak between 940-930 cm^{-1}. In fact, this peak was observed only when the laser with higher photon energy at 647.1 nm, was used on T64000 (Figure 4-5) and not with the higher wavelength (lower photon energies) lasers of 752.5 nm and 785 nm (hand-held or Senterra). The peak was found in sample Stanrock, a form of ADU as seen in the same figure.

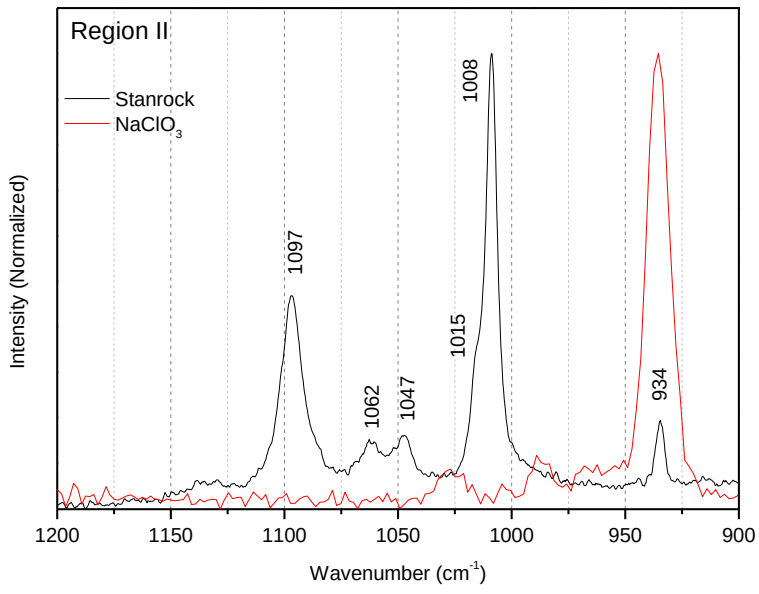

Figure 4-5: Raman spectra of Stanrock (taken with T64000 at 647.1 nm) and $NaClO_3$ (taken with the hand-held spectrometer at 785 nm).

It is noteworthy that chlorate ions have 4 peaks of differing intensities namely; 987-975 cm^{-1} (medium weak), 940-930 cm^{-1} (strong), 625-620 cm^{-1} (weak) and 490-480 cm^{-1} (medium) [143]. In

this case, the most intense peak at 934 cm^{-1} (black line) was weak and thus, its identity could not be further verified by other peaks that were absent.

Next, the impurity peak at 1009 cm^{-1} was investigated. This peak was often found in reasonably high content. This peak was already seen in Figure 4-4 (at 1008 cm^{-1}). Another example is given in Figure 4-6 for the sample Blind River (a form of uranyl hydroxide). According to Degen *et al.* [143] , sulphate ions have the following bands; 1180-1080 cm^{-1} (very weak), 1035-965 cm^{-1} (strong), 670-610 cm^{-1} (weak) and 490-400 cm^{-1} (medium weak). Some sulphate salts possibly present in UOCs, such as sodium sulphate and calcium sulphate were measured to identify the peak of interest. Hydrated calcium sulphate was found to match the peaks observed in the sample (Figure 4-6). Henceforth, the presence of this particular band in the UOCs was assigned to $CaSO_4.2H_2O$ (gypsum). $CaSO_4.2H_2O$ has a few other peaks such as 1137 cm^{-1} (possibly 671 cm^{-1} and 492 cm^{-1} as well) and its presence seen in the same UOC sample further confirmed its identity. The anhydrous form of calcium sulphate has the main peak at around 1015 cm^{-1}. This peak can also be found in the UOCs and in fact, it appears as a shoulder at 1015 cm^{-1} in Figure 4-5 (black line).

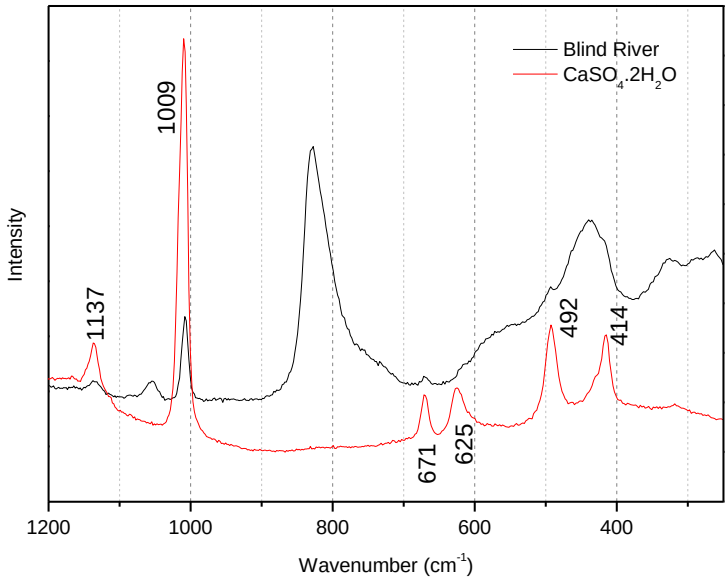

Figure 4-6: Raman spectra of Blind River and $CaSO_4.2H_2O$ (taken with the hand-held spectrometer).

In the industrial process, it is necessary to purify the material further and thus contaminants have to be removed. The precipitation with lime is often carried out to remove iron and other impurities like sulphates and hydroxides. In this case, the sulphates are precipitated as calcium sulphate [12]. Hence, the observation of this impurity is correlated to the use of lime. As the solubility of gypsum is very low, it could be understood that the filtration or dewatering steps were not able to remove this impurity completely. Therefore, the observation of the gypsum peak can provide clue to the processing history of the UOC sample.

A weak peak at about 1047-1054 cm^{-1} was often seen in ADU (Stanrock, Brunhilde, Ellweiler and Milliken Lake) and uranyl hydroxides (Blind River and North Span). In this region of Raman

bands, several anions share an overlapping range of frequencies. The bicarbonates, bisulphates and nitrates fall into the range of 1045-1025 cm^{-1}, 1062-1027 cm^{-1}, 1070-1040 cm^{-1} respectively corresponding to the most intense peaks [143]. Bicarbonate is also one of the common reagents used especially in the leaching of alkaline ores. However, the samples reported in this paper did not go through the alkaline leaching process and thus its presence is ruled out. As for the bisulphates, although they have a similar range as the nitrates, it should be noted that there are two overlapping intense peaks associated with the bisulphate, HSO_4^- ion. For instance, sodium bisulphate has two strong peaks at 1062 and 1038 cm^{-1} and ammonium bisulphate at 1040 and 1014 cm^{-1} [143]. The single peak observed at 1047 cm^{-1} in Figure 4-7 from sample Stanrock was therefore, unlikely to be a bisulphate.

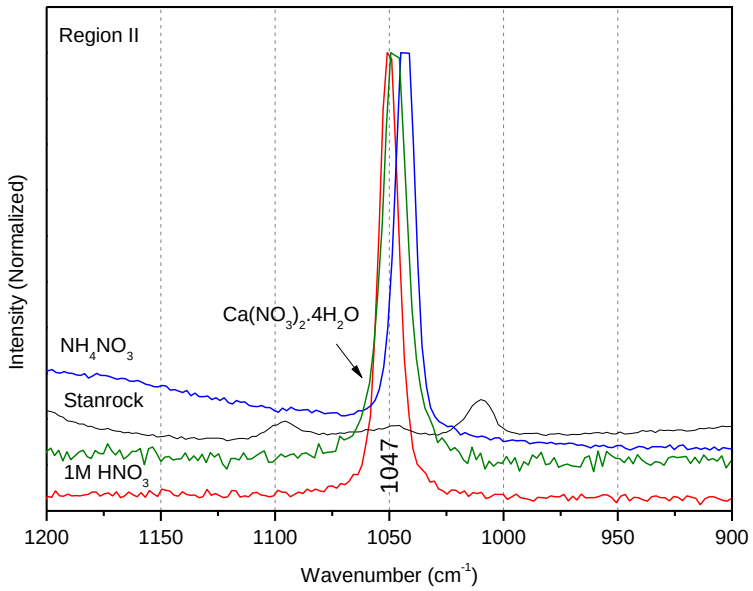

Figure 4-7: Raman spectra of Stanrock and different forms of nitrates (taken with the hand-held spectrometer).

A comparison of the various nitrates made with sample Stanrock and a few possibilities such as ammonium nitrate (1043 cm^{-1}), calcium nitrate tetrahydrate (1050 cm^{-1}) as well as nitric acid (1047 cm^{-1}) were found. These compounds showed small but significant shifts in the vibrational bands of the nitrate peaks. However, in the ADU sample from Stanrock, the band at around 1050 cm^{-1} was rather broad and of low intensity and hence, the nitrate peak could not be unambiguously identified. Most nitrates are soluble in water and thus, it corroborates with the observation of rather low level of impurities. The detection limit is in the range of parts per million.

In addition, a second peak at 1067 cm^{-1} was also found for the sample North Span (Figure 4-8). This peak was found to coincide with the peak from sodium nitrate. As this nitrate peak appeared only at slightly higher wavenumber than 1050 cm^{-1}, the two peaks of nitrate were not resolved.

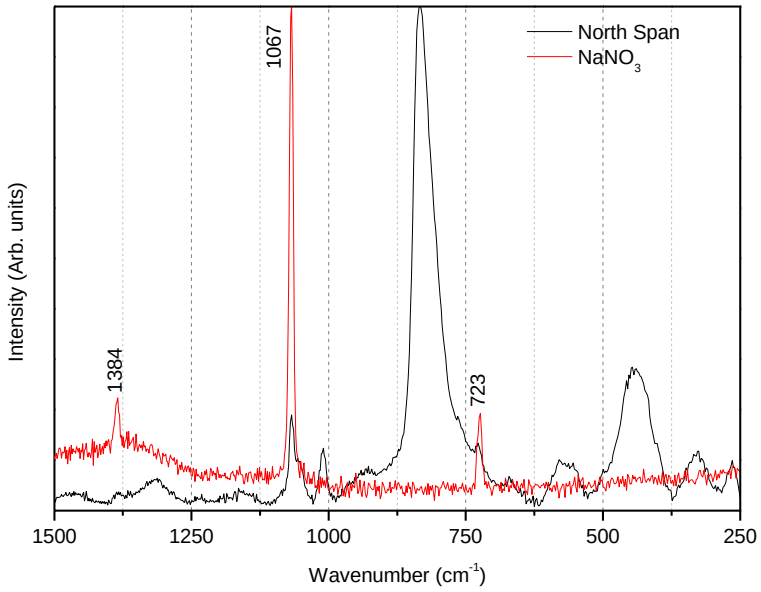

Figure 4-8: Raman spectra of North Span and $NaNO_3$ (taken with the hand-held spectrometer).

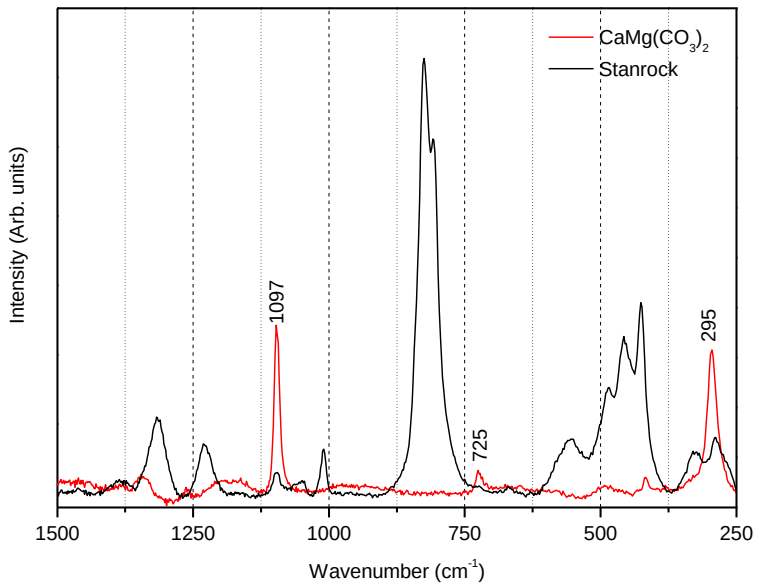

Figure 4-9: Raman spectra of Stanrock and $CaMg(CO_3)_2$ taken with the hand-held spectrometer.

Lastly, peaks found around the region of 1095-1097cm^{-1} were identified. According to Degen *et al.* [143], carbonates possess peaks in the range between 1095-1075 cm^{-1}. Based on the identification of the data shown thus far, most of the salts were found to be associated with sodium or calcium and therefore, carbonates of sodium and calcium were measured and peaks corresponding to 1078 and 1086 cm^{-1} (υ_1; symmetric stretch mode of CO_3^{2-}) were found respectively. Since these cannot be responsible for the band at 1097 cm^{-1}, other possibilities such as manganese carbonate and magnesium carbonate were measured too. Their respective bands were found at 1084 and 1120 cm^{-1}. The search was subsequently extended to calcium-magnesium carbonate minerals [144]. In this case, a strong band was successfully identified at 1097 cm^{-1} and was associated with dolomite, $CaMg(CO_3)_2$

(Figure 4-9). The use of lime for pH adjustments and removal of contaminants followed by the precipitation of yellow cake using magnesia [12] is the most plausible explanation for the formation of this naturally occurring compound. However, this is not an unequivocal indication of the above process as this impurity was also found in UOC samples that had undergone the precipitation step with ammonia instead.

Finally, a third region, region III defined as the spectral range beyond 1200 cm^{-1} is discussed. Figure 4-10 depicts the Stanrock sample measured with different excitation wavelengths of 647.1 nm, 752.5 nm and 785 nm.

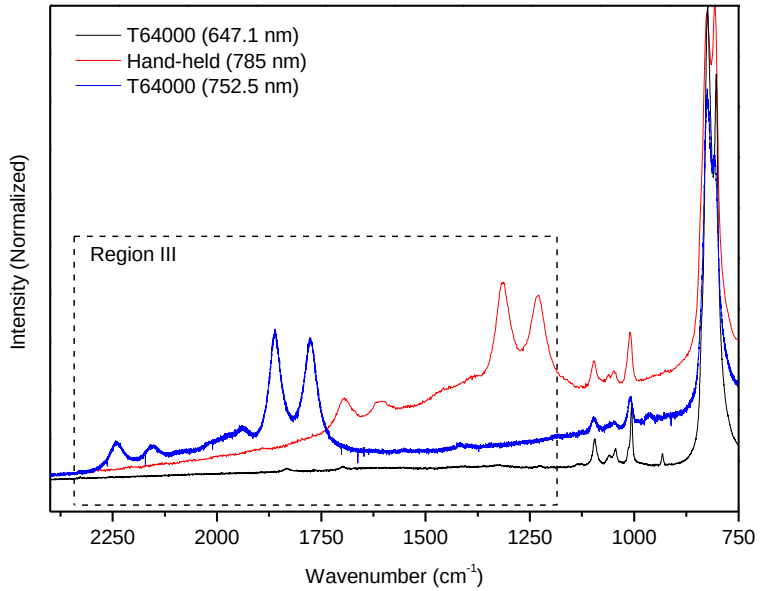

Figure 4-10: Raman spectra of Stanrock measured at different excitation wavelengths using hand-held and T64000.

Four peaks were found in this region with the 752.5 nm and 785 nm lasers. These peaks were considerably intense and interestingly, these were the only peaks found shifted as a function of the wavelength of the laser used for excitation. Each of the 4 peaks was shifted by ca. 546.5 cm^{-1}. The same peaks were no longer observed (shifted out of the measured spectral range) when the measurement was repeated with 647.1 nm laser. It therefore became clear that these were not typical Raman vibrational modes. In fact, vibrational Raman shifts (expressed in wavenumber difference with respect to the central excitation laser line, taken as zero) always remain the same irrespective of the laser used. On the other hand, with the above values expressed in absolute wavelength (nanometers), these transitions occur at the same absolute spectral position. The apparent shift seen in Figure 4-10 is therefore only relative to the different lasers used as excitation sources. In the light of such observations, it became obvious that these peaks originated from electronic transitions (fluorescence) occurring at wavelengths close enough to those of the excitation lasers to be detected in the current spectra. There is no useful information that can be used to correlate the data for nuclear forensics purposes. Henceforth, this part of the spectra is not interpreted. It is noteworthy such peaks were only

observed in few industrial UOC samples and were completely absent in the case of laboratory prepared UOCs.

4.3 Evaluation of hand-held Raman spectrometer for the measurement of UOCs

4.3.1 'Demographics' of the samples

Referring to Appendix B (Table B-1), 126 samples have been analysed with the hand-held spectrometer. Pertaining to the evaluation of hand-held Raman, 116 samples were related to this study. These include 111 industrial UOCs (mostly) and non-UOCs, as well as 5 UOCs from Batch I laboratory synthesis. UO_2 powder, UO_2 fuel pellet and UF_4 were among the samples analysed and these were not UOCs.

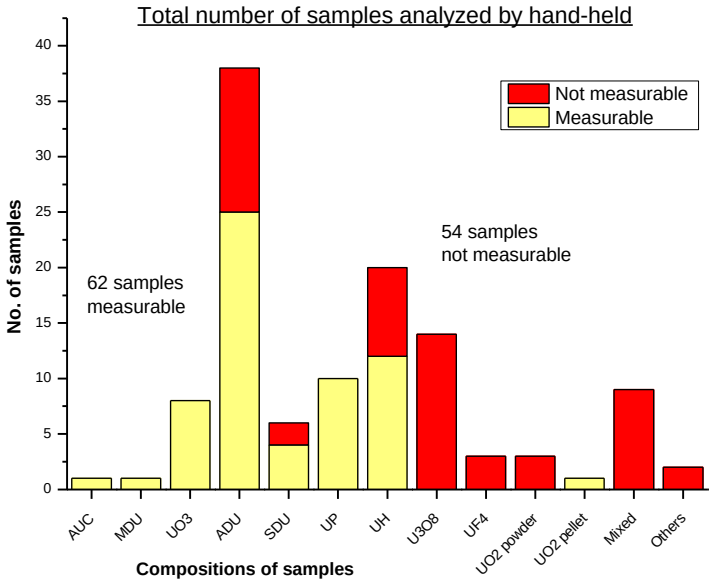

Figure 4-11: Breakdown of the total number of samples measured by hand-held spectrometer (in-vial geometry)

As shown in Figure 4-11, nearly half the samples were not analysable by the hand-held device using the in-vial geometry. These were mostly calcined samples such as U_3O_8 or other dark coloured powder samples and non-calcined samples with high fluorescence background. The lack of capability to measure all of the above samples is dealt with in the next section.

Out of the 62 measurable samples including some replicates, 48 samples were measured in the library mode and subsequently stored in the device. The measurements for the library were done using both in-vial and point-and-shoot mode and therefore, there were two library spectra per sample with the exception of the UO_2 pellet, which was done with only the point-and-shoot mode. For the point-and-shoot geometry, a sample holder with the function to rotate the sample pellet was designed and contructed in-house. The ability to rotate the sample allowed the laser to probe at different spots and thus, the signal was taken over a larger area rather than a single point. Besides, the interfering peak associated with the use of glass vials (Figure 4-2) was avoided in this mode of measurement.

Occasionally, slight differences in the spectra taken from the two geometries could be observed. The differences are often related to peak intensities which could also be observed between normal scan and library scan for the same geometry [145].

4.3.2 Matching accuracy of the algorithm in the device

In the process of identifying the unknown using the database, there are typically three steps involved in the algorithm [87]. Firstly, the pre-processing step includes the removal of background followed by smoothing. Secondly, the parameterization step is carried out where the position, amplitude and width of the peaks are assessed. Lastly, the detection algorithm browses the library for possible match to substances or mixture of substances. Due to proprietary issues, no detailed information is available about the algorithm of FirstDefender|RM.

22 samples out of the 48 indexed in the library were selected and tested as unknowns. The objective was to determine the accuracy of the identification algorithm and the usefulness of this hand-held Raman in the analysis of measurable UOCs and non-UOCs. For each sample with the exception of UO_2 pellet, both geometries were tested with 10 scans per geometry. Altogether, 20 normal scans per sample were made for 21 samples and 10 normal scans for UO_2 pellet.

The assessment of 5 uranyl peroxides, 3 sodium diuranates, 5 uranyl hydroxides, 6 ammonium diuranates, 2 UO_3 and a UO_2 pellet was two-fold. The ability of the device to match the UOC to its original facility and the ability to match the UOC to its composition or class were investigated. Apart from these two aspects, any form of misidentifications was also captured. Comparison was also made between the two geometries for measurement. Table 4-2 shows the typical recording of the data from 8 different categories. These categories were formulated on the basis of the results given after the measured spectrum was compared with the library of the hand-held. The following scenarios were possible; more than one match, no matches or matched to mixture(s). Some assumptions were also made here; that the sequence of appearance was related to its likelihood as a match. The first compound provided on the screen of the hand-held spectrometer was assumed to have the highest possibility as a match [146].

Table 4-2: Typical record from the confidence trial. As an example, two UO_4 are shown.

Sample Name/Type	Mobil (UO_4)		Rabbit Lake (UO_4)	
Its library name	YC UO4-4	YC UO4-4a	YC UO4-1	YC UO4-1a
Geometry	**In-vial**	**Point-and-shoot**	**In-vial**	**Point-and-shoot**
Scan No.	141-150	341-350	151-160	351-360
No. of such type of UOC in library	10	5	10	5
1. No of scans (out of 10) that correctly classify the 'unknown'- appears anywhere in the sequence of match(es). Regardless of origin	10	10	10	10
2. No of scans (out of 10) that correctly matches the 'unknown' to its facility- appears as the 1st line in the sequence of match(es)	7	0	2*	3
3. No of scans (out of 10) that correctly matches the 'unknown' to its facility- appears anywhere in the sequence of match(es)	10	10	10	10
4. No of scans (out of 10) that had a different class of UOC appearing as a match	0	0	0	0
5. No of scans (out of 10) that have a non-UOC appearing as a match	0	0	0	0
6. No of scans (out of 10) that were matched as a **'mixture'**	0	0	0	0
7. No of scans (out of 10) that had **'No match'**	0	0	0	0
8. Others			*1 of the 2 scans were matched to RL	

As an example, Figure 4-12 shows the outcome of the trials undertaken for five industrial uranyl peroxides originating from the facilities of USA Mobil, Canada Rabbit Lake, USA El Mesquite, Irigaray and Everest Yellow. In all 5 cases, the samples were correctly identified as peroxides (100 % under the category of Composition). Categories 4-7 were not observed which meant that there were no misidentifications as well. In the aspect of identifying the origin of the sample(s), there were two categories, ‘Origin (definite)’ and ‘Origin (Indefinite)’. The former requires the correct name of the origin to appear as the first line. The latter allows the correct name to be found anywhere in the sequence. By using a less stringent definition, it can be observed that identifying the origin of

the sample is possible (although not absolute since it is not the only possibility presented) and is 100 % in all cases except for El Mesquite. El Mesquite is a sample characterized by high background or fluorescence in comparison with the other four peroxide samples.

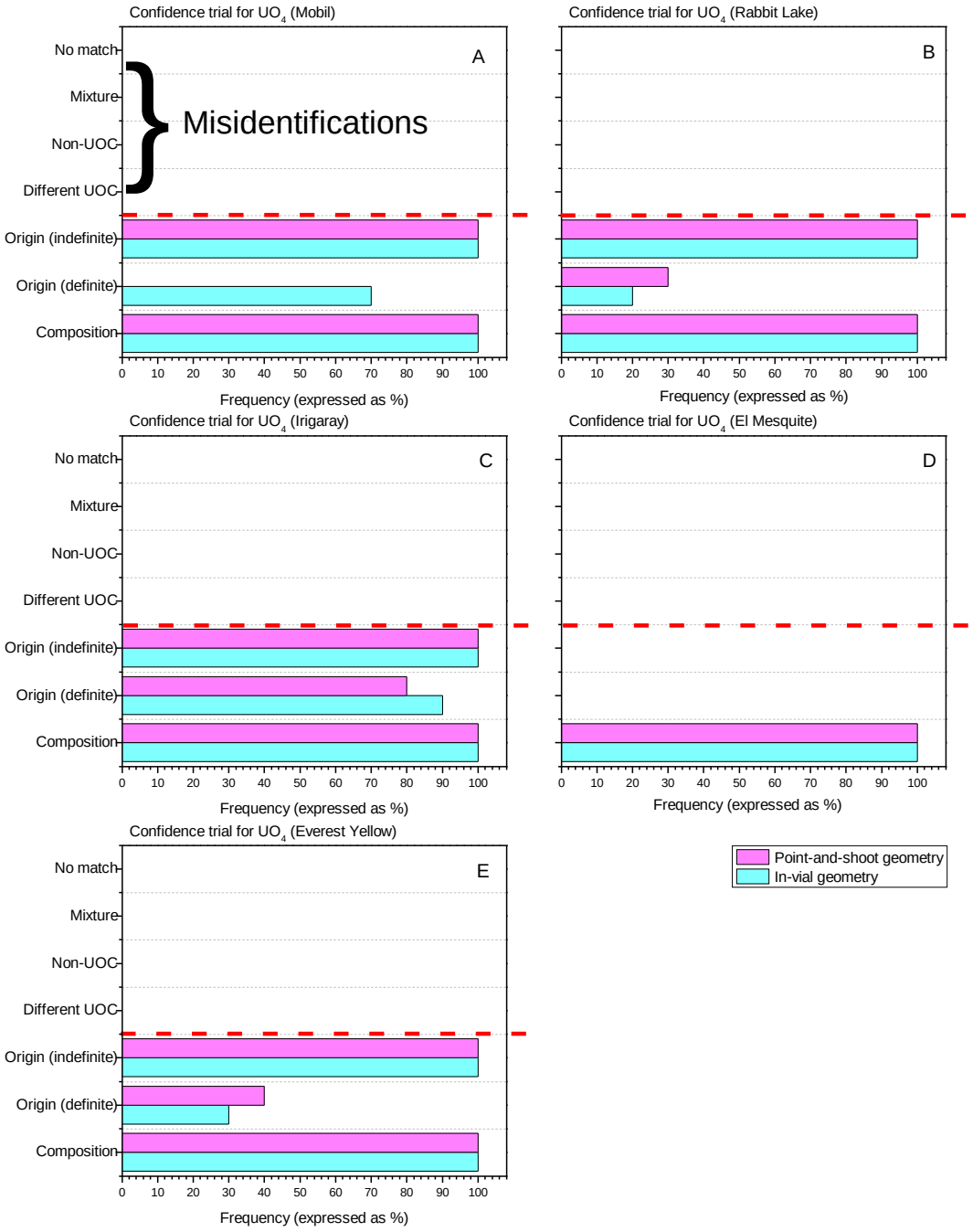

Figure 4-12: Confidence trial for five different UO_4 samples from Mobil (A), Rabbit Lake (B), Irigaray (C), El Mesquite (D) and Everest Yellow (E). Red line shows the division between positive identifications and misidentifications of the samples.

The main difference between the results from the two geometries appears to manifest only in the category of 'Origin (definite)'. There is no clear indication that one of the geometries is better than the other. On the other hand, both geometries gave identical results in the remaining six categories.

Another class of UOCs is illustrated in Figure 4-13. The results are completely different from those seen in the previous example.

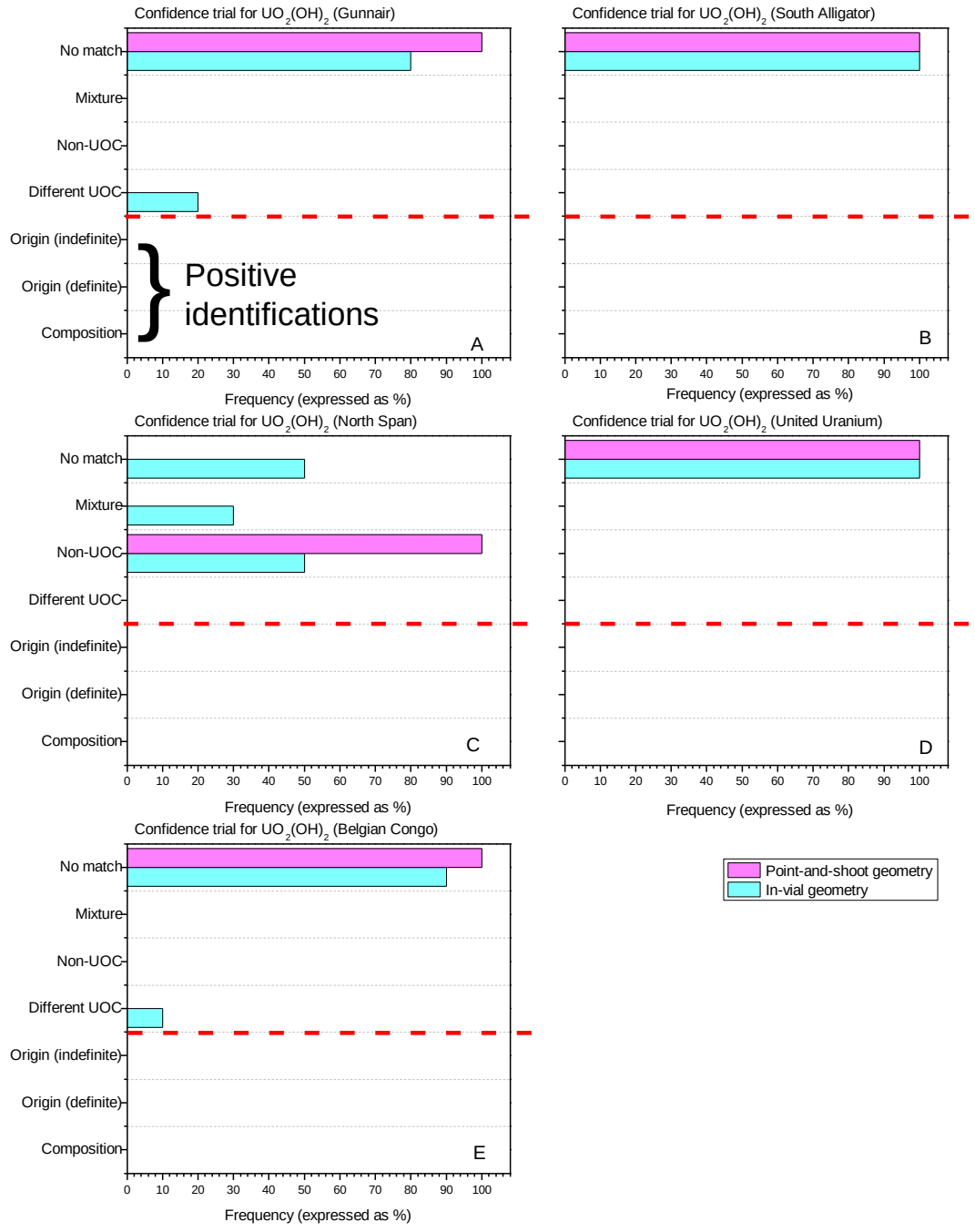

Figure 4-13: Confidence trial for five different $UO_2(OH)_2$ samples from Gunnair (A), South Alligator (B), North Span (C), United Uranium (D) and Belgian Congo (E). Red line shows the division between positive identifications and misidentifications of the samples.

None of the five samples could be identified as uranyl hydroxide. No matches were common and there were some cases of misidentifications, either as non-UOCs or mixtures. There could be an important explanation for the above findings. It was likely that the quality of the library spectra for this type of compound were not good as they frequently contained high fluorescence background.

These industrial materials are not pure and logically, only spectra of pure materials should be stored in the library. Although the spectra of the measured 'unknown' sample resembled the library spectra, pre-processing of the former such as baseline correction would already render the spectra different from that of the library spectra. Similar plots belonging to the remaining 12 samples can be found in Appendix D.

In summary, the identification of certain UOCs such as UO_4, SDU, UO_3 and some ADUs using hand-held Raman yield promising results. Exception applied to uranyl hydroxide where several samples could not be positively identified.

4.4 Comparison of three Raman spectrometers in the measurement of seven uranium compounds

In this section, the performances of three Raman spectrometers are evaluated based on measurements of seven different uranium compounds. These spectrometers are hand-held FirstDefender|RM as already seen in previous section, Senterra and T64000.

Figures of merit such as sensitivity, signal-to-noise ratio and the detection capabilities with respect to the different compounds are discussed. Other features such as acquisition time, advantages and limitations pertaining to each spectrometer are also mentioned in view of the general applications to nuclear forensics.

4.4.1 Sensitivity

The sensitivity of the different Raman spectrometers can be compared following the analysis performed by Fryling *et al*. [147]. Let S be the absolute scattered intensity recorded by the spectrometer. In order to compare the sensitivity of different spectrometers based on Raman scattering signal originating from the same sample, S can be normalised to S_N based on equation 4.1.

$$S_N = \frac{S}{A \cdot P_D \cdot t \cdot f(\nu,\ T)} \tag{4.1}$$

A = Sample scattering area (μm^2)
P_D = Laser power density ($W.cm^{-2}$)
t = Acquisition time per spectral unit ($s\ cm^{-1}$)
$f(\nu, T)$ = Factor accounting for the Raman scattering intensity dependency on photon frequency, ν and absolute temperature T

In Eq. 4.1, parameters typical of the analysed material such as its differential Raman cross-section ($cm^2 \cdot$scattering $unit^{-1} \cdot sr^{-1}$) and density on the scattering surface (scattering units$\cdot cm^{-2}$) are simplified, considering that these quantities are the same for all the spectrometers for a given compound. Finally, because the present spectra are recorded using different laser excitation wavelengths, when comparing the intensity of similar Raman modes measured, different S values should also be normalised with respect to the factor $f(\nu, T)$. Factor f is based on the theoretical determination of the Raman scattering cross-section and depends also on temperature through boson statistics [148]. When ν is expressed in cm^{-1}, f can be simplified to the following equation 4.2 [149].

$$f(\nu,T) = \frac{(\nu_0 - \nu)^4}{\left(1 - \exp\left(-\frac{hc\nu}{kT}\right)\right)} \quad (4.2)$$

ν_0 = Photon wavenumber of the excitation laser source (cm^{-1})
ν = observed Raman shift (cm^{-1})
h = Planck's constant (6.626 x 10^{-34} m^2 kg s^{-1})
c = speed of light in vacuum (2.99 x 10^8 m s^{-1})
k = Boltzmann's constant (1.381 x 10^{-23} m^2 kg s^{-2} K^{-1})

Comparison of the sensitivity among the spectrometers for different compounds is graphically presented in Figure 4-14. The values for the most prominent Raman band can also be found in Table 4-3. All the values in this table have been normalized with reference to the sample that yielded the highest intensities.

In all the seven compounds measured, Senterra yielded the highest sensitivity, followed by the hand-held Raman and T64000. The latter is featured by a longer focal distance of 64 cm, which results in a higher spectral resolution at the expense of sensitivity. It is also obvious that for dark coloured UOCs such as both UO_2 and U_3O_8 powders, the sensitivity of Senterra and T64000 dropped by 2-3 orders of magnitude and in the case of hand-held spectrometer, these compounds were not measurable. As for the UO_2 fuel pellet, the sensitivity was better for Senterra and T64000 and it was also measurable by the hand-held spectrometer with reasonably good sensitivity. It is interesting to note that the hand-held spectrometer produced a very good UO_2 spectrum of the fuel pellet in contrast to the inability to measure the powder form. This is due to the higher sensitivity of the portable device to the macroscopic surface optical properties (reflectivity, absorptivity) of the sample (on a spot of approximately 1 mm in diameter). In the powder form, the already low reflectivity of uranium dioxide (about 15% in the visible-NIR range) [150] is reduced even more, resulting in a very faint back-scattered light intensity. In contrast, the T64000 and the Senterra facilities are equipped with microscopes through which micro-Raman spectra can be measured. In these latter cases, only the roughness of the sample surface on a micrometric scale matters. This is the main reason why poorly reflecting dark powder samples like UO_2 and U_3O_8 can be measured with micro-Raman spectrometers and hardly at all with devices operating on macroscopic spots. The same observation applies as well to U_3O_8 powder. Differences between the Raman spectra of oxides and that of the uncalcined yellow cakes have a similar explanation. Peaks are poorly defined in oxides owing to their dark or almost black colour. Preferential absorption of laser energy occurs as a result when compared to scattering/reflection.

4.4.2 Signal-to-noise ratio

The signal-to-noise ratio was determined by taking the same normalised signal from equation 4.1 and the value divided by the noise level. The noise level was determined by first smoothing the spectra by averaging over 100 points around each experimental datum, then the difference between

the smoothed and original curve was taken. The noise level was then defined as the amplitude of a 2-standard-deviation (95 % confidence) band of the points obtained by subtracting the smoothed curve from the original one. The noise amplitude was determined, following this procedure, in the vicinity of each Raman line investigated here.

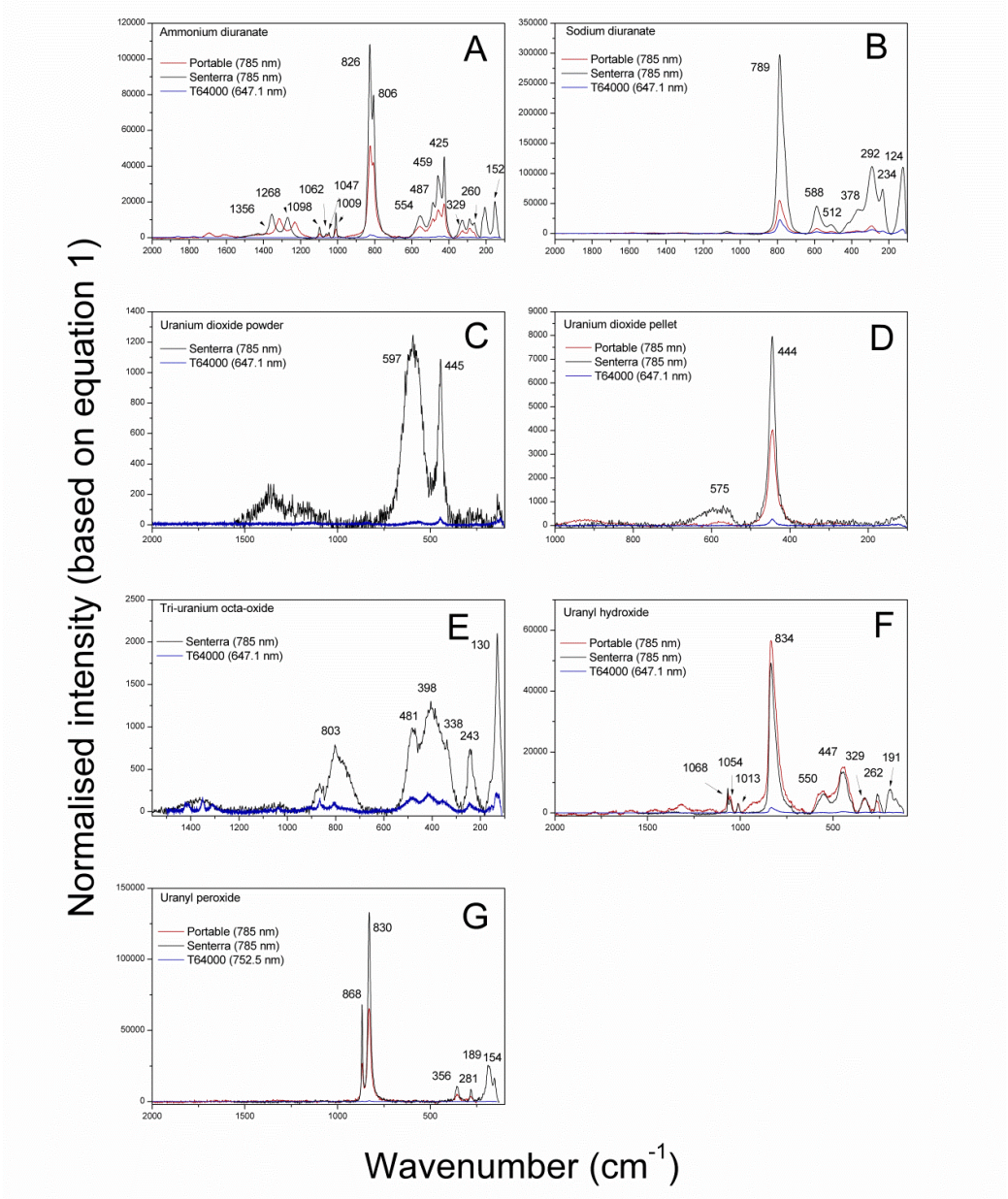

Figure 4-14: Raman spectra of each industrial compound measured by different spectrometers (normalised according to Eq. 4.1 and 4.2). A: Ammonium diuranate (Stanrock), B: Sodium diuranate (Somair), C: UO_2 powder (IAEA's sample), D: UO_2 pellet, E: U_3O_8 (Mary Kathleen), F: uranyl hydroxide (North Span) and G: uranyl peroxide (Mobil).

Referring to Table 4-3, T64000 has reasonably good signal-to-noise ratio (the best among the three spectrometers for the measurement of ammonium diuranate) due to the low level of noise in the spectra. Although there are exceptions, by taking into account the noise level, this has drastically improved the figure of merit for signal-to-noise ratio compared to that for sensitivity.

Table 4-3: Comparison of sensitivity, signal-to-noise ratio and the ability to detect characteristic bands and impurities present in measured compounds among the three spectrometers. Calculated values were further normalised to the Senterra spectrometer signal recorded on sodium diuranate within each figure of merit for better readability.

Type of compound	Sensitivity (Normalised based on Eq. 4.1 & 4.2)			Signal-to-noise ratio			Detection capability (Based on characteristic bands)			Ability to detect impurities (If present at ppm levels)		
	Hand-held[9]	Senterra[5]	T64000[10]	Hand-held	Senterra	T64000	Hand-held	Senterra	T64000	Hand-held	Senterra	T64000
Ammonium diuranate	17.5	36.8	1.9	31.2	47.3	56.4	✓	✓	✓	✓	✓	✓
Sodium diuranate	18.6	100.0	3.4	24.6	100.0	28.4	✓	✓	✓	MP	MP	MP
UO_2 powder	-	0.3	0.007	-	2.7	0.9	X	✓	✓	NA	NA	NA
UO_2 pellet	1.2	2.4	0.04	10.9	19.2	2.8	✓	✓	✓	NA	NA	NA
U_3O_8	-	0.4	0.03	-	4.8	1.6	X	✓	✓	X	X	X
Uranyl hydroxide	19.3	16.8	0.3	15.5	59.4	8.0	✓	✓	✓	✓	✓	✓
Uranyl peroxide	22.3	45.3	0.2	12.8	31.9	23.7	✓	✓	✓	MP	MP	MP

[9] 785 nm
[10] 752.5 nm/647.1 nm

4.4.3 Detection capability (of impurities and less characteristic bands)

Both Senterra and T64000 were capable of analysing the different types of yellow cakes as well as UO_2 pellet. On the other hand, the portable spectrometer could measure most of the compounds with good sensitivity except for both UO_2 and U_3O_8 powder. It is reiterated that impurities introduced during the production of yellow cake (milling process) can also be observed by Raman scattering. The presence of impurities such as nitrates, sulphates and carbonates can provide clues to the production history of yellow cakes thus critical for the application of nuclear forensics [151]. As seen in Figure 4-13A (ammonium diuranate) and 4-13F (uranyl hydroxide), small peaks can be observed above 1000 cm^{-1} with all the three spectrometers (although less visible for T64000 after normalisation). Nitrates and sulphates are very common impurities owing to the industrial use of nitric acid and sulphuric acid. Sulphuric acid is the preferred acid for leaching of the uranium ores while nitrate solutions can be used as an eluent on IX resins. The appearance of these peaks also corresponds to the level of nitrates and sulphates reflected in Table 4-4. These level of impurities from the same samples were determined with ion chromatography after extraction with water [40].

Table 4-4: Levels of NO_3^- and SO_4^{2-} present in 10 ml of water extract with 100 mg of UOC.

UOCs from various facilities	Composition	{impurities}[11] ppm	
		$\{NO_3^-\}$	$\{SO_4^{2-}\}$
Stanrock	$(NH_4)_2U_2O_7$	60.3	500
Somair	$Na_2U_2O_7$	0.022	4.216
North Span	$UO_2(OH)_2$	377	396
Mobil	UO_4	0.04	2.189
Mary Kathleen	U_3O_8	1.367	539.12

It is also noted from the same table that the sample from Mary Kathleen (U_3O_8) shows high content of sulphates, which is comparable to the level present in ADU from Stanrock facility. However, the impurities in the U_3O_8 sample were not detected by any of the spectrometers (Figure 4-14E). The sulphate peak, if present should appear at ca 1009 cm^{-1} [151]. This certainly suggests that the optical property of the sample affects the detection of impurities. The dark coloured samples absorb more light and scattering is less effective as a whole. Therefore, other techniques (for example, particle analysis by Raman spectroscopy) should be used if the impurities content of the uranium oxides are of interest.

It is also reiterated that certain vibrational bands such as nitrogen-hydrogen (N-H) and oxygen-hydrogen (O-H) present in ammonium diuranate and uranyl peroxide/uranyl hydroxide respectively are not observed by all the three spectrometers. Figure 4-14 depicts the comparison between industrial and laboratory prepared uranyl peroxide. As seen in Table 4-4, the impurities associated with the yellow cake originating from Mobil facility are extremely low. Consequently, no

11 The above values are within an uncertainty of 10%.

peaks were observed above the region of 1000 cm^{-1} in any of the spectra (Figure 4-15A). With the chemical formula of $UO_4.xH_2O$, one should also expect to observe O-H vibrational bands in the region of 1600 cm^{-1} (bending modes of water) and above 3000 cm^{-1} (stretching mode of water). However, there were no peaks in the region of 1600 cm^{-1} observed for the above sample, not even with the higher frequency laser at 532 nm which only resulted in fluorescence (the background is intentionally left untouched).

This was not the case for the laboratory prepared uranyl peroxide (Figure 4-15B). Measurements could be carried out with the 532 nm laser unlike the industrial sample that had somewhat higher background due to fluorescence. Both bending and stretching modes of water could thus be observed whereas the stretching mode was not observed with the 785 nm laser. It appeared that the higher frequency stretching modes were only observable with higher excitation energies. In the case of 647.1 nm, the spectral acquisition had to be stopped at 2500 cm^{-1} due to the hindrance by parasite lines at higher wavenumbers.

Hence, it can be deduced that the N-H bands might be observable if the green laser (532 nm) combined with low resolution could be used on ADU samples without any hindrance from the fluorescence. The vibrations of N-H bonds are known to be Raman active. As an intermediate energy between the red (785 nm) and green (532 nm) laser, the laser at 647.1 nm available with T64000 offers a possibility to observe N-H bands provided the parasite lines are removed.

By comparing the Raman spectra of an industrial sample of uranyl peroxide versus one that has been prepared in the laboratory, it can be postulated that the presence of impurities in the former material contributes to the observation of fluorescence, which impedes the use of higher frequency laser. Without such fluorescence, using a high frequency excitation source would yield higher intensities thus better sensitivity and permit the observation of more peaks (e.g.: the stretching and bending modes of water) [117]. Although these bands are less characteristic than the main uranyl ion band, their observation will nevertheless elevate the confidence in identification of the material during nuclear forensics investigations. It is also pertinent to note that the above observations deriving from the use of different lasers are also attributed to the fact that the response of multichannel detectors fall drastically with the use of longer wavelength lasers [152] (cf. Eq. 4.1 and 4.2).

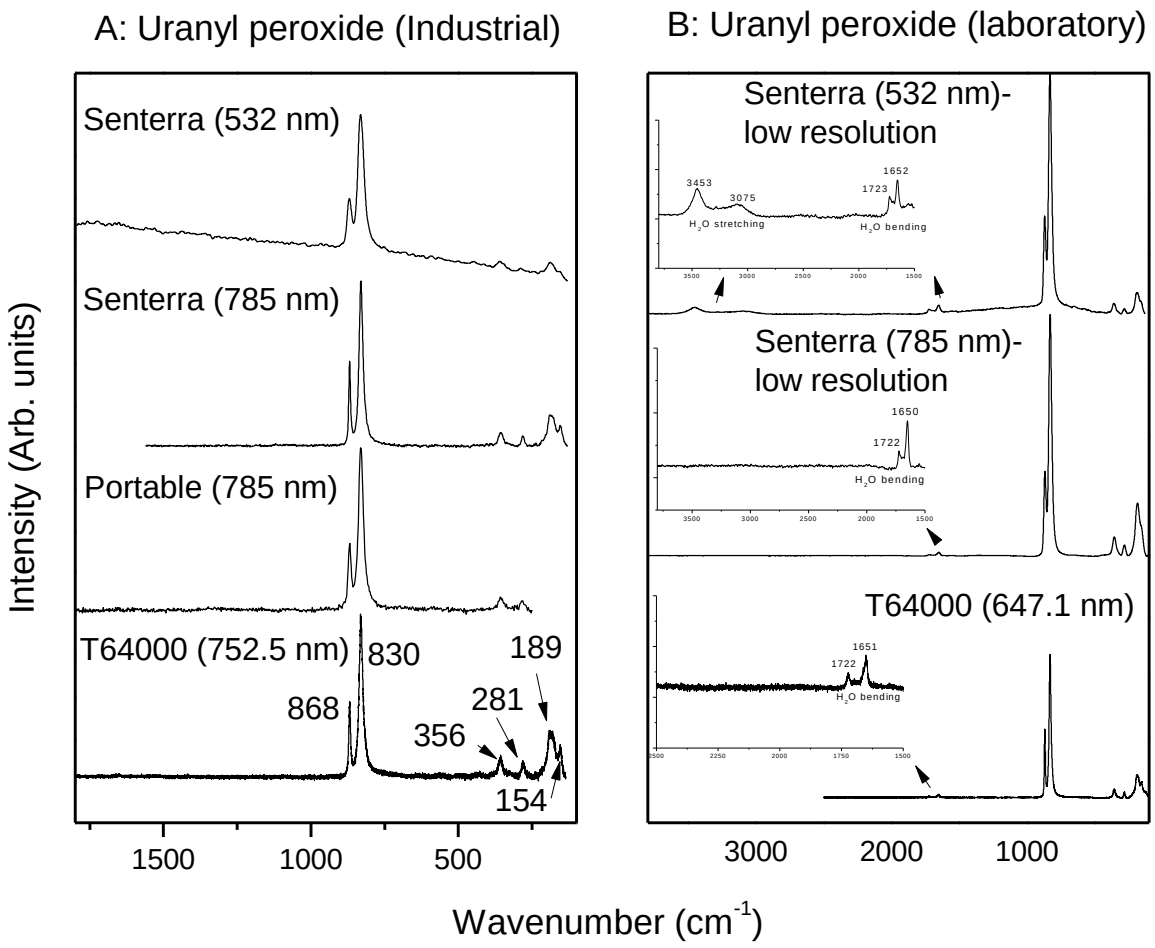

Figure 4-15: Raman spectra of two different origins of $UO_4.2H_2O$ measured by various spectrometers. A: Industrially produced (USA Mobil facility) and B: laboratory synthesized. Insets show the enlarged region of the original graphs.

4.4.4 Advantages and disadvantages of each spectrometer in view of nuclear forensic applications

Raman spectroscopy has been applied to UOCs and other uranium compounds like UO_2. Its potential as a tool for nuclear forensics has been demonstrated by the use of different Raman spectrometers and their respective performance compared.

Each of the spectrometer has its merits and limitations. The merits should be best utilized and the shortfalls should be complemented or replaced by other methods. The hand-held spectrometer is extremely attractive as it can be readily deployed in the field. Besides, it has shown great potential in measuring certain compositions of yellow cakes (mainly uncalcined) and UO_2 pellets. Spectra of compounds could be stored in the database and can be extremely useful in the event of identifying unknown substances. This spectrometer is also much easier to operate and requires no special skill. The shorter spectral range (250-2875 cm^{-1}) and single frequency laser (785 nm) may be limiting but remains less critical than the inability to measure UO_2 powders and U_3O_8 powders. Referring to Figure 4-15A, peaks at low wavenumbers such as 189 cm^{-1} and 154 cm^{-1} were not observed by the hand-held spectrometer but the peaks at 868 cm^{-1} (O-O stretch) and 830 cm^{-1} do provide unambiguous identification of uranyl peroxide.

A table-top device like Senterra has demonstrated excellent sensitivity in this study and it is certainly an excellent instrument to be equipped with for nuclear forensic investigations. However, it is not portable but certainly transportable if necessary. The availability of two frequency wavelengths may be an added advantage but is not particularly useful as the higher frequency laser of 532 nm can hardly be utilized for the measurement of yellow cakes due to fluorescence.

T64000 has the best spectral resolution among the three spectrometers, albeit a figure of merit less appreciated for nuclear forensics. The instrument is not designed for transportation. Although sensitivity is the lowest, due to the large focal distance and the complex optical path between sample and detector, the noise level is also the lowest and its flexibility in terms of the availability of lasers at several wavelengths, is an advantage. Especially the excitation source at 647.1 nm can be employed as a useful compromise between low-energy (inducing no fluorescence but resulting in a poorer scattered intensity) and high-energy photons (risk of fluorescence but larger scattered intensity). The higher spectral resolution can be exploited for a finer identification of peaks hardly measurable with the other spectrometers.

4.5 Multi-variate analysis of Raman spectra

This particular section addresses an important aspect as part of the assessment of Raman spectroscopy as a tool for nuclear forensics in view of the analysis of largely UOCs. The following multi-variate analysis highlights the strength and weakness in identifying each type of compound using Raman spctroscopy. In the preceeding section, the inability to detect O-H and N-H bands in industrial samples were already mentioned. In this section, some comparisons will also be made with a different technique, infrared spectroscopy.

Figure 4-16 shows the spectra of nine different samples with varying compositions. Although the spectra are visibly different, it is only possible to analyse 95 spectra using PCA. All the spectra were obtained using Senterra with the same spectral range of 1560-90 cm^{-1}. 95 spectra were selected from the 114 spectra obtained with Senterra (see Appendix B). Certain spectra were not analysed by PCA due to the reasons such as samples having unknown or mixed compositions. For PCA analysis, it is necessary to have information about the samples, in this case the compositions.

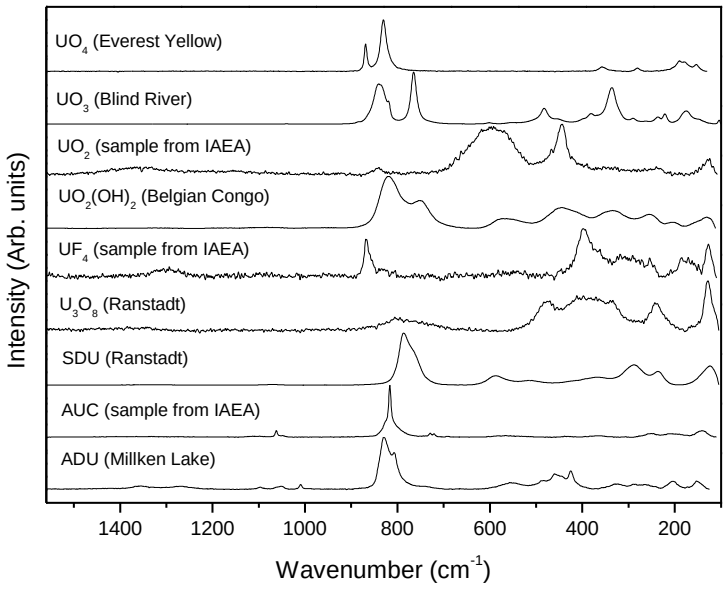

Figure 4-16: Raman spectra (baseline corrected) of various different UOCs and non-UOCs.

4.5.1 Principal Component Analysis applied to Raman data

4.5.1a Brief description of PCA

Principal component analysis forms the basis for multivariate data analysis [153]. It is primarily used as an exploratory technique to provide evidence of structure in the data, cluster or detect outliers [154] and therefore, it is the aim of this part of the work to observe clusters among the 95 samples analyzed by PCA.

Figure 4-17 depicts the representation of data where there are K columns of variables and N rows of observations [153]. In this study, the variables are the wavenumbers (cm^{-1}) which covers the modified range of 1150-120 cm^{-1}, with an interval of 0.5 cm^{-1}. This constituted 2061 variables. The observations refer to the 95 samples.

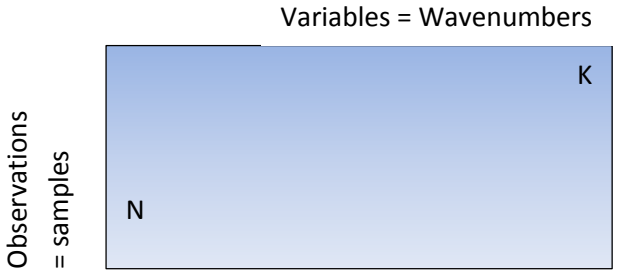

Figure 4-17: Notation used in PCA [153]. The variables represented by K refer to the Raman shifts (cm^{-1}) and observations by N refer to the samples.

What PCA does subsequently is to reduce the number of variables, 2061 in this context to as few variables as possible that could possibly explain as much the variance in the data. It does this by finding relationships (lines, planes and hyperplanes) among the variables in the K-dimensional space that approximates the data as well as possible in the least square sense and thus maximizing the

variance. These relationships are represented by the newly formed principal components (PCs) and the huge dataset of more than 2000 variables are reduced to a representation by just 2 to 5 dimensions or PCs.

4.5.1b Data pre-treatment

The raw Raman spectra had to be treated with some form of pre-processing (data pre-treatment) before they could be analyzed with PCA. The purpose is to re-shape the data such that important assumptions are better fulfilled. Pre-processing is important as it makes the difference between a useful model from one that is not useful [153]. It separates the physical phenomenon (such as scattering effects from particle sizes) from the chemical effects. Some examples of these so-called minor manipulations are smoothing, averaging, mean centering, baseline removal or zeroing and derivatives. Some of these methods are also commonly applied to Raman spectra [155].

Two classes of pre-processing can be identified by their purposes. The first type to be used serves to *remove artifacts* while the second type *highlights variability* in the dataset. Baseline, smoothing, derivatives belongs to the first type of pre-processing while mean centering and autoscaling belongs to the second type.

Figure 4-18 shows the evolution of the raw Raman data (A), followed by baseline correction (B) to remove the background that would otherwise be incorrectly modelled by PCA. Normalization (C) was necessary to account for the difference in response due to the application of different laser power. And finally, the normalized data was smoothed (D).

Although mean centering is commonly used, it was not used here. With mean centering, each column of variables is averaged and subtracted from the data and this is normally done to improve the interpretation of the model [153].

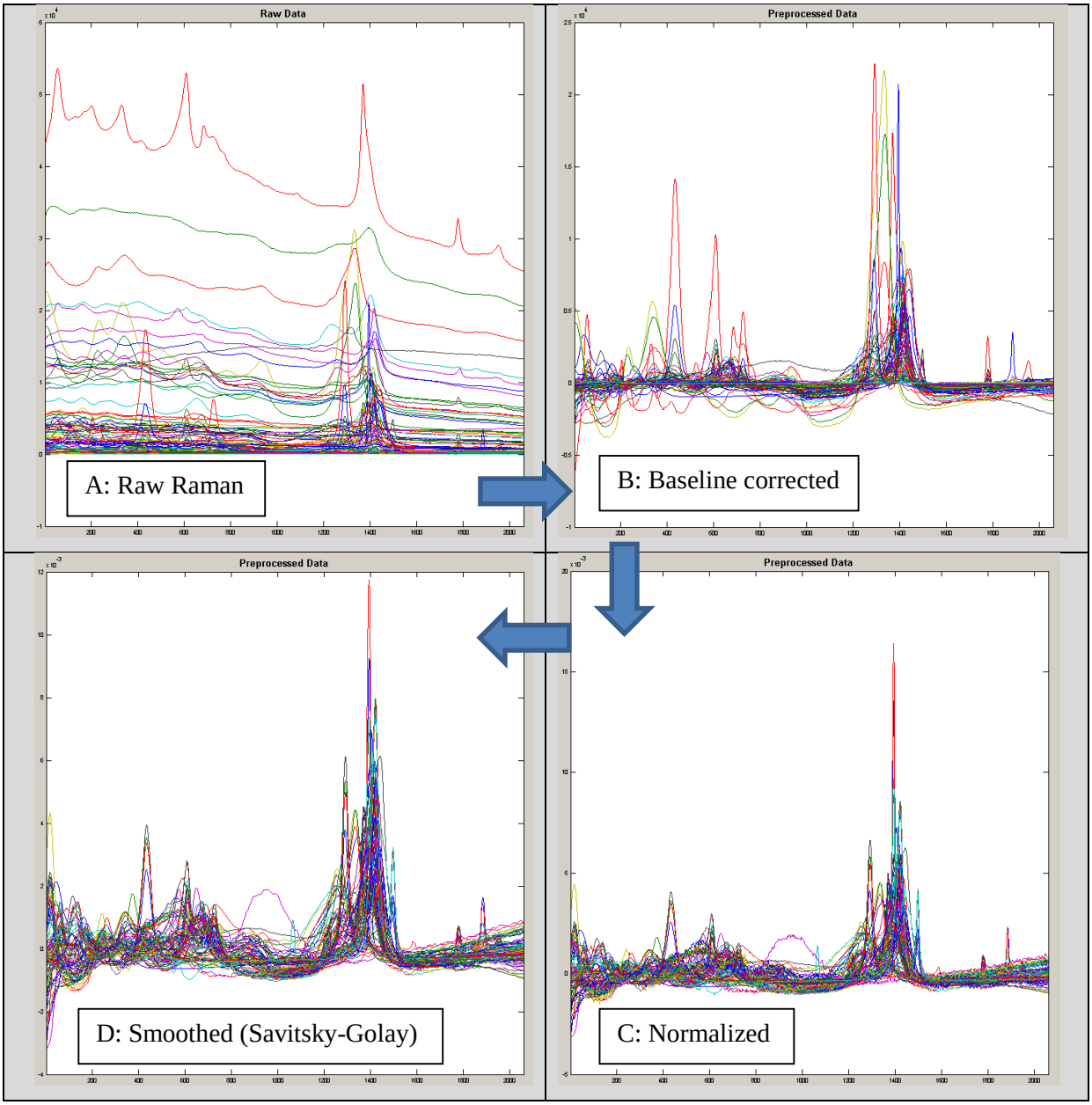

Figure 4-18: Raw Raman spectra (A) followed by baseline correction (B), then normalization (C) and finally smoothed (D).

4.5.2 PCA analysis

Figure 4-19A and 4-19B show the 2D and 3D score plot of the Raman data respectively, and Figure 4-19C the loading plot. About 65.2 % and 74.5 % variance in the data can be explained by the mere usage of 2 and 3 PCs respectively, out of the initial 2061 variables! Although several other combinations of pre-processing with even higher explanation of the variance in data have been tested, those combinations were not chosen for the model as outliers were observed. Outliers are defined as observations that are extreme or do not fit the PCA model [153]. In this case, the Raman data pre-processed by baseline correction, normalization and smoothing resulted in all the data falling within

the confidence limit of 95 % (Figure 4-18A). Mean centered data on top of the 3 pre-processing steps would reduce the variance by about 10 % for 3 PCs.

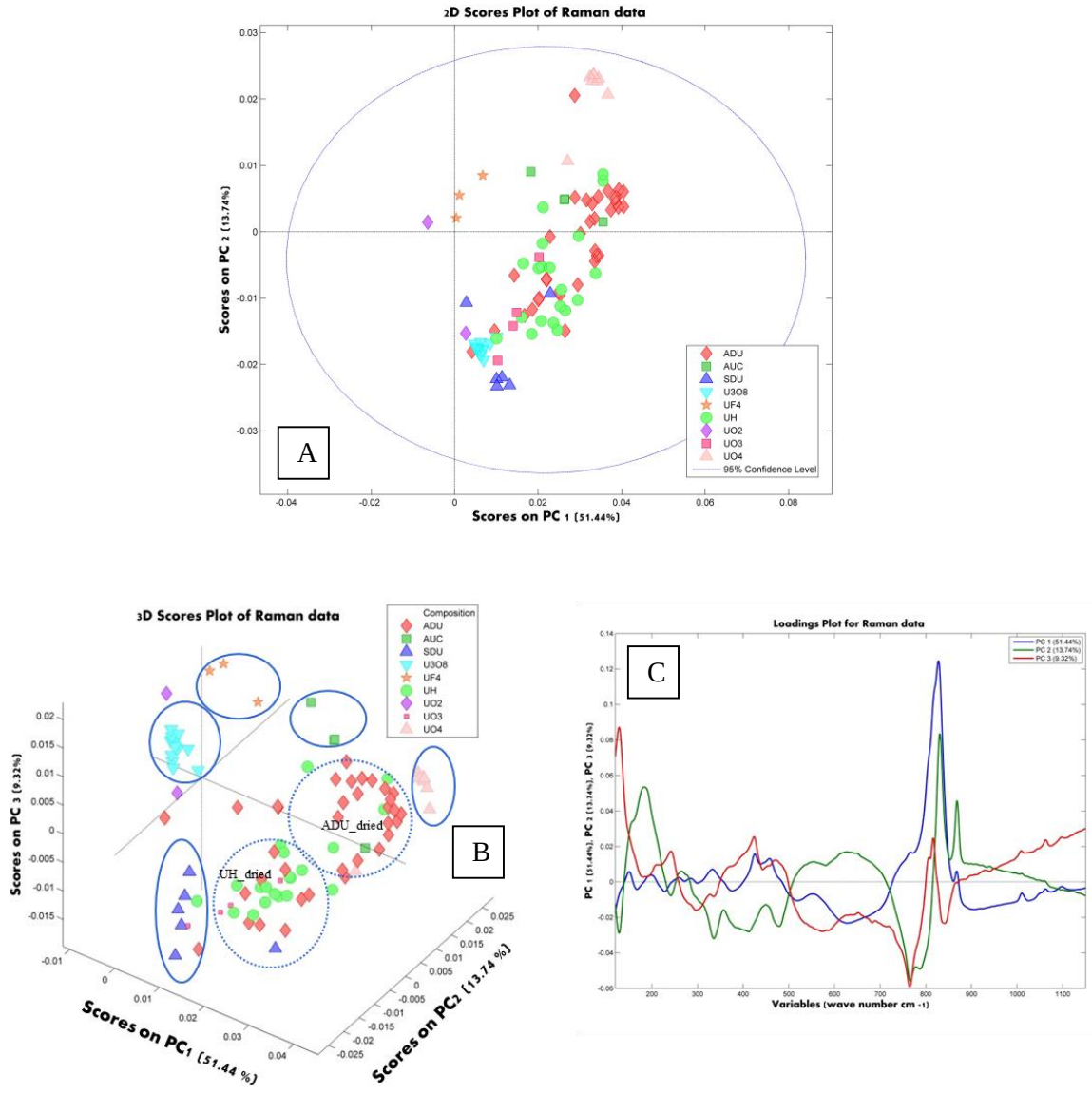

Figure 4-19: 2D score plot of 95 Raman spectra falling within the confidence limit of 95 % (A); 3D score plot of the same data (B); loadings plot (C).

From the 3D representation of the score plot, clusters of spectra corresponding to the same composition of UOCs are observed (full circles in Figure 4-19B). These are small clusters of U_3O_8, UF_4, AUC, UO_4 and SDU. Two major clusters of ADU and UH (dotted circles) can also be observed although there are some overlaps between these two clusters. Their overlaps can be readily explained by the high similarity of some Raman data between the assumed composition of ADU or $NH_3.2UO_3.3H_2O$, with uranyl hydroxide or $UO_2(OH)_2$. Figure 4-20B and 4-20D compare the Raman spectra of two pairs of industrial UOCs, El Dorado (ADU) and South Alligator (UH), Delft (ADU)

and North Span (UH) respectively. In contrast, Figure 4-20F depicts the Raman spectra of the ADU and UH pair that were prepared in the laboratory and there are more differences in the spectra. These figures had already appeared in Chapter 3 (Figures 3-2 and 3-6) where the spectra range was shown up to 3820 cm^{-1}.

As seen from the structural formulae of both compounds, one expects Raman active N-H vibrational bands from ADU and O-H bands from both compounds [143], as observed from infrared spectroscopy (IR) in Figure 4-20A, C and E. The IR bands at ~1400 cm^{-1} and ~3200 cm^{-1} (broad) are N-H bands while the bands at ~1600 cm^{-1} and 3500 cm^{-1} (broad) are O-H bands. These bands are however, not observed from the Raman spectra. One plausible explanation is that IR based on absorption is generally more sensitive technique than Raman spectroscopy (scattering is 10^{10} times less probable than absorption) [156]. Chapter 4.4.3 is also referred to, as a reminder that O-H bands (both bending and stretching modes) for laboratory prepared UO_4 could be observed with the lower wavelength laser at 532 nm while only the bending mode was observed with the higher wavelength at 785 nm. For the industrial UO_4 sample, the use of 532 nm invokes considerable fluorescence while the use of 785 nm at low resolution mode allows the observation of the bending mode. Therefore, it is generally more difficult, if not impossible to observe O-H and N-H bands in especially industrial UOCs using Raman spectroscopy. The use of lower wavelength lasers is desirable but not practical, as they often result in high background on top of destroying the sample. The laser wavelength at 785 nm or slightly lower are ideal for measurements but the Raman signals proportional to ν^4, where ν is frequency, are correspondingly much lower (cf. Eq. 4-2).

Another possible explanation is given based on the observation of the laboratory prepared ADU and UH. The Raman spectra for both compounds are considerably different (Figure 4-20F). And referring to Figure 4-19A (score plot), these 2 samples can be readily located within their clusters (dotted circles) and more importantly, they are not found close to each other. This implied and proved that the Raman spectra are indeed differentiable (despite the lack of N-H and O-H bands). These materials were prepared in the laboratory with known conditions. In the case of precipitation of ADU, only NH_4OH was added to uranyl nitrate and for that of UH, only magnesia was added to uranyl nitrate (Table 3-1). However, the opposite may apply for the industrial UOCs.

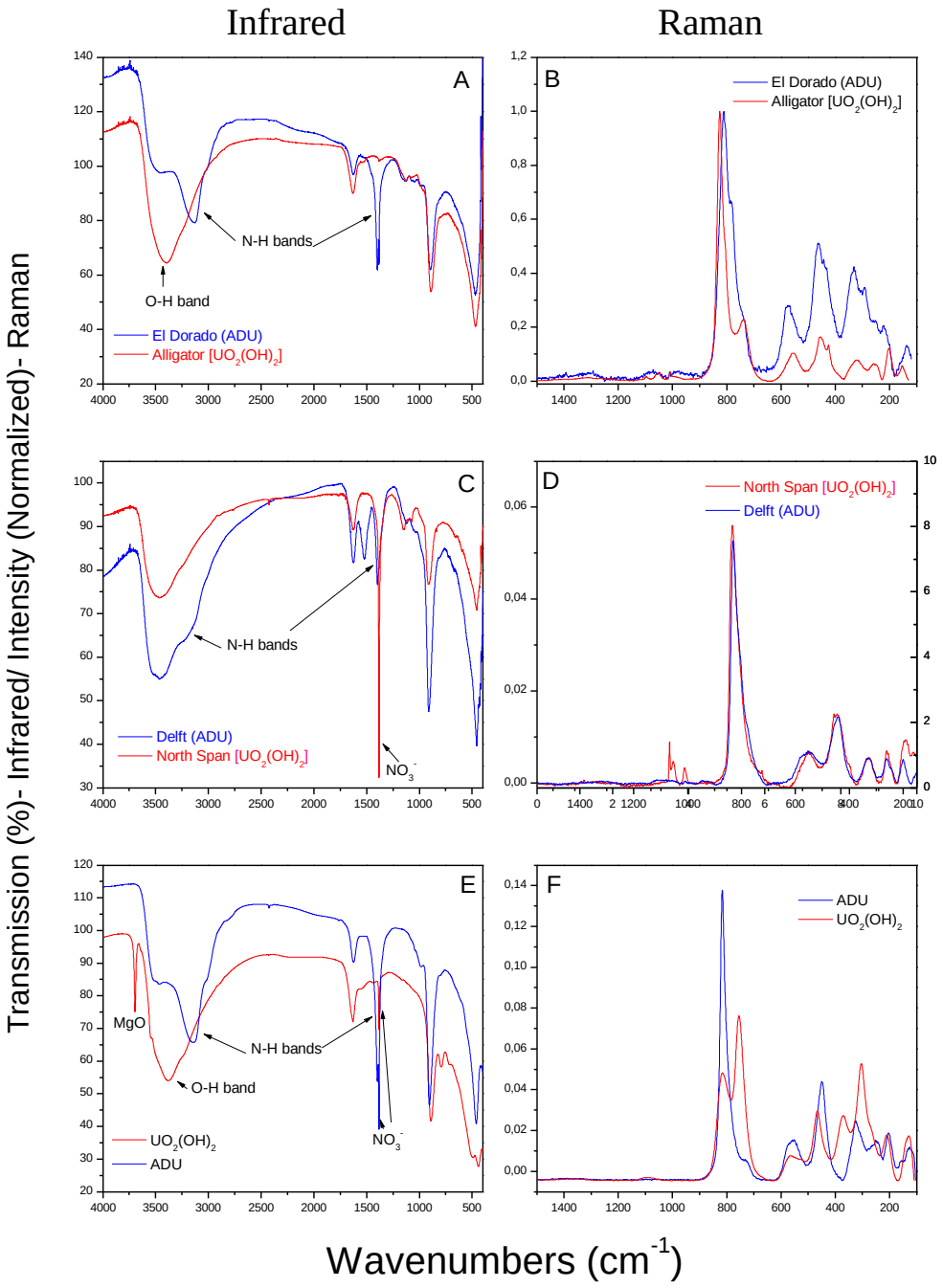

Figure 4-20: IR and Raman of El Dorado and South Alligator samples (A & B); IR and Raman of Delft and North Span samples (C & D); IR and Raman of laboratory synthesized ADU and $UO_2(OH)_2$ samples (E & F).

It may be the case that uranium solution has to be brought to optimum pH with NH_3, NaOH, lime or MgO before its subsequent precipitation [10]. The use of lime in the first step is also used to precipitate impurities [12]. These steps could have easily produce varying compositions of UOCs. It can be seen from Figure 4-20C that the sample Delft has only a very weak N-H band (at ~3200 cm^{-1}) comparable to El Dorado (A) or the laboratory ADU (E). For the latter two, their N-H bands were strong and much stronger than their corresponding O-H bands. This suggests that sample Delft is likely to be a mixture containing ADU and UH.

Finally, the loadings plot in Figure 4-19C helps to explain the variables or wavenumbers that are responsible for the position of the samples in the corresponding score plot. For PC1 and PC2, the uranyl peaks have a high influence in one direction and for PC3, the same influence goes into the opposite direction.

PCA has been used to provide a summarised visualisation of the Raman dataset. Clusters of UOCs and non-UOCs with similar compositions were grouped together and there were no outliers detected in this model using the selected pre-processing steps.

4.5.2 Partial Least Square-Discriminant Analysis

Upon 'grouping' the compounds, the model is evaluated for its predictability to identify or classify an unknown spectrum based on sensitivity and specificity. *Sensitivity* is defined as the number of samples predicted as in the class divided by the actual number in the class. *Specificity* is defined as the number of samples not in the class divided by actual number not in the class [89]. The technique used here is Partial Least Square-Discriminant Analysis (PLS-DA). Eight classes of compounds were modelled except for UO_2 that had only two samples.

The sensitivity and specificity of the calibration (Cal) and cross-validation (CV) were computed based on five latent variables that were deduced from the root mean square of calibration (RMSEC) and root mean square of cross validation (RMSECV) shown in Figure 4-21. Out of the several possibilities of cross-validation (Table 4-5), leave-one out was used. This is applicable as all the samples were independent, i.e. not related to each other.

The data from Table 4-5 clearly shows that the identification of AUC, U_3O_8 and UO_3 are 100 % (both sensitivity and specificity) and for compounds such as UO_4, UF_4 and SDU, the values are only slightly below 100 %. As seen in the previous section, the overlapping clusters of ADU and UH leads to a poorer identification rate. The sensitivities of both compounds are about 83-85 % (true positives) while the corresponding specificities are lower (true negatives).

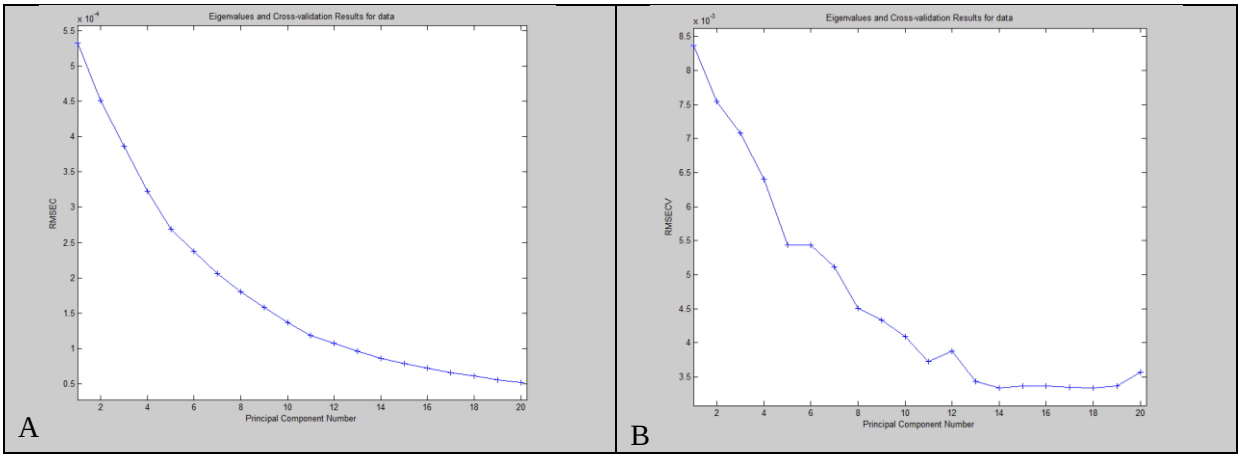

Figure 4-21: RMSEC (A) and RMSECV (B)

Table 4-5: Sensitivity and specificity of modelled compounds (values x 100 %).

Modeled	Class	ADU	AUC	SDU	U_3O_8	UF_4	UH	UO_3	UO_4
Sensitivity	Cal	0.829	1	1	1	1	0.85	1	1
Sensitivity	CV	0.829	1	0.667	1	0.667	0.85	1	0.875
Specificity	Cal	0.724	1	0.977	1	0.967	0.658	1	0.988
Specificity	CV	0.655	1	0.954	1	0.967	0.589	1	0.988

From the PCA and PLS-DA analysis, Raman spectroscopy is useful to discern the various compositions of UOCs in the context of nuclear forensics.

4.6 A study on the comparison between bulk analysis and particle analysis of UOC

The measurements made so far were done on bulk material. In this section, particle analysis of selected UOCs was made using Raman spectroscopy. This aspect is carried out in collaboration with CEA, France. The idea of particle analysis using Raman spectroscopy is interesting and practical. Particle-Raman analysis of UOCs can be applied in a few scenarios for nuclear forensics. Firstly, if a material is available in low quantities, particle-Raman measurement is relevant as 1 mg of material contains thousands of particles, sufficient for measurement. Secondly, such measurement can be useful for heterogenous samples. Different compositions of the material can possibly be deciphered.

Pointurier *et al* have demonstrated that this approach can be successfully applied to selected pure uranium compounds for nuclear safeguards purposes [75, 76, 157]. In those studies, a Raman spectrometer (Renishaw® inVia) coupled with SEM was used for analysis. In the present study, the measurement of five UOC samples is set up for comparison between bulk and particle Raman analysis. The comparison is centred upon the reproducibility of particle analysis with respect to bulk analysis [158]. Table 4-6 shows the comparison of the peaks detected by both methods after baseline correction and curve fitting for samples of El Mesquite, Ranstad, Denison, Olympic Dam and Susquehanna. For both methods, baseline correction and curve fit were done separately with the software provided by the different manufacturers of the Raman spectrometers.

Table 4-6: Main bands detected for the studied UOC compounds both on bulk samples and on individual particles. Only the bands detected in at least half of the spectra are reported. Peaks with wavenumbers lower than 200 cm^{-1} and higher than 1200 cm^{-1} are not taken into account. Uncertainties are ±1 SD. Wavenumbers in bold characters correspond to the most intense peak of the spectra.

	Raman analysis of bulk samples			Raman analysis of individual particles		
Sample	Average center of Raman band (cm^{-1}) ±1 SD	Number of detection / spectra	Average intensity of the Raman band	Average center of Raman band (cm^{-1}) ±1 SD	Number of detection / spectra	Average intensity of the Raman band
El Mesquite	253±5	8/8	w	269±13	7/7	w
	281±1	5/8	w	-	-	-
	327±2	7/8	w	328±6	2/7	w
	355±3	7/8	w	349±7	7/7	w
	412±9	8/8	w	-	-	-
	-	-	-	451±3	7/7	w
	555±3	8/8	w	552±13	7/7	w
	750±4	4/8	w	-	-	-
	830±1	8/8	s	**829±1**	7/7	s
	868±1	8/8	w	868±1	7/7	m
Ranstad	236±1	6/6	m	222±12	14/15	w
	288±1	6/6	m	290±4	14/15	m
	369±3	6/6	w	375±4	15/15	w
	-	-	-	441±2	14/15	w
	521±1	6/6	w	541±8	15/15	w
	589±1	6/6	w	592±2	15/15	w
		-	-	691±7	11/15	w(sh)
	774±1	6/6	m	758±8	15/15	m
	789±1	6/6	s	**796±8**	14/15	s
	-	-	-	829±5	15/15	m
	-	-	-	959±3	9/15	w
	1071±1	4/6	w	1051±4	13/15	w
	-	-	-	1150±6	9/15	w
Denison	255±1	10/10	w	260±5	10/10	w
	321±1	10/10	w	340±5	4/10	vw
	445±6	10/10	w	444±11	7/10	w
	559±1	10/10	w	546±7	10/10	w
	742±1	10/10	m	751±6	10/10	m
	809±2	10/10	m(sh)	-	-	-
	825±1	10/10	s	**830±2**	10/10	s
	994±3	7/10	w	-	-	-
	1015±1	4/10	w	1027±7	9/10	w
	1051±1	8/10	w	1059±3	5/10	w
Olympic Dam	240±3	9/9	m	241±5	7/13	m
	-	-	-	259±4	6/13	w
	344±4	9/9	w	327±9	7/13	w
	-	-	-	367±13	8/13	m(sh)
	406±2	9/9	s	**410±12**	12/13	s
	-	-	-	458±9	12/13	m(sh)
	481±2	9/9	m	492±10	5/13	w(sh)
	-	-	-	620±18	7/13	vw
	-	-	-	690±20	7/13	vw
	797±5	6/9	m(sh)	767±13	13/13	w(br)
	805±2	6/9	m	804±2	6/13	m
	-	-	-	832±7	13/13	m
	863±8	5/9	w	866±3	2/13	w
	-	-	-	1012±2	5/13	w
	1061±5	5/9	vw	-	-	-

Susquehanna	255±1	5/5	w	253±3	10/10	w
	-	-	-	275±6	7/10	w
	-	-	-	367±6	10/10	w
	381±12	5/5	w	397±1	8/10	w
	-	-	-	447±5	8/10	w
	535±2	5/5	w	537±3	8/10	w
	684±11	3/5	w	689±3	6/10	m(sh)
	747±7	5/5	m	755±5	9/10	m(br)
	-	-	-	832±2	6/10	m(sh)
	839±2	5/5	s	**841±2**	10/10	s
	1011±1	3/5	w	1011±1	10/10	w
	1093±1	3/5	w	1089±8	10/10	w

In general, 5-10 spectra were obtained for bulk analysis (BA) while 10-15 spectra were obtained for the single particle analysis (SPA). The most intense peaks have been bolded in Table 4-7. For both methods, these peaks are in close agreement with each other for all the five samples. The spread of the wavenumbers appeared to be bigger in the case of SPA for sample Ranstad and Olympic Dam. This also appears to be the case for the remaining peaks of all samples for SPA. It should be mentioned that peaks observed in SPA spectra often suffer from a poor spectral resolution. This is probably due to uneven surface of the particles. As a consequence, peak centers are not defined with good accuracy and reproducibility especially for the less intense peaks. Moreover, peaks are in many cases very close and must be de-convoluted by means of the algorithms provided by different softwares, which brings even higher uncertainty in the determination of the peak centers. Between the two methods, there is not always agreement about the presence of certain peaks. In nearly all cases, these peaks were classified as weak. Unless these peaks are deemed pertinent, the lack of agreement between the two methods can be accepted. Despite the challenges associated with SPA, the good agreement of wavenumbers with BA is noteworthy. It is also important to add that SPA on its own is likely to be capable of differentiating the different compositions of UOCs.

4.7 PCA and SIMCA analysis applied to IR spectra of the same set of samples

Figure 4-22 depicts the IR spectra of nine selected samples with varying compositions. The spectral range of 4000-400 cm^{-1} constitutes 7201 variables, with an interval of 0.5 cm^{-1}. This range of spectroscopy is also categorized as mid-IR. In this section, the work of infrared spectroscopy is re-visited due to its complementary nature to Raman spectroscopy. IR was previously applied to more than 70 yellow cakes and classification was done using SIMCA [35]. More than 20 samples were measured and added such that the samples used for IR were the same as that used for Raman spectroscopy.

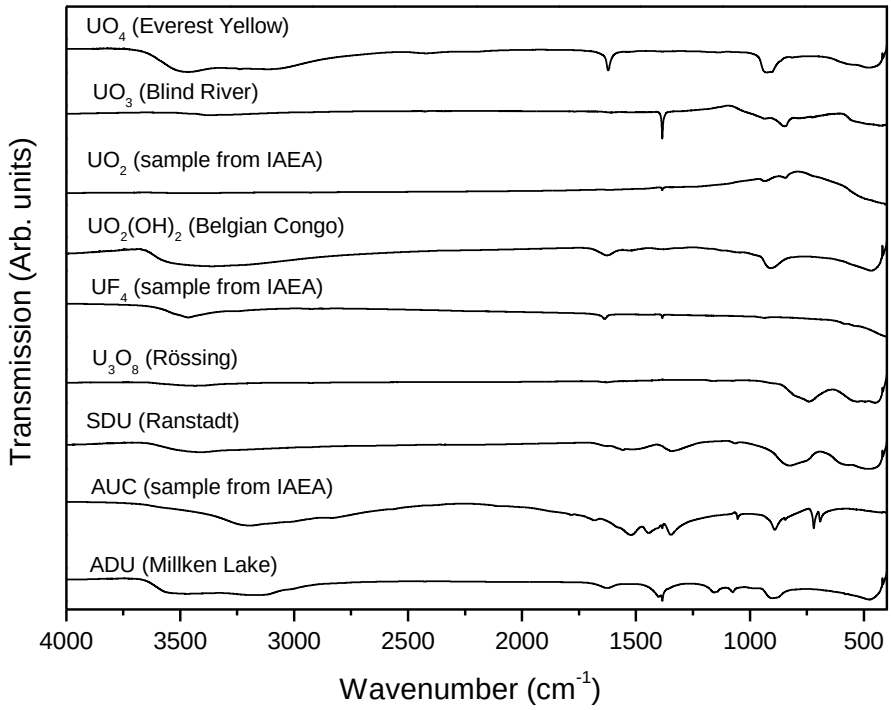

Figure 4-22: Infrared spectra of various different UOCs and non-UOCs.

PCA applied to the above mentioned IR data can be seen in Figure 4-23. The raw data was pre-processed with standard normal variate (SNV) followed by mean centering, according to the previous work mentioned [35]. As seen from the score plot, very few clusters could be clearly observed. The only obvious cluster is that of AUC while the remaining samples appeared rather dispersed. This is an example that shows that PCA is not necessary useful in differentiating multiple classes. This is because information regarding the classes of the samples are not being utilized by the model [159].

Hereby, SIMCA was used where nine different classes of compounds were modelled with PCA. There are therefore nine PCA models, one model for each class. Each class has its own number of prinicipal components as reflected in Table 4-8.

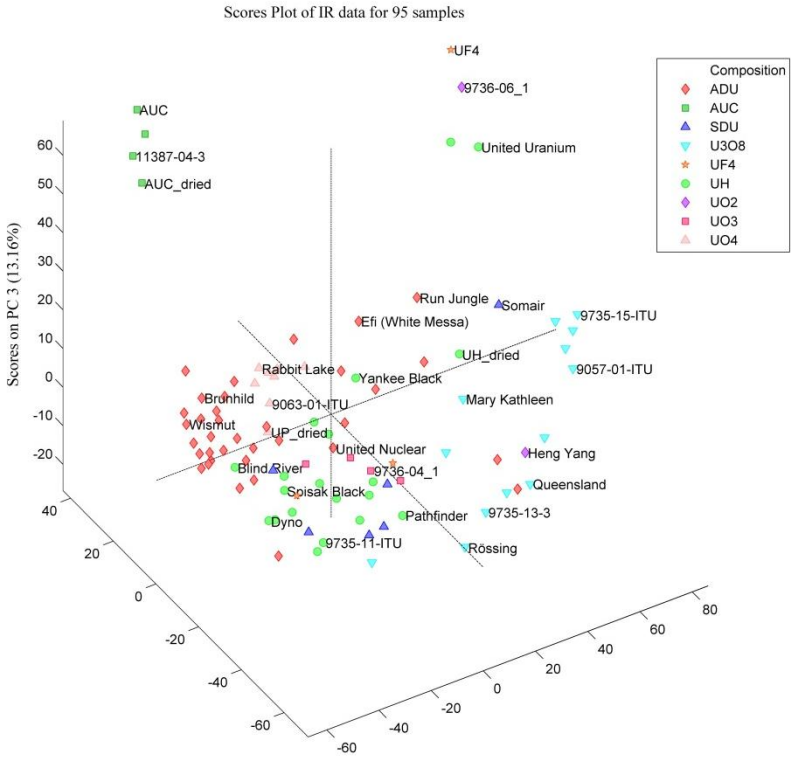

Figure 4-23: 3D score plot of IR data.

Table 4-7: Number of PCs used for each class of compound and its corresponding cumulative percentage of the variance of data explained.

Class	Composition	No. of PCs	% variance cumulative
1	ADU	5	90.60
2	AUC	3	100
3	SDU	3	93.34
4	U_3O_8	3	93.70
5	UF_4	2	100
6	UH	5	93.58
7	UO_2	1	100
8	UO_3	2	98.5
9	UO_4	4	95.56

Figure 4-24 shows the results of the SIMCA analysis obtained from the PLS toolbox. Figure 4-24A is the breakdown of the samples. Figure 4-24B is critical as it reveals that half of the uranyl hydroxides samples (most probably) belong to the class ADU (indicated by green dotted box). This means that based on the IR spectra of these samples, they resembles the IR spectra of ADU more than that of typical uranyl hydroxide and therefore, these samples are likely to fall into the class ADU.

Figure 4-24C indicates that all samples could be assigned, while that of Figure 4-24D shows that a significant number of ADU and UH and a few other samples of U_3O_8, UF_4, UO_2 and UO_4 have multiple class membership. This accounts for 28 out of 95 samples.

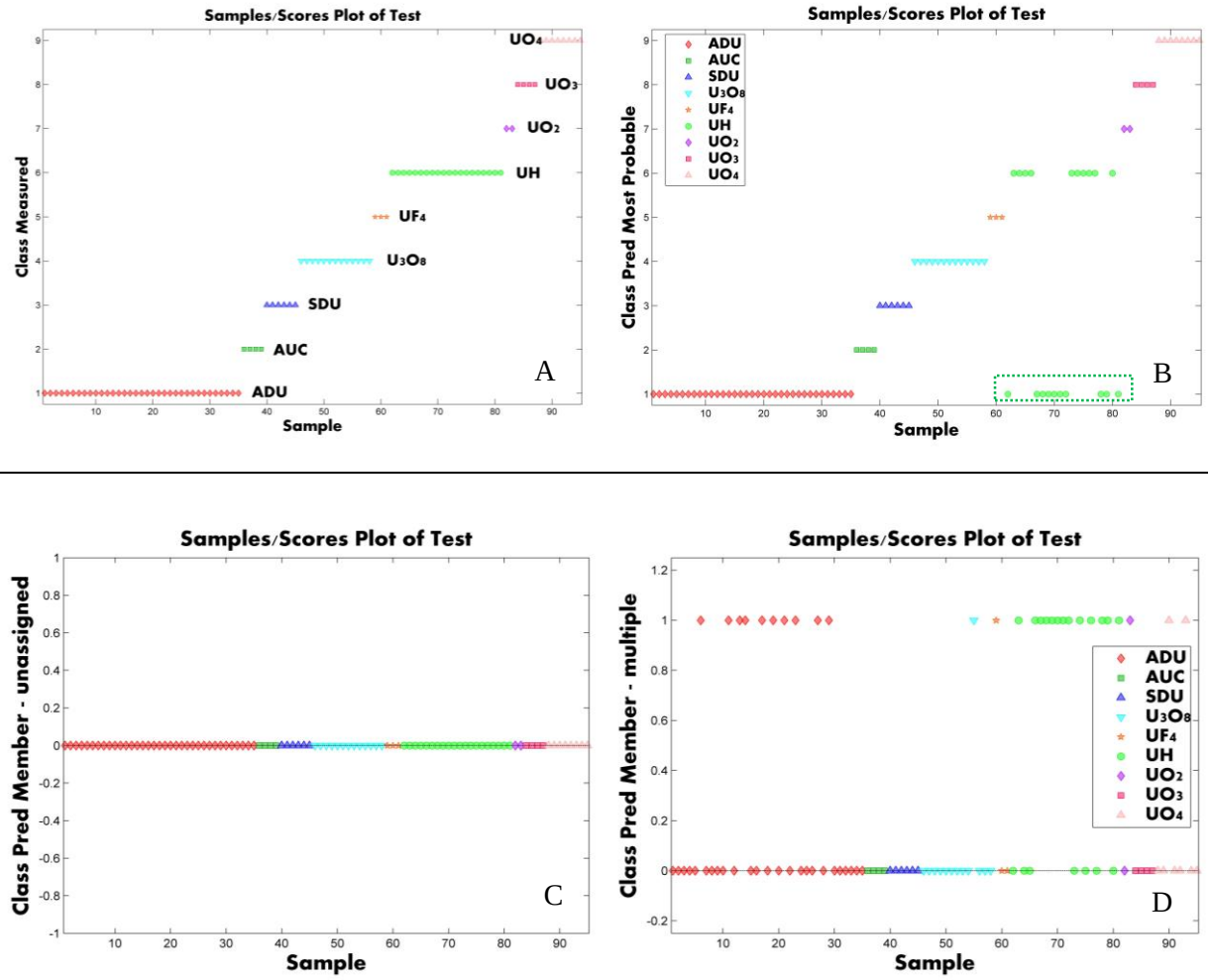

Figure 4-24: Class measured vs sample (A), Class Pred Most Probable vs sample (B), Class Pred Member (unassigned) vs sample (C), Class Pred Member (multiple) vs sample (D).

Table 4-8 shows the numerical interpretation of the class prediction using SIMCA analysis of the IR data. Its graphical representation can be found in Appendix D.

Table 4-8: Class prediction of samples (Actual class vs predicted class). Values within bolded square correspond to the percentage and number of samples classified correctly. Values highlighted in red are incorrect classifications.

Values in %; ( ) refers to no. of samples		**Predicted**								
		ADU	AUC	SDU	U_3O_8	UF_4	UH	UO_2	UO_3	UO_4
Actual	ADU	**100 (35/35)**			2.8 (1/35)		25.7 (9/35)			
	AUC		**100 (4/4)**							
	SDU			**100 (6/6)**						
	U_3O_8	7.7 (1/13)			**100 (13/13)**					
	UF_4					**100 (3/3)**				
	UH	55 (11/20)					**95 (19/20)**			
	UO_2				50 (1/2)			**100 (2/2)**		
	UO_3								**100 (4/4)**	
	UO_4						25 (2/8)			**100 (8/8)**

After SIMCA analysis, the IR data appeared to show some similarity with the Raman dataset. Despite the fact that IR detected N-H and O-H bands, there remained some challenges in identifying certain ADUs and UHs. This challenge must be solved by determining the accurate composition of some of these UOCs that are likely to contain more than a single composition.

4.8 Summary and suggested areas for future study

In this Chapter, the application of Raman spectroscopy to uranium compounds, largely UOCs for nuclear forensics has been studied. Four Raman spectrometers have been used in this work and more than a hundred UOC samples were measured. The performances of three spectrometers were compared and the matching accuracy of hand-held Raman was evaluated. Some IR data was also used for comparison. Multi-variate analysis was applied to both Raman and IR data. Single particle analysis using Raman spectroscopy was also explored. The main highlights of this study and possible future work is defined as follow.

- Raman spectra of UOCs have been thoroughly interpreted. Three regions (I, II and III) have been identified based on the spectral range of the hand-held spectrometer. These regions are classified as vibrations belonging to the main component (I from 900-250 cm^{-1}), vibrations belonging to impurities (II from 1200-900 cm^{-1}) and non-Raman vibrations (III for 1200 cm^{-1} and above).
- Varying compositions of UOCs results in different Raman fingerprints (Region I) that can be useful for nuclear forensic purposes. In Region II, smaller peaks are generally observed and these impurities have been identified and are related to the processing activities that samples had gone through. This region is important and adds value to Raman spectroscopy as a molecular fingerprint since important clues about the processing history of samples can be provided.
- Hand-held Raman spectrometer is extremely convenient and provides rapid analysis. In addition, identification of unknown samples can be done when spectra are compared to its customisable database. Evaluation was carried out and in general, certain compositions of UOCs such as UO_4, UO_3, SDU and some ADUs can be positively identified. Uranyl hydroxides cannot be identified by the hand-held and should be noted for further advancement.
- Three different Raman spectrometers were compared for their performance in terms of sensitivity, signal-to-noise ratio etc. Each spectrometer has its strengths and limitations and their relevance to nuclear forensics has been discussed. The bench top model, Senterra showed excellent performance and could be ideal for a nuclear forensics laboratory.
- PCA and PLS-DA applied to Raman data suggested Raman spectroscopy is a good technique for discerning UOCs.

- PCA and SIMCA applied to IR data showed similar and corroborating results to Raman data.
- The compositions of some UOCs are likely to be mixed. For the future, it is proposed that XRD could be performed on the industrial UOCs for a better characterization of the accurate composition of these materials.
- Single particle analysis using Raman spectrometer has been explored and compared to bulk Raman analysis. Such analysis expands and extends Raman spectroscopy to the field of nuclear safeguards. It has been demonstrated that particle Raman analysis can be reproducible. This technique will be extremely useful when the sample is available only in very low quantity and especially when it is heterogeneous.
- Raman and IR data could be combined for a stronger molecular fingerprint of UOCs for nuclear forensics.
- Raman spectroscopy is a feasible nuclear forensics tool for measuring UOCs and other uranium compounds.

5. Exploring morphology of yellow cakes as possible signature(s)

As seen from Introduction (Chapter 1), morphology of UOCs is a much less developed research area, owing to the challenges faced by researchers in this field. To fully capture the essence of this particular aspect of the work, one has to understand the crystallization process of the various precipitation reactions in order to establish the link between the morphology of the samples with the processing history of the samples.

One logical approach has been partly undertaken by preparing such materials in the laboratory (Chapter 3). Five different compositions of yellow cakes have been prepared and they have shown different morphologies, allowing one to distinguish them. In addition, drying or calcining the materials did not appear to influence the morphology, which was retained despite heating the studied materials to various temperatures. However, the work done so far does not provide a complete mean to the use of morphology as a signature for UOCs. It is inadequate as it is only qualitative and in the case of two samples originating from different facilities but using similar procedures, a more quantitative approach is necessary to probe the subtle differences between such samples. This Chapter is set to address and explore this quantitative aspect of morphology.

There are different techniques that can be used to study sizes of particles and obviously the techniques make use of different principles and the outcome on size measurement can vary. In this study, SEM is the selected instrument. Unlike other particle size measurement device, a bench-top SEM is present in a nuclear forensic laboratory. More importantly, SEM provides real time information about the size and in addition, shape of the particles that is often not the case for other types of instrument such as, a particle size analyser.

There are two main parts in this study. Firstly, the obtained SEM images are processed by software(s) which provide quantitative measures of these particles. Therefore, sample preparation is crucial to allow the observation of particle sizes and shapes. Sample preparation shall be addressed in details. Secondly, SEM images of samples are evaluated for their texture using the AMT technique. The numerical data obtained from these samples are subsequently processed by PCA and PLS-DA.

5.1 Materials & Method

5.1.1 Material

5.1.1a Certified and reference standards

A certified specimen with mean spacing of 50.8 µm was put into SEM to verify the accuracy of the instrument. 2 µm (S1941) and 0.5 µm spheres (S1940) standard sold by Agar Scientific/Elektron Technology (UK) were also used to control the instrumental magnification.

5.1.1b UOC of interest

Three different sample preparations were used in this study. Each preparation was catered to the requirement of the analysis. For the first part, 22 UOC samples were selected and their morphology studied qualitatively by taking images at different magnifications. For the second (size and shape characterization) and third part (image texture analysis), 26 samples were selected for the morphological study. All the samples have been indicated in Appendix B under the section "Scanning electron microscopy".

5.1.2 Method

5.1.2a Sample preparation for descriptive morphology

Samples were prepared by the surface transfer method. Small quantity of powder was placed onto 13 mm SEM aluminium (Al) disk holders with double-sided carbon adhesive tape. Excess powder (not attached to the tape) was removed by manually tilting and taping the sample holder. Samples were coated with 10 nm Au with a gold coating/sputtering device. SEM images were taken at several magnifications, starting with fish eye (FE) to as high as 25 000x.

5.1.2b Sample preparation for particle size and shape characterization

Different preparations were attempted, including the use of ultrasonic bath and different solvents to disperse the powder. Only the best preparation method is described here while the previous attempts are part of the discussion.

Very minute quantity of powder was placed in a mortar. 200 µl of analytical grade ethanol was added and the sample gently grinded to break up the soft agglomerates. The sample was then briefly pipetted for at least five times to ensure homogeneity. 10 µl of the sample mixture was immediately pipetted onto the same Al disk holder for SEM with an existing layer of Isopore^{TM} membrane filter (Pore size 0.1 µm, diameter 13 mm) from Millipore on top of the adhesive tape. Otherwise, the insignificant amount of ethanol would interact and partially dissolve the glue. The dried dispersed samples were also coated with 10 nm Au before SEM analysis. Images were taken at 500x magnification and at different positions of the same sample.

5.1.2c Sample preparation for image texture analysis

Samples were prepared by the surface transfer method, similar to the samples prepared in Section 5.1.2a. However, higher quantities were required per sample for this preparation and therefore the Al disk holder was inverted into a clean dish containing the sample. The disk was dabbed onto the dish to take up as much sample as possible. The prepared disks were carefully coated with 10 nm Au before SEM analysis. Images were taken at 250x and 1000x magnifications and for each magnification; five images were taken at different areas of the same sample.

5.1.3 Imaging software

5.1.3a Vision Assistant

Vision Assistant software version 2013 from National Instruments (Texas, USA) was used to process the SEM images. Up to 77 measurements output could be obtained but only the relevant ones were selected. Figure 5-1 depicts the steps that were used to process images for the standard material.

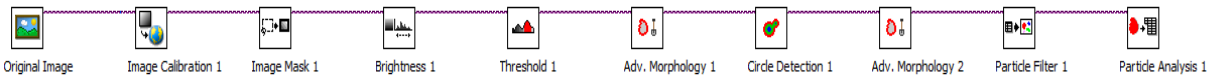

Figure 5-1: Steps used to process images of standard sized material

First, the original SEM image was calibrated to convert the pixels into a real world dimension (in µm). Next, the image was cropped to select only the ROI followed by adjusting the brightness. The cropped gray-scaled image was converted to a binary image through the threshold function, which essentially segmented the image into black and white. Advance morphology 1 and 2 removed the border objects and separated touching spheres, respectively. Particle Filter removed non-standard sized particles and particle analysis provided the final output.

5.1.3b Image Pro-Analyzer

For SEM images containing dispersed samples, the Image-Pro Analyzer 3D software v. 7.0 (Media Cybernetics, Inc., USA) with a pre-recorder macro was used to process the images. This results in an output of 30 parameters describing shapes and sizes of the particles (details provided in Table 5-1). A total of 26 samples with 10 images each were analysed.

Table 5-1: 30 descriptors of sizes and shapes with Image Pro-Analyzer.

Descriptors
Area, Aspect, Area/Box, Box X/Y, Center-X, Center-Y, Axis (major), Axis (minor), Diameter (max), Diameter (min), Diameter (min), Radius (max), Radius (min), Perimeter, Radius Ratio, Size (length), Size (width), Perimeter (conv), Perimeter (ellips), Perimeter (ratio), Area (polygon), Fractal Dimension, Center-X (mass), Center-Y (mass), Box width, Box Height, Feret (min), Feret (max), Feret (mean), Perimeter Length

5.1.3c ImageJ

ImageJ is a free software, made available by National Institutes of Health (Maryland, USA). In this work, it was used mainly for image texture analysis using AMT algorithm, available with the plugin version. This will be described later. All images were analysed with maximum scale and random samples, both set to value of 500 and 10000 respectively. Unfolding was set to spiral and statistical methods could be MA (mean angle), MDX (mean difference X) or MDY (mean difference Y). A total of 260 images from 26 samples were analysed, five images each at two magnifications.

5.2 PCA and PLS-DA analysis

The numerical data obtained from analysis is subsequently transported into Matlab for PCA and PLS-DA as described in Chapter 4.1.3. Auto-scaling is used for the pre-processing of the data and whenever applicable, the cross validation is either based on leave-one-out or contiguous block.

5.3 Validation with certified specimen

Figure 5-2 shows the SEM image of the 50.8 µm (mean spacing) certified specimen. The actual measurement entails the length of the square and a column grid as shown by the green line and should be represented by 50.8 µm if the SEM is correctly calibrated. However, it was estimated based on the yellow line that the SEM was slightly out of range by approximately 10 %. In other words, particles would appear bigger.

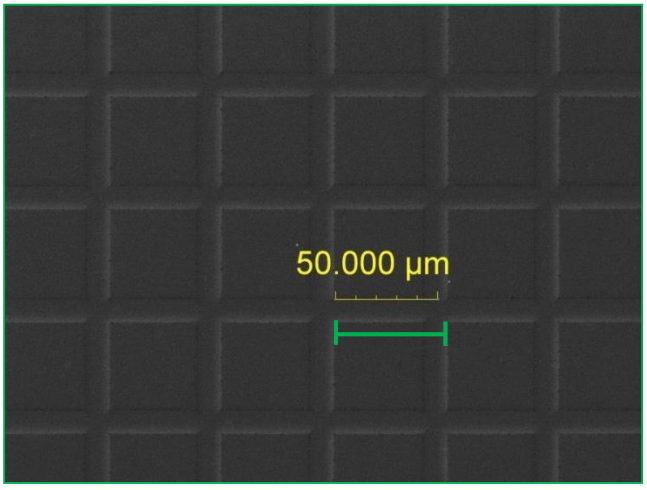

Figure 5-2: SEM image of certified specimen (50.8 µm) taken at 1000x magnification. Measurement includes the length of the square and a column grid (as indicated by the green line). Yellow line is equivalent to 50.000 µm.

5.4 Size characterization

Figure 5-3 (A1-A4) shows the SEM images belonging to the standard spheres taken without any dispersion or dilution. By taking a small volume of the standard (2.5 µm), there were obviously fewer spheres and these images could still be counted by image processing software to obtain the sizes of the spheres. A larger volume of the standard (10 µm) not only resulted in more spheres, but also the stacking of spheres, which made it difficult to count them. Figure 5-3 (B1-B4) shows the SEM images of standards that have been diluted by ethanol. Diluting the standard material dispersed the spheres and therefore, the sizes of particles could be evaluated by the software. It is noteworthy that although desirable, it was not possible to obtain 100 % separation of the spheres. Some of the spheres were still found close to each other or one another. Besides ethanol, acetone and chloroform were also tested but were found unsuitable as a dispersion medium. Water could also be used for dilution. Chloroform resulted in coagulation of the spheres and acetone appeared to cause slight deformation of the spheres.

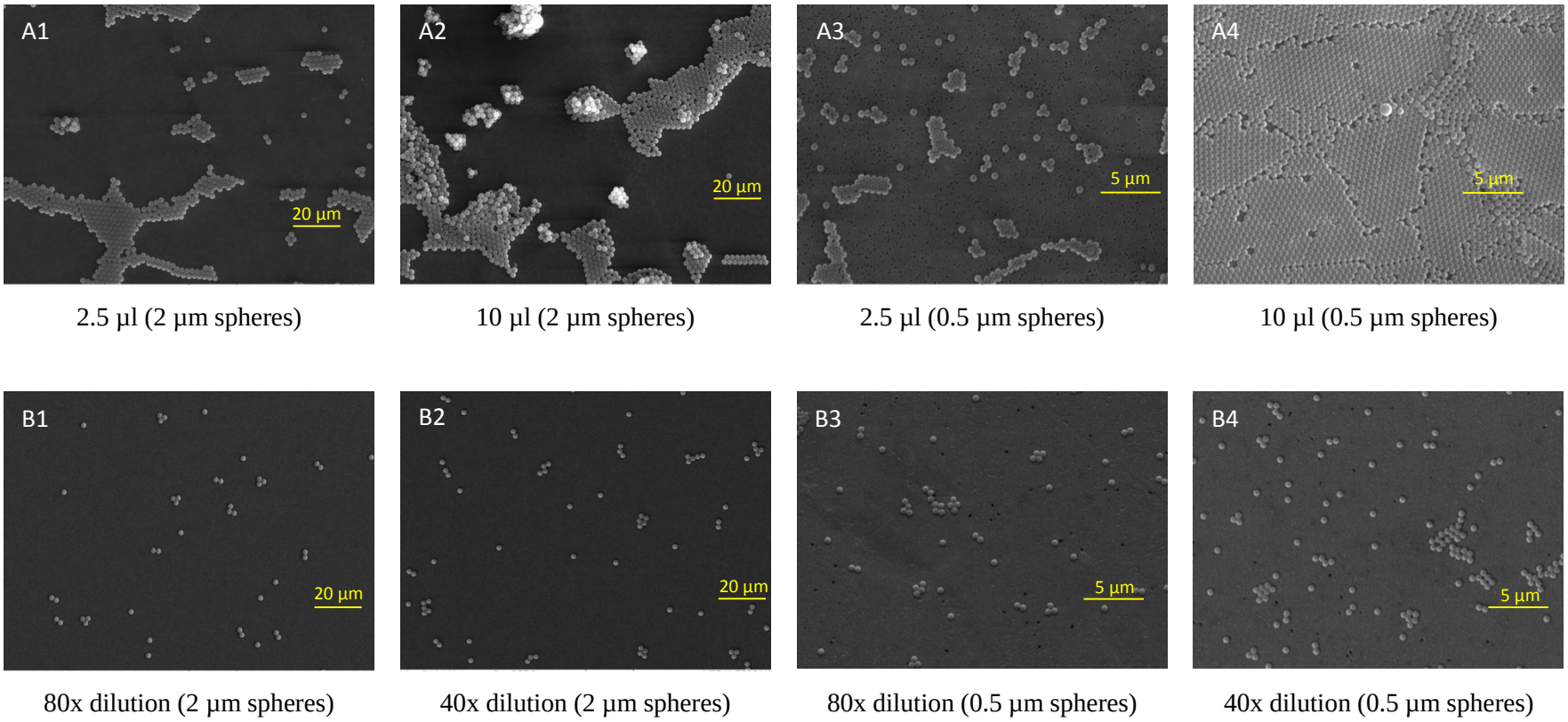

Figure 5-3: SEM images of undiluted standard spheres (A1-A4) and dispersed/diluted standard spheres (B1-B4) for size characterization.

Table 5-2 reflects the sizes of the spheres computed by Vision Assistant software. Two samples were prepared by gently grinding and mixing in ethanol. Images were taken at few magnifications and were calibrated by the software. The *Waddel disk diameter* (defined as the diameter of a disk with the same area as the particle) was determined. The mean values of the spheres were around 2.20 µm.

Table 5-2: Size characterization of 2 µm standard spheres

Sample	No. of particles counted	Magnification of images	Mean Waddel disk diameter (µm)	Standard deviation
1	45	2K	2.20	0.07
	11	3K	2.23	0.03
	6	4K	2.20	0.03
2	38	2K	2.25	0.07
	19	3K	2.22	0.07
	11	4K	2.23	0.03

Recalling that the dimension provided by SEM was approximately 10 % larger, based on the measurement of the certified specimen, the diameter of the standard spheres was therefore very close to 2.0 µm after correction (assuming this was a linear systematic deviation).

5.5 Morphology- A qualitative approach

Figure 5-4 shows the SEM images of four different samples from various mining facilities. These powder samples are black in colour and have the likely composition of U_3O_8 or UO_2 or mixture of oxides. Therefore, it is of interest to find a way to distinguish one sample from another. It is noteworthy that the colour of a UOC sample can provide a fair indication of its likely composition, or at the very least, eliminate the other compositions. In the above cases, one can already eliminate several UOC compositions such as ADU, SDU, AUC, $UO_2(OH)_2$, UO_3 and UO_4.

By studying Figure 5-4, some distinct differences between the samples can be observed. The samples from Canada Key Lake and Namibia Rössing are largely agglomerated while that of China Heng Yang consisted of single and large particles that are euhedral or subhedral [140]. The sample of Yugoslavia Spisak Black appeared mixed. There appears to be rather large particles that have a less regular shape and much smaller particles are also present. High magnification of the same sample also seems to suggest some degree of agglomeration. The sample from Key Lake can be further described as mono-disperse or grape-like [140] and the Rössing sample could possibly be described in a similar fashion. Although there are generally differences among the four samples, the morphology between

the first two samples is rather similar and therefore difficult to differentiate at first glance. In fact, majority of the UOCs are very much agglomerated and more examples can be found in Appendix D. This feature is commonly found in UOC samples [22, 94]. It is also important to define agglomerates in this context and it is used exclusively to refer to an assembly of particles as suggested in the literature [160]. Other terms such as aggregates and conglomerates are often found to be exchangeable but these often cause confusion due to the different definitions and are therefore not used in this work. In this particular aspect of studying morphology, it can be seen that the approach is generally qualitative (based on observation and description of particle morphology). Such qualitative approach is used in current nuclear forensics investigations [18, 22]. Comparisons can also be made between the unknown sample and sample(s) from suspected known facility [22]. This approach remains practical as SEM (and TEM) is the only way to study the morphology of the questioned sample. And in an actual investigation, SEM analysis of one or two samples and describing the morphology qualitatively is a manageable task. In this work, a total of 22 samples have been documented in the same manner and these images can possibly serve as useful references for the future.

In Chapter 3, it was highlighted that the morphology (shape and appearance) of material is retained throughout calcination. It is interesting to note that by looking at sample Heng Yang (3rd row of Figure 5-4) which is a mixed oxide, it is very likely that this sample had been produced from the AUC route. Although the processing history is not known, its distinct morphology (highly similar to AUC) has provided an important clue.

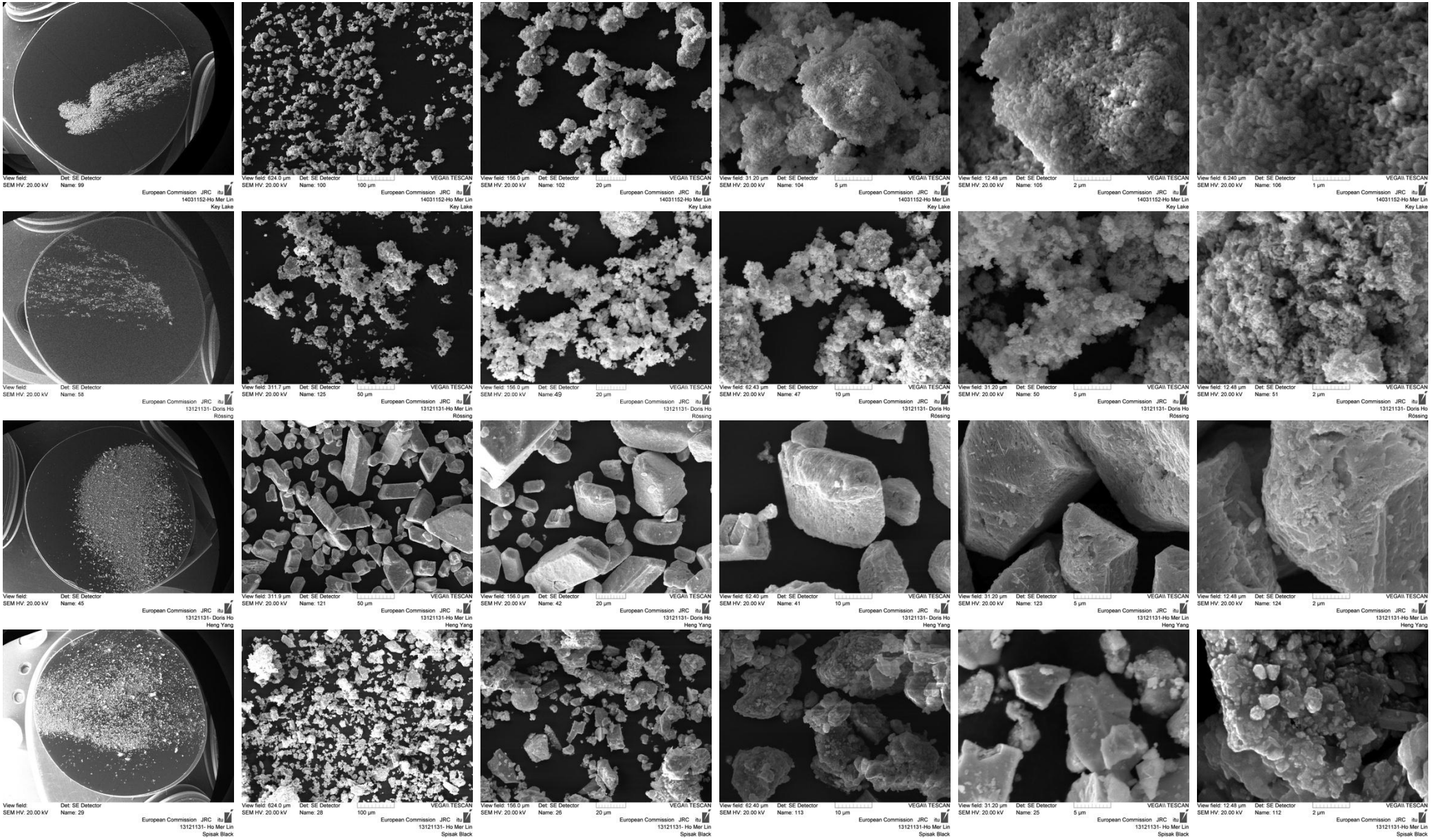

Figure 5-4: SEM images of UOC from Key Lake (1st row), Rössing (2nd row), Heng Yang (3rd row), Spisak Black (last row). Images are presented in increasing magnification from left to right per row.

5.6 Particle size and shape characterization- A quantitative approach

In order to study the sizes and shapes of the particles, they must first be dispersed. SEM images from the previous section clearly provide evidence for the need to disperse the samples before any quantitation could be carried out. In theory, there are few possible ways to disperse the samples and these include ultrasonication, the use of ball mills or by dispersing a small quantity in an organic solvent such as isopropanol, ethanol and acetone [161]. In this study, the first and last method was explored along with a few other methods such as the use of sieves, vacuum impactors and filtering samples that has been mixed with organics. A well-known dispersing agent, polyvinylpyrolidone (PVP) was also tested.

5.6.1 Use of ultrasonication for sample dispersal

Figure 5-5 shows the SEM images of ADU sample (Batch II) that had been ultra-sonicated. 200 µl of ethanol was added to 1 mg of the sample and sonicated for up to 2 hours. At specific time intervals, an aliquot was removed and analysed by SEM.

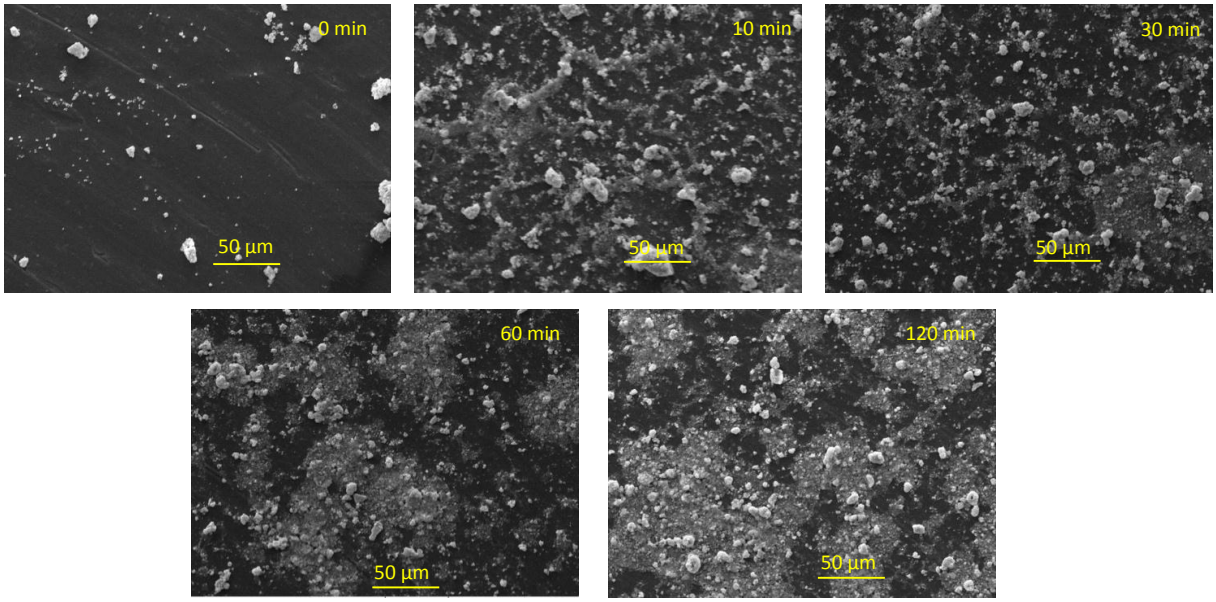

Figure 5-5: ADU sample subjected to ultrasonication for up to 2 hours. An aliquot is removed at different time points to study the effects on morphology. SEM images were taken at 1000x magnification.

The pictures in Figure 5-5 clearly showed the effects of ultra-sonication on the ADU sample. The sample broke down into much finer powder and this extent appeared to be correlated with the ultra-sonication time. On the other hand, it is worth noting that large agglomerates were still present up to 2 hours of sonication and this would most probably result in a very large particle size distribution. Besides, it can be challenging to analyse particles with large distribution using SEM. At a particular level of magnification, it is not expected that a dynamic range in terms of the sizes of particles can be obtained within the image. It is appropriate to suggest that this sample was likely

made up of both soft and hard agglomerates [160], of which the former was readily dispersed by ultra-sonication while the latter is not.

5.6.2 Dispersion of samples in ethanol

The samples have also been prepared in various organic solvents such as acetone, chloroform and ethanol. The best solvent was found to be ethanol. The grinding of the sample in ethanol helped to break down large agglomerates and prior to the transfer of sample onto the disk, the mixing step was essential, otherwise the sample distribution would not be homogenous. For each single sample mounted on the Al disk holder, five images were taken per disk. Each of the images was subsequently processed and compared to check the homogeneity of the sample preparation.

5.6.2a Comparison between two samples

Figure 5-6 illustrates the comparison of morphology between two samples in terms of their sizes and shapes. Sample Rössing is from a facility in Namibia while sample Key Lake is from a facility in Canada. Both samples are known to have the composition of U_3O_8. The details of the morphology are found in Figure 5-4 where both samples revealed high level of agglomeration. An example of each of the dispersed samples is shown in Figure 5-6A and 5-6B.

Five relevant parameters were selected out of the 30 descriptors computed by the Image Pro-Analyzer software. These parameters are area, perimeter, diameter, aspect and fractal dimension, also shown in Figure 5-6. The mean value obtained per image is illustrated and all ten images per sample are compared between the two samples. The ten images resulted from two independent preparation of each sample. Few observations can be made here.

Firstly, good reproducibility can be observed within the group of five images occurring within a single preparation (within-sample reproducibility). Table 5-3 reflects such values for each preparation of the sample. With the exception of the 2^{nd} set of sample of Key Lake (variation of nearly 20 % in the case of mean area), reproducibility is in good range for the samples. Therefore, it can be inferred that the sample preparation is sufficiently good to produce a rather homogenous distribution of particles on the sample holder so that images can be randomly obtained.

Secondly, a fairly good reproducibility appears to be achievable and is found within 10 % for all the five parameters in the case of sample Rössing. Table 5-4 reflects the between-samples reproducibility. The sample of Key Lake has a higher spread in values with the fractal dimension having a relative standard deviation (RSD) of more than 20 %.

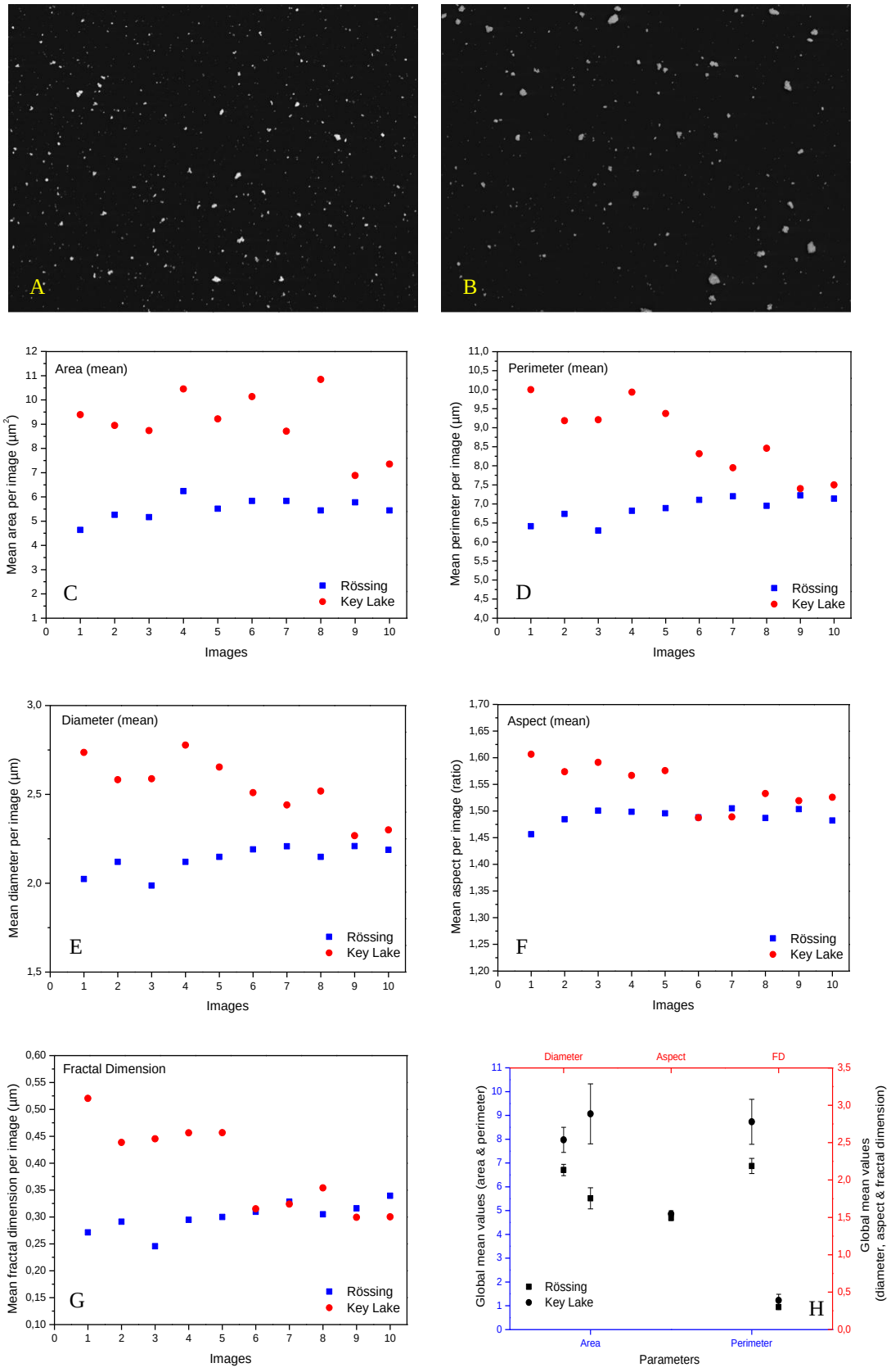

Figure 5-6: SEM image of dispersed sample of Rössing (A), Key Lake (B); Analysis of the samples, Mean values of Area (C), Perimeter (D), Diameter (E), Aspect (F), Fractal Dimension (G) considered per image, Global mean of all parameters (H).

Table 5-3: Within-sample reproducibility values of mean area, aspect, fractal dimension, diameter and perimeter[12]

Name of sample (Within-sample reproducibility)	**Area ± RSD %**	**Aspect ± RSD %**	**Fractal Dimension ± RSD %**	**Diameter ± RSD %**	**Perimeter ± RSD %**
Rössing (prep 1)	5.36 ± 10.92 %	1.49 ± 1.23 %	0.28 ± 7.94 %	2.08 ± 3.39 %	6.63 ± 3.92
Rössing (prep 2)	5.67 ± 3.65 %	1.49 ± 0.70 %	0.32 ± 4.41 %	2.19 ± 1.11 %	7.12 ± 1.51 %
Key Lake (prep 1)	9.35 ± 7.14 %	1.58 ± 1.01 %	0.46 ± 7.08 %	2.67 ± 3.28 %	9.54 ± 4.17 %
Key Lake (prep 2)	8.79 ± 19.50 %	1.511 ± 1.40 %	0.32 ± 7.01 %	2.41 ± 4.87 %	7.93 ± 5.99 %

Table 5-4: Between-sample reproducibility values of mean area, aspect, fractal dimension, diameter and perimeter[13]

Name of sample (Between-sample reproducibility)	**Area ± RSD %**	**Aspect ± RSD %**	**Fractal Dimension ± RSD %**	**Diameter ± RSD %**	**Perimeter ± RSD %**
Rössing	5.52 ± 3.88 %	1.49 ± 0.28 %	0.30 ± 9.23 %	2.13 ± 3.60 %	6.88 ± 5.08 %
Key Lake	9.07 ± 4.40 %	1.55 ± 3.29 %	0.39 ± 26.22 %	2.54 ± 7.25 %	8.73 ± 13.08 %

[12] Values have not been corrected and are therefore 10 % larger before the correction
[13] Same remark as above

Finally, both samples are compared and their mean area, perimeter and diameter for each image are shown in Figure 5-6C, 5-6D and 5-6E respectively. These parameters appear to be larger for Key Lake compared to Rössing. However, their mean aspect and fractal dimension appear to be similar (Figure 5-6F and 5-6G respectively). The first three parameters can be considered as size descriptors while the last two parameters are shape descriptors. Interestingly, both samples appeared to have different sizes but their aspect and fractal dimension are similar as seen in Figure 5-6H where the global mean of ten images are obtained and compared. This data supports the above observations.

By using the above method, it is reasonable to conclude that the above might be used in the case of determining if two samples are similar or not.

The facilities of Rössing and Key Lake have in general, slightly different flowsheets although both facilities precipitated uranium with NH_3. The calcination temperature of ADU to U_3O_8 was carried out at 750 °C at Key Lake while it is not known for Rössing. However, similar temperature would be expected. Prior to precipitation, IX followed by SX was used for purification at Rössing while Key Lake had used SX [12]. Although processes are known for both facilities, it is not straightforward to pinpoint the exact step or steps that could result in the differences in the observed mean size of the particles. However it is noteworthy that given both facilities had produced ADU using NH_3, the shapes of the pre-cursors had to be similar and they were similar (aspect and fractal dimension). And in Chapter 1, it has been demonstrated that the morphology is retained for the different forms of yellow cakes when these were calcined to U_3O_8. Therefore, it is reasonable to expect that U_3O_8 from both facilities would possess ultimately, the same shape parameters.

However, due to the lack of a standard size (or size distribution) yellow cake, this method cannot be validated. The plausible approach could be to repeat the sample preparation for more samples to increase the level of confidence. In addition, two different techniques could be used to verify the size or size distribution of a sample. For instance, a cascade impactor is deemed suitable for such an application and is likely to provide complementary information from SEM.

5.6.2b Comparison of samples

In this section, 26 different yellow cake samples are evaluated by PCA using all the 30 sizes and shapes descriptors computed by Image Pro-analyzer. The best three out of five images per sample preparation were selected and the processed data can be seen in Figure 5-7 where 25 samples could be found. The sample of Heng Yang was clearly an outliner and was therefore removed. Its general morphology has been shown in Figure 5-4 (3rd row) and is distinctly different by visual comparison of the SEM images.

All 25 samples are therefore represented by 25 individual facilities. From the score plot, it is clear that the sample from Rabbit Lake (denoted RaL) is clearly different from the remaining sample. This is the only yellow cake with the composition of uranyl peroxide found in this group of samples. The sample of United Nuclear (denoted UnN) is also different from the rest of the group.

About 81 % variance of the data could be explained by the use of just 2 PCs. The loadings plot reveals the relationship among the 30 variables, of which three groups are closely related (two pair of variables and 1 large group of remaining 26 variables). Along PC1, nearly 70 % of the variance in the dataset is explained by the large group of 26 variables. The sample of United Nuclear, located on the far right of the plot (along PC1) has distinct features, defined particularly by these parameters or variables.

In the case of PC2, the additional 11 % is explained by Area/Box and Perimeter (ratio), Aspect and Radius Ratio Aspect, which have opposite effects or influence on the samples. For example, the sample from Rabbit Lake (denoted RaL) has bigger aspect and radius ratio but smaller area/box and perimeter (ratio).

In general, it was not easy to observe cluster(s) for the same sample. There are a few possible explanations. First of all, there is simply too much information on the plot. More than 150 images have been analysed and each image is represented by a point in the plot. Second of all, the between-sample variation could be significant for certain samples, thus resulting the points to be scattered in the score plot. This can be attributed to the lack of standardization in the developed method. The quantity of sample required for each preparation was in fact, very minute (ca 1 mg) and it was rather difficult to weigh such an amount accurately. The grinding of sample in ethanol was done manually and the strength cannot be readily monitored nor controlled. Besides, only a fraction of the dispersed sample in ethanol was subsequently transferred onto the SEM disk holder. The representative transfer could pose a problem if heavier or bigger particles stayed at the bottom of the mortar while lighter particles were being suspended in ethanol. While grinding of the sample was aimed at breaking down the agglomerates and mixing of the suspension created a more homogenous particle size distribution, there was no way to ensure that the outcome was desired and reproducible.

Considering the fact that only such a small amount of sample is required, it is understandable that representative sampling is an issue to be addressed. Besides, the number of particles counted per image can vary substantially and influence the results. To overcome this, numerous preparations should be made followed by the computation of images with similar counts of particles. However, this can be extremely laborious.

Figure 5-8 shows the result of reducing 26 samples down to just 14 samples that are mainly oxide in composition. These samples are collectively investigated as they have a common feature, that is, these powders are all black in colour. Apart from the physical appearance, what is noteworthy is the inference; these samples have all been calcined and their main composition is clearly an oxide (U_3O_8). It is therefore of interest to study the texture property of this particular set of samples.

The sample from Heng Yang is again removed from the plot. There is observable improvement in this score plot compared to that of Figure 5-7. More clusters of samples can now be observed. From this plot, one can deduce that the use of size and shape descriptors may be helpful to distinguish certain samples. For instance, two Australian samples originating from different facilities

Queensland (denoted Que) and Mary Kathleen (denoted MaK) are found on different sides of the plot. A third Australian sample from Olympic Dam (denoted OlD) is more scattered but appears to be different from the other two samples. However, repetition of this sample should be carried out to strengthen the findings. On the other hand, some samples do overlap in the plot such as the sample of Namibia Rössing (denoted Ros) and South Africa Palabora (denoted Pal) as well as possibly South Africa Nufcor (denoted Nuf).

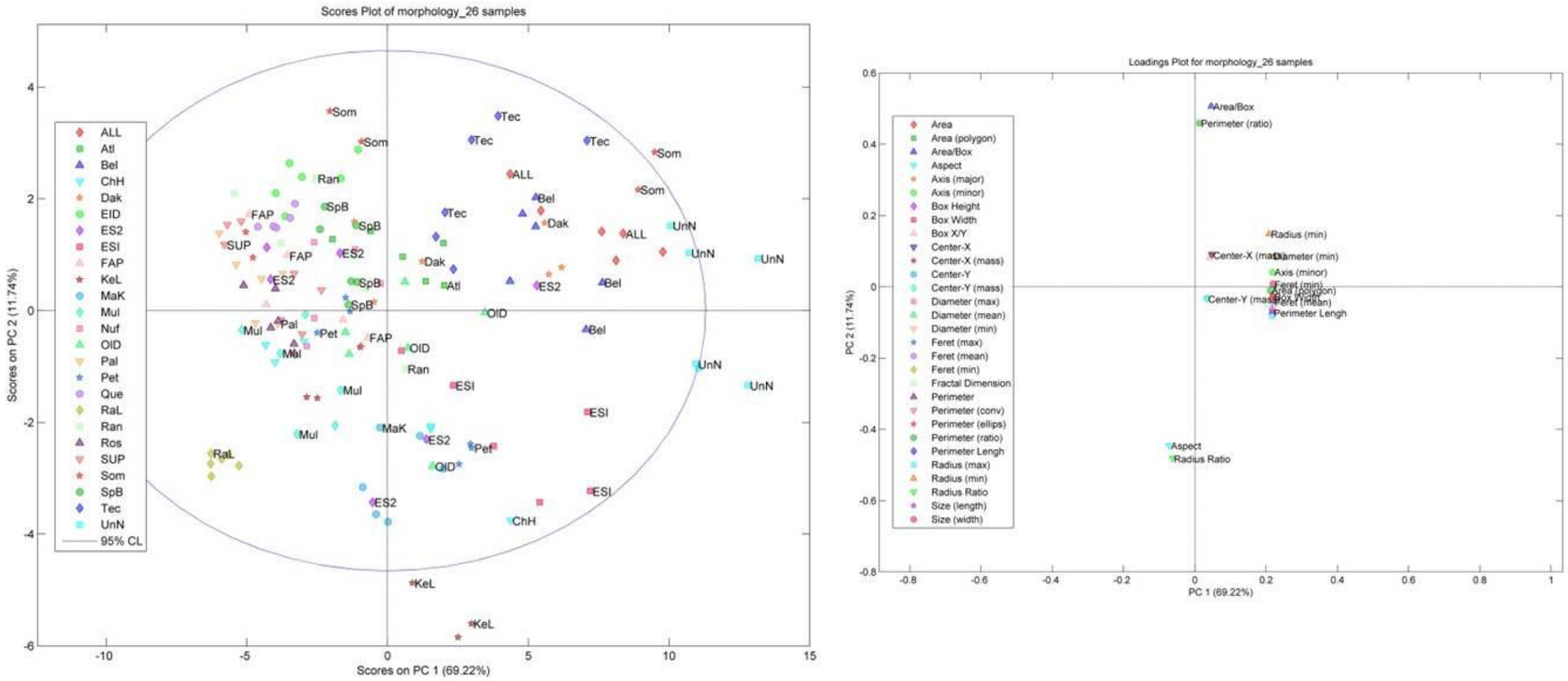

Figure 5-7: PCA score plot & loadings plot of 26 yellow cake samples. Sample Heng Yang is removed as it is clearly an outliner.

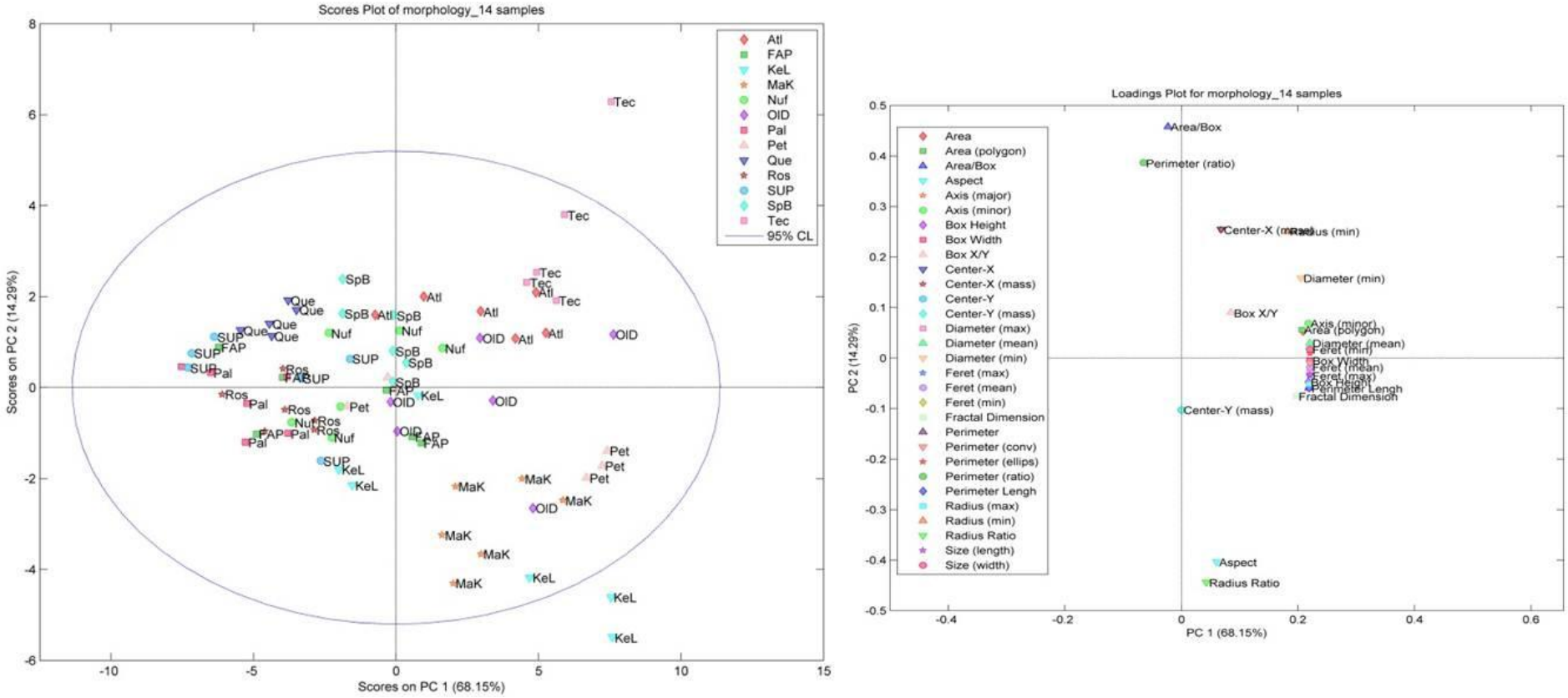

Figure 5-8: PCA score plot & loadings plot of 14 yellow cake (oxides) samples. Sample Heng Yang is removed as it is clearly an outliner.

The results reviewed in this section are promising but ought to be strengthened further. This can be done in a few ways. A more rigorous sample preparation should be carried out to reduce the between-sample reproducibility. In addition, a second technique providing size and preferably shape measurement should be considered to increase the level of confidence in the data, especially when there is no standard size yellow cake available for validation.

5.7 Correlation of morphology of samples with processing history

In Chapter 1, it was demonstrated that the use of different precipitating reagents led to the formation of samples with differing morphologies. In order to investigate the link between the morphology with the processes, the logical approach would be to vary the conditions for the preparation of the yellow cakes and to capture the change in the morphology (quantitatively) with the methods described in the current chapter.

Conditions such as pH, temperature and concentrations of the reagents were varied, as well as the sequence of addition exchanged and carrying out the precipitation with or without mixing. Only one single parameter was varied each time and the precipitated material studied by SEM. However, the changes in any of the single parameters did not influence the morphology of the material (in terms of shape). For instance, the discrete particles of AUC and agglomerated UO_4 were always observed regardless of any change in the parameters.

Therefore, in view of the above observations, the correlation of morphology with processing history could not be further advanced. Changes to sizes or size distribution are foreseen and they could be investigated in the future, with other automated instruments.

5.8 Image texture analysis

5.8a Angle Measure Technique

In this section, a relatively new feature is explored as a signature for morphology. Image texture analysis is applied here for nuclear forensics purposes. An algorithm known as AMT is used here for the image analysis. It was designed to describe signal complexity in function of geometrical scale from local to global [162]. By doing so, it eliminates the need for tedious sample preparation such as having to disperse the samples prior to SEM imaging as carried out in the preceding section of this chapter. By simply taking images of the powder samples, the AMT approach can extract and characterize various powder features such as particle sizes and shapes, smoothness, coarseness etc. It is noteworthy that by not dispersing the sample powder, AMT is very useful for characterizing both individual particles as well as the bulk powder properties at the same time. Therefore, image texture analysis is certainly of great interest and is explored in this work, as a possible morphological or microstructural fingerprint for nuclear forensics to the existing large variety of UOC powders.

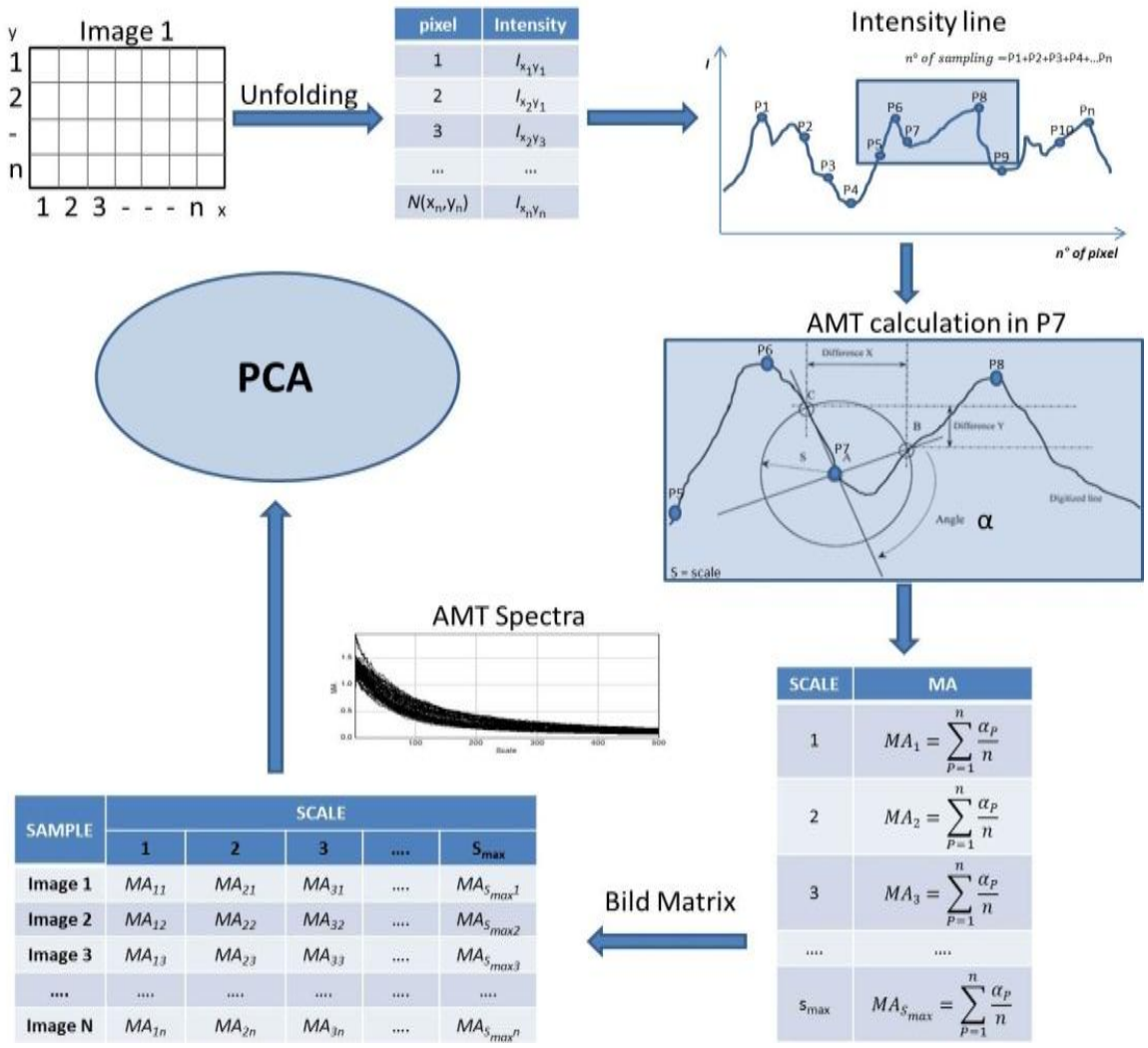

Figure 5-9: Explanation of the AMT approach [163].

The AMT approach is described pictorially in Figure 5-9. A 2-D SEM image is first unfolded based on the intensity value of each pixel, thus creating an intensity spectrum in function of the number of pixels. Secondly, 10000 points are randomly chosen on the intensity spectrum as centres of 10000 circles, with radius 's' defined as the scale (set to 500). On the example above, point A is the centre of a circle with radius s and the circle cuts the measurement series by two other points, B and C. The supplementary angle of CAB is subsequently computed. For all the angles obtained at the same scale but at different random points, the mean angle (MA) is obtained thus creating a data matrix, which can be readily analysed by PCA.

5.8b Experimental approach

Figure 5-10 and 5-11 are SEM images of UOC samples taken at 250x and 1000x magnifications respectively. Each row of five images belonged to the same sample and was taken at different positions of the sample.

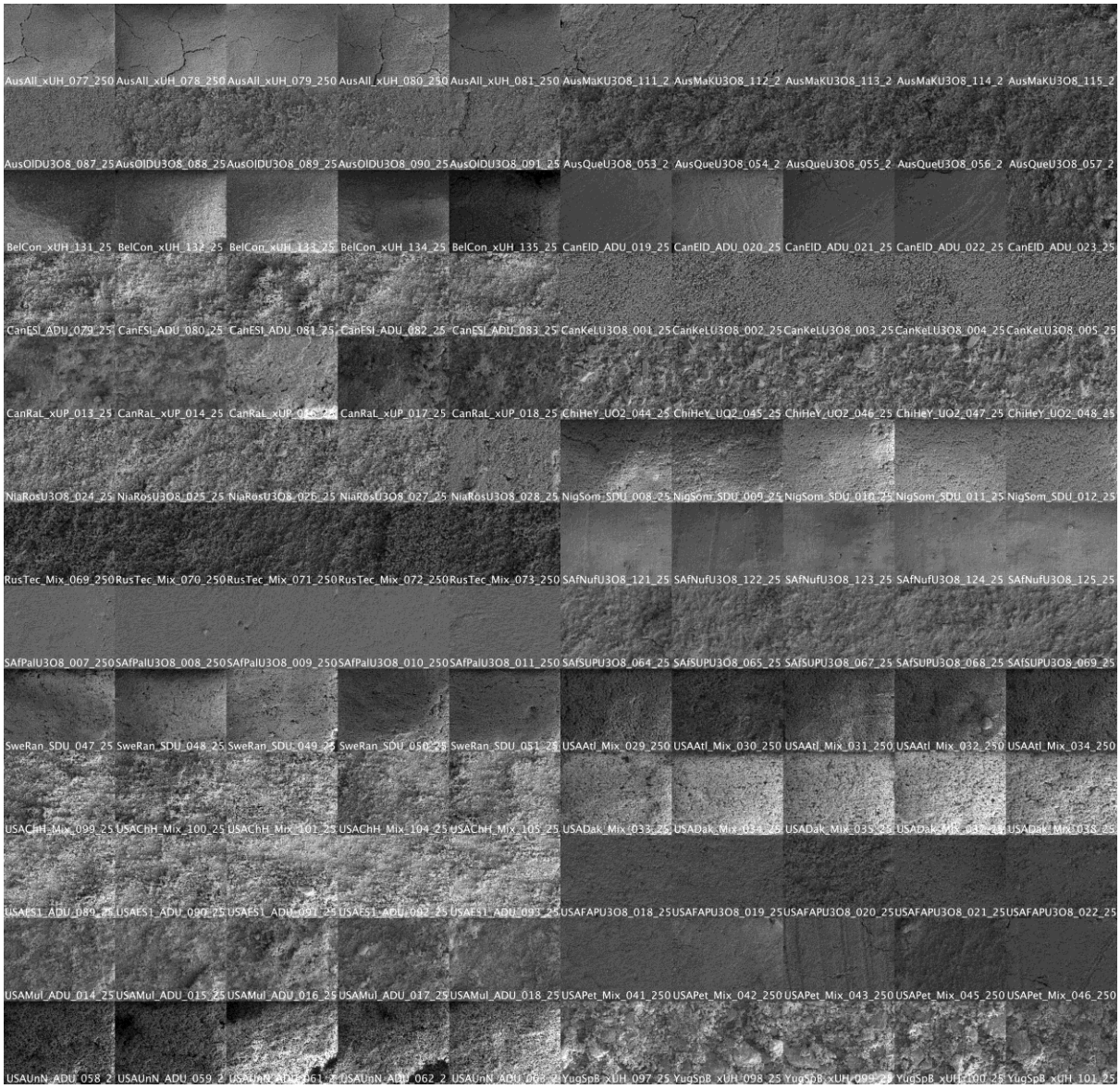

Figure 5-10: SEM images of 26 samples (5 replicates per sample) taken at 250x magnification.

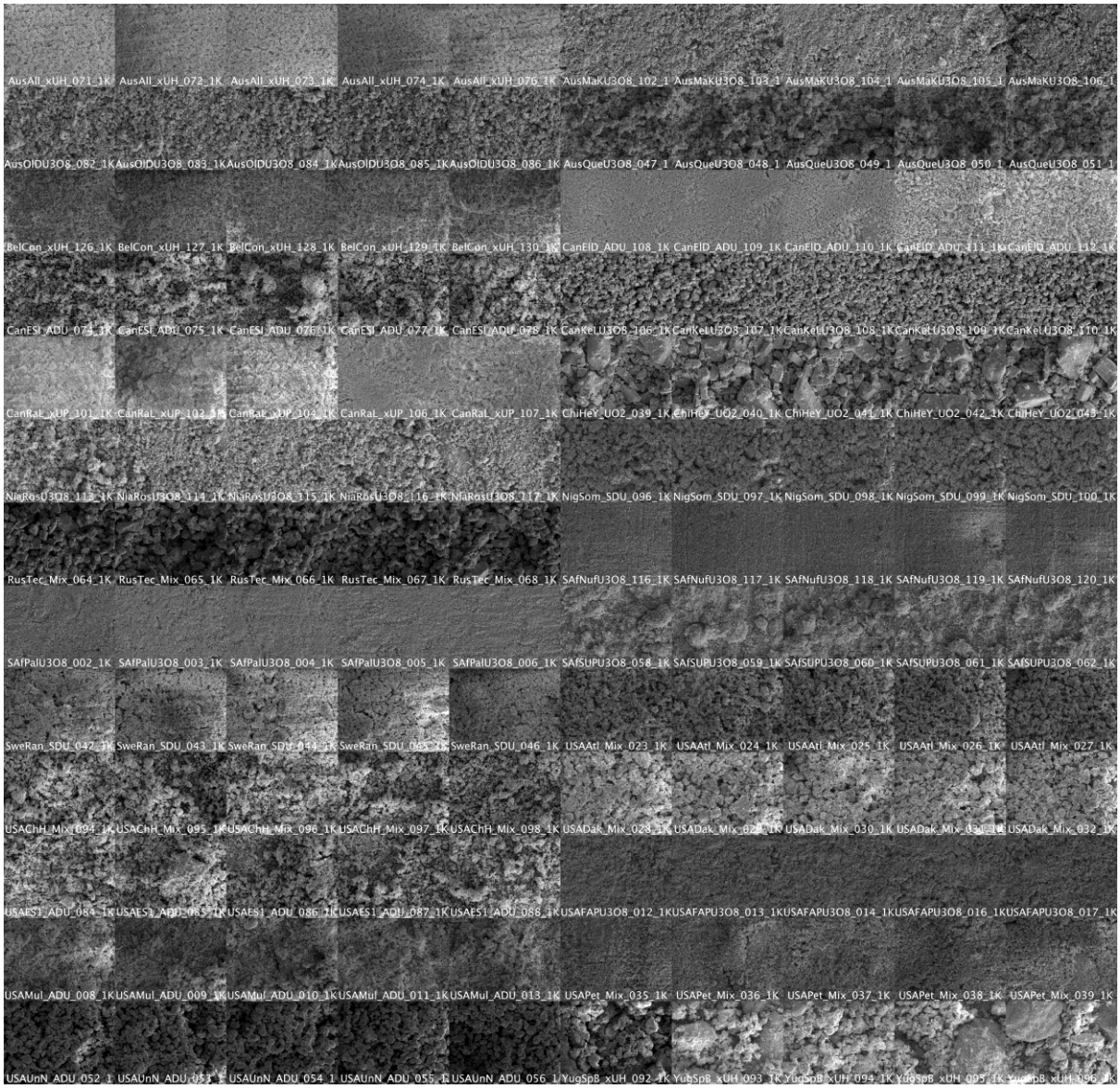

Figure 5-11: SEM images of 26 samples (5 replicates per sample) taken at 1000x magnification.

Each original SEM image (2560 x 2320 pixels) was further divided into five ROIs (1000 x 800 pixels each) where the first four ROIs (termed as S1, S2, S3 and S4) represented regions around or near the four corners of the image and the fifth ROI (S5) was in the centre of the original image. For both magnifications, the same ROI was applied and for images taken at 250x magnification, there was corresponding more material than there was for the same ROI in the case of 1000x magnification. The results from both investigated levels of magnification are subsequently compared.

AMT algorithm was applied to all the five regions and the MA data was subsequently fed into PCA. In this section, the results are mainly focused on 1000x magnification. The results for 250x magnification can be found in Appendix E. However, the main findings will still be delineated here.

5.9 PCA Analysis of the MA data

5.9.1a Evaluation of image texture at 1000x (26 samples)

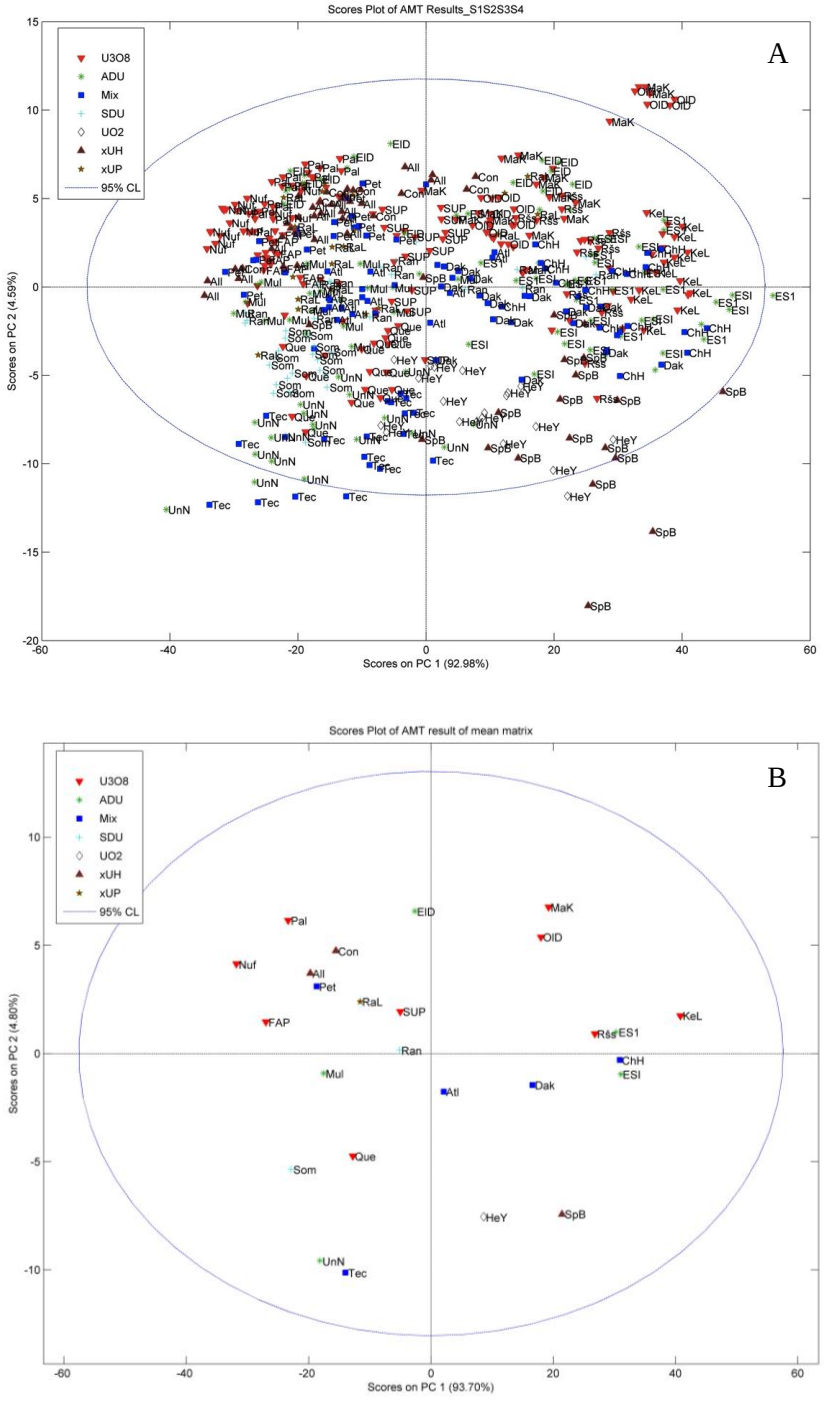

Figure 5-12: PCA score plot of MA data from 26 samples (20 replicates per sample) taken at 1000x magnification (A); PCA score plot of averaged MA data from 26 samples taken at 1000x magnification (B).

Figure 5-12A and 5-12B reflect respectively, the scores plot of the MA data computed from 26 samples, each comprising 20 replicates and the grand mean of the MA data. The two plots are opposite in nature. Although the top plot appears cluttered, one can observe the close grouping of images belonging to the same sample (denoted by the same three letters). The bottom plot shows

clearly the relative position of these samples when the data has been averaged. It is meant to provide a better or clearer relationship among the samples. There is in general, separation of the samples, which suggests that the investigated samples have different image textures. Figure 5-13 provides the evidence.

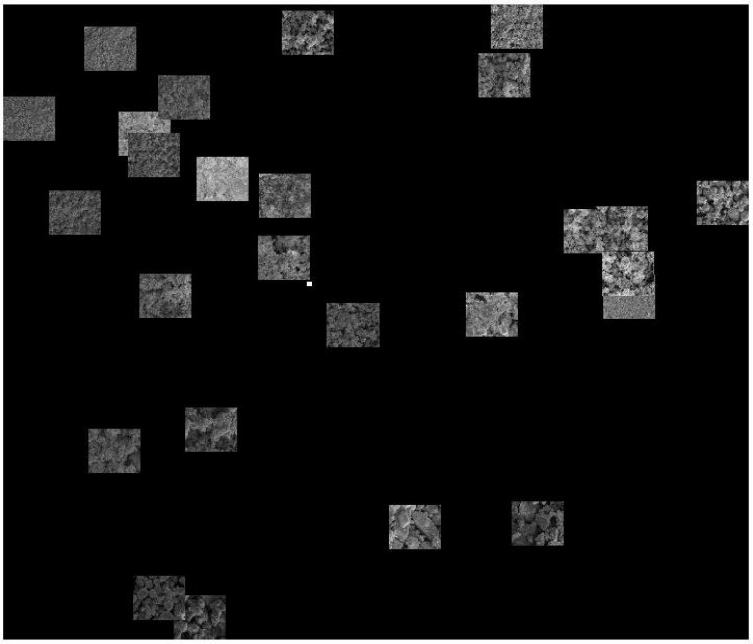

Figure 5-13: Selected SEM images of the 26 samples. Their position corresponds to the score plot in Figure 5-12B.

The particles are visibly larger for samples found at the bottom of the plot. Samples on the left have smaller grains and appear smoother or more homogenous while going towards the right or bottom of the plot; the samples appear coarser and more heterogeneous.

Figures 5-14 to 5-18 reveal the PCA scores plots of the five different ROIs, S1 to S5 respectively. The plots labelled as 'A' represent PC1 vs PC2 while plots labelled as 'B' represent PC1 vs PC3. In all the five plots, the 1st PC explains on average, 93 % variance in the data. This particular PC appears to define "homogeneity" or "powder complexity" [162]. Samples on the left hand side of the plot are more homogenous than samples on the right hand side of the plot (with reference to Figure 5-13). In the case of PC2, another 4 % variance in the data is explained. This PC seems to be influenced by the grain or particle size of the samples. PC3 explains in addition, 1 % of the variance of the dataset. It is not straightforward to envisage what this 3rd PC might explain. Nonetheless, the use of just 2 PCs could already explain and capture 97 % of the variance in the data.

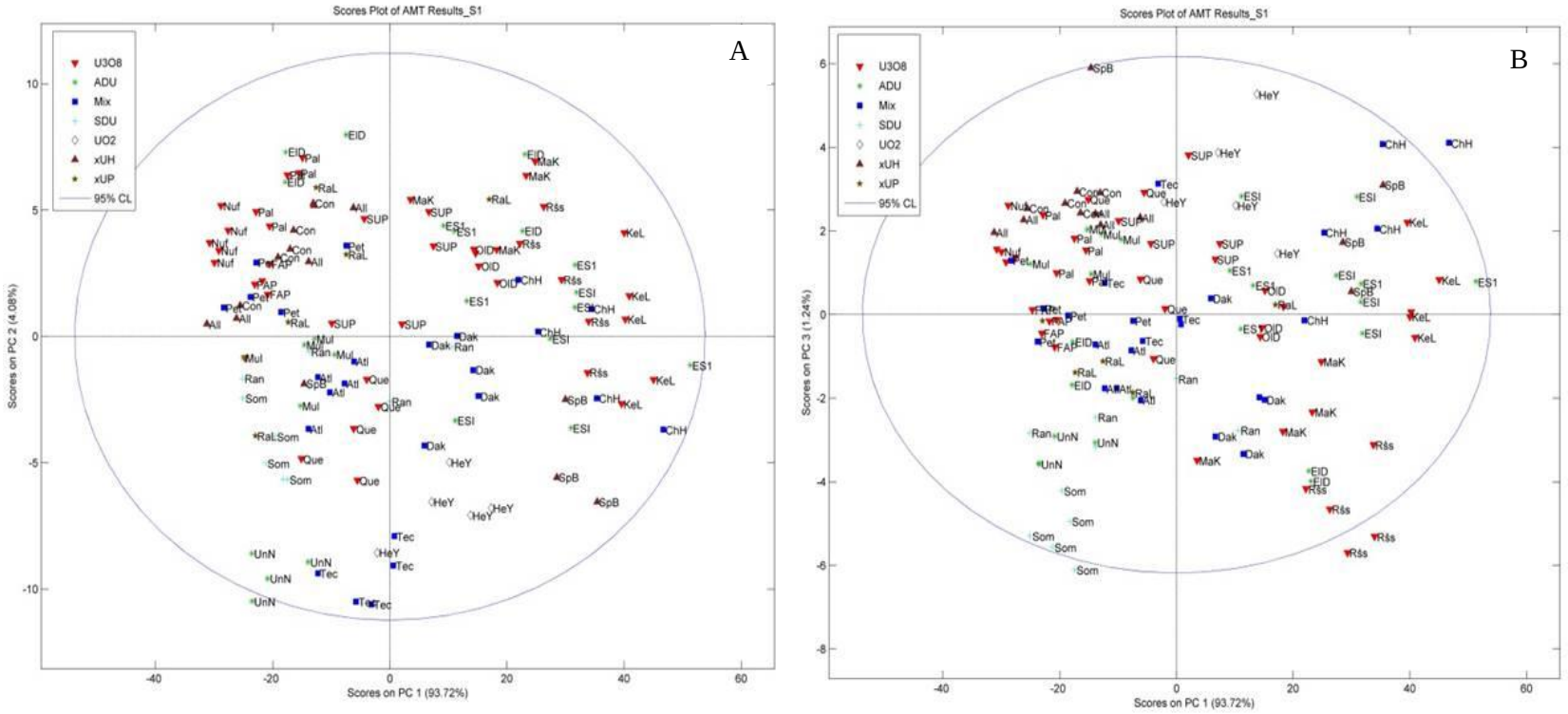

Figure 5-14: PCA scores plot of MA data obtained from region S1 of the original sample at 1000x magnification (26 samples in total); PC1 vs PC2 (A), PC1 vs PC3 (B).

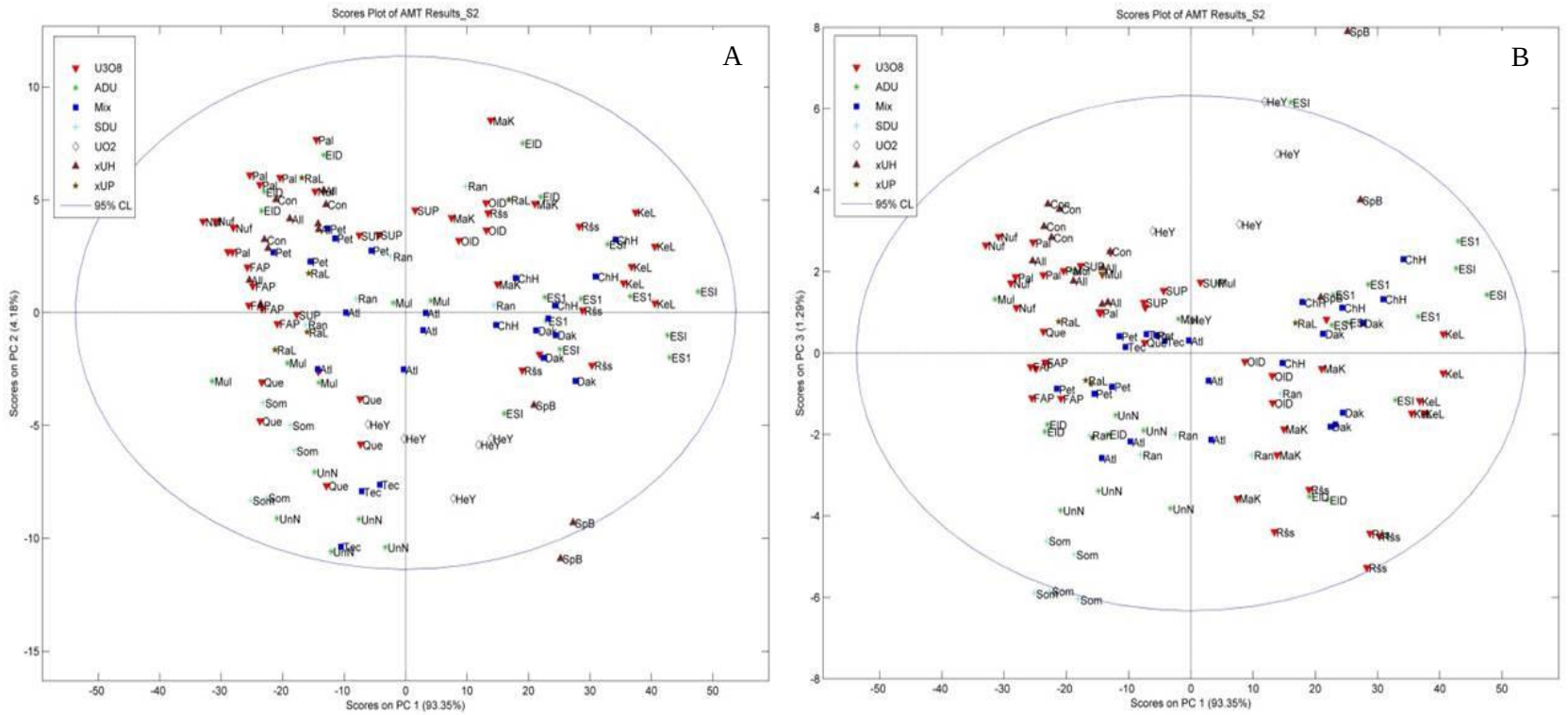

Figure 5-15: PCA scores plot of MA data obtained from region S2 of the original sample at 1000x magnification (26 samples in total); PC1 vs PC2 (A), PC1 vs PC3 (B).

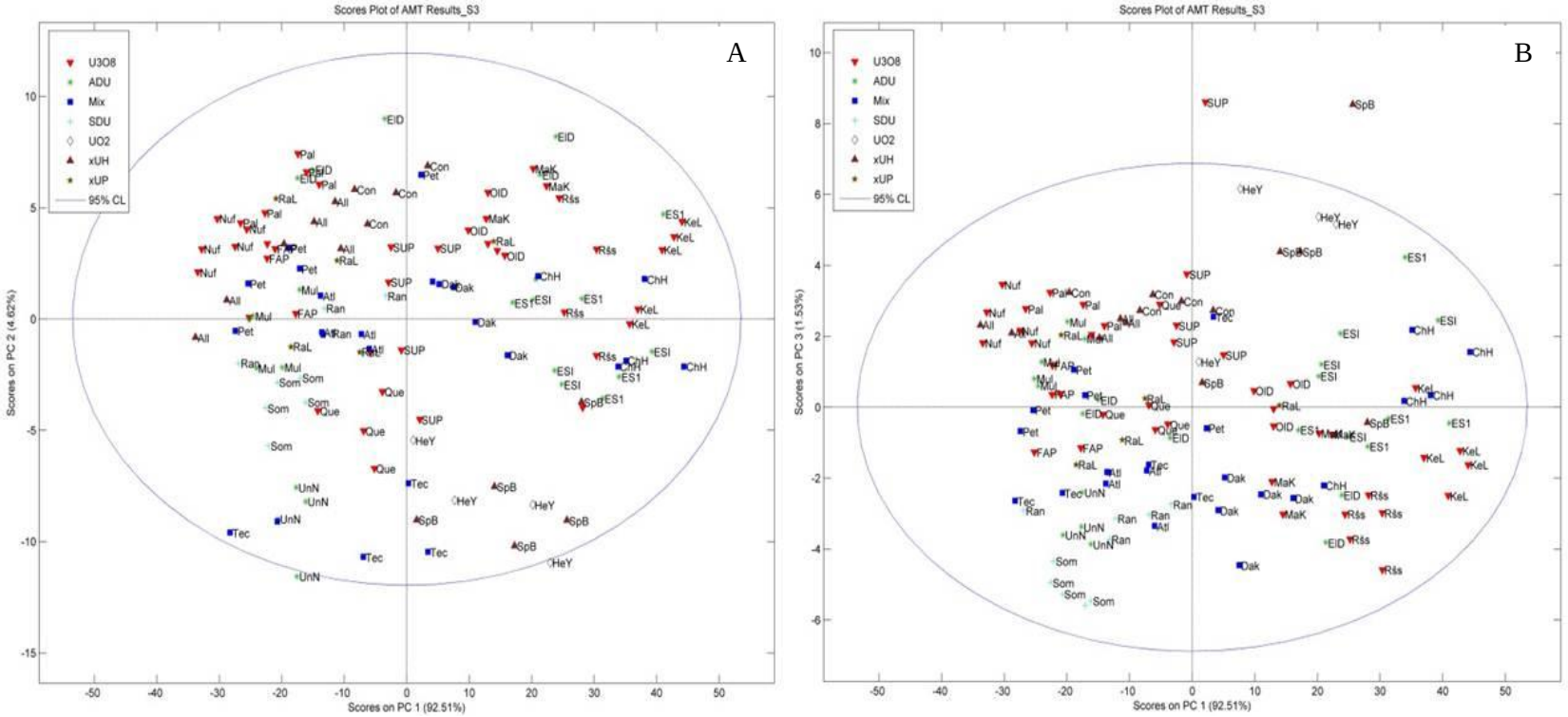

Figure 5-16: PCA scores plot of MA data obtained from region S3 of the original sample at 1000x magnification (26 samples in total); PC1 vs PC2 (A), PC1 vs PC3 (B).

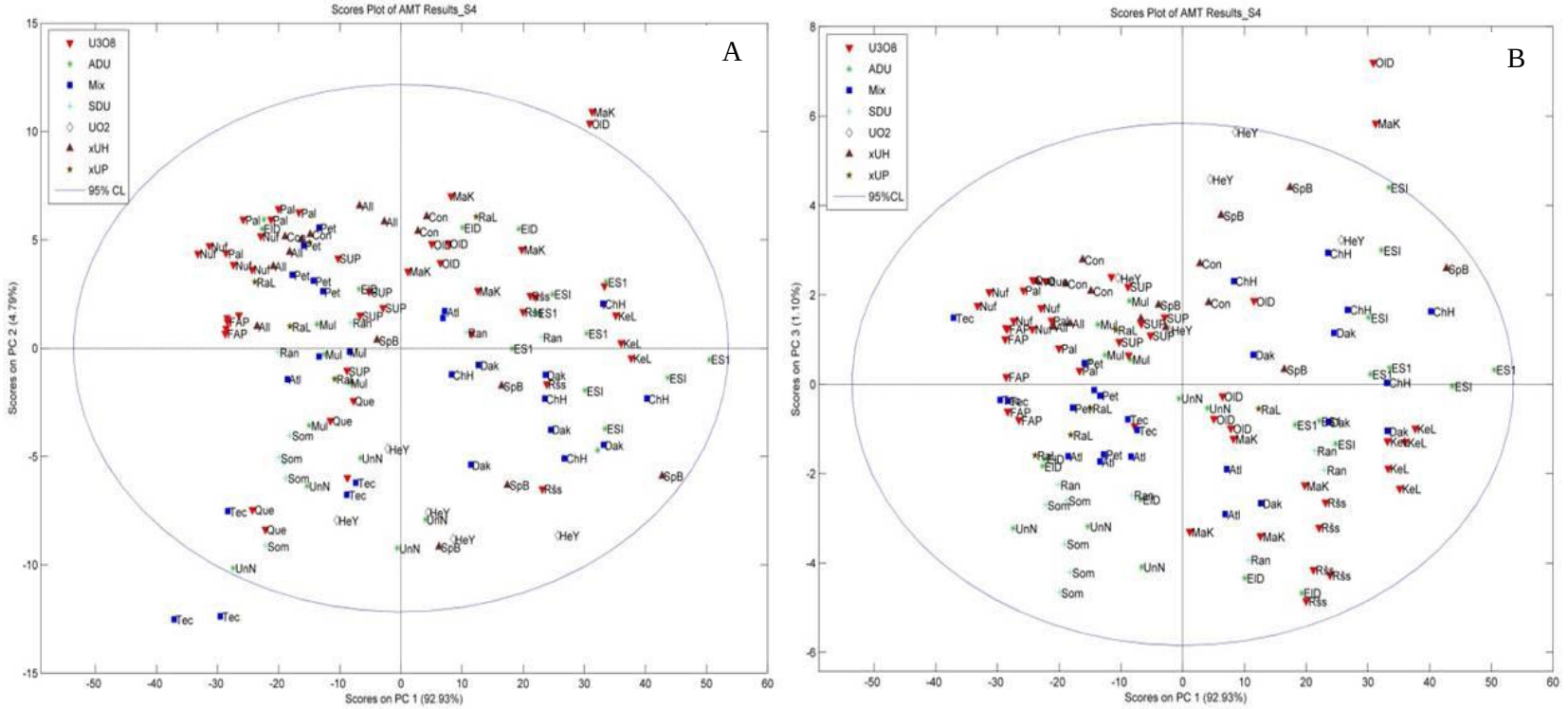

Figure 5-17: PCA scores plot of MA data obtained from region S4 of the original sample at 1000x magnification (26 samples in total); PC1 vs PC2 (A), PC1 vs PC3 (B).

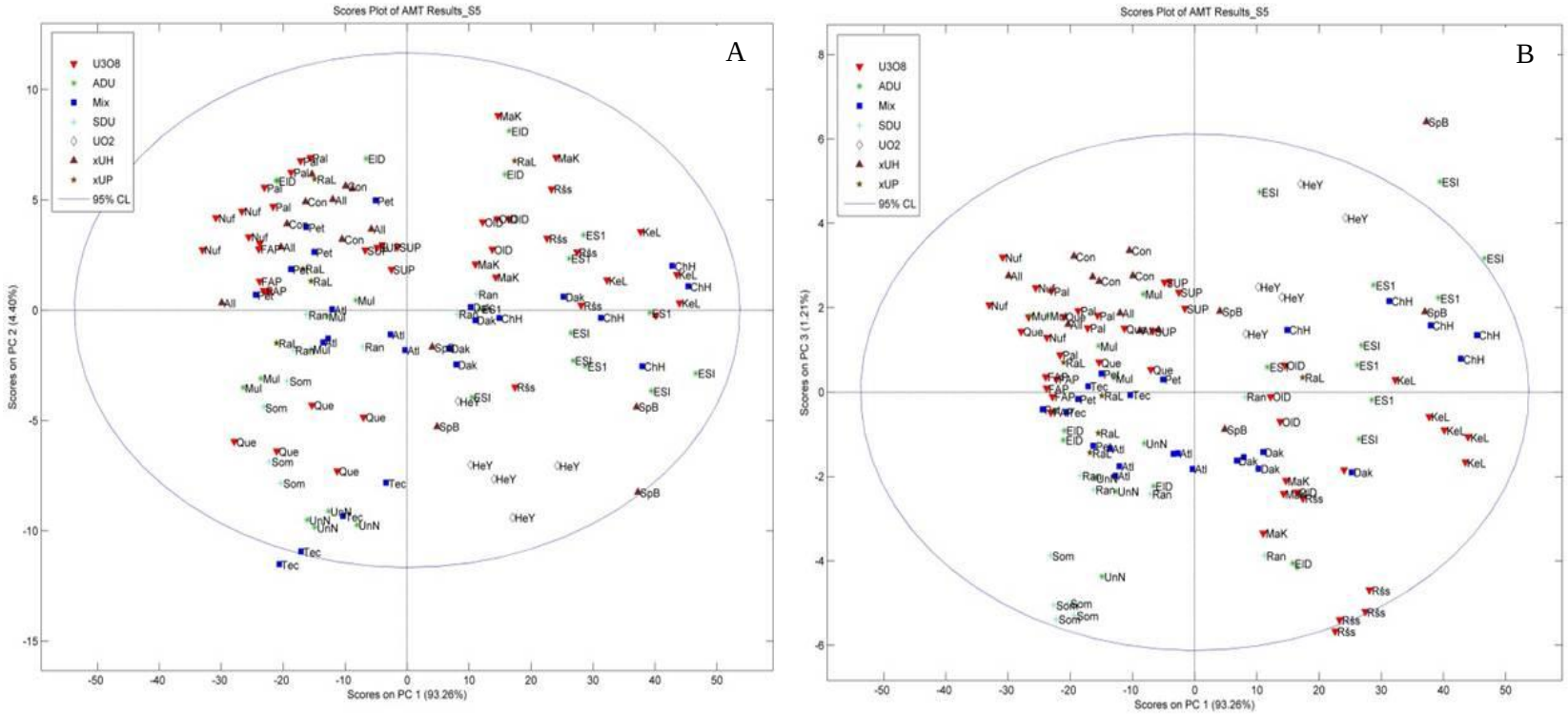

Figure 5-18: PCA scores plot of MA data obtained from region S5 of the original sample at 1000x magnification (26 samples in total); PC1 vs PC2 (A), PC1 vs PC3 (B).

In general, the scores plots for the five regions are similar for PC1 vs PC2 and PC1 vs PC3. Each region represents 1000 x 800 pixels, a stark reduction from the original image containing 2560 x 2320 pixels. This makes it less intensive to compute the MA spectra and can also lead to the use of smaller quantity of sample.

The general positions of each sample image are comparable across the plot. Therefore, each sample preparation is rather uniform. Images of the same samples (for example, Nufcor and Rabbit Lake), with lesser variation in particle sizes are found to be closely located while on the other hand, particles with large variation in sizes have understandably, a bigger spread in the points as well (for example, Techsnab and Heng Yang denoted as Tec and HeY respectively).

There is no association between the composition of the samples and their textured images. For instance, half the sample population are oxides (U_3O_8) and these samples are scattered over the plot. For the future, it will be interesting to investigate the texture of samples of U_3O_8 with varying morphologies as well as their pre-cursors.

5.9.1b Evaluation of image texture at 1000x (14 samples)

The 26 samples analysed for their image texture have varying compositions and origins as tabulated in Table 5-5. While some samples may be yellow, orange or dark green, about half of the samples are black. It can be readily envisaged that it will be relevant to apply image texture analysis to samples that have very similar appearance, in this case, black powder samples. Therefore, the 14 samples were removed and re-analyzed accordingly. Figures 5-19 to 5-23 show the score plots presented in a similar manner as the ones analysed for 26 samples. However, the legends are presented differently and in the following case, the 14 samples are treated as 14 different facilities.

As it can be seen from the figures, the same points belonging to the same sample are found in close proximity within the score plot, thus forming separable clusters. The results suggest that the 14 samples have different and possibly differentiable image textures and it will be further assessed by PLS-DA in the following section. The five ROIs produce similar score plots with subtle differences occurring with the positions of the sample points.

Table 5-5: Details of the 26 different investigated UOC samples

Facility[14] & Abbreviation	**Country**	**Composition[15]**
South Alligator (ALL)	Australia	Uranyl hydroxide
Atlas (Atl)*	USA	U_3O_8
Chevron Hill (ChH)	USA	Mixed (ADU + oxide)
Congo (Con)	Belgian	Uranyl hydroxide
South Dakota (Dak)	USA	Mixed (oxide + hydroxide)
ESI (ESI)	Canada	ADU
ESI (ES2)	USA	ADU
El Dorado (ElD)	Canada	ADU
Federal American Partners (FAP)*	USA	U_3O_8
Heng Yang*	China	UO_2 (+ U_3O_8)
Key Lake (KeL)*	Canada	U_3O_8
Mary Kathleen (MaK)*	Australia	U_3O_8
Mulberry (Mul)	USA	ADU
Nufcor (Nuf)*	South Africa	U_3O_8
Olympic Dam (OlD)*	Australia	U_3O_8
Palabora (Pal)*	South Africa	U_3O_8
Petromics (Pet)*	USA	Mixed oxide
Queensland (Que)*	Australia	U_3O_8
Rabbit Lake (RaL)	Canada	Uranyl peroxide
Ranstad (Ran)	Sweden	Sodium diuranate
Rössing (Rös)*	Namibia	U_3O_8
South Uranium Plant (SUP)*	South Africa	U_3O_8
Somair (Som)	Niger	Sodium diuranate
Spisak Black (SpB)*	Yugoslavia	Uranyl hydroxide
Techsnab (Tec)*	Russia	Mixed (U_3O_8 + ADU)
United Nuclear (UnN)	USA	ADU

[14] 14 samples that are physically black in colour are denoted with an *

[15] The compositions are assumed from their corresponding infrared and/or Raman spectra

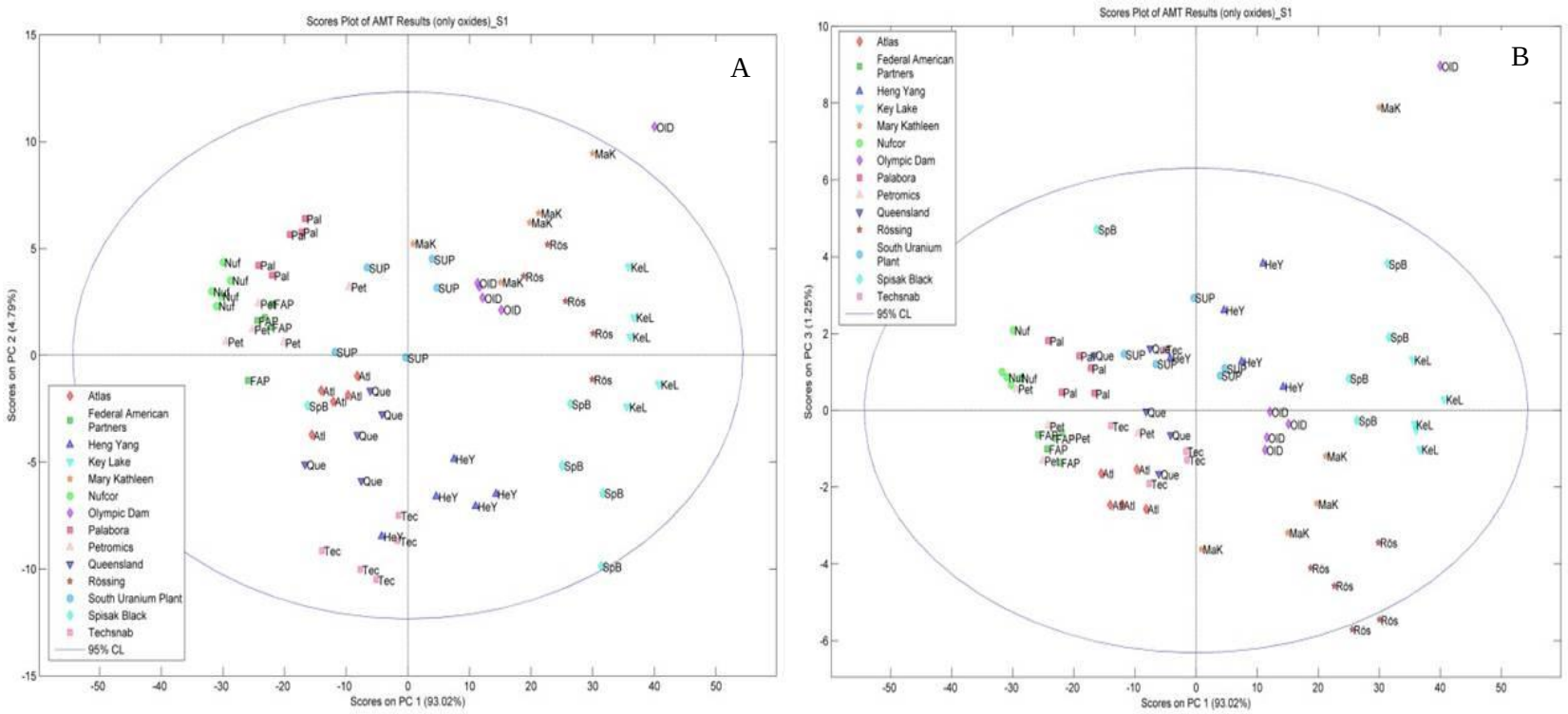

Figure 5-19: PCA scores plot of MA data obtained from region S1 of the original sample at 1000x magnification (14 samples in total); PC1 vs PC2 (A), PC1 vs PC3 (B).

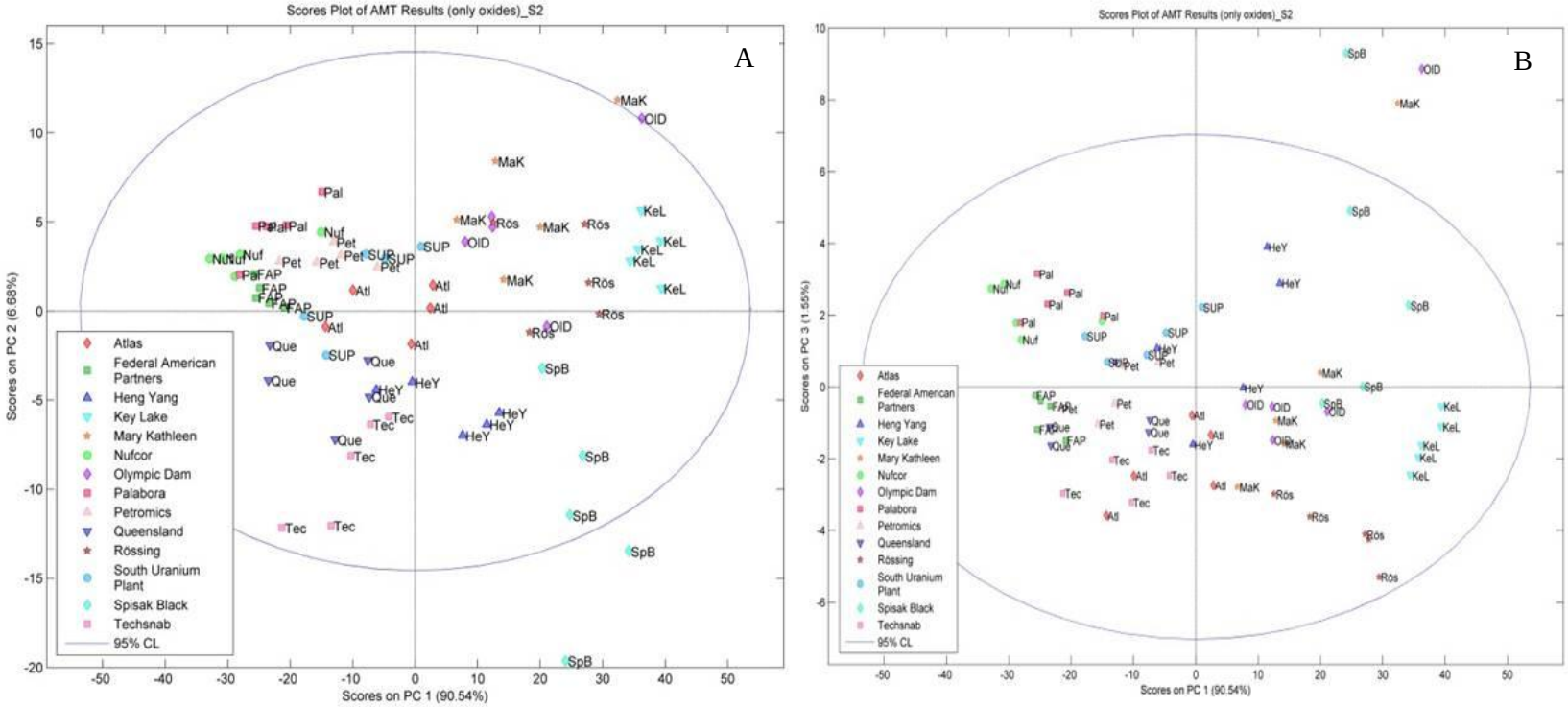

Figure 5-20: PCA scores plot of MA data obtained from region S2 of the original sample at 1000x magnification (14 samples in total); PC1 vs PC2 (A), PC1 vs PC3 (B).

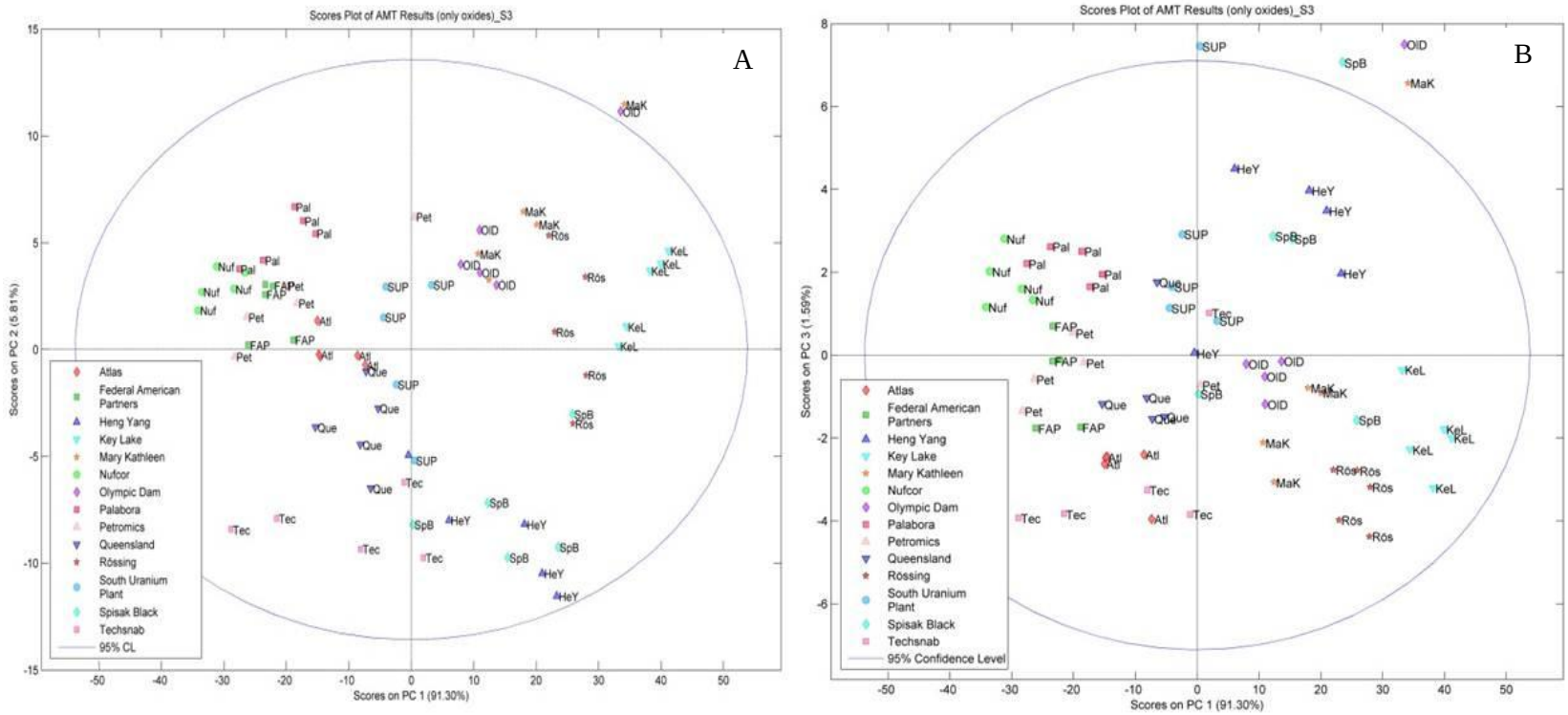

Figure 5-21: PCA scores plot of MA data obtained from region S3 of the original sample at 1000x magnification (14 samples in total); PC1 vs PC2 (A), PC1 vs PC3 (B).

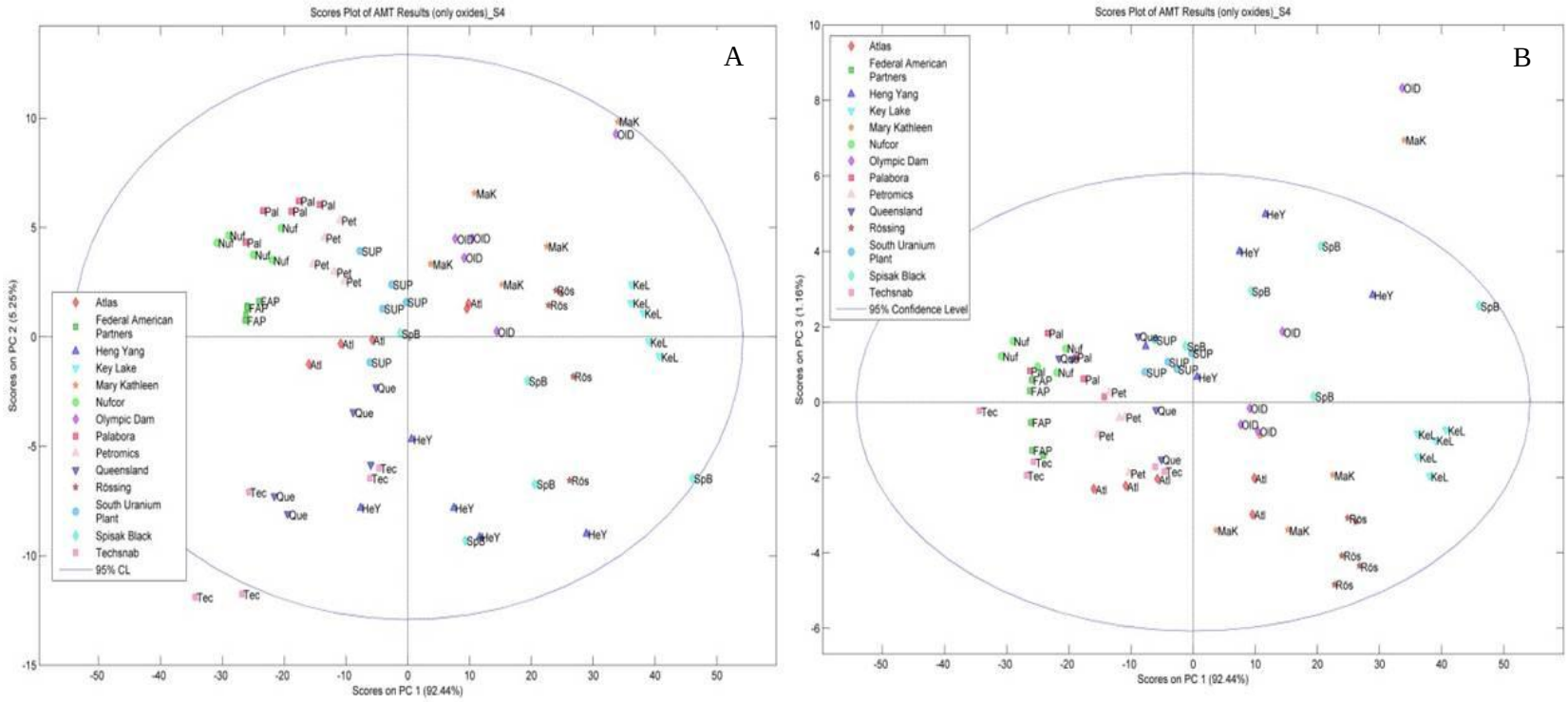

Figure 5-22: PCA scores plot of MA data obtained from region S4 of the original sample at 1000x magnification (14 samples in total); PC1 vs PC2 (A), PC1 vs PC3 (B).

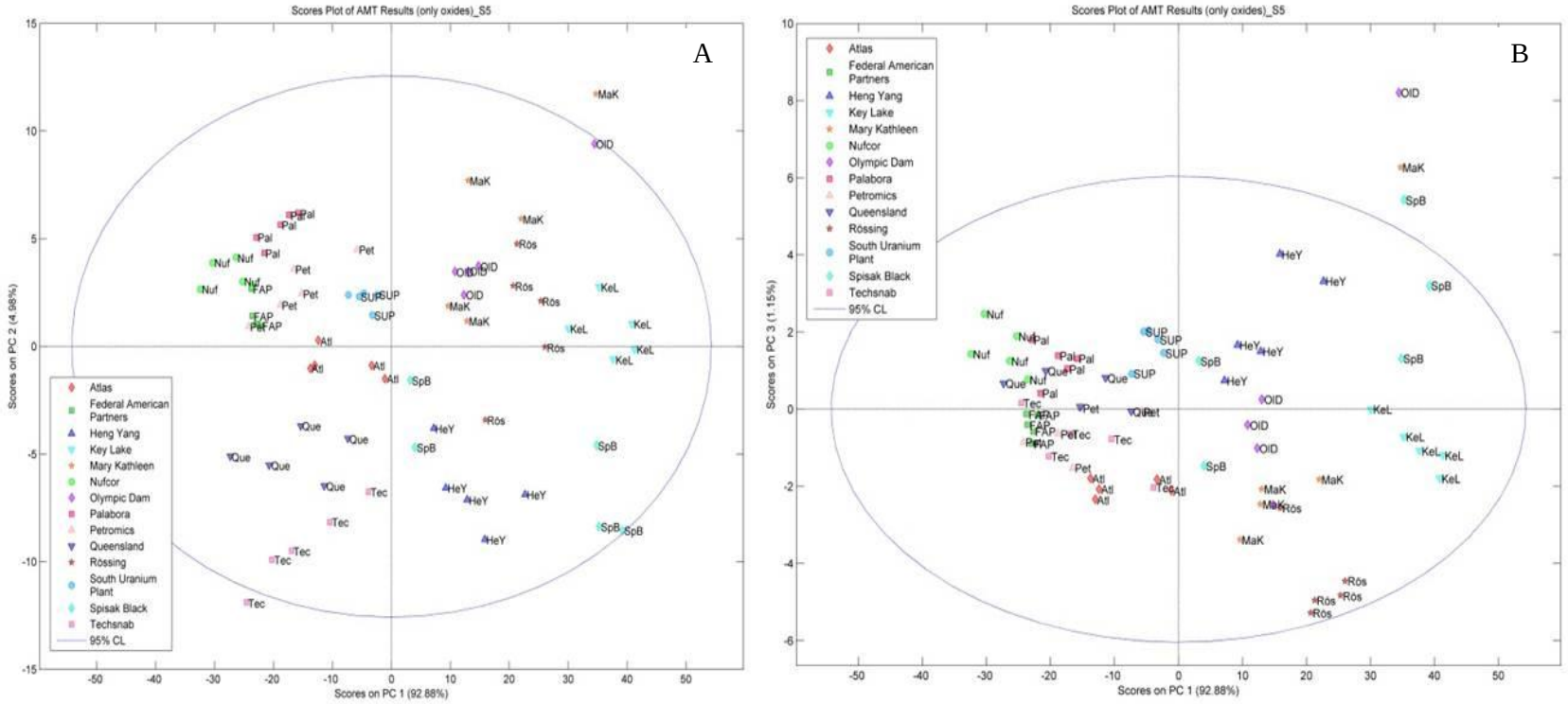

Figure 5-23: PCA scores plot of MA data obtained from region S5 of the original sample at 1000x magnification (14 samples in total); PC1 vs PC2 (A), PC1 vs PC3 (B).

5.9.2 Evaluation of image texture at 250x magnification

Besides 1000x magnification, the same samples were also imaged at a much lower magnification of 250x. At this magnification, it is expected that lesser macroscopic details will be revealed and the texture is likely to be more associated with the bulk properties of the sample compared to the higher magnification where details of the particles are more prominent (Figures 5-10 and 5-11) [163]. The SEM images were processed in a similar manner with the images taken at 1000x and in this section, the focus is placed mainly on the PCA results of the 14 black oxide samples.

Figure 5-24 shows the scores plots of ROI S1, represented by PC1 vs PC2 and PC1 vs PC3 on the left (A) and right hand side (B), respectively. The plots suggest that most of the samples are able to form individual clusters within its group of images at this magnification level of 250x. Therefore, the difference in their image texture remains detectable. This could also be attributed to the presence of much more sample within the same number of pixels per ROI at this magnification compared to 1000x magnification. If this is the case, such studies could also be carried out and tested with less expensive instrument such as an optical microscope.

Although the data is not shown here, the five different ROIs have produced rather similar scores plots. The general positions of the sample points are reproducible while it is understandable that the exact positions are not necessarily reproducible.

5.10 PLS-DA

PLS-DA is used to determine the goodness of the prediction by the model. This has also been used (Chapter 4) to verify the model based on the data from Raman spectroscopy.

Table 5-6 and 5-7 show the results in an attempt to classify or identify the samples that had been imaged at both magnifications and these are expressed as sensitivity and specificity, as the ones reported in Chapter 4. It is reiterated here the definitions of both terms. *Sensitivity* is defined as the number of samples predicted as in the class divided by the actual number in the class. *Specificity* is defined as the number of samples not in the class divided by the actual number not in the class. Cal and CV represent calibration and cross-validation respectively, and correspond to the training dataset used to build the model and part of the dataset that has been used to validate the model.

The results in Table 5-6 is based on the model for 26 different UOC samples while that in Table 5-7 is based on the model for 14 oxide samples. The class prediction is based on 26 classes and 14 classes respectively since all the samples have different origins as they come from different facilities. The sensitivity CV is 100 % across both tables for all the samples. This means that each time a sample is kept out from the model, the model is still capable of predicting the class of remaining samples. With the training set, some of the sensitivity values fell to as low as 84 % for the sample of Spisak Black (denoted SpB) in the larger dataset compared to 64 % for the sample of Olympic Dam (denoted OlD) in the smaller dataset. Specificity, on the other hand is lower than sensitivity in general. It ranges from 56 % - 97 % and 61 % - 99 % for CV and Cal respectively for

the larger dataset. In the case of the smaller set of 14 samples, specificity ranges from 70 % - 98 % and 63 % - 95 % for Cal and CV respectively. Specificity can also be viewed in terms of true negatives. A lower value for true negative would mean that there would be more false positive samples.

Tables 5-8 and 5-9 depict similar results for the samples imaged at 250x magnification. Again, sensitivity CV is 100 % for both datasets. Sensitivity Cal drops to 72 % for sample El Dorado (denoted ElD) in the larger dataset while sensitivity remains high for the rest of the 25 samples (> 88 %). In the case of the 14 samples dataset, there is only a slight drop to 92 %. Therefore, prediction of the sample in its correct class remains high. In fact, there is a noticeable improvement compared to the data at 1000x magnification. This is also evident by the specificity CV values that are reportedly all 100 % for the larger 26 samples dataset and its specificity Cal ranges from 77 % - 98 %. For the smaller dataset of 14 samples, specificity Cal and CV fall into the range of 73 % - 99 % and 62 % - 95 % respectively. This is comparable to the same dataset taken at 1000x magnification.

Texture image analysis has been applied to 26 UOC samples originating from totally different facilities. Five SEM images were taken at 1000x and 250x magnifications and each image was further divided into five regions (four separate ROIs and fifth ROI in the centre of image). 26 samples have been treated as a dataset and a subset of 14 samples (black powder) was also extracted as a smaller dataset for evaluation.

The MA spectra obtained using AMT algorithm has been analysed by PCA. Score plot reveal positions of the sample relative to the principal components (PC1, PC2) axes. A very high proportion of the variance in the datasets can be explained by just 2 PCs, compared to the actual number of variables of 500.

PLS-DA quantitates the success of the PCA model by calculating the sensitivity and specificity values of the calibration and cross validation data. Sensitivity is repeatedly better than specificity for both dataset at two magnification levels. In addition, at 250x magnification, the values are better than the ones reported for the higher magnification of 1000x. Although the scores plots illustrating 14 samples provide a better discrimination visually than the ones representing 26 samples, the sensitivity and specificity values for the smaller dataset generally decreases when compared to that for the larger sample set. This observation suggests that the 14 samples have more similar texture properties and this similarity is defused among a larger dataset with differing compositions.

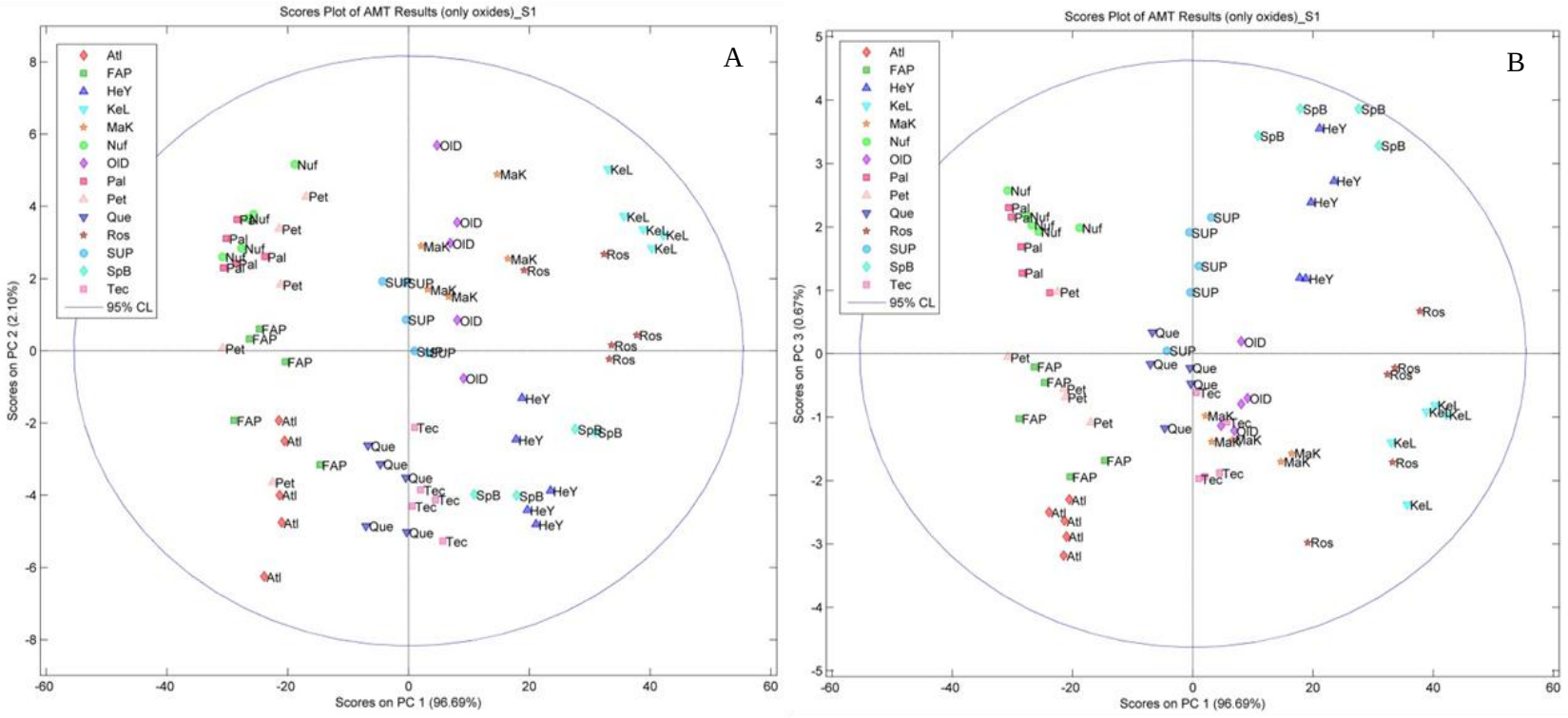

Figure 5-24: PCA scores plot of MA data obtained from region S1 of the original sample at 250x magnification (14 samples in total); PC1 vs PC2 (A), PC1 vs PC3 (B).

Table 5-6: Results of PLS-DA of 26 samples with 5 SEM images taken per sample at 1000x magnification and each image is subdivided into 5 ROI (Values x 100 %).

Samples	Facilities	Sensitivity Cal	Sensitivity CV	Specificity Cal	Specificity CV	RMSEC	RMSECV
1	All	1±0	1±0	0.92±0.02	0.91±0.04	0.18±0	0.21±0
2	Atl	0.92±0.11	1±0	0.74±0.07	0.7±0.07	0.19±0	0.21±0
3	ChH	0.92±0.11	1±0	0.8±0.06	0.76±0.06	0.18±0	0.21±0
4	Con	1±0	1±0	0.96±0.01	0.94±0.01	0.18±0	0.22±0
5	Dak	0.92±0.11	1±0	0.75±0.11	0.7±0.11	0.19±0	0.21±0.01
6	ES2	0.96±0.09	1±0	0.79±0.08	0.76±0.09	0.18±0	0.21±0
7	ESI	0.96±0.09	1±0	0.82±0.06	0.78±0.07	0.18±0	0.21±0.01
8	ElD	1±0	1±0	0.96±0.02	0.93±0.03	0.18±0	0.22±0
9	FAP	1±0	1±0	0.83±0.04	0.77±0.06	0.19±0	0.21±0
10	HeY	0.92±0.11	1±0	0.88±0.03	0.86±0.03	0.17±0.01	0.22±0
11	KeL	1±0	1±0	0.95±0.02	0.94±0.02	0.17±0	0.22±0
12	MaK	0.96±0.09	1±0	0.82±0.03	0.79±0.03	0.18±0	0.21±0
13	Mul	0.88±0.18	1±0	0.76±0.06	0.72±0.05	0.19±0	0.21±0
14	Nuf	1±0	1±0	0.92±0.01	0.91±0.02	0.18±0	0.22±0
15	OlD	0.88±0.18	1±0	0.9±0.02	0.87±0.01	0.18±0	0.22±0
16	Pal	1±0	1±0	0.92±0.01	0.92±0.02	0.18±0	0.21±0
17	Pet	1±0	1±0	0.73±0.04	0.68±0.04	0.19±0	0.21±0
18	Que	0.88±0.18	1±0	0.8±0.04	0.75±0.04	0.19±0	0.21±0
19	RaL	0.84±0.09	1±0	0.61±0.08	0.56±0.08	0.19±0	0.2±0
20	Ran	1±0	1±0	0.84±0.1	0.8±0.12	0.18±0.01	0.21±0
21	Rös	1±0	1±0	0.98±0.01	0.96±0.03	0.17±0	0.22±0
22	SUP	0.88±0.27	1±0	0.8±0.03	0.77±0.04	0.18±0	0.21±0
23	Som	1±0	1±0	0.99±0.01	0.97±0.02	0.17±0	0.22±0
24	SpB	0.84±0.17	1±0	0.88±0.05	0.86±0.06	0.17±0.02	0.22±0
25	Tec	1±0	1±0	0.95±0.02	0.94±0.04	0.17±0.01	0.22±0
26	UnN	1±0	1±0	0.95±0.03	0.93±0.04	0.17±0	0.22±0

Table 5-7: Results of PLS-DA of 14 samples with 5 SEM images taken per sample at 1000x magnification and each image is subdivided into 5 ROI (Values x 100 %).

Samples	Facilities	Sensitivity Cal	Sensitivity CV	Specificity Cal	Specificity CV	RMSEC	RMSECV
1	Atl	0.96±0.09	1±0	0.81±0.12	0.72±0.14	0.24±0	0.31±0.01
2	FAP	1±0	1±0	0.85±0.06	0.77±0.03	0.24±0	0.3±0.01
3	HeY	0.88±0.11	1±0	0.87±0.05	0.83±0.03	0.22±0.01	0.34±0.03
4	KeL	1±0	1±0	0.96±0.02	0.9±0.04	0.22±0.01	0.32±0.01
5	MaK	1±0	1±0	0.8±0.04	0.75±0.01	0.24±0	0.32±0.01
6	Nuf	1±0	1±0	0.93±0.02	0.92±0.01	0.23±0	0.31±0
7	OlD	0.64±0.41	1±0	0.88±0.05	0.85±0.08	0.23±0.01	0.31±0.01
8	Pal	1±0	1±0	0.91±0.02	0.9±0.02	0.23±0	0.31±0
9	Pet	1±0	1±0	0.72±0.02	0.65±0.05	0.25±0	0.3±0
10	Que	1±0	1±0	0.78±0.09	0.7±0.11	0.25±0	0.31±0.02
11	Rös	1±0	1±0	0.97±0.04	0.95±0.04	0.2±0.02	0.32±0.01
12	SUP	0.92±0.18	1±0	0.7±0.07	0.63±0.09	0.25±0	0.3±0.01
13	SpB	0.76±0.17	1±0	0.9±0.06	0.85±0.08	0.21±0.03	0.31±0.01
14	Tec	1±0	1±0	0.98±0.03	0.95±0.05	0.2±0.02	0.31±0

Table 5-8: Results of PLS-DA of 26 samples with 5 SEM images taken per sample at 250x magnification and each image is subdivided into 5 ROI (Values x 100 %).

Samples	Facilities	Sensitivity Cal	Sensitivity CV	Specificity Cal	Specificity CV	RMSEC	RMSECV
1	All	0.96±0.09	1±0	0.84±0.03	1±0	0.18±0	0.21±0
2	Atl	0.96±0.09	1±0	0.9±0.09	1±0	0.18±0	0.22±0
3	ChH	0.96±0.09	1±0	0.87±0.02	1±0	0.18±0	0.22±0
4	Con	0.88±0.11	1±0	0.82±0.08	1±0	0.18±0	0.21±0
5	Dak	1±0	1±0	0.81±0.03	1±0	0.18±0	0.21±0
6	ES2	1±0	1±0	0.93±0.02	1±0	0.17±0	0.22±0
7	ESI	1±0	1±0	0.86±0.04	1±0	0.18±0.01	0.22±0
8	ElD	0.72±0.11	1±0	0.8±0.02	1±0	0.18±0	0.21±0
9	FAP	1±0	1±0	0.83±0.05	1±0	0.18±0	0.21±0
10	HeY	1±0	1±0	0.92±0.04	1±0	0.17±0	0.22±0
11	KeL	1±0	1±0	0.98±0.02	1±0	0.17±0	0.22±0
12	MaK	0.92±0.11	1±0	0.77±0.04	1±0	0.19±0	0.21±0
13	Mul	0.96±0.09	1±0	0.83±0.05	1±0	0.18±0	0.21±0
14	Nuf	1±0	1±0	0.95±0.01	1±0	0.17±0	0.22±0
15	OlD	1±0	1±0	0.9±0.03	1±0	0.18±0	0.21±0
16	Pal	1±0	1±0	0.93±0.02	1±0	0.17±0	0.22±0
17	Pet	0.96±0.09	1±0	0.78±0.06	1±0	0.18±0	0.21±0
18	Que	1±0	1±0	0.88±0.05	1±0	0.18±0	0.21±0
19	RaL	0.96±0.09	1±0	0.76±0.08	1±0	0.18±0	0.21±0
20	Ran	1±0	1±0	0.85±0.02	1±0	0.18±0	0.22±0
21	Rös	0.92±0.11	1±0	0.84±0.03	1±0	0.18±0	0.21±0
22	SUP	0.96±0.09	1±0	0.77±0.08	1±0	0.18±0	0.21±0
23	Som	0.96±0.09	1±0	0.94±0.02	1±0	0.17±0	0.22±0
24	SpB	1±0	1±0	0.93±0.02	1±0	0.17±0	0.22±0.01
25	Tec	1±0	1±0	0.91±0.04	1±0	0.17±0	0.22±0
26	UnN	0.92±0.18	1±0	0.9±0.05	1±0	0.17±0.01	0.22±0

Table 5-9: Results of PLS-DA of 14 samples with 5 SEM images taken per sample at 250x magnification and each image is subdivided into 5 ROI (Values x 100 %).

Samples	Facilities	Sensitivity Cal	Sensitivity CV	Specificity Cal	Specificity CV	RMSEC	RMSECV
1	Atl	1±0	1±0	0.93±0.08	0.89±0.09	0.21±0.01	0.32±0.01
2	FAP	1±0	1±0	0.84±0.04	0.74±0.07	0.24±0.01	0.31±0
3	HeY	0.96±0.09	1±0	0.92±0.01	0.85±0.05	0.23±0.01	0.35±0.02
4	KeL	1±0	1±0	0.99±0.01	0.95±0.07	0.2±0	0.32±0.01
5	MaK	0.92±0.11	1±0	0.78±0.02	0.7±0.09	0.24±0	0.31±0.01
6	Nuf	1±0	1±0	0.94±0.01	0.93±0.02	0.21±0.01	0.32±0.01
7	OlD	0.92±0.11	1±0	0.84±0.12	0.78±0.14	0.23±0.02	0.32±0.02
8	Pal	1±0	1±0	0.93±0.01	0.92±0.01	0.22±0.01	0.32±0
9	Pet	1±0	1±0	0.78±0.05	0.73±0.06	0.24±0.01	0.31±0.01
10	Que	1±0	1±0	0.83±0.04	0.77±0.07	0.23±0.01	0.31±0
11	Rös	1±0	1±0	0.92±0.04	0.86±0.05	0.21±0.03	0.34±0.04
12	SUP	0.96±0.09	1±0	0.73±0.1	0.62±0.1	0.24±0.01	0.31±0.02
13	SpB	1±0	1±0	0.94±0.01	0.9±0.02	0.18±0.02	0.31±0.01
14	Tec	1±0	1±0	0.88±0.05	0.85±0.04	0.23±0.01	0.31±0

5.11 Summary and suggested areas for future study

In this chapter, the concept of morphology as a possible signature for UOCs for nuclear forensic purposes had been explored in three main areas, using only SEM. Firstly, a qualitative approach including taking SEM images at various magnifications was proposed. Next, a more quantitative and novel approach was undertaken. A small quantity of sample was dispersed in ethanol for size and shape characterization. Lastly, image texture of samples was carried out using AMT algorithm. PCA and PLS-DA analyses were used to evaluate the data. The main highlights of this study and possible future work is defined as follow.

- The grinding and mixing of small quantity of UOC sample in ethanol was found to be the optimum method for dispersing particles, among the different methods that were tested.
- Such sample preparation has the potential to be reproducible but as the method cannot be readily standardized (in terms of representative sampling, weighing an extremely low amount of sample, obtaining a homogenous suspension and counting the same number of particles in each image), there should be more preparation per sample to increase the confidence in the data.
- Two UOC samples were compared and differences in their sizes but not their shapes were detected. 26 samples were evaluated globally with PCA, which also revealed the relationship between size and shape descriptors that are often related.
- Due to the lack of a standard sized yellow cake reference material, it is not possible to validate the method. Alternatively, a 2nd technique should also be used to investigate the sizes and shapes of the UOC samples. However, SEM is the only instrument that can provide both of such information simultaneously.
- The image texture of UOCs is a promising signature to differentiate the origin of the samples. Each SEM image (magnifications of 1000x and 250x) was sub-divided into five ROIs (s1-s5) and analysed with both PCA and PLS-DA. Besides analysing 26 different UOC samples, 14 of those black coloured samples were also analysed as a separate group.
- PCA score plots of the data showed that different regions of the sample are reproducible (i.e. texture is homogenous) as the positions of the MA data (obtained from SEM images) are reproducible for all the samples. These apply for both magnifications and for both data sets (26 samples and 14 samples).
- PLS-DA provided a quantitative mean of evaluating the prediction of each of these samples by the model. The results were expressed as sensitivity and specificity and are generally good. At a lower magnification of 250x compared to 1000x, the PLS-DA values were better than the latter. At 250x magnification, the textures of the samples are more related to their bulk properties whereas at 1000x, the textures are more related to the grain sizes.

- Samples common to both group of datasets, that were, the 14 oxide samples, were better predicted in the larger dataset (26 samples) compared to the model based on the 14 samples.
- Future work can include using even lower magnification (<250x) with SEM or the use of less expensive optical microscope for image texture analysis.

6. Conclusions

Three broad scientific goals were identified in Chapter 1 for studying, in particular UOCs, for nuclear forensic purposes. The goals were constructed based on exploring or developing new signatures to complement current signatures, in a multi-faceted analytical field.

Firstly, the goal of correlating morphology of UOC with production process was partially fulfilled through the preparation of five different compositions of yellow cakes in the laboratory (Chapter 3). Although many industrial samples were already available in the laboratory, it was not straightforward to correlate the observed morphology with their known processes as many steps and reagents were typically involved. By keeping only to the precipitation step in the laboratory, the differences in the observed morphologies using SEM are directly related to the use of different precipitating reagents. All the five materials were also characterized by several other techniques. Three materials were selected and calcined up till temperatures of 800 ^{o}C and in all cases, the morphology (shape and appearance) of the starting material was retained throughout the heat treatment. Therefore, an important link has been established. It is possible to obtain information about the processing history of the material based on its morphology.

It has also been established that changing the pH or temperature of the precipitation reaction did not affect the appearance (in particular, shape) of the particles. However, there could be notable differences in the sizes or particle size distribution when such conditions are varied. In Chapter 5, a sample preparation method was developed in view of the need to study sizes and shapes of particles using SEM. While this method showed promising results, it needed to be validated or improved further. It was not possible to determine whether this method could pick up size difference(s), if any between two materials, produced with exact conditions but with only one parameter varied between them.

The above mentioned was part of the next goal to systematically investigate morphology of UOCs as signatures for nuclear forensics. The method of dispersing particles in ethanol was applied to industrial UOCs and it appeared that samples could be distinguished based on size and shape attributes. However, as the method cannot be standardized, more sample preparation should be repeated and a 2nd technique should be considered for complementary reasons.

Another morphological aspect involved texture image analysis applied to UOCs using AMT algorithm. 26 UOCs samples were analysed using SEM at 1000x and 250x magnification. Their images were transformed into MA numeric data and subsequently evaluated by PCA and PLS-DA. Results were extremely encouraging and strongly suggested that different UOC samples could be differentiated by their image texture. Image texture is therefore potentially a useful fingerprint, for origin assessment.

The information provided by Raman spectroscopy was fully exploited and the final goal of this work was achieved. Raman spectra obtained from yellow cakes were interpreted and impurities

related to their processing history were also identified. Spectra of different compositions of UOCs were analysed by PCA and the results are largely promising. Different types of yellow cakes can be discerned based on their spectra. Three different Raman spectrometers were also evaluated for measuring selected compounds. Besides bulk analysis of the powder samples, Raman spectroscopy was also applied to analysis of particles and comparisons were made between the two analyses. Raman particle analysis is interesting as the application is useful not just for nuclear forensics, but it is also relevant for nuclear safeguards. In general, the spectra produced by particle analysis were also reproducible (in terms of the peak positions).

Appendix A

Supplementary information for Chapter 1

In Chapter 1, the concepts and the state-of-art of nuclear forensics have been introduced. The production of various nuclear materials from the uranium fuel cycle has also been delineated. This section outlines research that has been carried out on certain nuclear materials (not irradiated in a nuclear reactor), largely for the purposes of reactor fuel production. The list of references compiled in this section is certainly not exhaustive.

Ammonium Diuranates

There has been a long controversy over the composition and structure of ammonium uranates/diuranates [121, 164-168]. Known for its complexity, it has been sufficiently demonstrated that the composition $(NH_4)_2U_2O_7$ does not exist even in the presence of excess ammonia. Hence, the term "ammonium diuranate" is a misnomer although it is still commonly used. In the studies reported by Cordfunke [164], he concluded that the ternary system of NH_3-UO_3-H_2O (aqueous solution at 40 ^oC) resulted in the following distinct compounds and each of them having its own X-ray diffraction pattern.

$UO_3.2H_2O$ designated as (I) NH_3: U molar ratio of 0.00

$3UO_3.NH_3.5H_2O$ designated as (II) NH_3: U molar ratio of 0.33

$2UO_3.NH_3.3H_2O$ designated as (III) NH_3: U molar ratio of 0.50

$3UO_3.2NH_3.4H_2O$ designated as (IV) NH_3: U molar ratio of 0.66

In the studies done by Stuart and Whateley [167], the authors maintained that the ammonium uranate system is homogenous and continuous with the composition shown below:

$$UO_2(OH)_{2-x}(O^-NH_4^+)_x$$

And x varies from 0 to 0.7.

The discrepancies have been attributed to the different methods of preparation of material. The presence or absence of equilibrium and possible hydrolysis due to washing would affect the final products. Equilibrium as reflected by the pH values of the system was established after several weeks or months. In Stuart's and Whateley's study, ammonium uranates were obtained by either equilibrating β-$UO_3.2H_2O$ with NH_4OH or by adding NH_4OH solution to uranyl nitrate solution. In the study done by Cordfunke, UO_3, water and ammonia were equilibrated. He reported that products made from the reaction of uranyl nitrate and ammonia resulted in the compound I (pH 3.5), II (pH 4-

7) and III (pH > 7) that could not be isolated in the pure form due to the presence of nitrate. He concluded that such studies done by several others did not give a true picture of ammonium uranates. It has also been highlighted that different types of $UO_3.2H_2O$ exist and would naturally influence the final structure with respect to the replacement of water by ammonia.

To add further to the controversy, the manner in which ammonia was bonded has also become questionable. In the report by Hermans and Markenstein [165], the strong resemblance of the three products (α, β, γ) and $UO_3.2H_2O$ led to the suggestion that water was replaced by ammonia as NH_3 and not NH_4^+. The work of Stuart's and Whateley's indicated otherwise and that the incorporation of ammonia took place via a cationic exchange. It is noteworthy that NH_4OH was used to prepare ammonium uranates. The absence of NH_3 deformation bands from infrared spectroscopy led to the deduction that NH_4^+ was present. The variation of the uranyl ion asymmetric stretch frequency with the NH_3: U molar ratio and the absence of two bands emphasized the fact that the ammonium uranate system was homogenous and continuous. The XRD pattern of a mixture of two separate ammonium uranate was also found to be different from that of a continuous system with the same molar ratio. Cordfunke concurred that ammonia was bonded as ammonium ions.

Subsequently, it was contested by Urbanek *et al* that uranates were not formed simply by the following mechanism [168]

$$UO_2(OH)_2 + xNH_4^+ \leftrightarrow UO_2(OH)_{2-x}(O^-NH_4^+)_x + xH^+ \quad \text{(A-1)}$$

but rather through the following mechanism

$$HO[UO_2(OH)_2UO_2]OH + xNH_4^+ \leftrightarrow HO[UO_2(OH)_{2-x}(O^-NH_4^+)_xUO_2]OH + xH^+ \quad \text{(A-2)}$$

In their work involving IR spectroscopy, they deduced that the precipitates formed at a lower pH from solution containing incompletely precipitated uranium would result in ammonia bonded as NH_4^+ and NH_3. At higher pH, ammonia is bonded purely in the form of NH_4^+. At lower pH, NH_3 would replace the coordinated water molecules in the complex $[HOUO_2(OH)_2UO_2OH].2H_2O$ as well as the exchange shown above. As the pH continued to rise, the spatial conditions and the distribution of electric charge around the large NH_4^+ would exclude both H_2O and NH_3.

Table A-1: Summary of literature information pertaining to different aspects of studies involving ADU.

Year, Author, Country	Studies	Techniques
1962, Cordfunke (The Netherlands)	Composition	Chemical analysis, XRD [164]
1963, Debets & Loopstra (The Netherlands)	Composition, crystalline structure	XRD [121]
1964, DOI & ITO (Japan)	Properties of ADU on UO_2	Optical & electron microscopy, sedimentation analysis, surface area by BET[16] [93]
1969, Stuart & Whateley (Australia)	Composition	Infrared (IR), XRD [167]
1970, Cordfunke (The Netherlands)	Composition	IR [166]
1972, Janov *et al* (Australia)	Properties of ADU (1-stage/ 2-stage precipitation, pH) on properties of UO_2	Surface area by BET, filterability, electron microscopy [94]
1972, Stuart & Miller (Australia)	Composition	IR [169]
1973, Price & Stuart (Australia)	Thermal decomposition	IR, TG/DTA [128]
1974, Steepper & Zink (USA)	Particle size distribution	Andreasen pipet-sedimentation technique [170]
1978, Woolfrey (Australia)	Properties of ADU affecting decomposition and the influence on UO_2 properties	XRD, thermal decomposition [96]
1978, Urbanek *et al* (Czechoslovak)	Formation and composition	IR, chemical analysis [168]
1982, El-Fekey *et al* (Egypt)	Thermal decomposition of AU prepared/calcined under different conditions, kinetics of decomposition	TG/DTA, BET, XRD [129]
1983, El-Fekey *et al* (Egypt)	Thermal decomposition of AU prepared from nitrate and sulphate solutions, kinetics of thermal decomposition, effect of thickness on decomposition	TG/DTA, XRD [130]
1985, Sato *et al* (Japan)	Thermal decomposition	TG/DTG, IR, XRD [131]
1996, Rajagopal *et al* (India)	Particle size analysis on AU and U_3O_8 produced by homogenous vs conventional methods	Particle size analyser, SEM [97]
2000, Rajagopal *et al* (India)	Thermal studies on AU produced by homogenous vs conventional methods	TG/DTA, XRD [132]
2001, Murty *et al* (India)	Influence of temperature of precipitation on agglomeration & powder characteristics	Manual determination of settling characteristics [171]
2012, Manna *et al* (India)	Monitoring crystal growth & morphology of ADU at different stages of precipitation	SEM, TEM, XRD, particle size analyser [98]
2012, Manna *et al* (India)	Effect of calcination temperature on properties of uranium oxides	BET, XRD, SEM [172]

[16] Brunauer, Emmett and Teller

Ammonium uranyl carbonate

Although this yellow cake was not mentioned in Chapter 1, the conversion of UO_2 via ammonium uranyl carbonate has been practiced by KWU and RBU. It was initiated in the sixties by NUKEM in Germany [99, 103, 105]. The advantages of the conversion to UO_2 via AUC over other ore concentrates have been well documented. The AUC process is associated with lower fluorine contents which makes it more amenable for further processing than ammonium uranate [115, 135]. Besides, owing to the free flowing nature of AUC powder, direct pelletizing without the need for granulation simplifies the process [99, 103]. Subsequently, the resulting UO_2 also possesses better reactivity and powder characteristics for the production of reactor elements [115]. The powder is further pressed into green pellet without the use of lubricants, additives or poreformers [103, 135].

Following the production of crude uranium hydroxides, peroxides, uranates and other uranyl salts, AUC can be formed via two stage process. First, the crude products are dissolved in dilute ammonium carbonate to form $[UO_2(CO_3)]^{4-}$. Next, ammonium carbonate is added as a precipitating agent to form AUC [12].

It has been proposed that the AUC precipitation process using gaseous carbon dioxide and ammonia are more advantages than the addition of ammonium carbonate [105] but it is not known if this method is used industrially [104]. Unlike ADU, AUC is a stoichiometric compound and its crystals are known to be monoclinic [12, 115]. Infrared and XRD of AUC [103, 115] as well as TGA/DTG studies have been reported [99, 104, 135, 137].

Table A-2: Summary of literature information pertaining to different aspects of studies involving AUC.

Year, Author, Country	Studies	Techniques
1975, Bachmann *et al* (Germany & USA)	Heat of decomposition, molecular heat capacity, refinement of XRD data, thermal analysis	Chemical analysis, XRD, TG/DTA [122]
1981, Pan *et al* (Taiwan)	Varied conditions for the precipitation of AUC & investigation of the powder properties of UO_2 & comparison to the ADU process	SEM, sieve analysis, BET, TG/DTA, single crystal XRD, chemical analysis [99]
1985, Hälldahl & Nygren (Sweden)	Thermal analysis in various atmospheres	TG/DTA, XRD [135]
1988, Choi *et al* (South Korea)	Properties of AUC on UO_2	XRD, BET, immersion method, sedimentation [100]
1991, Lee & Wu (Taiwan)	Quasi-optimization of the AUC process	SEM, TG/DTA, XRD [136]
1993, Rofail (Egypt)	Precipitation studies	IR & XRD [115]
1994, Kim *et al* (South Korea)	Thermal decomposition & kinetics	TG/DTA, particle size analyser, SEM [137]
1996, Tel & Eral (Turkey)	Production conditions & powder properties	Chemical analysis, IR, TG/DTA, sieve & sedimentation, single crystal XRD [103]
2001, Govindan *et al* (India)	Comparative study with ADU	TG/DTA, EGA-MS[17], XRD [104]
2007, Mellah *et al* (Algeria)	Thermodynamic & kinetic investigations of precipitation	UV spectrophotometry, SEM, BET, particle size analyser, XRD, pycnometry [105]

Uranyl peroxide

The use of H_2O_2 as a precipitant results in a high purity product of uranyl peroxide as a yellow cake. Its advantages over ammonia precipitation have been mentioned in Chapter 1. The natural form of this compound, exist in nature as minerals albeit being rare and unusual. Known structurally or chemically as $[UO_2(O_2).2H_2O](2H_2O)$, $UO_2(O_2).4H_2O$ or $UO_4.4H_2O$, studtite and its dehydration product, metastudtite represented as $UO_2(O_2).2H_2O$ or $UO_4.2H_2O$ have been known and these compounds have drawn much attention, owing to the fact they are the only known naturally occurring peroxide-containing minerals [117, 125, 127]. Besides, it has been reported that these minerals are formed on spent nuclear fuel when stored in a disposal repository through the incorporation of peroxide that is formed by the alpha radiolysis of water [45, 117, 125].

It has also been reported that $UO_4.4H_2O$ is obtained when the synthesis is carried out at temperatures below 50 °C whereas $UO_4.2H_2O$ is obtained above 70 °C and a mixture of both hydrates

[17] Evolved gas analysis-mass spectrometry

exists at 60 °C (4). The dihydrate is also obtained by drying the tetrahydrate in air at 100 °C or in vacuo at room temperature for at least 24 hours [173]. This conversion is irreversible [126].

IR [173] and Raman [117] of both the compounds have been reported. The IR measurements revealed that the chemical bonding of H_2O groups with uranyl group is different in both the hydrates. An alternative formula of $UO_3.H_2O_2.H_2O$ was once postulated based on decomposition studies that H_2O_2 was lost between 90 °C and 180 °C which led to the formation of $UO_3.H_2O$ [174, 175]. The existence of another peroxide, U_2O_7 between the temperature range 90 and 195 °C appeared evident from the decomposition of $UO_4.2H_2O$ [175]. However, the decomposition studies carried out by Sato had ruled out both the above [138]. The structure of studtite has been determined to be monoclinic with a space group of C2/c [125] while that of metastudtite, orthorhombic and Immm [127].

Table A-3: Summary of literature information pertaining to different aspects of studies involving UO_4.

Year, Author, Country	**Studies**	**Techniques**
1957, Boggs (USA)	Thermal decomposition of $UO_4.2H_2O$	Weight loss [175]
1961, Taichi (Japan)	Thermal decomposition of $UO_4.2H_2O$	TG/DTA, XRD, IR [174]
1962, Debets (The Netherlands)	XRD of two peroxides	XRD [124]
1963, Taichi (Japan)	Varying conditions of preparation of peroxides	Loss in weight on ignition, TG, XRD, IR [173]
1963, Cordfunke and Giessen (The Netherlands)	Pseudomorphic decomposition of uranium peroxide into UO_3	Electron microscope, electron diffraction [176]
1974, Walenta (Germany)	Composition of studtite	Electron microprobe, XRD, Optical properties [126]
1976, Taichi (Japan)	Thermal decomposition of two peroxides	TG/DTA, XRD, IR [138]
1983, Deliens and Piret (Belgium)	Composition of metastudtite	Electron microprobe, XRD [127]
1990, Cahill and Burkhart (USA)	Varying processes for the precipitation of peroxide	SEM, XRD [13]
2003, Burns and Hughes (USA)	Crystallography of studtite	Refinement [125]
2004, Gupta *et al* (India)	Varying conditions for precipitation of peroxide	Recovery/yield [120]
2004, Bastians *et al* (UK)	studtite and metastudtite	IR and Raman, TGA, DSC (studtite) [117]
2005, Morais *et al* (Brazil)	precipitation of uranium peroxide	[177]
2011, Kim *et al* (Korea)	Behaviour of precipitation based on varying conditions of uranyl and H_2O_2 solutions	UV-VIS spectrophotometry, particle size analyser, SEM, TEM [45]
2012, Weck *et al* (USA)	Structures of studtite and metastudtite	Density functional theory [178]

The oxides of uranium

Figure A-1 shows the phase diagram of the different forms of U-O. In the context of this work, only the oxides that relevant to yellow cakes are collectively discussed.

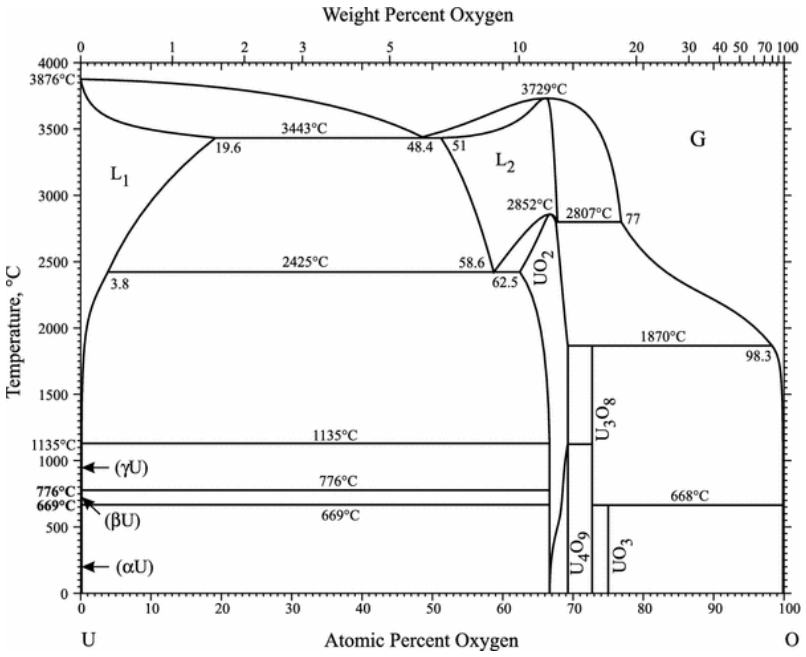

Figure A-1: Phase diagram of U-O [179]

As intermediates and pre-cursors of uranium dioxide, different types of uranium oxides, in particular uranium tri-oxide has also been studied. At least five different crystalline phases of UO_3 (α, β, γ, δ, ε) and an amorphous phase have been reported [180]. Closely related hydrated uranium (IV) oxides such as uranyl hydroxide, $UO_2(OH)_2$ or $UO_3.H_2O$ is in fact, one of the different compositions of uranium ore concentrates. Schoepite, $UO_3.2.25H_2O$ is known to exist as a mineral.

Table A-4: Summary of literature information pertaining to different aspects of studies involving different oxides of uranium.

Year, Author, Country	**Studies**	**Techniques**
1961, Clayton and Aronson (USA)	Different preparation of UO_2 powder and their characterisation	Titration, XRD, BET and Innes methods, air permeability methods, air sedimentation, microscopy [101]
1961, Hoekstra and Siegel (USA)	Preparation and characterization of six different phases of UO_3	IR, XRD, calorimetry, chemical analysis [180]
1961, Deane (USA)	Characterization of hydrated UO_3	IR [181]
1963, Wheeler *et al* (USA)	Preparation and characterization different phases of UO_3	TG/DTA, XRD, IR [182]
1964, Cordfunke and Debets (The Netherlands)	Preparation of ε-$UO_3.H_2O$	XRD, DTA [183]
1967, Cordfunke and Giessen (The Netherlands)	Different preparation and characterization of UO_2	Density measurements, microscopy [95]
1971, Taylor (Australia)	Structure of α-$UO_2(OH)_2$	XRD, structure analysis [184]
1988, Glodeanu *et al* (Romania)	Correlating UO_2 powder and pellet quality	[185]
1994, Allen and Holmes (UK)	Characterization of binary uranium oxides	IR [186]
2011, Nipruk *et al* (Russia)	Preparation and characterisation of $UO_3.nH_2O$	XRD, IR, DSC [119]
2013, Sweet *et al* (USA)	Preparation of different polymorphs of UO_3	XRD, Raman, Fluorescence spectroscopy [187]

Appendix B

Supplementary information for Chapter 2

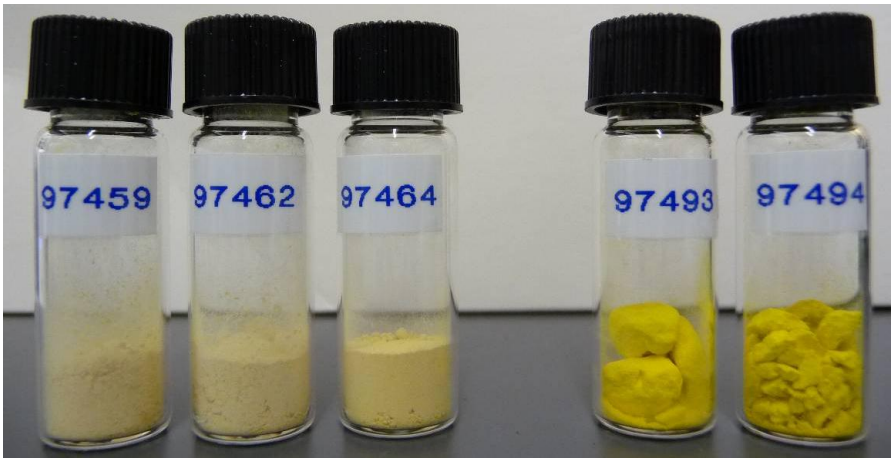

Figure B-1: (left to right) 97459, 97462, 97464, 97493, 97494.

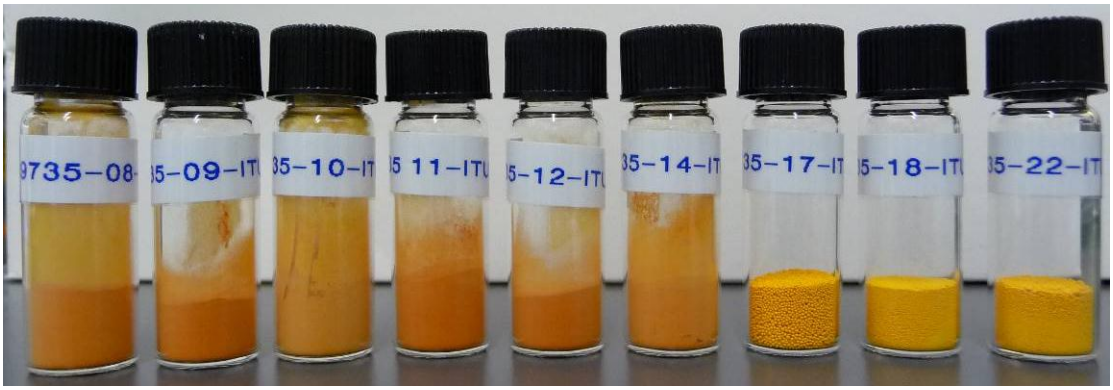

Figure B-2: (left to right) 9735-(08)-3, (09), (10), (11), (12), (14), (17), (18), (22).

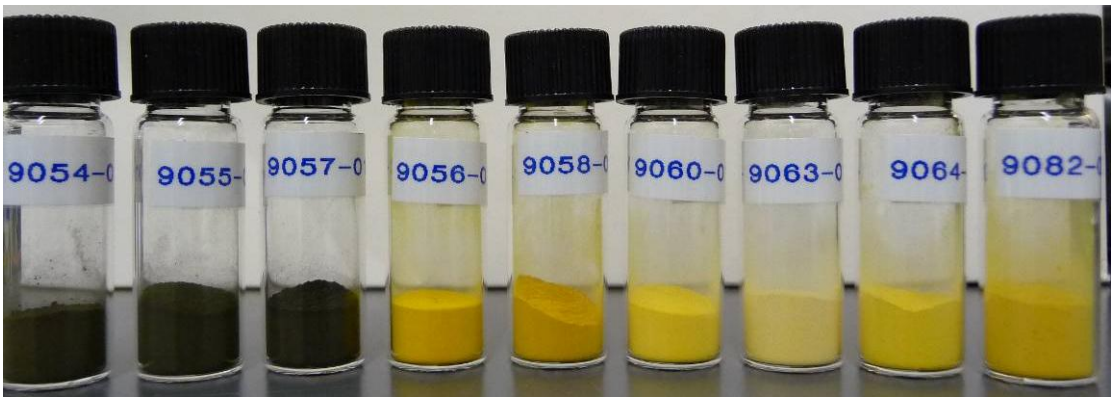

Figure B-3: (left to right) 90(54)-01-ITU, (55), (57), (56), (58), (60), (63), (64), (82).

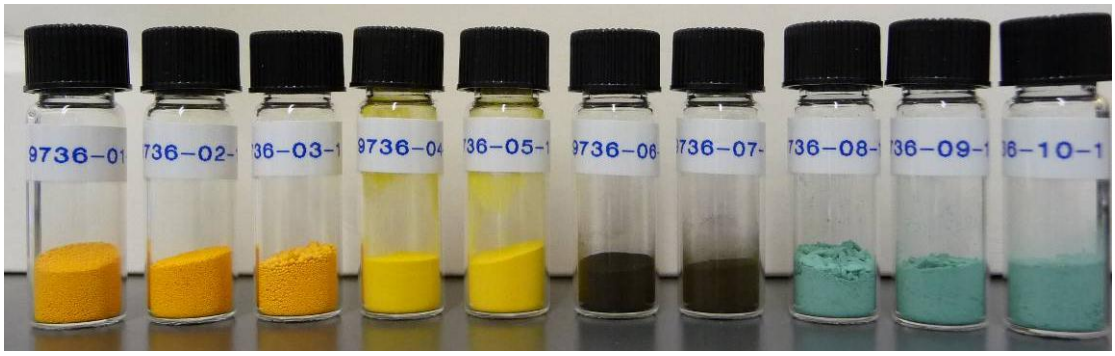

Figure B-4: (left to right) 9736-(01)-1, (02), (03), (04), (06), (07), (08), (09), (10).

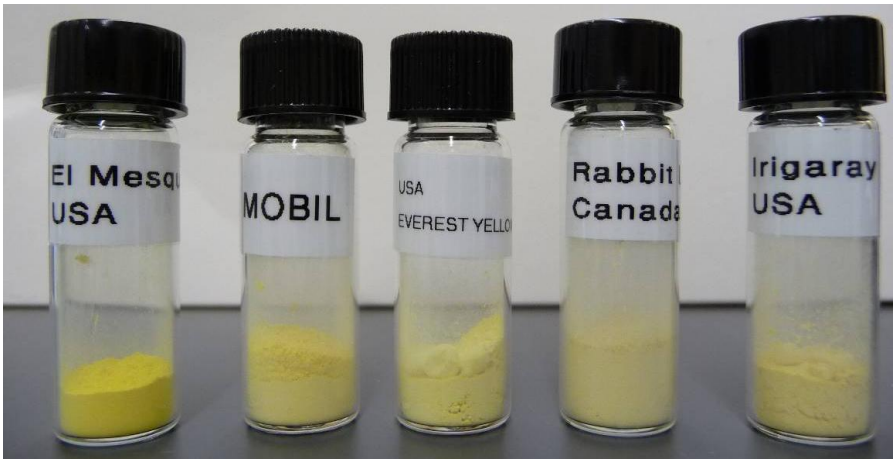

Figure B-5: (left to right) USA El Mesquite, USA Mobil, USA Everest Yellow, Canada Rabbit Lake, USA Irigaray.

Figure B-6: (left to right) Gabon (Efi) Mouand, Brazil Nuclebras, USA Dawn, Holland Delft, USA United Uranium, USA Mulberry (IMC), Australia South Alligator, Canada North Span, Canada Stanrock.

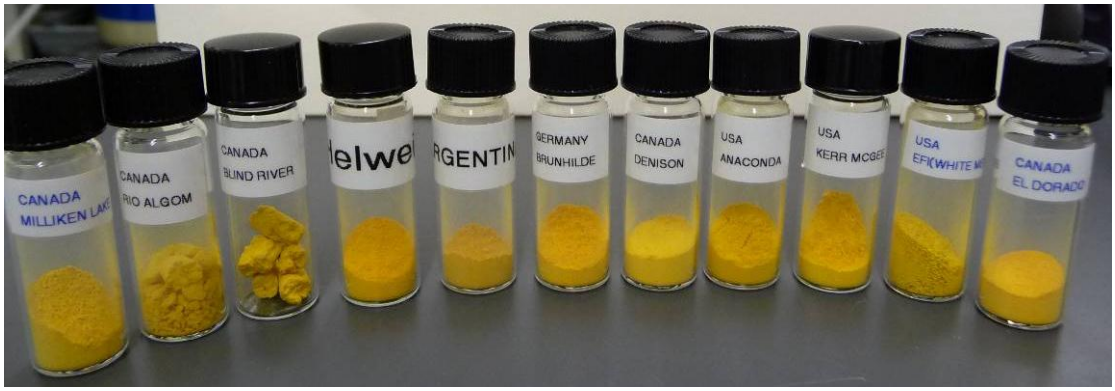

Figure B-7: (left to right) Canada Milliken Lake, Canada Rio Algom, Canada Blind River, Germany Ellweiler, Argentina (mine not specified), Germany Brunhilde, Canada Dension, USA Anaconda, USA Kerr McGee, USA Efi (White Messa), Canada El Dorado.

Figure B-8: (left to right) Sweden Ranstad, South Africa Somair, USA Sesquehan, Yugoslavia Rudnik.

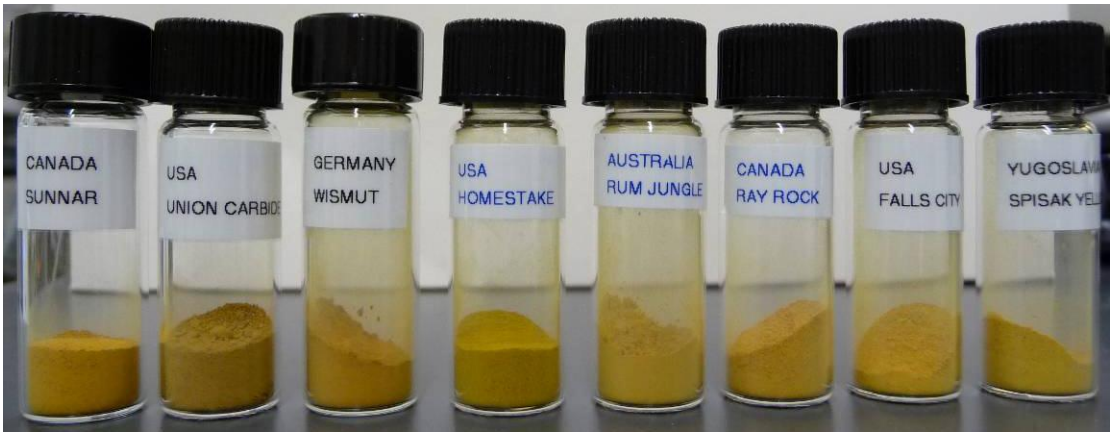

Figure B-9: (left to right) Canada Gunnair, USA Union Carbide, Germany Wismut, USA Homestake, Australia Rum Jungle, Canada Ray Rock, USA Falls City, Yugoslavia Spisak Yellow.

Figure B-10: (left to right) Spain Jen, Belgian Congo, Canada Stanleigh, Canada Macassa, USA Yankee Yellow, Canada Dyno, USA Cotter, Australia Radium Hill.

Figure B-11: (left to right) USA South Dakota, Canada ESI, USA Utah, USA United Nuclear, USA Lucky McGill, USA Everest Black, England Wheal Edward, Zambia Mindola.

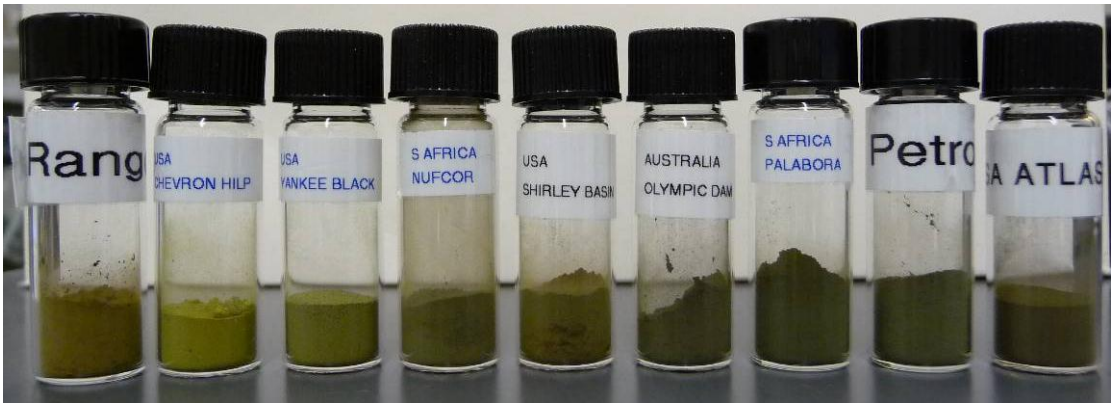

Figure B-12: (left to right) Australia Ranger, USA Chevron Hill, USA Yankee Black, South Africa Nufcor, USA Shirley Basin, Australia Olympic Dam, South Africa Palabora, USA Petromic, USA Atlas.

Figure B-13: (left to right) USA Federal American Partners, Russia Techsnab, China Heng Yang, Yugoslavia Spisak Black, Australia Queensland, Australia Mary Kathleen, South Africa Rossing, Canada Keylake.

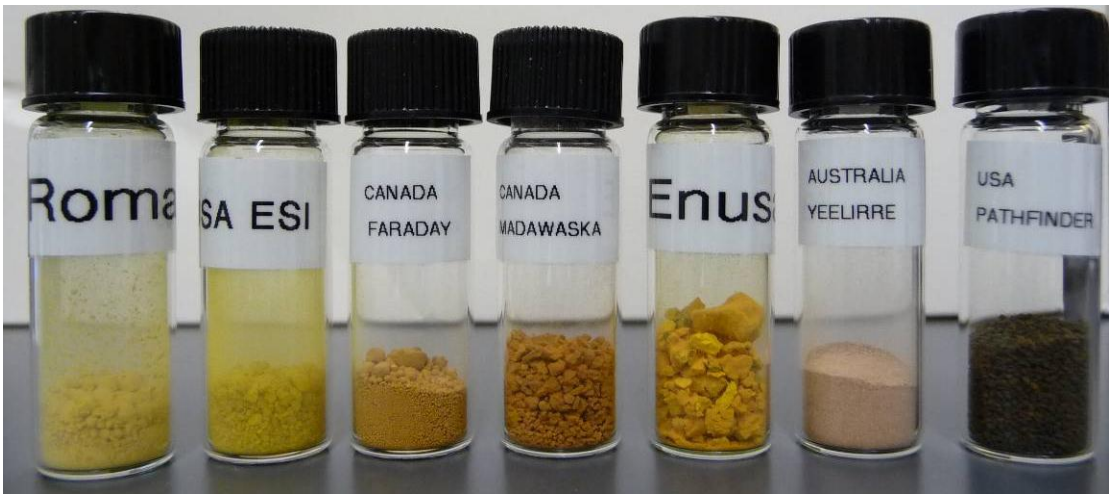

Figure B-14: (left to right) Romania, USA ESI, Canada Faraday, Canada Madawaska, Spain Enusa, Australia Yeelirre, USA Pathfinder.

Table B-1: Overview of samples and the techniques that had been used to make measurements (marked as 1).

Sample name	Composition	T64000 (ITU)	Senterra (INE)	Hand-held Raman (IAEA)	Raman-SEM (CEA)	Infrared	Scanning electron microscopy		
							General morphology	Size	Texture
Springfield									
Australia Rum Jungle	ADU		1	1					
Australia Yeelirre	not typical YC			1					
England Wheal Edward				1					
Mozambique Maruzi	not known								
Portugal (unspecified mine)	not known		1						
USA Everest Black	ADU + oxides		1	1					
USA Falls City	ADU + oxides		1	1					
USA Mulberry(IMC)	ADU		1	1			1	1	1
USA Shirley Basin	SDU + oxides		1	1	1				
Australia Ranger	ADU	1	1	1		1			
Australia Radium Hill	ADU	1	1	1					
Brazil Nuclebras	ADU	1	1	1			1		
Canada El Dorado	ADU	1	1	1				1	1
Canada Milliken Lake	ADU	1	1	1					
Canada Stanleigh	ADU	1	1	1			1		
Canada Denison	ADU	1	1	1	1				
Canada Rio Algom	ADU	1	1	1					
Canada Stanrock	ADU	1	1	1	1				
Gabon EFI(Mouand)	ADU	1	1	1					
Germany Brunhilde	ADU	1	1	1	1				
Germany Ellweiler	ADU	1	1	1	1				
Germany Wismut	ADU	1	1	1					
Holland Delft	ADU	1	1	1					
Spain Enusa	ADU	1	1	1					
Spain Gen	ADU	1	1	1					
USA Cotter	ADU	1	1	1			1		
USA Dawn	ADU	1	1	1	1				
USA Homestake	ADU	1	1	1					
USA Utah	ADU		1	1					
USA Anaconda	ADU	1	1	1			1		
USA Efi(White Messa)	ADU	1	1	1					
USA ESI	ADU		1	1			1	1	1
USA Kerr McGee	ADU	1	1	1					

Table B-1 continued

Sample name	Composition	T64000	Senterra	Hand-held	inVia	Infrared	Morphology	Size	Texture
USA Lucky McGill	ADU	1	1	1					
USA United Nuclear	ADU	1	1	1				1	1
Yogoslavia Rudnik	ADU	1	1	1					
Yogoslavia Spisak Yellow	ADU	1	1	1					
Russia Techsnab	ADU + oxide		1	1	1			1	1
USA Chevron Hill	ADU + oxide	1	1	1	1		1	1	1
USA Yankee Black	ADU + U_3O_8 + oxide		1	1					
Australia South Alligator	Hydroxide	1	1	1			1	1	1
Belgian Congo	Hydroxide	1	1	1				1	1
Canada Faraday	Hydroxide		1	1					
Canada North Span	Hydroxide	1	1	1	1				
Canada Ray Rock	Hydroxide		1	1					
Canada Blind river	Hydroxide	1	1	1					
Canada Dyno	Hydroxide		1	1					
Canada Macassa	Hydroxide	1	1	1					
Canada Gunnair	Hydroxide		1	1					
USA Sesquehanna	Hydroxide		1	1	1				
USA Pathfinder	Hydroxide		1	1					
USA United Uranium	Hydroxide		1	1					
USA Petromic	mixed oxide	1	1	1				1	1
Yogoslavia Spisak Black	Hydroxide (possibly)		1	1			1	1	1
Australia Olympic Dam	Oxide		1	1	1			1	1
Canada Madawaska	Oxide		1	1					
USA Union Carbide	Oxide		1	1	1				
USA South Dakota	Oxide + hydroxide	1	1	1	1			1	1
Zambia Mindola	Oxide (possibly)		1	1					
Canada Eldore(Rabbit Lake)	Peroxide	1	1	1	1		1	1	1
Canada ESI	ADU		1	1	1		1	1	1
USA El Mesquite	Peroxide	1	1	1	1		1		
USA Everestr Yellow	Peroxide		1	1			1		
USA Irigaray	Peroxide	1	1	1			1		
USA Mobil	Peroxide	1	1	1			1		
Argentina (unspecified mine)	SDU		1	1	1		1		
Niger Somair	SDU	1	1	1				1	1
Romania	SDU	1	1	1					
Sweden Ranstadt	SDU	1	1	1	1		1	1	1
USA Yankee Yellow	SDU	1	1	1					

Table B-1 continued

Sample name	Composition	T64000	Senterra	Hand-held	inVia	Infrared	Morphology	Size	Texture
Australia Mary Kathleen	U_3O_8	1	1	1	1			1	1
Australia Queensland	U_3O_8		1	1				1	1
Canada Key Lake	U_3O_8		1	1			1	1	1
Namibia Rossing	U_3O_8	1	1	1			1	1	1
South Africa Nufcor	U_3O_8	1	1	1				1	1
South Africa Palabora	U_3O_8		1	1				1	1
USA Federal American Partners	U_3O_8		1	1				1	1
USA Atlas	U_3O_8 + oxide		1	1	1			1	1
China Hengyang	UO_2 + U_3O_8	1	1	1			1	1	1
Samples from IAEA									
9054-01-ITU	oxide		1	1		1			
9055-01-ITU	oxide			1					
9056-01-ITU	hydroxide		1	1		1			
9057-01-ITU	oxide		1	1		1			
9058-01-ITU	Mg diuranate		1	1		1			
9060-01-ITU	ADU		1	1		1			
9063-01-ITU	UO_4		1	1		1			
9064-01-ITU	ADU		1	1		1			
9082-01-ITU	UOC		1	1		1			
97459 (Beverly mine)	UO_4		1	1		1			
97462 (Beverly mine)	UO_4			1					
97464 (Beverly mine)	UO_4			1					
97493 (Ranger mine)	ADU			1					
97494 (Ranger mine)	ADU		1	1		1			
11387-02-3	AUC		1			1			
11387-04-3	AUC		1			1			
samples from Blind River and Port Hope									
9736-01-1 (Port Hope)	UO_3		1	1		1	1		
9736-02-1 (Port Hope)	UO_3			1					
9736-03-1 (Port Hope)	UO_3			1					
9736-04-1 (Port Hope)	UO_3		1	1		1			
9736-05-1 (Port Hope)	UO_3			1					
9736-08-1 (Port Hope)	UF_4			1					
9736-09-1 (Port Hope)	UF_4			1			1		

Table B-1 continued

Sample name	Composition	T64000	Senterra	Hand-held	inVia	Infrared	Morphology	Size	Texture
9736-10-1 (Port Hope)	UF_4			1					
9736-06-1 (Port Hope)	UO_2	1	1	1		1			
9736-07-1 (Port Hope)	UO_2			1					
9736-08_1 (Port Hope)	UF_4		1			1			
9736-12_1 (Port Hope)	UF_4		1			1			
9735-01-ITU/3 (Blind River)	UOC (U_3O_8) feed		1			1			
9735-03-ITU/3 (Blind River)			1			1			
9735-05-ITU/3 (Blind River)			1			1			
9735-07-ITU/3 (Blind River)			1			1			
9735-13-ITU/3 (Blind River)			1			1			
9735-15-ITU/3 (Blind River)			1			1			
9735-08-ITU/3 (Blind River)	UOC (uranium peroxide feed)		1	1		1			
9735-09-ITU/3 (Blind River)			1	1		1			
9735-10-ITU/3 (Blind River)			1	1		1			
9735-11-ITU/3 (Blind River)			1	1		1			
9735-12-ITU/3 (Blind River)				1					
9735-14-ITU/3 (Blind River)				1					
9735-17-ITU/3 (Blind River)	UO_3			1					
9735-18-ITU/3 (Blind River)	UO_3		1	1		1			
9735-20-ITU/3 (Blind River)	UO_3		1			1			
9735-22-ITU/3 (Blind River)	UO_3			1					
samples from South Uranium plant-Nufcor (from IAEA)									
12850-15	ore			1		1	1		
12850-02	leach			1					
12850-04	IX eluate			1					
12850-06	SX load			1					
12850-08	SX raffinate			1					
12850-12	ADU slurry			1		1	1		
12850-10	barrren liquor			1					
12851-05	feed ADU slurry			1		1	1		
12851-08	ADU powder			1		1	1		
12851-02	U_3O_8			1		1	1	1	1

Table B-1 continued

Sample name	Composition	T64000	Senterra	Hand-held	inVia	Infrared	Morphology	Size	Texture
Laboratory prepared UOC									
ADU_RT	ADU			1		1			
AUC_RT	AUC		1	1		1			
SDU_RT	SDU			1		1			
UP_RT	UO_4			1		1			
UH_RT	$UO_2(OH)_2$			1		1			
ADU_105°C	ADU		1			1			
AUC_105°C	AUC		1			1			
SDU_105°C	SDU		1			1			
UP_105°C	UO_4	1	1			1			
UH_105°C	$UO_2(OH)_2$		1			1			
Other samples (from ITU)									
UO_2 fuel pellet	UO_2	1	1	1					
UF_4	UF_4		1			1			
UO_2F_2	UO_2F_2		1			1			
	Total	49	114	126	20	47	27	26	26

Appendix C

Supplementary information for Chapter 3

High temperature and room temperature XRD studies on Batch I ADU

ADU that was prepared by drying at room temperature overnight was subjected to in-situ high temperature XRD studies, from 30 °C to 1000 °C [188]. The data was also compared to ex-situ XRD (room temperature XRD) performed on the same sample that had previously been heat treated at 150 °C, 400 °C, 600 °C, 800 °C and 1000 °C.

HT-XRD is reportedly carried out for the first time, for yellow cake and in particular ADU. It is investigated as a possible tool for nuclear forensic investigations, by studying the structural/compositional change in the material as a function of temperature. It has also been used in a complementary manner to TG/DTA, where the magnitude in mass loss as a function of temperature (also taken for the same temperature range of 30 ^{o}C to 1000 ^{o}C) provides additional information to the changes taking place. The comparison of in-situ XRD with ex-situ XRD of ADU is novel as well.

Figure C-1 illustrates such a comparison between the two. On the left, selected HT-XRD patterns representing ADU are reflected for 150 °C, 400 °C, 600 °C, 800 °C and 1000 °C. The sample was treated continuously from 30 ^{o}C to 1000 ^{o}C and the patterns were taken at the selected temperature. On the right, the room temperature XRD patterns are reflected for the same selected temperature. The difference was, the sample was removed at each temperature and subsequently cooled and stored at room temperature.

There were in general, stark differences between both patterns. At 150 ^{o}C corresponding to the on-going loss of water according to TG/DTA, some disorder was induced in the material as suggested by the broad peaks in pattern a. When the material was allowed to cool, a more defined pattern a' comparable to the starting material was observed. At 400 ^{o}C, the material was rather amorphous (pattern b) and the removal of ammonia was on-going. The cooled down version was depicted in pattern b' where some similarities to a' could be observed but with lower intensities and linewidths. At 600 ^{o}C, crystallization was almost abruptly observed by the appearance of sharp peaks in pattern c. This was readily attributed to U_3O_8 with an orthorhombic structure. The cooled down version (pattern c') fitted the pattern of β-UO_3 with a monoclinic structure after refinement. The patterns d and d' at 800 ^{o}C reflected a more stable state of U_3O_8, and the difference between both patterns was attributed to lattice expansion. However, at 1000 °C (pattern e), extra peaks appeared (indicated by arrows) that were not observed at 800 °C. However, the cooling of the sample in air indicated the recovery of the stable structure due to the presence of one single phase. Oxygen lost upon heating U_3O_8 above 800 °C was rapidly replaced upon cooling [189].

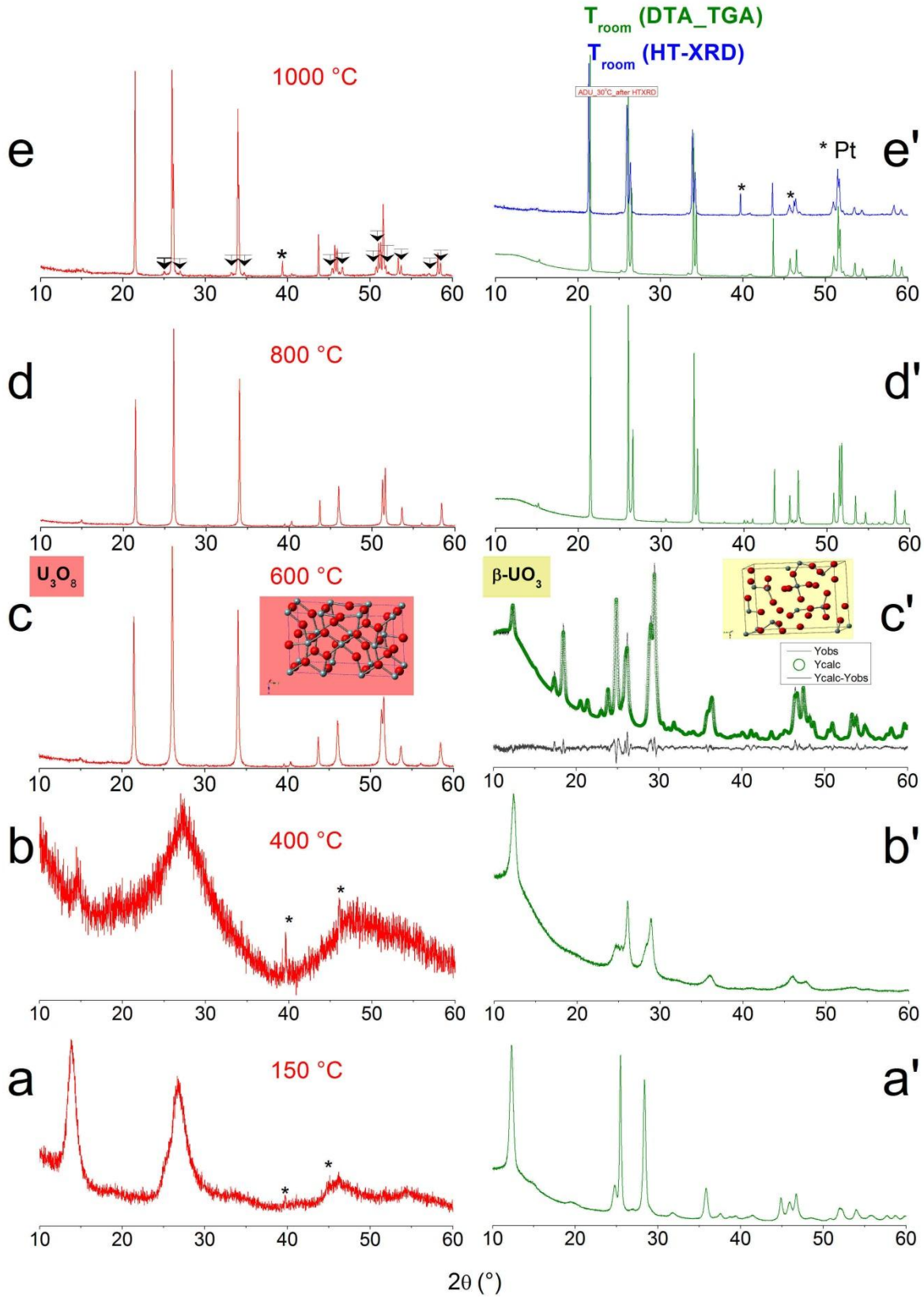

Figure C-1: In-situ HT-XRD of an ADU sample measured at 150 °C, 400 °C, 600 °C, 800 °C and 1000 °C (left). Ex-situ XRD of ADU samples measured at room temperature after heat treatment at 150 °C, 400 °C, 600 °C, 800 °C and 1000 °C (right).

In order to demonstrate that ex-situ XRD measurements made at room temperature can be correlated to in-situ HT-XRD, the XRD patterns recorded at room temperature on the sample obtained after heat treatment at1000 °C in in-situ HT-XRD and in ex-situ with TG/DTA were compared. Both patterns are completely identical, indicating that the processes taking place through ex-situ heat treatment can be correlated to the in-situ process [188].

IR and Raman characterization of ADU (Batch I) and its calcined products

Figure C-2 depicts the spectroscopic features of ADU and its calcined products. The IR and Raman spectra are on the left and right of the figure respectively. The IR (a) and Raman (a') spectra of ADU (Batch I) is similar to that reflected in Figure 3-2 for ADU (Batch II). Both IR and Raman spectra have already been interpreted in section 3.3.1.

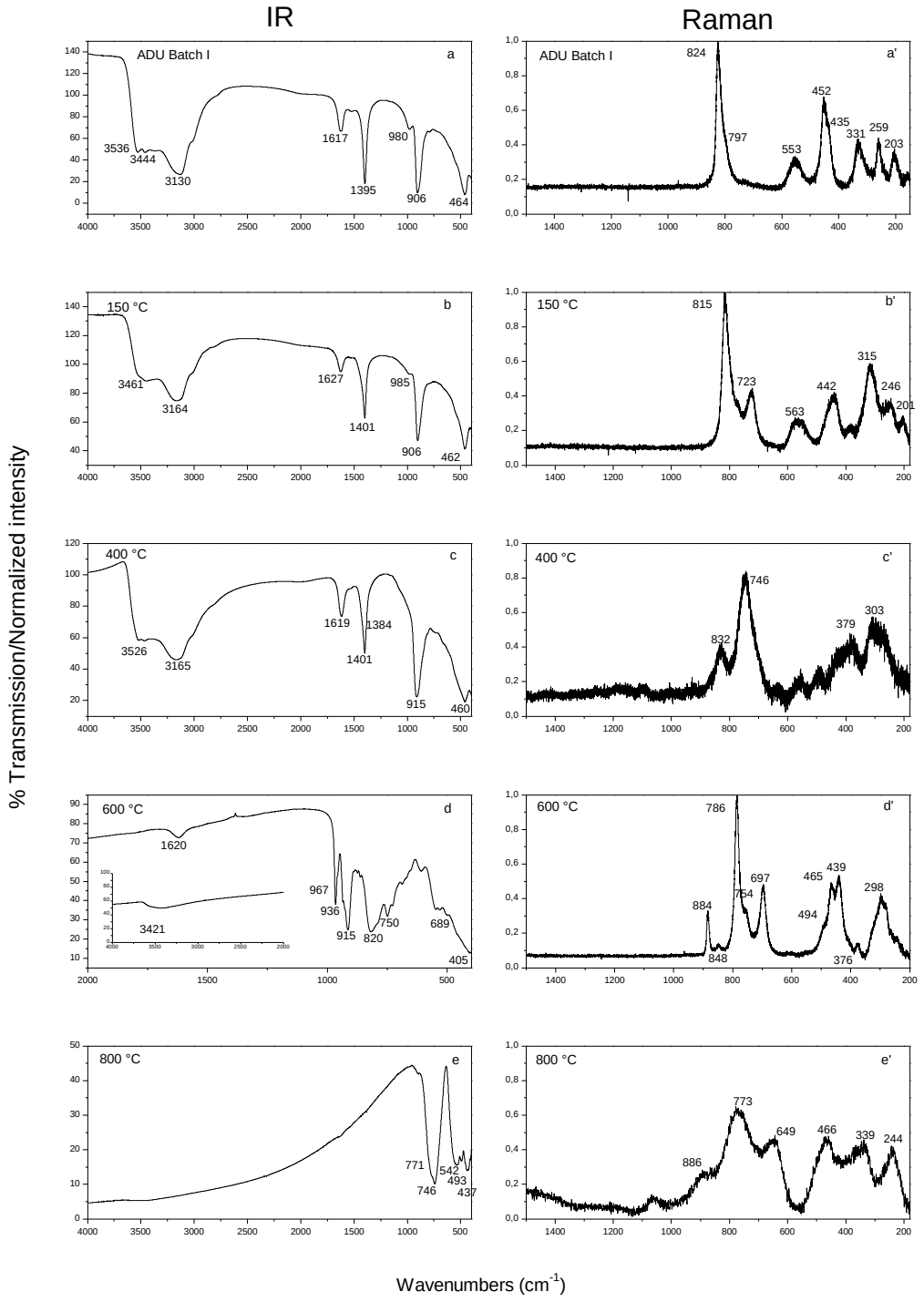

Figure C-2: IR (left) and Raman (right) spectra of ADU and ADU calcined at 150 °C, 400 °C, 600 °C and 800 °C.

After heating ADU to 150 °C, the IR spectrum (b) resembles that of its precursor (a). This corroborates with the ex-situ XRD data. This temperature is clearly not sufficient to remove all the water that is still present. In contrast, the Raman spectrum (b') is notably different from that of ADU (a'). There is an appearance of a peak at ca 723 cm^{-1}. This suggests that the uranyl ions UO_2^{2+}, are in at least two different environments. After heat treatment at 400 °C, the same but shifted peak became the most dominant peak. This Raman spectrum (c') is rather representative of amorphous UO_3 (A-

UO_3) with broad peaks. The IR spectrum (c') does not appear to have changed much from its precusors. The vibrational bands of N-H and O-H are still present in the material. This spectrum differs from published IR spectra of A-UO_3 [180]. As seen from the XRD data, ADU that has been calcined at 600 ^oC produces U_3O_8 that subsequently cools down to form β-UO_3. The presence of the β-UO_3 is evident in the IR spectrum (d) and the spectrum is very similar to published data [180, 186]. In the same reference, α, β, γ, and δ modifications of UO_3 have distinguishable spectra. The corresponding Raman spectrum (d') of β-UO_3 shows the appearance of sharp peaks, supporting the presence of crystalline material as seen in XRD data. No Raman spectrum of β-UO_3 has been reported. After treatment at 800 ^oC, U_3O_8 is produced. Its presence is evident in the IR spectrum (e) and fits the profile typical of α-U_3O_8 [35, 186]. The corresponding U_3O_8 peaks are slightly less typical of usual Raman profiles. However, the broad peaks are derived from measuring the sample which absorbs more than reflects the energy of the laser. And this is always observed for dark colored powder material.

There are generally some differences between the IR and Raman results for the same material. At lower temperatures of drying or calcination up to 400 ^oC, the Raman spectra appeared to capture the change in structure while IR spectra remained similar. IR peaks tend to be broad and are not affected by the color of the material. The crystallinity or amorphous state of the material is also not reflected in the spectrum. In contrast, Raman peaks can be sharp or broad, depending on the color or the order in the material. Both methods are complementary and the results from both techniques support the observations of XRD and TG/DTA data.

Appendix D

Supplementary information for Chapter 4

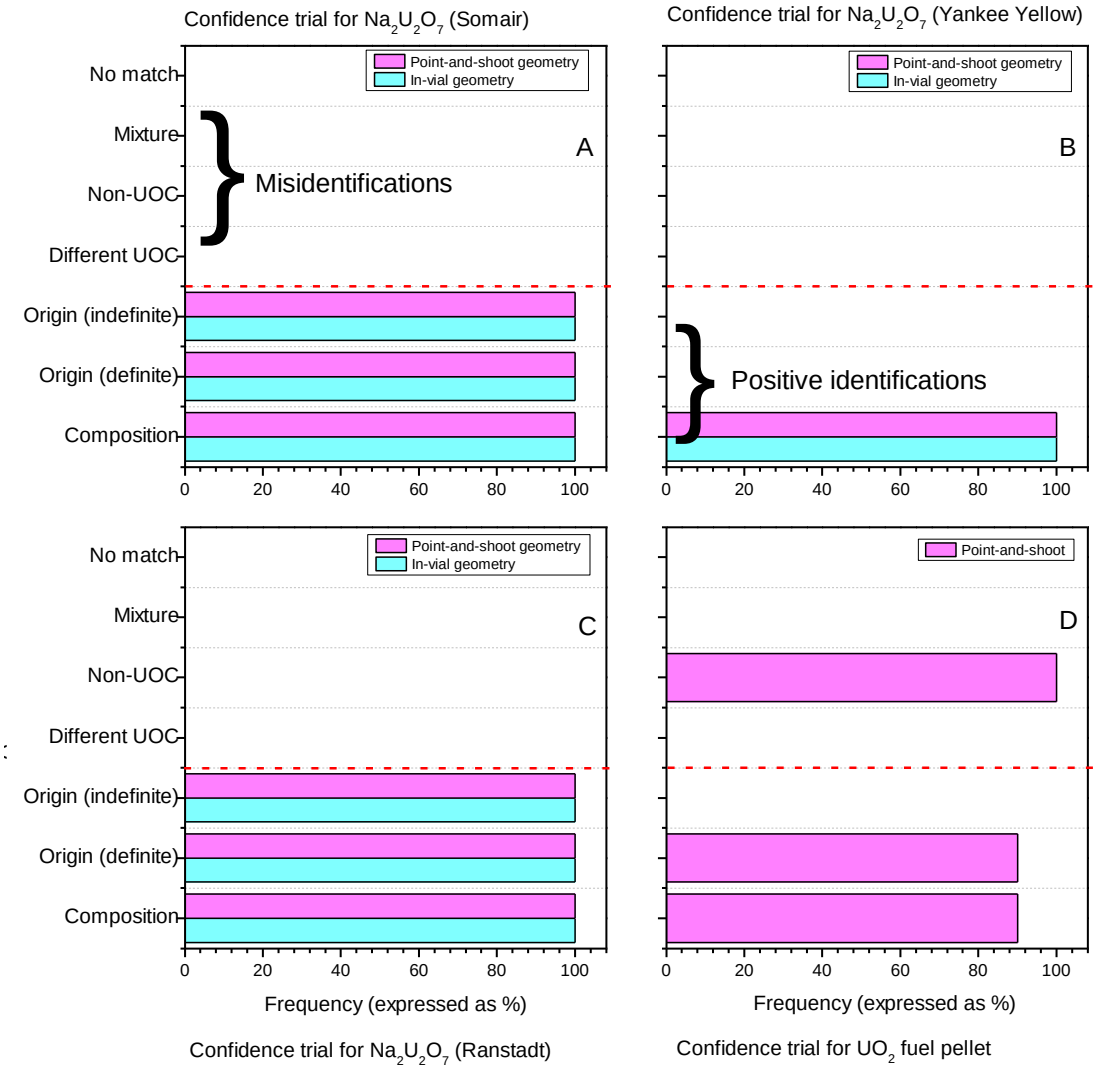

Figure D-1: Confidence trial for three different $Na_2U_2O_7$ samples from Somair (A), Yankee Yellow (B), Ranstad (C) and UO_2 pellet (D). Red line shows the division between positive identifications and misidentifications of the samples.

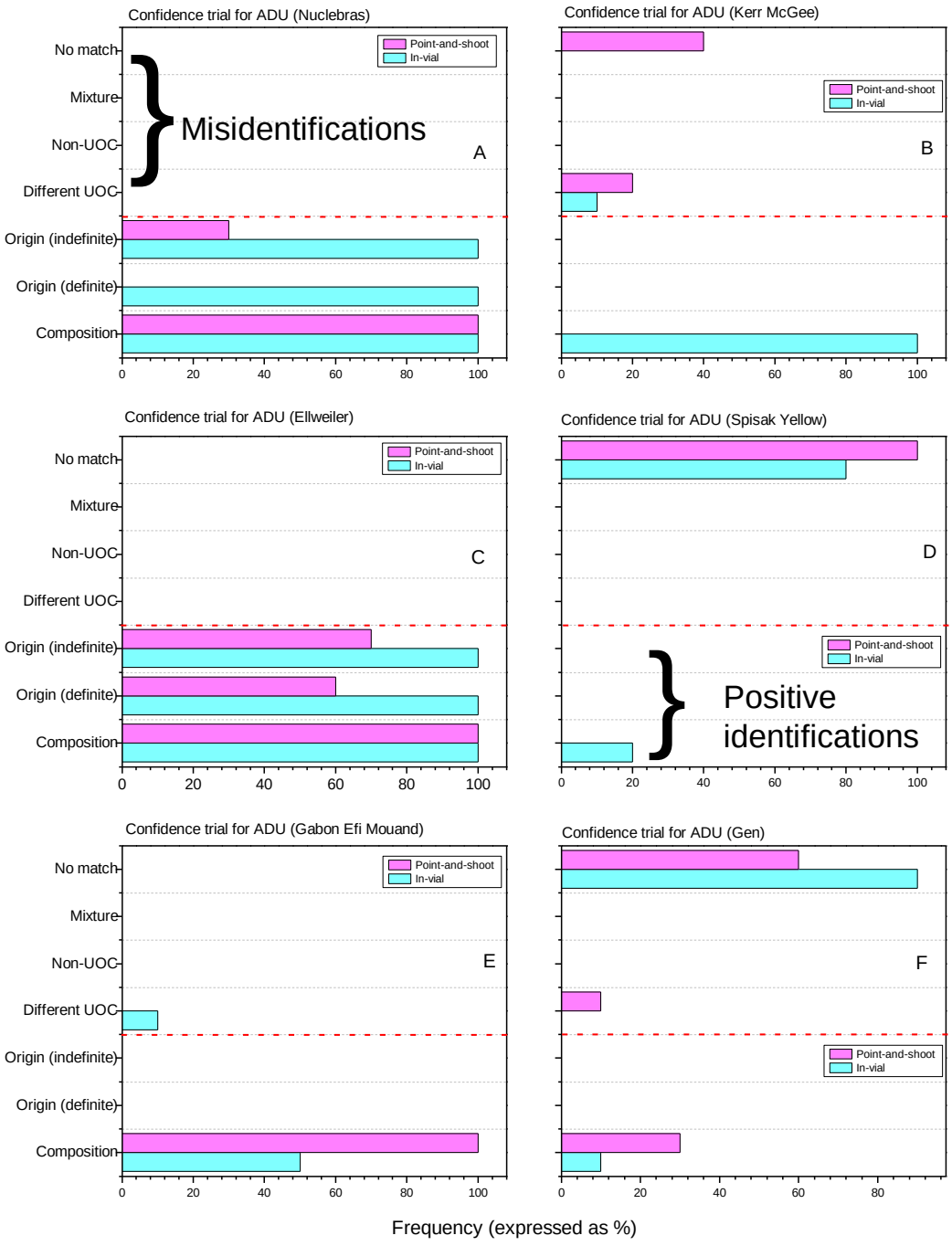

Figure D-2: Confidence trial for six different ADU samples from Nuclebras (A), Kerr McGee (B), Ellweiler (C), Spisak Yellow (D), Gabon Efi Mouand (E) and Gen (F). Red line shows the division between positive identifications and misidentifications of the samples.

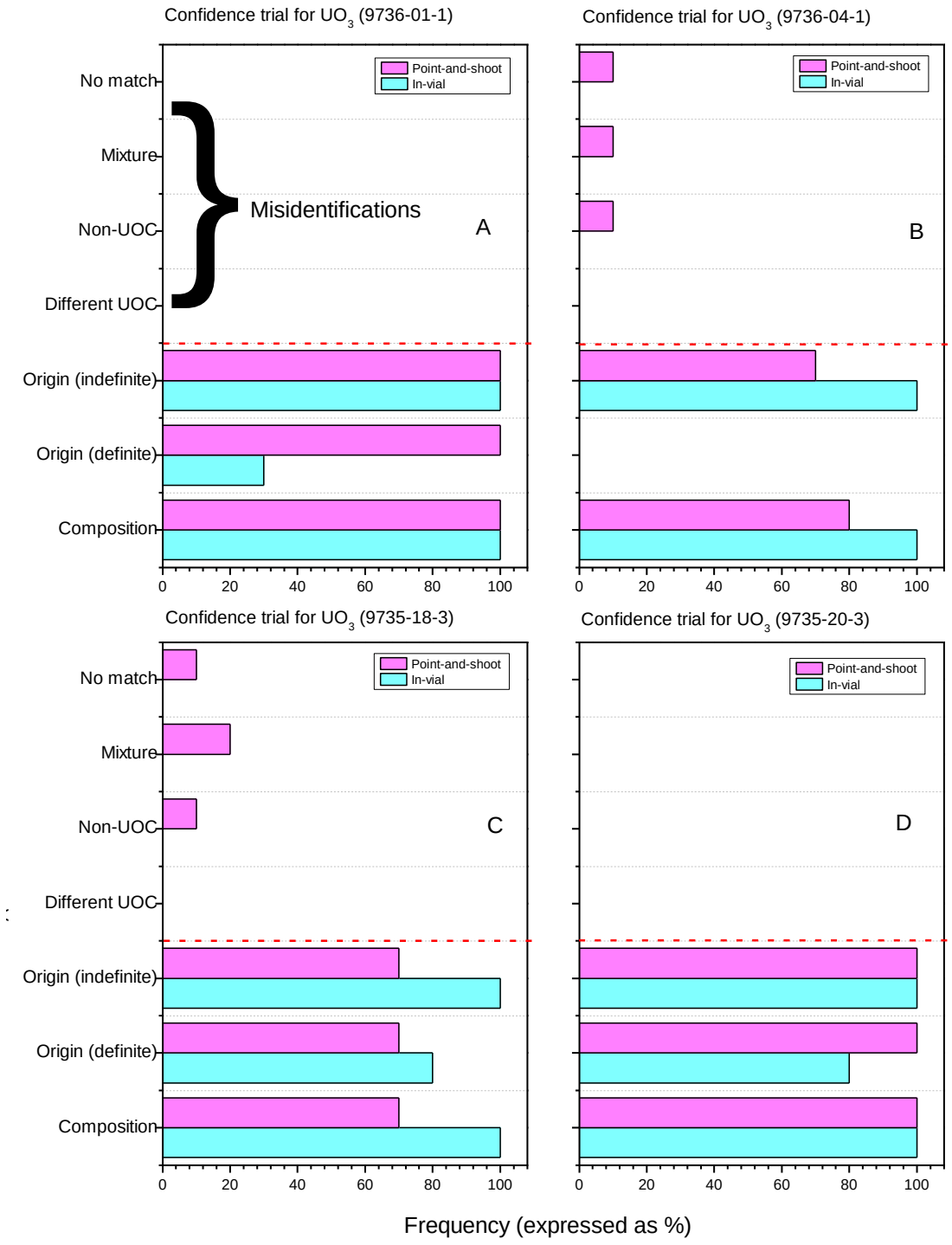

Figure D-3: Confidence trial for four UO_3 samples from Port Hope 9736-01-1 (A), 9736-04-1 (B), Blind River 9735-18-3 (C), 9735-20-3 (D). Red line shows the division between positive identifications and misidentifications of the samples.

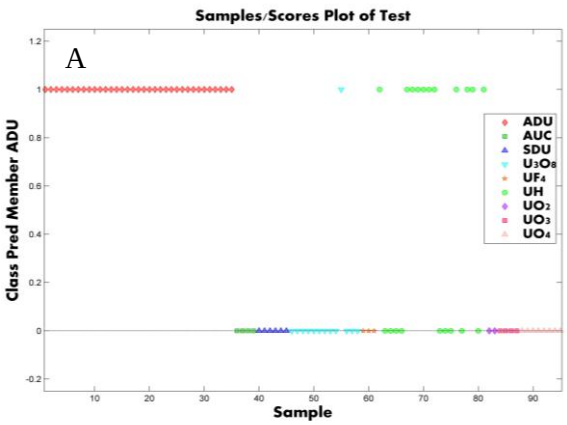
Samples/Scores Plot of Test
A
Class Pred Member ADU
Sample
ADU
AUC
SDU
U3O8
UF4
UH
UO2
UO3
UO4

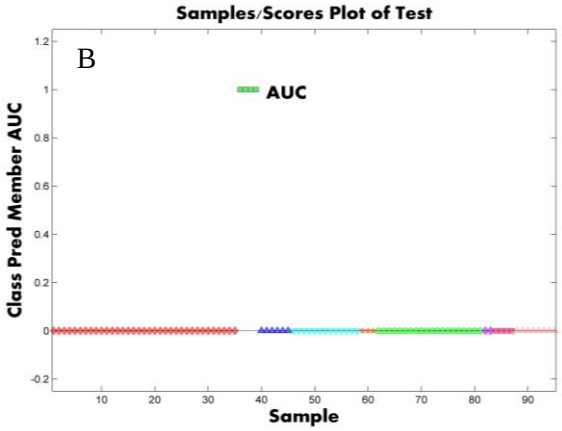
Samples/Scores Plot of Test
B
Class Pred Member AUC
Sample
AUC

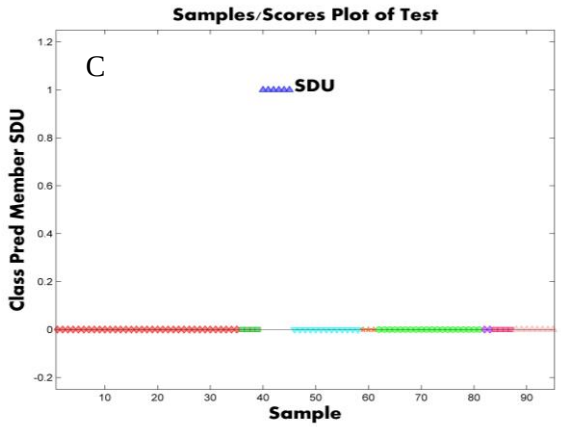
Samples/Scores Plot of Test
C
Class Pred Member SDU
Sample
SDU

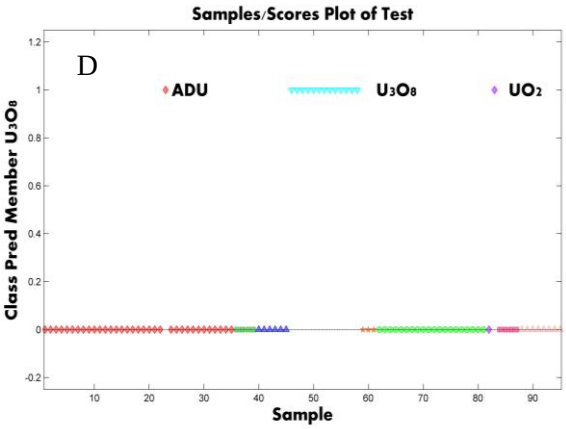
Samples/Scores Plot of Test
D
Class Pred Member U3O8
Sample
ADU
U3O8
UO2

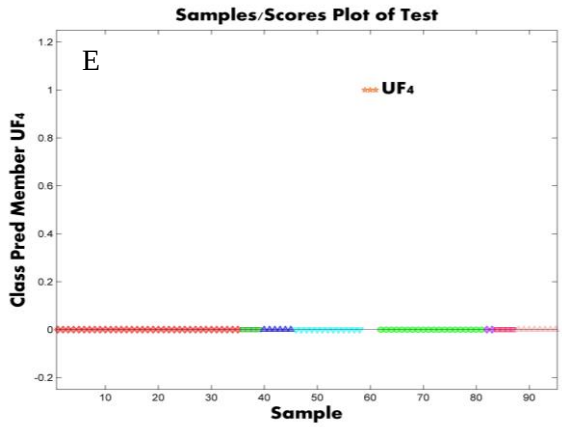
Samples/Scores Plot of Test
E
Class Pred Member UF4
Sample
UF4

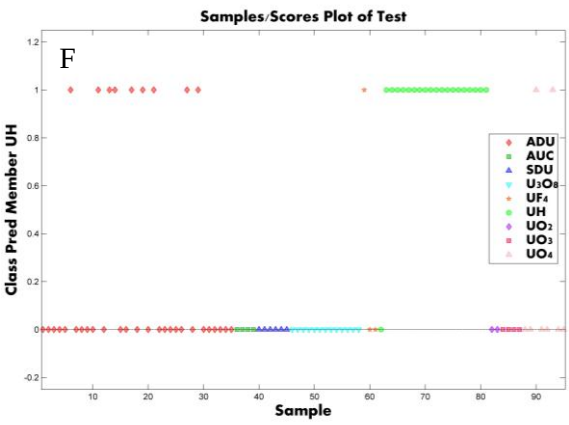
Samples/Scores Plot of Test
F
Class Pred Member UH
Sample
ADU
AUC
SDU
U3O8
UF4
UH
UO2
UO3
UO4

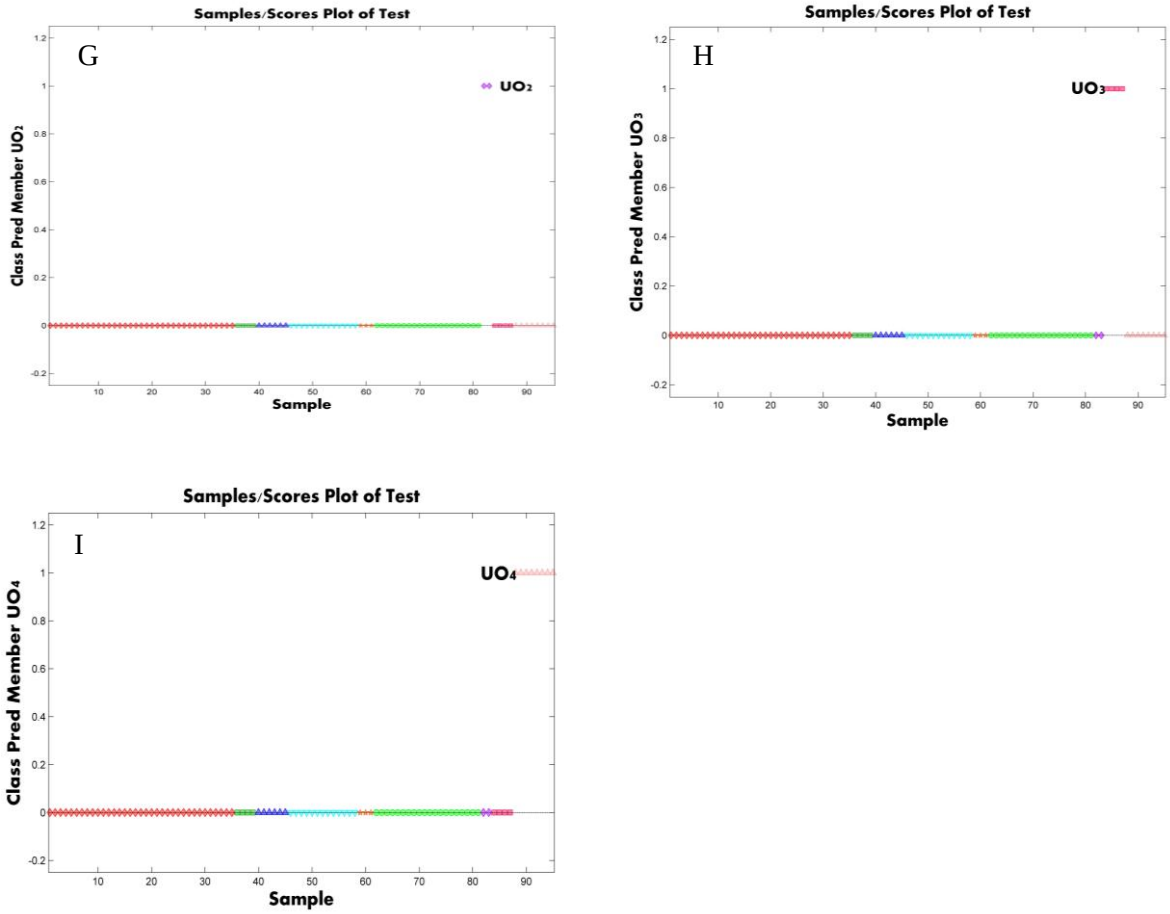

Figure D-4: Class member predictions for ADU (A), AUC (B), SDU (C), U_3O_8 (D), UF_4 (E), UH (F), UO_2 (G), UO_3 (H), UO_4 (I).

Appendix E

Supplementary information for Chapter 5

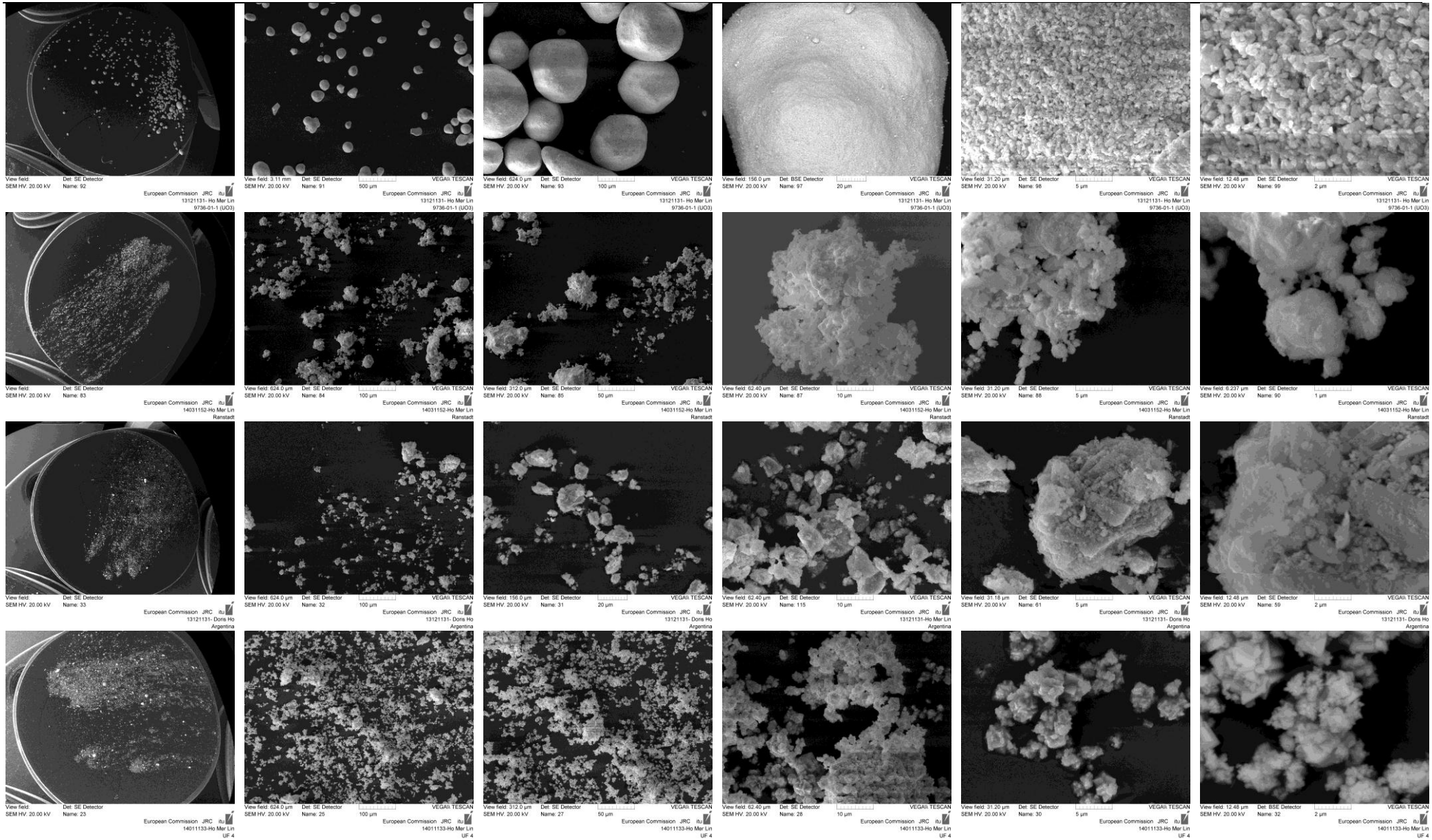

Figure E-1: SEM images of UOC from Port Hope (1st row), Ranstad (2nd row), Argentina unspecified mine (3rd row) and UF_4 (last row). Images are presented in increasing magnification from left to right per row.

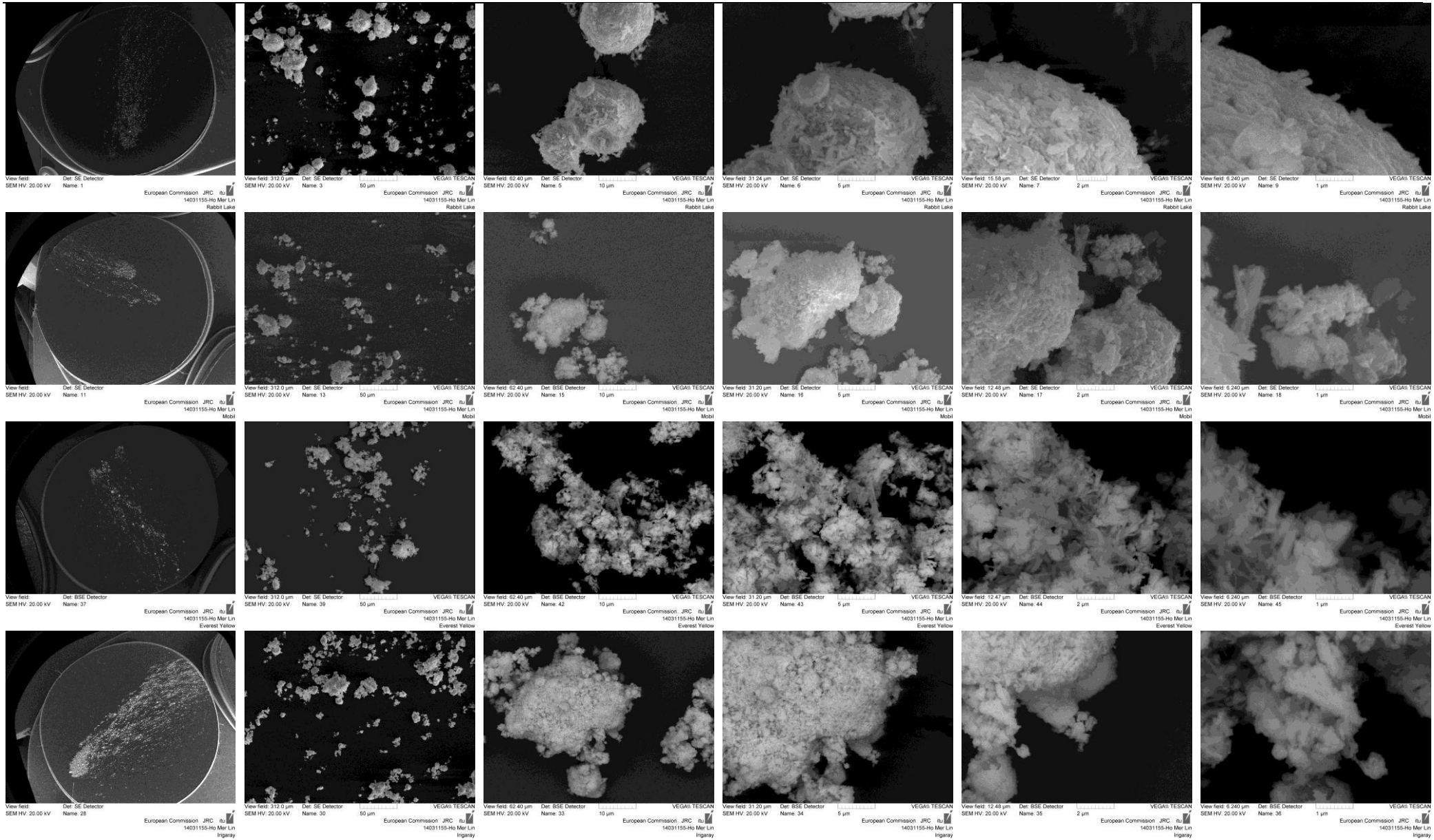

Figure E-2: SEM images of uranyl peroxides from Rabbit Lake (1st row), Mobil (2nd row), Everest Yellow (3rd row) and Irigaray (last row). Images are presented in increasing magnification from left to right per row.

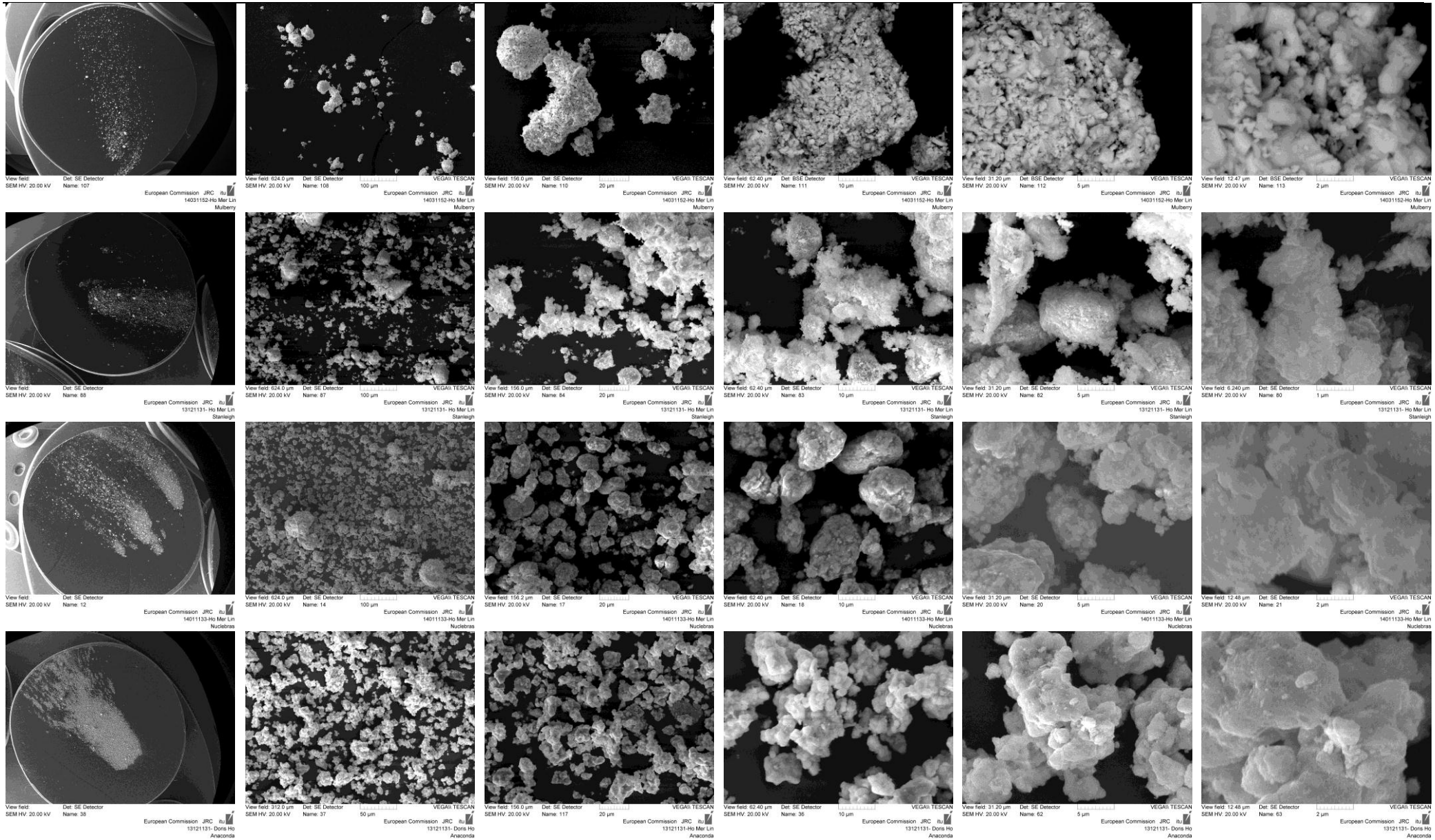

Figure E-3: SEM images of UOCs from Mulberry (1st row), Stanleigh (2nd row), Nuclebras (3rd row) and Anaconda (last row). Images are presented in increasing magnification from left to right per row.

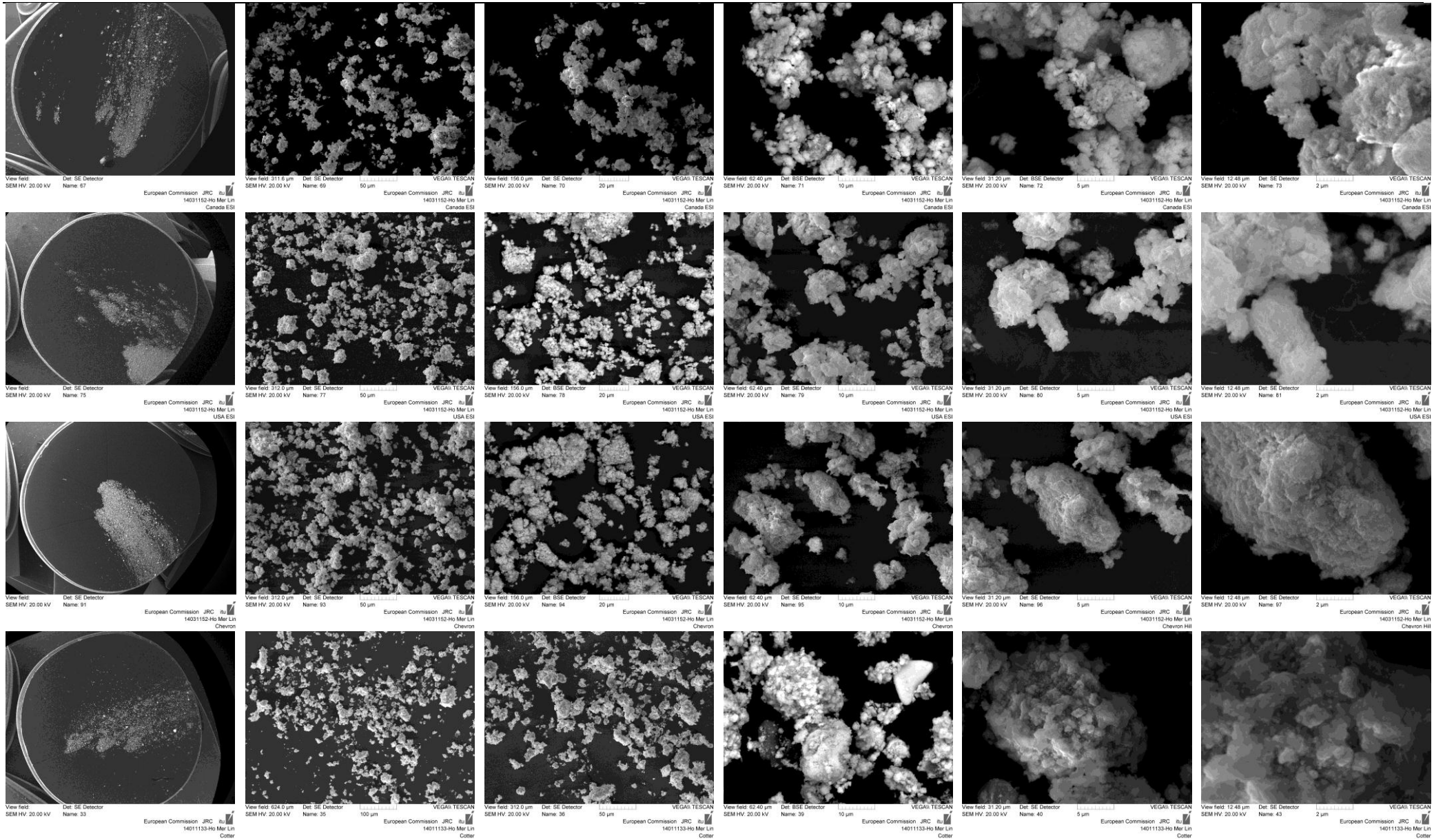

Figure E-4: SEM images of UOCs from Canada ESI (1st row), USA ESI (2nd row), Chevron Hill (3rd row) and Cotter (last row). Images are presented in increasing magnification from left to right per row.

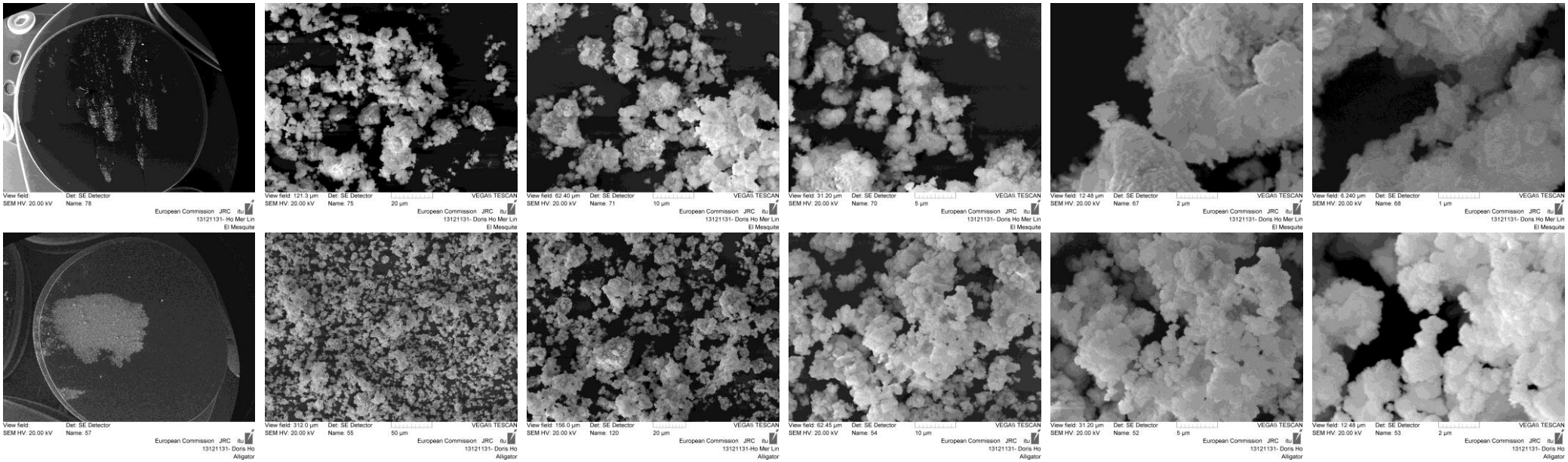

Figure E-5: SEM images of UOCs from El Mesquite (1st row) and Alligator (2nd row). Images are presented in increasing magnification from left to right per row.

Publications

Peer reviewed articles

- Andrey Berlizov, Doris Ho Mer Lin, Adrian Nicholl, Thomas Fanghänel and Klaus Mayer, *Assessing hand-held Raman spectrometer FirstDefender RM for Nuclear Safeguards Applications*, in preparation.

- Lorenzo Fongaro, Doris Ho Mer Lin, Thomas Fanghänel, Klaus Mayer and Vincenzo V. Rondinella, *Identification/classification of uranium ore concentrate samples from their textured images using Angle Measure Technique (AMT): new perspective in nuclear forensics,* in preparation.

- Fabien Pointurier, Olivier Marie, Christophe Moulin, Doris Ho Mer Lin, Dario Manara, Thomas Fanghänel and Klaus Mayer, *A comparative study between bulk and particle Raman analysis of uranium ore concentrates for nuclear forensics and safeguards*. Journal of Raman Spectroscopy, in press.

- Doris Ho Mer Lin, Andrew E. Jones, John Y. Goulermas, Philip Turner, Zsolt Varga, Lorenzo Fongaro, Thomas Fanghänel and Klaus Mayer, *Raman spectroscopy of uranium compounds and the use of multivariate analysis for unsupervised and supervised visualization*. Forensic Science International, submitted for review.

- Rachel Eloirdi, Doris Ho Mer Lin, Klaus Mayer, Roberto Caciuffo and Thomas Fanghänel, *Investigation of ammonium diuranate calcination with high-temperature X-ray diffraction.* Journal of Material Science, 2014 (49) p. 8436-8443.

- Doris Ho Mer Lin, Dario Manara, Patric Lindqvist-Reis, Thomas Fanghänel and Klaus Mayer, *The use of different dispersive Raman spectrometers for the analysis of uranium compounds*. Vibrational Spectroscopy, 2014 (73) p. 102-110.

- Doris Ho Mer Lin, Dario Manara, Zsolt Varga, Andrey Berlizov, Thomas Fanghänel and Klaus Mayer, *Applicability of Raman spectroscopy as a tool in nuclear forensics for analysis of uranium ore concentrates*. Radiochimica Acta, 2013 (101) p. 779-784.

Conference presentations

- Doris Ho Mer Lin, Dario Manara, Zsolt Varga, Lorenzo Fongaro, Adrian Nicholl, Markus Ernstberger, Andrey Berlizov, Patric Lindqvist-Reis, Thomas Fanghänel and Klaus Mayer, *Exploring spectroscopic and morphological data as new signatures for uranium ore concentrates*, in International Conference on Advances in Nuclear Forensics- IAEA, Vienna, Austria, 7-10 July 2014.

- Zsolt Varga, Doris Ho Mer Lin, Marton Novak, Zsuzsanna Eke, Zsolt Bodai, Adrian Nicholl and Klaus Mayer, *Measurement of organic residues of uranium ore concentrates (yellow cakes) for nuclear forensic investigations*, in International Conference on Advances in Nuclear Forensics- IAEA, Vienna, Austria, 7-10 July 2014.

- Doris Ho Mer Lin, *Characterization of uranium ore concentrates by Raman spectroscopy for nuclear forensics*, in GDCh Wissenschaftsforum, Darmstadt, Germany, 1-4 September 2013.

- Doris Ho Mer Lin, Andrey Berlizov, Adrian Nicholl, Dario Manara, Zsolt Varga, Klaus Mayer and Thomas Fanghänel, *The use of portable Raman spectrometer for analysis of uranium ore concentrates*, in International Conference on Nuclear Security, IAEA, Vienna, Austria, 1-5 July 2013 (IAEA-CN-203/162)

- Andrey Berlizov, Doris Ho Mer Lin, Adrian Nicholl and Klaus Mayer, *Assessing capabilities of Handheld Raman spectrometer FirstDefender RM for complementary access applications*, in ESARDA Symposium (35th Annual Meeting), Bruges, Belgium, 27-30 May 2013.

- Doris Ho Mer Lin, Adrian Nicholl, Dario Manara, Zsolt Varga, Christo Apostolidis, Klaus Mayer and Thomas Fanghänel, *Raman spectroscopy as a possible tool for nuclear forensics*, in 7th Singapore International Symposium on Protection against Toxic Substances/3rd International Chemical, Biological, Radiological & Explosives Operations Conference, Singapore, 4-7 Dec 2012.

References

1. Mayer, K., M. Wallenius, and T. Fanghänel, *Nuclear forensic science-From cradle to maturity*. Journal of Alloys and Compounds, 2007. **444-445**(0): p. 50-56.
2. Wallenius, M., K. Mayer, and I. Ray, *Nuclear forensic investigations: Two case studies.* Forensic Science International, 2006. **156**(1): p. 55-62.
3. Wallenius, M., et al., *Nuclear forensic investigations with a focus on plutonium.* Journal of Alloys and Compounds, 2007. **444-445**(0): p. 57-62.
4. *Nuclear Forensics Support*. 2006, International Atomic Energy Agency: Vienna, Austria.
5. Nicholas, M., *Analysis of incidents reported during 2007-2012 to the IAEA's Incident and Trafficking Database*, in *IAEA Nuclear Forensics*. 2014, International Atomic Energy Agency: Vienna, Austria.
6. Hutcheon, I.D., M.J. Kristo, and K.B. Knight, *Nonproliferation Nuclear Forensics*. Glenn Seaborg Institute, Lawrence Livermore National Laboratory.
7. *The Nuclear Fuel Cycle*. August 2011 [cited 2013 1st January]; Available from: http://www.iaea.org/Publications/Booklets/NuclearFuelCycle/nfc0811.pdf.
8. *The Nuclear Fuel Cycle*. June 2011; Available from: http://www.world-nuclear.org/info/inf03.html
9. Connelly, D., *Uranium Processing.* International Mining, January 2008: p. 58-61.
10. Preez, J.G.H.d., *A review of the industrial processes involving uranium- from the ore to the reactor*. Radiation Protection Dosimetry, 1989. **26**(1/4): p. 7-13.
11. Edwards, C.R. and A.J. Oliver, *Uranium Processing: A Review of Current Methods and Technology*. JOM, 2000. **52**(9): p. 12-20.
12. *Uranium Extraction Technology*. 1993, International Atomic Energy Agency.
13. Cahill, A.E. and L.E. Burkhart, *Continuous precipitation of uranium with hydrogen peroxide.* Metallurgical Transactions B, 1990. **21**(5): p. 819-826.
14. Mayer, K., M. Wallenius, and I. Ray, *Nuclear forensics- a methodology providing clues on the origin of illicitly trafficked nuclear materials.* Analyst, 2005. **130**: p. 433-441.
15. Kristo, M.J. and S.J. Tumey, *The state of nuclear forensics.* Nuclear Instruments and Methods in Physics Research Section B: Beam Interactions with Materials and Atoms, 2012. **294**(0): p. 656-661.
16. Koch, L., *Traces of Evidence; Nuclear Forensics & Illicit Trafficking*. 2003, International Atomic Energy Agency: Vienna Austria.
17. Budinger, P.A., et al., *The Case of the Great Yellow Cake Caper*. Analytical Chemistry, 1980. **52**(8): p. 942A-948A.
18. Varga, Z., *et al.*, *Analysis of uranium ore concentrates for origin assessment.* Proc. Radiochim. Acta, 2011. **1**: p. 1-4.
19. Keegan, E., *et al.*, *The provenance of Australian uranium ore concentrates by elemental and isotopic analysis.* Applied Geochemistry, 2008. **23**(4): p. 765-777.
20. Rosman, K.J.R. and P.D.P. Taylor, *Isotopic Composition of the Elements*. 1997, International Union of Pure and Applied Chemistry (IUPAC).
21. Varga, Z., *et al.*, *Application of Lead and Strontium Isotope Ratio Measurements for the Origin Assessment of Uranium Ore Concentrates.* Analytical Chemistry, 2009. **81**(20): p. 8327-8334.
22. Keegan, E., *et al.*, *Nuclear forensic analysis of an unknown uranium ore concentrate sample seized in a criminal investigation in Australia.* Forensic Science International, 2014. **240**(0): p. 111-121.
23. Tamborini, G., *et al.*, *Oxygen Isotopic Measurements by Secondary Ion Mass Spectrometry in Uranium Oxide Microparticles: A Nuclear Forensic Diagnostic.* Analytical Chemistry, 2002. **74**(23): p. 6098-6101.
24. Pajo, L., K. Mayer, and L. Koch, *Investigation of the oxygen isotopic composition in oxidic uranium compounds as a new property in nuclear forensic science.* Fresenius J Anal Chem, 2001. **371**(3): p. 348-52.

25. Pajo, L., *et al.*, *A novel isotope analysis of oxygen in uranium oxides: comparison of secondary ion mass spectrometry, glow discharge mass spectrometry and thermal ionization mass spectrometry.* Spectrochimica Acta Part B: Atomic Spectroscopy, 2001. **56**(5): p. 541-549.
26. Han, S.-H., *et al.*, *Measurement of the sulphur isotope ratio (34S/32S) in uranium ore concentrates (yellow cakes) for origin assessment.* Journal of Analytical Atomic Spectrometry, 2013. **28**(12): p. 1919-1925.
27. Krajkó, J., *et al.*, *Application of neodymium isotope ratio measurements for the origin assessment of uranium ore concentrates.* Talanta, 2014. **129**(0): p. 499-504.
28. Wallenius, M. and K. Mayer, *Age determination of plutonium material in nuclear forensics by thermal ionisation mass spectrometry.* Fresenius J Anal Chem, 2000. **366**(3): p. 234-8.
29. Wallenius, M., *et al.*, *Determination of the age of highly enriched uranium.* Analytical and Bioanalytical Chemistry, 2002. **374**(3): p. 379-384.
30. Morgenstern, A., C. Apostolidis, and K. Mayer, *Age Determination of Highly Enriched Uranium: Separation and Analysis of 231Pa.* Analytical Chemistry, 2002. **74**(21): p. 5513-5516.
31. Varga, Z. and G. Surányi, *Production date determination of uranium-oxide materials by inductively coupled plasma mass spectrometry.* Analytica Chimica Acta, 2007. **599**(1): p. 16-23.
32. Varga, Z., *et al.*, *Development and validation of a methodology for uranium radiochronometry reference material preparation.* Analytica Chimica Acta, 2012. **718**(0): p. 25-31.
33. Wallenius, M., P. Peerani, and L. Koch, *Origin Determination of Plutonium Material in Nuclear Forensics.* Journal of Radioanalytical and Nuclear Chemistry, 2000. **246**(2): p. 317-321.
34. Mayer, K., M. Wallenius, and Z. Varga, *Nuclear Forensic Science: Correlating Measurable Material Parameters to the History of Nuclear Material.* Chemical Reviews, 2012. **113**(2): p. 884-900.
35. Varga, Z., *et al.*, *Characterization and classification of uranium ore concentrates (yellow cakes) using infrared spectrometry.* Radiochim. Acta, 2011. **99**: p. 1-7.
36. Klunder, G.L., *et al.*, *Application of Visible/Near-Infrared Reflectance Spectroscopy to Uranium Ore Concentrates for Nuclear Forensic Analysis and Attribution.* Applied Spectroscopy, 2013. **67**(9): p. 1049-1056.
37. Plaue, J.W., *et al.*, *Near infrared reflectance spectroscopy as a process signature in uranium oxides.* Journal of Radioanalytical and Nuclear Chemistry, 2012.
38. Sirven, J.-B., *et al.*, *Towards the determination of the geographical origin of yellow cake samples by laser-induced breakdown spectroscopy and chemometrics.* Journal of Analytical Atomic Spectrometry, 2009. **24**(4): p. 451-459.
39. Keegan, E., *et al.*, *Attribution of uranium ore concentrates using elemental and anionic data.* Applied Geochemistry, 2012. **27**(8): p. 1600-1609.
40. Badaut, V., M. Wallenius, and K. Mayer, *Anion analysis in uranium ore concentrates by ion chromatography.* Journal of Radioanalytical and Nuclear Chemistry, 2009. **280**(1): p. 57-61.
41. *Rare Earth Elements 101*. April 2012 [cited 2014 07/09/2014]; Available from: http://www.iamgold.com/files/ree101_april_2012.pdf.
42. Varga, Z., M. Wallenius, and K. Mayer, *Origin assessment of uranium ore concentrates based on their rare-earth elemental impurity pattern*, in *Radiochimica Acta International journal for chemical aspects of nuclear science and technology*. 2010. p. 771.
43. Varga, Z., *et al.*, *Determination of rare-earth elements in uranium-bearing materials by inductively coupled plasma mass spectrometry.* Talanta, 2010. **80**(5): p. 1744-1749.
44. Kennedy, A.K., *et al.*, *Non-volatile organic analysis of uranium ore concentrates.* Journal of Radioanalytical and Nuclear Chemistry, 2012.
45. Kim, K.-W., *et al.*, *Effects of the different conditions of uranyl and hydrogen peroxide solutions on the behavior of the uranium peroxide precipitation.* Journal of Hazardous Materials, 2011. **193**: p. 52-58.

46. Švedkauskaite-LeGore, J., *et al., Investigation of the isotopic composition of lead and of trace elements concentrations in natural uranium materials as a signature in nuclear forensics*, in *Radiochimica Acta*. 2007. p. 601.
47. Švedkauskaitė-LeGore, J., *et al., Investigation of the sample characteristics needed for the determination of the origin of uranium-bearing materials.* Journal of Radioanalytical and Nuclear Chemistry, 2008. **278**(1): p. 201-209.
48. Brennecka, G.A., *et al., Natural variations in uranium isotope ratios of uranium ore concentrates: Understanding the 238U/235U fractionation mechanism.* Earth and Planetary Science Letters, 2010. **291**(1–4): p. 228-233.
49. Varga, Z., *et al., Alternative method for the production date determination of impure uranium ore concentrate samples.* Journal of Radioanalytical and Nuclear Chemistry, 2011. **290**(2): p. 485-492.
50. Frost, R.L. and M. Weier, *Raman microscopy of autunite minerals at liquid nitrogen temperature.* Spectrochim Acta A Mol Biomol Spectrosc, 2004. **60**(10): p. 2399-409.
51. Amayri, S., et al., *Spectroscopic Characterization of the Uranium Carbonate Andersonite $Na_2Ca[UO_2(CO_3)_3]\cdot 6H_2O$.* Environmental Science & Technology, 2004. **38**(22): p. 6032-6036.
52. Frost, R.L., *et al., A Raman spectroscopic study of the uranyl sulphate mineral johannite.* Spectrochim Acta A Mol Biomol Spectrosc, 2005. **61**(11-12): p. 2702-7.
53. Frost, R.L., *et al., A Raman spectroscopic study of the uranyl phosphate mineral parsonite.* Journal of Raman Spectroscopy, 2006. **37**: p. 879-891.
54. Frost, R.L., *et al., A Raman spectroscopic study of the uranyl selenite mineral haynesite.* Journal of Raman Spectroscopy, 2006. **37**: p. 816-821.
55. Frost, R.L., *et al., Raman spectroscopic study of the uranyl phosphate mineral dewindtite.* Journal of Raman Spectroscopy, 2006. **37**: p. 1362-1367.
56. Frost, R.L., *et al., Raman spectroscopic study of the multi-anion uranyl mineral schroeckingerite.* Journal of Raman Spectroscopy, 2007. **38**(12): p. 1609-1614.
57. Frost, R.L., *et al., Vibrational spectroscopic study of hydrated uranyl oxide: Curite.* Polyhedron, 2007. **26**(14): p. 3724-3730.
58. Frost, R.L., M.J. Dickfos, and J. Cejka, *Raman spectroscopic study of the uranyl carbonate mineral zellerite.* Journal of Raman Spectroscopy, 2008. **39**: p. 582-586.
59. Čejka, J., *et al., Raman spectroscopic study of the uranyl mineral natrouranospinite $(Na_2,Ca)[(UO_2)(AsO_4)]_2\cdot 5H_2O$.* Journal of Raman Spectroscopy, 2009. **40**(11): p. 1521-1526.
60. Frost, R.L., J. Cejka, and M.J. Dickfos, *Raman spectroscopic study of the uranyl minerals vanmeersscheite $U(OH)_4[(UO_2)_3(PO_4)_2(OH)_2].4H_2O$ and arsenouranylite $Ca(UO_2)[(UO_2)_3(AsO_4)_2(OH)_2].(OH)_2.6H_2O$.* Spectrochimica Acta Part A: Molecular and Biomolecular Spectroscopy, 2009. **71**: p. 1799-1803.
61. Čejka, J., *et al., Raman spectroscopic study of the uranyl carbonate mineral čejkaite and its comparison with synthetic trigonal Na4[UO2(CO3)3].* Journal of Raman Spectroscopy, 2010. **41**(4): p. 459-464.
62. Frost, R.L. and B.J. Reddy, *Raman spectroscopic study of the uranyl titanate mineral brannerite $(U,Ca,Y,Ce)_2(Ti,Fe)_2O_6$: effect of metamictisation.* Journal of Raman Spectroscopy, 2011. **42**: p. 691-695.
63. Frost, R.L., S.J. Palmer, and B.J. Reddy, *Raman spectroscopic study of the uranyl titanate mineral euxenite $(Y,Ca,U,Ce,Th)(Nb,Ta,Ti)_2O_6$.* Journal of Raman Spectroscopy, 2011. **42**: p. 1160-1162.
64. Stefaniak, E.A., *et al., Combined SEM/EDX and micro-Raman spectroscopy analysis of uranium minerals from a former uranium mine.* J Hazard Mater, 2009. **168**(1): p. 416-23.
65. Biwer, B.M., W.L. Ebert, and J.K. Bates, *The Raman spectra of several uranyl-containing minerals using a microprobe.* Journal of Nuclear Materials, 1990. **175**(3): p. 188-193.
66. Butler, I.S., G.C. Allen, and N.A. Tuan, *Micro-Raman Spectrum of Triuranium Octoxide, U_3O_8.* Applied Spectroscopy, 1988. **42**(5): p. 901-902.
67. Palacios, M.L. and S.H. Taylor, *Characterization of Uranium Oxides Using in-situ Micro-Raman Spectroscopy.* Applied Spectroscopy, 2000. **54**(9): p. 1372-1378.

68. Manara, D. and B. Renker, *Raman spectra of stoichiometric and hyperstoichiometric uranium dioxide.* Journal of Nuclear Materials, 2003. **321**(2-3): p. 233-237.
69. Stefaniak, E.A., *et al.*, *New insight into UO2F2 particulate structure by micro-Raman spectroscopy.* Journal of Molecular Structure, 2013. **1040**(0): p. 206-212.
70. Armstrong, D.P., R.J. Jarabek, and W.H. Fletcher, *Micro-Raman Spectroscopy of Selected Solid $U_xO_yF_z$ Compunds.* Applied Spectroscopy, 1989. **43**(3): p. 461-468.
71. Desgranges, L., *et al.*, *Raman spectrum of U4O9: a new interpretation of damage lines in UO2.* Journal of Raman Spectroscopy, 2012. **43**(3): p. 455-458.
72. Stefaniak, E.b.A., *et al.*, *Recognition of uranium oxides in soil particulate matter by means of μ-Raman spectrometry.* Journal of Nuclear Materials, 2008. **381**(3): p. 278-283.
73. Mellini, M. and F. Riccobono, *Chemical and mineralogical transformations caused by weathering in anti-tank DU penetrators ("the silver bullets") discharged during the Kosovo war.* Chemosphere, 2005. **60**(9): p. 1246-52.
74. M.Amme, *et al.*, *Raman microspectrometric identification of corrosion products formed on UO2 nuclear fuel during leaching experiments.* Journal of Nuclear Materials, 2002. **306**(2-3): p. 202-212.
75. Pointurier, F. and O. Marie, *Identification of the chemical forms of uranium compounds in micrometer-size particles by means of micro-Raman spectrometry and scanning electron microscope.* Spectrochimica Acta Part B: Atomic Spectroscopy, 2010. **65**(9-10): p. 797-804.
76. Pointurier, F. and O. Marie, *Use of micro-Raman spectrometry coupled with scanning electron microscopy to determine the chemical form of uranium compounds in micrometer-size particles.* Journal of Raman Spectroscopy, 2013. **44**: p. 1753-1759.
77. Ruan, C., *et al.*, *Surface-enhanced Raman spectroscopy for uranium detection and analysis in environmental samples.* Anal Chim Acta, 2007. **605**(1): p. 80-6.
78. Colomban, P., *The on-site/remote Raman analysis with mobile instruments: a review of drawbacks and success in cultural heritage studies and other associated fields.* Journal of Raman Spectroscopy, 2012. **43**(11): p. 1529-1535.
79. Lauwers, D., *et al.*, *Characterisation of a portable Raman spectrometer for in situ analysis of art objects.* Spectrochimica Acta Part A: Molecular and Biomolecular Spectroscopy, 2014. **118**(0): p. 294-301.
80. Jehlička, J., *et al.*, *Application of portable Raman instruments for fast and non-destructive detection of minerals on outcrops.* Spectrochimica Acta Part A: Molecular and Biomolecular Spectroscopy, 2009. **73**(3): p. 410-419.
81. Jehlička, J., *et al.*, *Critical evaluation of a handheld Raman spectrometer with near infrared (785nm) excitation for field identification of minerals.* Spectrochimica Acta Part A: Molecular and Biomolecular Spectroscopy, 2011. **80**(1): p. 36-40.
82. Vítek, P., *et al.*, *Evaluation of portable Raman spectrometer with 1064nm excitation for geological and forensic applications.* Spectrochimica Acta Part A: Molecular and Biomolecular Spectroscopy, 2012. **86**(0): p. 320-327.
83. Izake, E.L., *Forensic and homeland security applications of modern portable Raman spectroscopy.* Forensic Science International, 2010. **202**: p. 1-8.
84. Weyermann, C., *et al.*, *Applications of a transportable Raman spectrometer for the in situ detection of controlled substances at border controls.* Forensic Science International, 2011. **209**(1–3): p. 21-28.
85. Mogilevsky, G., *et al.*, *Raman Spectroscopy for Homeland Security Applications.* International Journal of Spectroscopy, 2012. **2012**: p. 12.
86. Angel, S.M., *et al.*, *Remote Raman spectroscopy for planetary exploration: a review.* Appl Spectrosc, 2012. **66**(2): p. 137-50.
87. GNYBA, M., *et al.*, *Portable Raman spectrometer- design rules and applications.* BULLETIN OF THE POLISH ACADEMY OF SCIENCES (TECHNICAL SCIENCES), 2011. **59**(3).
88. Ray, I.L.F., A. Schubert, and M. Wallenius. *The concept of a 'microstrucutral fingerprint' for characterization of samples in nuclear forensic science*. in *International Conference on Advances in Destructive and Non-Destructive Analysis for Environmental Monitoring and Nuclear Forensics*. 2002. Karlsruhe, Germany: International Atomic Energy Agency.

89. Fongaro, L. and K. Kvaal, *Surface texture characterization of an Italian pasta by means of univariate and multivariate feature extraction from their texture images.* Food Research International, 2013. **51**(2): p. 693-705.
90. Plaue, J., *Forensic Signatures of Chemical Process History in Uranium Oxides*, in *Department of Chemistry*. 2013, University of Nevada: Las Vegas, USA.
91. Esbensen, K.H., K.H. Hjelmen, and K. Kvaal, *The AMT approach in chemometrics — first forays.* Journal of Chemometrics, 1996. **10**(5-6): p. 569-590.
92. *Comparison of Particle Sizing Methods*. [cited 2014 15/09/2014]; Available from: http://www.cpsinstruments.eu/pdf/Compare%20Sizing%20Methods.pdf.
93. DOI, H. and T. ITO, *Significance of physical state of starting precipitate in growth of uranium dioxide particles.* Journal of Nuclear Materials, 1964. **11**(1): p. 94-106.
94. Janov, J., P.G. Alfredson, and V.K. Vilkaitis, *The influence of precipitation conditions on the properties of ammonium diuranate and uranium dioxide powders.* Journal of Nuclear Materials, 1972. **44**: p. 161-174.
95. Cordfunke, E.H.P. and A.A. van der Giessen, *Particle properties and sintering behaviour of uranium dioxide.* Journal of Nuclear Materials, 1967. **24**(2): p. 141-149.
96. J.L.Woolfrey, *The preparation of UO_2 powder: Effect of ammonium uranate properties.* Journal of Nuclear Materials, 1978. **74**: p. 123-131.
97. Rajagopal, S., T.P.S. Asari, and C.S.P. Iyer, *Particle size analysis of ammonium uranate prepared by conventional and homogenous methods of precipitation and their corresponding oxides.* Journal of Nuclear Materials, 1996. **227**: p. 300-303.
98. Manna, S., S.B. Roy, and J.B. Joshi, *Study of crystallization and morphology of ammonium diuranate and uranium oxide.* Journal of Nuclear Materials, 2012. **424**: p. 94-100.
99. Pan, Y.-M., C.-B. Ma, and N.-N. Hsu, *The conversion of UO_2 via ammonium uranyl carbonate: study of precipitation, chemical variation and powder properties.* Journal of Nuclear Materials, 1981. **99**: p. 135-147.
100. Choi, C.S., *et al., The influence of AUC powder characteristics on UO_2 pellets.* Journal of Nuclear Materials, 1988. **153**: p. 148-155.
101. Clayton, J.C. and S. Aronson, *Some Preparative Methods and Physical Characteristics of Uranium Dioxide Powders.* Journal of Chemical & Engineering Data, 1961. **6**(1): p. 43-51.
102. Wold, S., *Chemometrics; what do we mean with it, and what do we want from it?* Chemometrics and Intelligent Laboratory Systems, 1995. **30**: p. 109-115.
103. H.Tel and M.Eral, *Investigation of production conditions and powder properties of AUC.* Journal of Nuclear Materials, 1996. **231**(1-2): p. 165-169.
104. Govindan, P., *et al., Development of a reconversion method for uranyl nitrate to oxide in the reconversion step of reprocessing of irradiated fuel.* Journal of Radioanalytical and Nuclear Chemistry, 2001. **254**(1): p. 65-70.
105. A.Mellah, S.Chegrouche, and M.Barkat, *The precipitation of ammonium uranyl carbonate (AUC): Thermodynamic and kinetic investigations.* Hydrometallurgy, 2007. **85**: p. 163-171.
106. J.E.Litz and R.B.Coleman. *Production of yellow cake and uranium fluorides* in *Advisory Group Meeting*. 1979. Paris: International Atomic Energy Agency.
107. E.H.Y.Abowslama, A.K.SAM, and E.Ebraheem. *Precipitation and purification of uranium from rock phosphate*. in *3rd-International Nuclear Chemistry Congress*. 2011. Sicily-Italy.
108. Rasmussen, G., *Single element analysis at high precision by ICP-MS*. 2013, Institute for Transuranium Elements: Karlsruhe.
109. Nucifora, S., *Determination of uranium and plutonium isotopic content and concentration in nitric acid solutions by thermal ionization mass spectrometry using the total evaporation technique*. 2012, Institute for Transuranium Elements: Karlsruhe.
110. Rasmussen, G., *Elemental analysis at trace levels by ICP-MS*. 2013, Institute for Transuranium Elements: Karlsruhe.
111. Morel, S., *Carbon content assay by Fusion Extraction-Infrared Determination*. 2014, Institute for Transuranium Elements: Karlsruhe.
112. Casteleyn, K., *Nitrogen content assay by Direct Combustion-Thermal Conductivity*. 2011, Institute forTransuranium Elements: Karlsruhe.

113. Wiss, T., *et al.*, *Recent Results of Microstructural Characterization of Irradiated Light Water Reactor Fuels using Scanning and Transmission Electron Microscopy.* JOM, 2012. **64**(12): p. 1390-1395.
114. Volkovich, V.A., T.R. Griffiths, and R.C. Thied, *Raman and infrared spectra of rubidium and caesium uranates (VI) and some problems assigning diuranate site symmetries.* Vibrational Spectroscopy, 2001. **25**(2): p. 223-230
115. N.H.Rohail, *Infrared and X-ray diffraction spectra of ammonium uranyl carbonate.* Materials Chemistry and Physics, 1994. **36**(3-4): p. 241-245.
116. Anderson, A., et al., *An X-ray crystallographic, Raman and infrared spectral study of crystalline potassium uranyl carbonate $K_4UO_2(CO_3)_3$.* Canadian Journal of Chemustry, 1980. **58**: p. 1651-1658.
117. Bastians, S., *et al.*, *Raspite and studtite: Raman spectra of two unique minerals.* Journal of Raman Spectroscopy, 2004. **35**: p. 726-731.
118. Volkovich, V.A., *et al.*, *Vibrational spectra of alkali metal (Li, Na and K) uranates and consequent assignment of uranate ion site symmetry.* Vibrational Spectroscopy, 1998. **17**: p. 83-91.
119. O.V.Nipruk, *et al.*, *Synthesis and Study of Hydrated Uranium (VI) Oxides, $UO_3.nH_2O$.* Radiochemistry, 2011. **53**(2): p. 146-150.
120. R.Gupta, *et al.*, *Study of an improved technique for precipitation of uranium from eluted solution.* Hydrometallurgy, 2004. **71**(3-4): p. 429-434.
121. Debets, P.C. and B.O. Loopstra, *On the uranates of ammonium-II X-ray investigation of the compounds in the system NH_3-UO_3-H_2O.* Journal of Inorganic Nuclear Chemistry, 1963. **25**: p. 945-953.
122. Bachmann, H.-G., *et al.*, *X-Ray powder diffraction and some thermodynamic data for $(NH_4)_4[UO_2(CO_3)_3]$.* Journal of Inorganic Nuclear Chemistry, 1975. **37**: p. 735-737.
123. Graziani, R., G. Bombieri, and E. Forsellini, *Crystal structure of tetra-ammonium uranyl tricarbonate.* Journal of the Chemical Society, Dalton Transactions, 1972(19): p. 2059-2061.
124. Debets, P.C., *X-ray diffraction data on hydrated uranium peroxide.* Journal of Inorganic Nuclear Chemistry, 1963. **25**: p. 727-730.
125. Burns, P.C. and K.-A. Hughes, *Studtite, $[(UO_2)(O_2)(H_2O)_2]$: The first structure of a peroxide mineral.* American Mineralogist, 2003. **88**: p. 1165-1168.
126. Walenta, K., *On Studtite and its composition.* American Mineralogist, 1974. **59**: p. 166-171.
127. Deliens, M., *Metastudtite, $UO_4.2H_2O$, a new mineral from Shinkolobwe, Shaba, Zaire.* American Mineralogist, 1983. **68**: p. 456-458.
128. Price, G.H. and W.I. Stuart, *Thermal decomposition of ammonium uranates*. 1973, Australian Atomic Energy Commission.
129. El-Fekey, S.A., M.N.A. El-Hakim, and N.H. Rofail, *Solid phase decomposition of ammonium uranate.* Thermochimica Acta, 1982. **54**: p. 327-336.
130. El-Fekey, S.A., N.H. Rofail, and M.A. Khilla, *The thermal decomposition of ammonium uranates precipitated from sulphate and nitrate media by urea.* Thermochimica Acta, 1983. **67**: p. 137-146.
131. Sato, T., F. Ozawa, and S. Shiota, *Thermal decomposition of ammonium uranates precipitated from uranyl nitrate solution with ammonium hydroxide*. Thermochimica Acta, 1985. **88**: p. 313-318.
132. Rajagopal, S., S. Rajagopalan, and C.S.P. Iyer, *Thermal studies on ammonium uranates.* Journal of Thermal Analysis and Calorimetry, 2000. **61**: p. 99-105.
133. J.L.Woolfrey, *The preparation and calcination of ammonium uranates-A literature survey*. 1968, Australian Atomic Energy Commission.
134. Eloirdi, R., *et al.*, *Investigation of ammonium diuranate calcination with high-temperature X-ray diffraction.* Journal of Materials Science, 2014: p. 1-8.
135. Hälldahl, L. and M. Nygren, *Thermal analysis studies of the reactions occurring during the decomposition of ammonium uranyl carbonate in different atmospheres.* Journal of Nuclear Materials, 1986. **138**: p. 99-106.
136. Lee, M.-C. and C.-J. Wu, *Conversion of UF_6 to UO_2: A quasi-optimization of the ammonium uranyl carbonate process.* Journal of Nuclear Materials, 1991. **185**: p. 190-201.

137. Kim, E.H., *et al.*, *Thermal decomposition kinetics of ammonium uranyl carbonate.* Journal of Nuclear Materials, 1994. **209**: p. 294-300.
138. Sato, T., *Thermal decomposition of uranium peroxide hydrates.* Journal of applied Chemical Biotechnology, 1976. **26**: p. 207-213.
139. Baran, V. and M. Tympl, *Thermal Analysis of Sodium Uranates*. Zeitschrift für anorganische und allgemeine Chemie, 1966. **347**(3-4): p. 184-190.
140. *Glossary of Morphology Terms* 12th August 2009 [cited 29th August 2014; Available from: http://www.nist.gov/lispix/doc/particle-form/part-morph-gloss.htm.
141. Siebert, F. and P. Hildebrandt, *Theory of Infrared Absorption and Raman Spectroscopy*, in *Vibrational Spectroscopy in Life Science*. 2008, Wiley-VCH Verlag GmbH & Co. KGaA. p. 11-61.
142. *Standard Guide for Raman Shift Standards for Spectrometer Calibration*. 2002, ASTM International.
143. Degen, I.A. and G.A. Newman, *Raman spectra of inorganic ions.* Spectrochimica Acta, 1993. **49A**(5/6): p. 859-887.
144. Edwards, H.G.M., *et al.*, *FT-Raman spectroscopic study of calcium-rich and magnesium-rich carbonate minerals.* Spectrochimica Acta Part A: Molecular and Biomolecular Spectroscopy, 2005. **61**(10): p. 2273-2280.
145. Ho, D.M.L., *Analysis of Uranium Ore Concentrates using Handheld Raman Spectrometer*, in *JRC Technical Reports*. 2013, Institute for Transuranium Elements: Germany.
146. Berlizov, A., *et al.*, *Assessing Capabilities of Handheld Raman Spectrometer FirstDefender RM for Complementary Access Applications*. in *Esarda 35th Annual Meeting*. 2013. Gruges, Belgium: European Safeguards Research and Development Association.
147. Fryling, M., C.J. Frank, and R.L. McCreery, *Intensity Calibration and Sensitivity Comparisons for CCD/Raman Spectrometers.* Applied Spectroscopy, 1993. **47**(12): p. 1965-1974.
148. Long, D.A., *Raman Spectroscopy*. 1977, Great Britain: McGraw-Hill, Inc.
149. Prip-Buus, C., *et al.*, *Role of aluminium in the silicate network: In situ, high-temperature study of glasses and melts on the join SiO_2-$NaAlO_2$.* Geochimica et Cosmochimica Acta, 1996. **60**(10): p. 1727-1737.
150. Shi, H., M. Chu, and P. Zhang, *Optical properties of UO2 and PuO2.* Journal of Nuclear Materials, 2010. **400**(2): p. 151-156.
151. Ho, D.M.L., *et al.*, *Applicability of Raman Spectroscopy as a Tool in Nuclear Forensics for Analysis of Uranium Ore Concentrates.* Radiochimica Acta, 2013. **101**(12): p. 779-784.
152. Gerrard, D.L. and H.J. Bowley, *Instrumentation for Raman Spectroscopy*, in *Analytical Instrumentation Handbook*, G.W. Ewing, Editor. 1990, Dekker. p. 313-335.
153. Eriksson, L., *et al.*, *Multi- and Megavariate Data Analysis: Principles and Applications*. 2001: Umetrics Academy.
154. Muehlethaler, C., G. Massonnet, and P. Esseiva, *The application of chemometrics on Infrared and Raman spectra as a tool for the forensic analysis of paints.* Forensic Science International, 2011. **209**(1–3): p. 173-182.
155. Ferraro, J.R., K. Nakamoto, and C.W. Brown, *Chapter 5 - Analytical Chemistry*, in *Introductory Raman Spectroscopy (Second Edition)*, J.R. Ferraro, K. Nakamoto, and C.W. Brown, Editors. 2003, Academic Press: San Diego. p. 267-293.
156. McCreery, R.L., *Raman Spectroscopy for Chemical Analysis*, ed. J.N. Winefordner. 2000, Canada: John Wiley and Sons, Inc
157. Pointurier, F. and O. Marie, *Use of micro-Raman spectrometry for nuclear forensics*, in *International Conference on Advances in Nuclear Forensics: Countering the Evolving Threat of Nuclear and Othe Radioactive Material out of Regulatory Control*. 2014, International Atomic Energy Agency: Vienna, Austria.
158. Pointurier, F., *et al.*, *A comparative study between bulk and particle Raman analysis of uranium ore concentrates for nuclear forensics and safeguards.* in preparation, 2014.
159. Wise, B.M., et al., *Chemometrics Tutorial for PLS_Toolbox and Solo*. 2006, Eigenvector Research, Inc: USA.

160. Nichols, G., *et al., A review of the terms agglomerate and aggregate with a recommendation for nomenclature used in powder and particle characterization.* J Pharm Sci, 2002. **91**(10): p. 2103-9.
161. Jillavenkatesa, A., S.J. Dapkunas, and L.-S.H. Lum, *Particle Size Characterization*. 2001, National Institute of Standards and Technology: Washington. p. 164.
162. Huang, J. and K.H. Esbensen, *Applications of Angle Measure Technique (AMT) in image analysis: Part I. A new methodology for in situ powder characterization.* Chemometrics and Intelligent Laboratory Systems, 2000. **54**(1): p. 1-19.
163. Fongaro, L., *et al., Identification/classification of uranium ore concentrates samples from their textured images using Angle Measure Technique (AMT): new perspective in nuclear forensics.* In preparation, 2014.
164. Cordfunke, E.H.P., *On the uranates of ammonium-I The ternary system NH_3-UO_3-H_2O.* Journal of Inorganic Nuclear Chemistry, 1962. **24**: p. 303-307.
165. HERMANS, M.E.A. and T. MARKESTEIN, *Ammonium uranates and UO_3-hydrates-ammoniates.* Journal of Inorganic Nuclear Chemistry, 1963. **25**: p. 461-462.
166. Cordfunke, E.H.P., *Composition and structure of ammonium uranates.* Journal of Inorganic Nuclear Chemistry, 1970. **32**: p. 3129-3131.
167. Stuart, W.I. and T.L. Whateley, *Composition and structures of ammonium uranates.* Journal of Inorganic Nuclear Chemistry, 1969. **31**: p. 1639-1647.
168. URBANEK, V., V. SARA, and J. MORAVEC, *Study of formation and composition of ammonium uranates.* Journal of Inorganic Nuclear Chemistry, 1979. **41**: p. 537-540.
169. Stuart, W.I. and D.J. Miller, *The nature of ammonium uranates.* Journal of Inorganic Nuclear Chemistry, 1973. **35**(6): p. 2109-2111.
170. Steeper, T.J. and J.C. Zink, *Particle-size distribution of ammonium diuranate precipitate.* Proceedings of the Oklahoma Academy of Science, 1974. **54**: p. 83-87.
171. Murty, B.N., *et al., Influence of temperature of precipitation on agglomeration and other powder characteristics of ammonium diuranate.* Powder Technology, 2001. **115**: p. 167-183.
172. Manna, S., *et al., Study of calcinations of ammonium diuranate at different temperatures.* Journal of Nuclear Materials, 2012. **426**: p. 229-232.
173. Sato, T., *Preparation of uranium peroxide hydrates.* Journal of Applied Chemistry, 1963. **13**: p. 361-365.
174. Sato, T., *Thermal decomposition of uranium peroxide hydrate.* Naturwissenschaften, 1961. **48**(2): p. 693.
175. Boggs, J.E. and M. El-Chehabi, *The thermal decomposition of uramium peroxide, $UO_4.2H_2O$.* Journal of American Chemical Society, 1957. **79**(16): p. 4258-4260.
176. Cordfunke, E.H.P. and A.A. Van Der Giessen, *Pseudomorphic decomposition of uranium peroxide into UO_3.* Journal of Inorganic and Nuclear Chemistry, 1963. **25**(5): p. 553-555.
177. C.A.Morais, et al., *Uranium stripping from tertiary amine by sulfuric acid solution and its precipitation as uranium peroxide.* Minerals Engineering, 2005. **18**: p. 1331-1333.
178. Weck, P.F., *et al., Structures of uranyl peroxide hydrates: a first-principles study of studtite and metastudtite.* Dalton Transactions, 2012. **41**(32): p. 9748-9752.
179. Okamoto, H., *O-U (Oxygen-Uranium).* Journal of Phase Equilibria and Diffusion, 2007. **28**(5): p. 497-497.
180. Hoekstra, H.R. and S. Siegel, *The uranium-oxygen system: U3O8□UO3.* Journal of Inorganic and Nuclear Chemistry, 1961. **18**(0): p. 154-165.
181. Deane, A.M., *The infra-red spectra and structures of some hydrated uranium trioxides and ammonium diuranates.* Journal of Inorganic and Nuclear Chemistry, 1961. **21**(3–4): p. 238-252.
182. Wheeler, V.J., R.M. Dell, and E. Wait, *Uranium trioxide and the UO_3 hydrates.* Journal of Inorganic and Nuclear Chemistry, 1964. **26**(11): p. 1829-1845.
183. Cordfunke, E.H.P. and P.C. Debets, *Preparation and properties of a new monohydrate of uranium trioxide ε-UO3·H2O.* Journal of Inorganic and Nuclear Chemistry, 1964. **26**(10): p. 1671-1677.
184. Taylor, J., *The structure of the [alpha] form of uranyl hydroxide.* Acta Crystallographica Section B, 1971. **27**(6): p. 1088-1091.

185. Glodeanu, F., M. Spinzi, and V. Bălan, *Correlation between UO_2 powder and pellet quality in PHWR fuel manufacturing.* Journal of Nuclear Materials, 1988. **153**(0): p. 156-159.
186. Allen, G.C. and N.R. Holmes, *Characterization of Binary Uranium Oxides by Infrared Spectroscopy.* Applied Spectroscopy, 1994. **48**(4): p. 525-530.
187. Sweet, L.E., *et al.*, *Investigation of the polymorphs and hydrolysis of uranium trioxide.* Journal of Radioanalytical and Nuclear Chemistry, 2013. **296**(1): p. 105-110.
188. Eloirdi, R., *et al.*, *Investigation of ammonium diuranate calcination with high-temperature X-ray diffraction.* Journal of Materials Science, 2014. **49**(24): p. 8436-8443.
189. Katz, J.J., G.T. Seaborg, and L.R. Morss, *The chemistry of the Actinide Elements*. 2nd ed. Vol. 1. 1986, New York: Chapman and Hall.